UNIVERSITÄT BAYREUTH

Development of a photo redox flow battery based on nanostructured semiconducting metal oxides as photoanodes

Dissertation

Zur Erlangung des akademischen Grades

“doctor rerum naturalium”

(Dr. rer. nat.)

eingereicht in der

Bayreuther Graduiertenschule für Mathematik und Naturwissenschaften (BayNAT) der Universität Bayreuth

vorgelegt von

Mirco Kai Ade
geboren in Freudenstadt

Bayreuth, 2025

Die vorliegende Arbeit wurde in der Zeit von Dezember 2020 bis August 2025 in Bayreuth am Lehrstuhl für Physikalische Chemie III unter Betreuung von Herrn Prof. Dr. Roland Marschall angefertigt.

Vollständiger Abdruck der von der Bayreuther Graduiertenschule für Mathematik und Naturwissenschaften (BayNAT) der Universität Bayreuth genehmigten Dissertation zur Erlangung des akademischen Grades eines Doktors der Naturwissenschaften (Dr. rer. nat.)

Form der Dissertation: Monographie

Dissertation eingereicht am: 18.09.2025

Zulassung durch das Leitungsgremium: 13.10.2025

Wissenschaftliches Kolloquium: 10.02.2026

Amtierender Direktor: Prof. Dr. Jürgen Senker

Prüfungsausschuss:

Prof. Dr. Roland Marschall (Gutachter)

Prof. Dr.-Ing. Christina Roth (Gutachterin)

Prof. Dr. Matthias Breuning (Vorsitz)

Prof. Dr. Jürgen Senker

Die vorliegende Arbeit ist als Monographie verfasst.

Teile der Arbeit sind bereits in den folgenden Publikationen erschienen:

Seed layer formation determines photocurrent response of hydrothermally-grown WO_3 photoanodes.

Ade, Mirco; Schumacher, Lion; Marschall, Roland

Sustainable Energy & Fuels Bd. 7 (**2023**) Heft 17. - S. 4332-4340

DOI: 10.1039/D2SE01490D

Diese Publikation ist in der vorliegenden Arbeit mit der Literaturstelle [111] zitiert.

Danksagung

Mein größter Dank gilt Prof. Dr. Roland Marschall, welcher mir ermöglichte meine Promotion an seinem Lehrstuhl der Physikalischen Chemie III durchzuführen. Darüber hinaus bedanke ich mich für die langjährige Betreuung und Unterstützung, um komplexe und herausfordernde Problemstellungen während meiner Promotion zu lösen.

Zusätzlich möchte ich mich bei Prof. Dr. Lianzhou Wang und Prof. Dr. Martin Eickhoff für die guten Kooperationen während meiner Promotion bedanken.

Mein Dank gilt auch Dr. Jana Timm für die konstante fachliche Unterstützung und stetige Hilfsbereitschaft bei allen Herausforderungen. Anschließend möchte ich mich bei Dr. Zhiliang Wang für die Betretung an der University of Queensland, Dr. Manuel Alonso-Orts für die ALD-Beschichtungen und Dr. Alexander Karg für die XPS und AFM-Charakterisierung bedanken.

Besonders möchte ich mich bei Dr. Michael Fink für die erfolgreiche Kooperation und die Entwicklung einer neuen Photo-Redox Fluss Batterie bedanken.

Insbesondere möchte ich mich bei Jonas Jungmann für die unersetzliche Hilfe im Labor und bei meinen Kollegen, speziell Judith, Lion, Julian, Teresa und Kevin, für die kollegiale und immer freundliche Atmosphäre bedanken. Darüber hinaus gilt ein besonderer Dank Lion Schumacher und Dr. Morten Weiß für die Durchführung von XPS-Messungen. Allgemein bedanke ich mich bei allen ehemaligen und aktuellen Mitgliedern des Lehrstuhls PC III für die gemeinsamen Unternehmungen und den freundlichen Wettbewerb am Kuchenmontag.

Nicht zu vergessen ist der Dank an all die Studierenden, welche ich während meiner Promotion betreuen durfte und welche mich mit ihren Arbeiten unterstützt haben: Marie Harder, Lukas Mayer, Sebastian Egner, Sofie Knies und Frank Kilchert.

Für die Finanzierung meines Forschungsaustauschs an der University of Queensland in Brisbane bedanke ich mich beim Deutschen Akademischen Austauschdienst.

Diese Arbeit wäre nicht möglich gewesen ohne die persönliche Unterstützung meiner Freunde nicht nur während der Promotion, sondern auch während meines gesamten Studiums. Besonders hervorheben möchte ich dabei Elena Herzog, Paula Wolf und Tobias Krafft. Dazu zählen auch die gewonnen Freunde Christof Bauer, Patrick Länger und Jonas Schwan, welche darüber hinaus die Kaffeepausen oder die Freunde-Freitage zu dem gemacht machen, was sie waren.

Für das Korrekturlesen dieser Arbeit möchte ich mich nochmals bei Elena Herzog und bei Lara Beesdo bedanken.

Zuletzt möchte ich mich bei meiner Familie, die mich über viele Jahre hinweg sowohl finanziell als auch persönlich unterstützt haben und meine Entscheidung, Chemie zu studieren und zu promovieren, von Anfang an uneingeschränkt akzeptiert und ermöglicht haben, bedanken. Ein besonders herzlicher Dank geht dabei an meine Partnerin Lara, die mich vor allem in den schwierigen Momenten emotional aufgebaut und motiviert hat.

Table of Content

Abstract

In this thesis, semiconducting electrodes are investigated for the application of the photo redox flow battery. Thus, a Photo Redox Flow Battery was designed and constructed to enable continuous flow charging during light illumination. As electrode materials were WO_3 and $Mo:BiVO_4$ chosen and optimized in the water oxidation reaction in advance. The goal was to build a $WO_3/Mo:BiVO_4$ heterostructure with high performance for effective charging.

The investigation starts with the WO_3 base for electron extraction. A detailed coating study showed that optimizing the interface by adjusting the seed layer density can influence the performance of the electrode. The highest photocurrent of 1.51 mA cm^{-2} was achieved by a hydrothermally grown electrode using a seed layer synthesized with 5000 rpm and 30 s spinning duration. It resulted in a 2.3 µm thick film with a flat band potential of 0.39 V_{RHE}, an IPCE of 60 % and a separation efficiency of 34 % without using a cocatalyst.

Subsequently, the formation of the $WO_3/Mo:BiVO_4$ heterostructure was analyzed in detail. The dip-coating parameters, the role of the individual materials and their contribution to the heterostructure, as well as different morphologies of WO_3, were evaluated. The performance was found to be better when $Mo:BiVO_4$ serves as the absorber and WO_3 functions as the electron extractor for charge carrier separation. Additionally, it was shown that different layer structures can be achieved by adjusting the dip coating parameters regardless of the WO_3 morphology.

In addition, the conversion of WO_3 to α-$SnWO_4$ was studied in this work using a hydrothermal and a coating approach.

Finally, the synthesized electrodes were used in the photo redox flow battery. The stability of the electrodes and the optimal operating voltage for photo-assisted charging of the battery were investigated.

Kurzfassung

Die vorliegende Arbeit behandelt die Optimierung halbleitender Elektroden für den Einsatz in einer dafür entwickelten und konstruierten Photo Redox Fluss Batterie. Hierfür wurden die Materialien WO_3 und Mo:$BiVO_4$ gewählt und im Voraus in der photoelektrochemischen Wasseroxidation getestet, um deren Eigenschaften zu optimieren. Das Ziel war eine Heterostruktur aus WO_3 und Mo:$BiVO_4$ aufzubauen, welche die Batterie unter kontinuierlichem Fluss und Lichteinstrahlung lädt.

Dabei begann die Untersuchung mit WO_3, welches die Basis für die Heterostruktur bildet und die Elektronenextraktion fördert. Es konnte mit einer ausführlichen Beschichtungsstudie gezeigt werden, dass die Leistung der Elektrode durch die Impfkristallschicht beeinflusst wird. So erreichte die in einer hydrothermalen Wachstumsreaktion synthetisierte Elektrode aus einer rotationsbeschichteten Impfkristallschicht mit 5000 rpm und 30 s Dauer, einen hohen Photostrom von 1.51 mA cm^{-2}, mit einem Flachbandpotential von 0.39 V_{RHE}, einer Filmdicke von 2.3 µm, eine IPCE von 60 % und einer Ladungsträgertrennungseffizienz von 34 % ohne Cokatalysator.

Anschließend wurde die Bildung der WO_3/$BiVO_4$ im Detail analysiert. Hierfür wurden die Tauchbeschichtungsparameter, die Rolle der einzelnen Materialien und deren Beitrag zur Heterostruktur als auch unterschiedliche Morphologin für WO_3 untersucht. Eine bessere Leistung konnte erzielt wird, wenn Mo:$BiVO_4$ den Absorber und WO_3 der Elektronenextraktor zur Ladungsträgertrennung darstellen. Darüber hinaus konnten, durch das Anpassen der Tauchbeschichtungsparameter unabhängig von der WO_3 Morphologie, unterschiedliche Schichtstrukturen realisiert werden.

Darüber hinaus beschäftigte sich diese Arbeit mit der Umwandlung von WO_3 zu α-$SnWO_4$. Dabei wurden sowohl hydrothermale als auch Beschichtungs- und Kalzinierungsverfahren verwendet.

Abschließend wurden die synthetisierten Elektroden in der Photo Redox Fluss Batterie eingesetzt. Hierfür wurden die Stabilität der Elektroden und die optimale Arbeitsspannung für das lichtunterstützende Laden der Batterie untersucht.

1. Introduction

One of the greatest challenges in the 21st century is to achieve a sustainable and reliable energy supply. Despite great technological achievements and ongoing development, the main energy source is still based on endless resources. In 2019 still 86 % of the total primary energy supply is covered by endless resources including fossil fuels and nuclear power. [1,2] The reliance on fossil fuel led to multiple issues, including air pollution, environmental and ecological damage. Since the beginning of the use of fossil fuels during the industrial revolution the emission of greenhouse gases (GHGs) increased steadily. (Figure 1.1) In 2019 the global net anthropogenic GHG emission were 59±6.6 $GtCO_2$-eq which is 54 % higher than 1990. This resulted in 42 % of the historical cumulative GHG emissions since 1850 were emitted after 1989. As a consequence the atmosphere reached concentrations of 410 ppm CO_2 and the global surface temperature increased by 1.1 °C.[3,4]

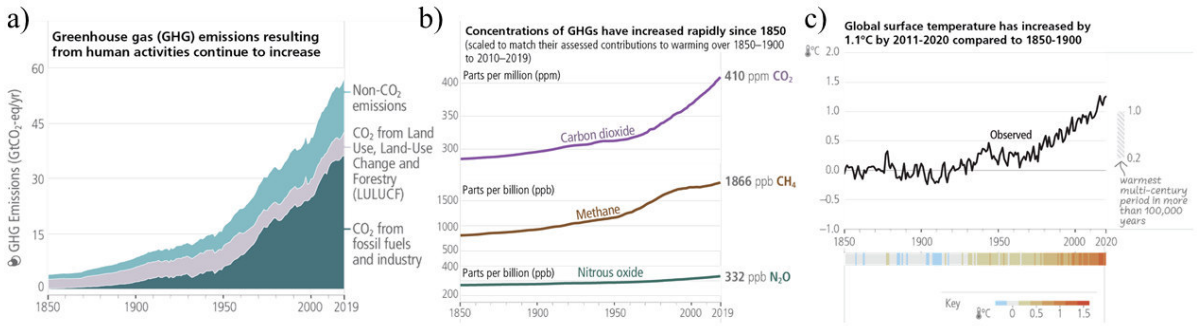

Figure 1.1: a) The global greenhouse gas emissions from human activities between 1850-2019 divided into non-CO_2, Land-Use Change CO_2 and CO_2 from fossil fuels and industry. b) The concentration of the three most common GHGs CO_2, CH_4 and N_2O in the atmosphere since 1850. c) The global surface temperature variation from 1850 to 2019. This data was retrieved from the Climate Change Report 2023 reported by the Intergovernmental Panel of Climate Change (IPCC).[3]

If the trend of the GHGs emission continues, the global surface temperature is expected to rise to 4 °C by the end of the century. This extreme temperature increase has devastating effects on the world.[5–7] Entire areas of the world are becoming uninhabitable for humans due to heat-humidity risks. In the equatorial region there is a risk of losing up to 100% of the living species and crop production and fishing are becoming harder and more expensive. Additionally, the usage of hydrocarbons will lead eventually to the expire of natural reserves. Based on the global growth of energy demand the coal reserves will expire in 114 years, the oil reserves in 51 years and the natural gas reserves in 53 years.[8] Beyond that an important aspect is that a that not all fossil reserves are equally distributed, which can lead to strong dependencies and political challenges.[9] All things considered this results in a socio-economic disaster which the world society never faced before.

To avoid this the Paris agreement, which is signed by 197 nations, decided to limit the global warming to a temperature of 2 °C and aim for 1.5 °C to lower the risks and consequences mentioned before.[10] That is why it is important to drastically lower the GHGs emissions as fast as possible in all sectors.[11] The comparison of the sectors shows that with 34 % (20 $GtCO_2$-eq) the energy sector is biggest contributor of the net global GHG emissions followed by the industry with 24 % (14 $GtCO_2$-eq).[3] To change our energy infrastructure to a renewable source can therefore be a deciding step into a sustainable future.

In 2021 a statistical evaluation showed that the world consumed 165.3 PWh of energy with 28.5 PWh were only used for electricity generation.[12] Therefore, it is necessary to have renewable energy source that can provide more than this values to secure growth and stability. Due to is infinite character the sun is an attractive sustainable energy source, and it can provide 1.1 ZWh of energy yearly which exceeds the consumption in 2021 by a million times.[13] (Figure 1.2 a) One of the reasons why solar energy is not the main supplier is the periodicity and inconsistency of this source. To guarantee a constant energy supply it is necessary to combine this technology with sustainable energy storage systems. A solution which is currently pursued is to convert solar energy into chemical energy. This can be bonds in valuable chemicals like hydrogen or methanol or in electrochemical oxidation states as it is used in batteries.

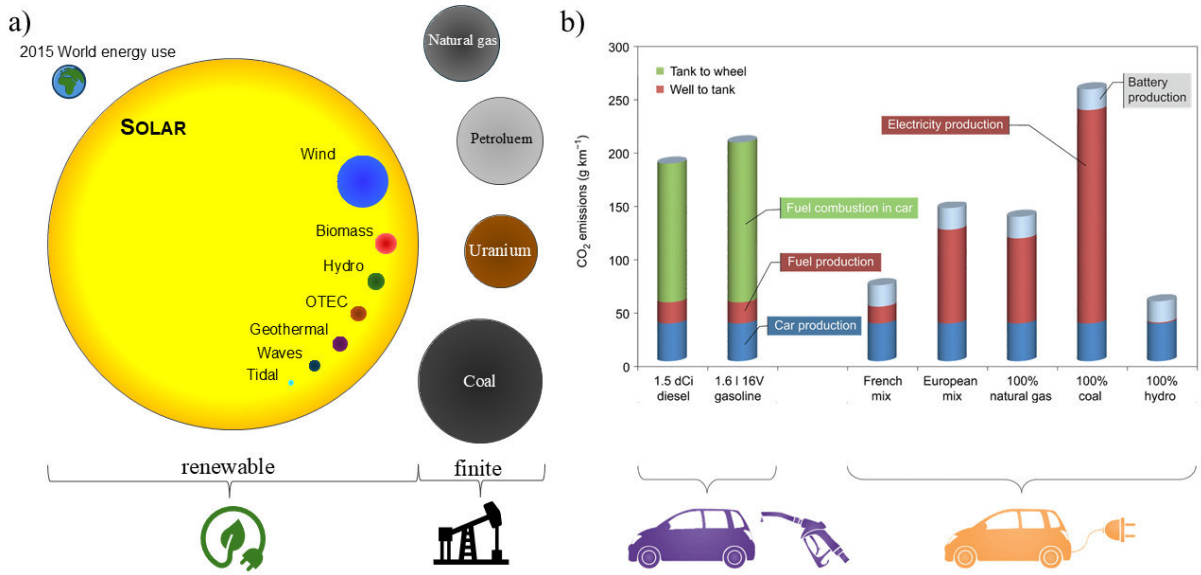

Figure 1.2: a) 2015 estimated finite and renewable planetary energy reserves. The sphere shows the potential annual yield of the sustainable source – adapted with permission from Perez *et al.* (Copyright Elsevier 2022).[14] b) Total CO_2 emission for combustion and electric vehicles with various electricity origins – adapted with permission from D. Larcher & J-M. Tarascon (Copyright Nature chemistry 2015).

Batteries are fundamental pillars of our infrastructure especially in the grid, portable and mobility sector. The quest for these sectors is to obtain high energy densities combined with

low costs. Therefore, it is inarguable to not discuss the sustainability of Li^+-ion battery because it is leading the market. The sustainability of Li^+-ion batteries is mainly driven by the electrode materials. The abundance, mining, processing and manufacturing of the electrodes is determined. Life cycle assessments (LCA) estimations have revealed that more than 75 kg of CO_2 are getting emitted to make a 1 kWh Li^+-ion battery.[15] Furthermore, Li and Co are not widely abundant elements which leads to geopolitical issues. In addition, in the case of a battery it is always important to discuss the origin of the stored electricity. For example, if the electricity used in electric vehicles is only produced by coal in can exceed the CO_2 emissions of standard gasoline.[15,16] (Figure 1.2 b).

Therefore, hydrogen can be a good alternative because there are no direct GHGs emission in hydrogen fuel cells, and it provides a high gravimetric energy density of 143 MJ kg^{-1}.[2,17] Water as source of hydrogen would make it a circular process, and it can be further used in industrial established chemical processes like Haber-Bosch and Fischer-Tropsch synthesis.[18] However, currently the main source of hydrogen is produced by steam reforming. In this process, nine tons of CO_2 are created during the production of one tons of hydrogen.[19,20] To replace the steam reforming it needs an economically attractive process that can compete with the cost of 0.96 \$ kg^{-1} hydrogen.[21] Despite that, the long-term hydrogen storage is still complicated and dangerous because high pressure cryogenic conditions are needed.

An alternative process is the conversion of sunlight into a hydrogen using photocatalysis and photoelectrochemistry of water. This method uses light absorbing semiconductors to convert photons into charge carriers, which is described in detail in the theoretical background (chapter 3).

This approach provides green hydrogen, but its currently still limited by the high cost due to the low efficiencies that can be achieved.[22] Increasing the efficiencies by developing low cost, abundant , highly stable semiconductor is a promising approach to make this process competitive.

Since the discovery of the photoelectrochemical water splitting, the research focused on transition metal oxides due to their abundance and low cost.[22–26] Metal oxides like WO_3, $BiVO_4$ or $ZnFe_2O_3$ are natural semiconductors and are feasible to absorb visible light which is discussed in detail later in the theoretical background (chapter 3.6).

To conclude, it is necessary for the transition from fossil fuels to sustainable alternatives to have a low cost, easy scalable and efficient storage method to enable the sun to be the main energy source. Therefore, this thesis focuses on a new approach to address these criteria with a photo redox flow battery (PRFB). (Figure 1.3)

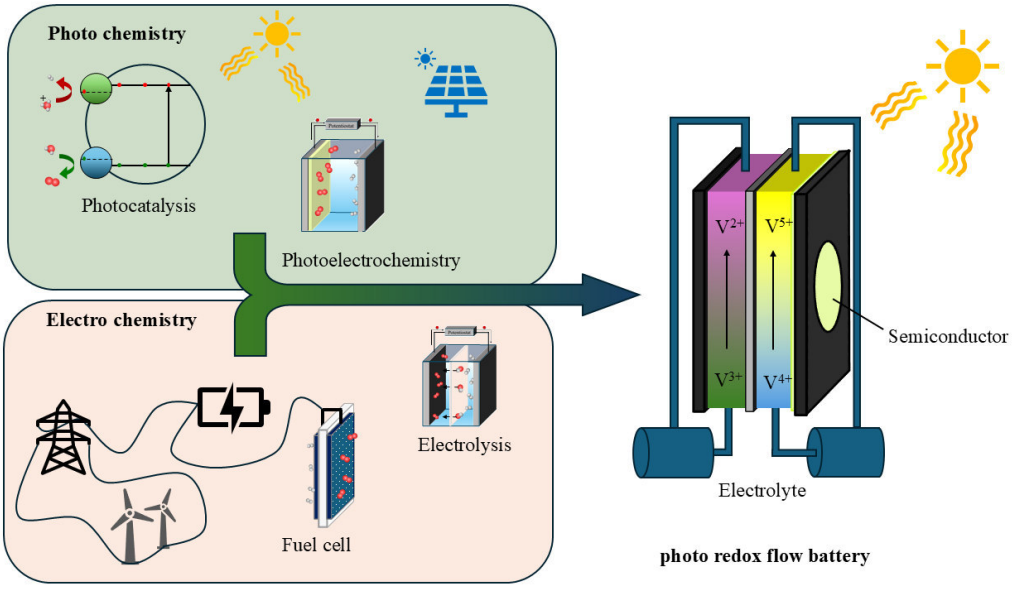

Figure 1.3: The photo redox flow battery is combining the idea of harvesting solar light by using a semiconductor with electro chemistry by directly charging a battery. The illustration shows the vanadium photo redox flow battery which is used in this thesis.

This technology combines the advantages of the chemical energy storage of an accumulator with the solar energy conversion of photo electrochemistry. The advantage of a redox-flow battery is that its capacity can be adjusted by the size of the electrolyte tanks. Especially the vanadium electrolyte is advantageous because of the kinetics and crossovers which are described later in chapter 3.8. The PRFB would be ideal for bridging the inconsistency of renewable energy, and the implementation of a light absorbing semiconductor into the battery would make it possible to charge the battery by illumination. This means that the use of transition metal oxides and the direct harvesting of sunlight the abundancy and the origin of electricity can be addressed simultaneously. In theory it is possible to achieve a higher degree of efficiency than photovoltaic because solar energy is directly converted into chemical energy.

2. Aim of this work

This thesis focuses on building and put in operation a photo redox flow battery with a vanadium electrolyte. Furthermore, the chemical focus is set on synthesizing a semiconductor for efficient light harvesting with the ability to charge the vanadium electrolyte. To minimize possible photocharging durations, the goal is to achieve the highest possible photocurrents. Therefore, a WO_3/Mo:$BiVO_4$ thin film electrode is going to be synthesized via hydrothermal growth of WO_3 and dip coating Mo:$BiVO_4$. The heterostructure WO_3/$BiVO_4$ is known to achieve high photocurrents with up to 6.72 mA cm^{-2}. In addition, *Rohloff et al.* could show that a Molybdenum doping of $BiVO_4$ can increase the performance from 0.23 mA cm^{-2} to 1.9 mA cm^{-2}.[27,28] Therefore, a WO_3 nanostructured surface is going to be combined with the optimized Mo:$BiVO_4$ thin film.

Firstly, the WO_3 hydrothermal growth is going to be optimized to provide effective electron transport to the back contact. Despite having good electric properties the electron extraction of WO_3 to the back contact is still the performance limiting factor.[29] Therefore, the focus is to improve the seed layer formation which is used for the hydrothermal growth. The performance is evaluated with water chopped light voltammetry (CLV), incident photon-to-current efficiency (IPCE), and MOTT-SCHOTTKY analysis. The second step is to use a sol-gel dip coating approach to form a WO_3/Mo:$BiVO_4$ heterostructure. The goal is to optimize the parameters that the nanostructure of WO_3 remains. Additionally, it is important to cover the entire surface so that the electrolyte is only in contact with the Mo:$BiVO_4$ which is discussed later in this thesis (chapter 3.6.4). Furthermore, the performance is evaluated with the same measurements used for WO_3 to assure comparability.

Every electrode is characterized by UV-Vis spectroscopy, Raman, grazing incidence X-ray diffraction (GIXRD), and scanning electron microscopy (SEM).

The synthesised and characterized electrodes are in the end transferred to the PRFB setup to measure chronoamperometry and if possible, perform photocharging.

3. Theoretical Background

3.1.Semiconductor

The electronic structure of a solid can be described with the band structure model. Herein a solid consists of a valence band (VB), consisting of only occupied states, and a conduction band (CB) formed by unoccupied states. The energy difference between the VB and CB is called band gap E_g. In metals the VB and CB are overlapping or in range of k_BT therefore electrons can be easily exited resulting in conductivity. In an insulator the band gap is > 4 eV which makes it impossible to excite electrons without an extreme external force.

Semiconducting materials are the connecting link between conductor and insulator. They exhibit a band gap between 0 and 4 eV and can be divided into two categories.[30] A direct semiconductor is defined by having the conduction band minimum at the same wave vector (*k*-vector) as the valence band maximum. This des Therefore, a photon *hv* can be absorbed and generate an electron-hole pair. Instead, in an indirect semiconductor the CB minimum and VB maximum are located at different *k*-vectors. The absorption of a photon is for an indirect semiconductor only possible if it is coupled with a phonon *hω* (Figure 3.1).

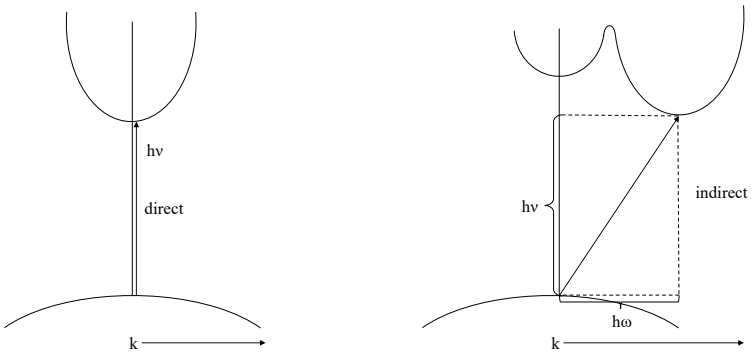

Figure 3.1: Optical excitement of a direct and indirect semiconductor by illumination of a photon *hv*. The indirect semiconductor excitement is coupled with a phonon *hω*.

Considering the FERMI level, it is possible to classify semiconducting material further. The FERMI level E_F is defined by the electron occupation probability to be 0.5. In an n-type semiconductor this probability is shifted to the conduction band whereas in a p-type semiconductor it is shifted to the valence band (Figure 3.2).

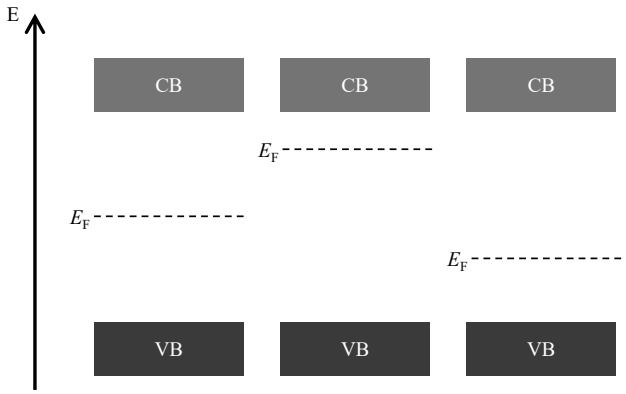

Figure 3.2: The scheme illustrates the different types of semiconductors categorized by the position of the FERMI level E_F. A undoped on the left, a n-type in the middle and p-type semiconductor on the right.

3.2.Semiconductor metal interface

In an isolated case the FERMI level and the band structure are constant throughout the material, as shown in Figure 3.2. If the semiconductor is in contact with a metal with a different FERMI level an electron transfer is happening to equalize the difference. The FERMI level come to an equilibrium which causes the material to form a space charge layer W as shown in Figure 3.3. It is dependent on the FERMI level of the semiconductor if a depletion or accumulation layer is formed. Is the FERMI level of the semiconductor higher than the FERMI level of the metal the electrons will transfer from the semiconductor to metal. This leaves an excess of positive charges in the semiconductor resulting in a depletion layer. The formation of an accumulation layer is exactly vice versa. The excess of the respective charge leads to a band bending at the interface. This is shown in Figure 3.3 and indicated by Φ_{SCL}.

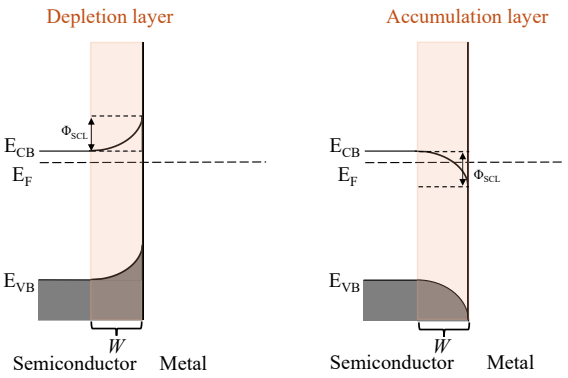

Figure 3.3: Illustration of the space charge layer W at the semiconductor metal interface. The resulting band bending is indicated with Φ_{SCL}.

The depth of the space charge layer W is indirect proportional to the square root of the donor density (N_D). The correlation is given by the formula (3.1) with ε_0 the dielectric field constant, ε the material depending permittivity and e representing the elemental charge.[2,31]

$$W = \sqrt{\frac{2\varepsilon_0 \varepsilon}{eN_D}\left(\Phi_{SCL} - \frac{kT}{e}\right)} \tag{3.1}$$

A metal semiconductor contact can show two different behaviours. In general, it gets distinguished between a SCHOTTKY and a OHMIC contact depending on the electron affinity and the work function. In this thesis fluorine doped tin oxide (FTO) is used as a back contact and due to the high donor density it can be regarded as a metal.[32,33] The difference between the work function and the electron affinity decides if the contact becomes more OHMIC or more SCHOTTKY. It can be stated that the higher the difference between the work function and the electron affinity is the more SCHOTTKY like is the metal semiconductor contact.[34]

Which type of contact is formed is decisive for the charge carrier transfer in the semiconductor. A SCHOTTKY contact is shown in Figure 3.4 and it is known for the characteristic potential energy barrier called SCHOTTKY barrier. The resulting barrier only allows current to flow in one direction of the metal-semiconductor contact. In this SCHOTTKY barrier no current flow is possible until a breakdown voltage is reached. Whereas an OHMIC contact shows linear current to voltage trend following Ohm's law. The charge carrier can therefore be transferred in both directions.

The work function of FTO is Φ_M = 5.00 eV [32] and the electron affinity of WO_3 is EA_{HL} = 5.13 eV [35]. Therefore, the small difference of 0.13 eV shows that contact between FTO and WO_3 has OHMIC character. To fully understand the system, it is also important to consider the semiconductor-electrolyte contact and the semiconductor-semiconductor heterojunctions.

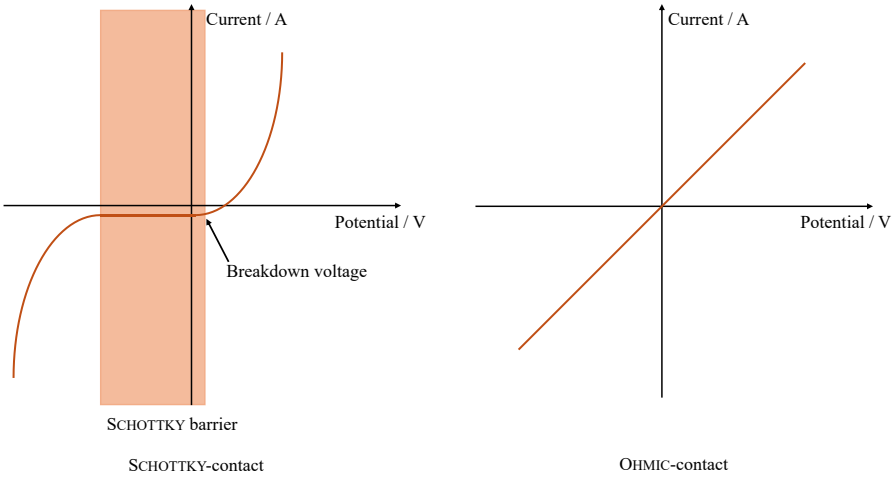

Figure 3.4: Illustration of a current-voltage characteristic from a SCHOTTKY-contact and a OHMIC contact with the SCHOTTKY barrier and breakdown voltage indicated.

3.3.Semiconductor electrolyte interface

If the semiconducting metal oxide is in contact with an aqueous electrolyte an equilibrium between the surface hydroxyl groups and H^+ is formed. The adsorption or desorption of protons leads to pH-dependent charged surface. The equilibrium reactions are shown in (3.2) and (3.3).

$$M\text{-}OH \rightarrow M\text{-}O^- + H^+ \quad (3.2)$$

$$M\text{-}OH + H^+ \rightarrow M\text{-}OH_2^+ \quad (3.3)$$

How strong the charge is, and which charged is formed is dependent on the pH-value and the BRØNSTED acidity of the surface. The special case in which the total surface charge is zero is called point of zero charge, and it is a characteristic value for each surface composition. Due to the auto-dissociation of water, the surface charge of the semiconductor is going to be compensated by the respective counter ions. The resulting decrease in charge over the distance (Figure 3.5) is called double layer and was described by HELMHOLTZ and GOUY-CHAPMAN.[36]

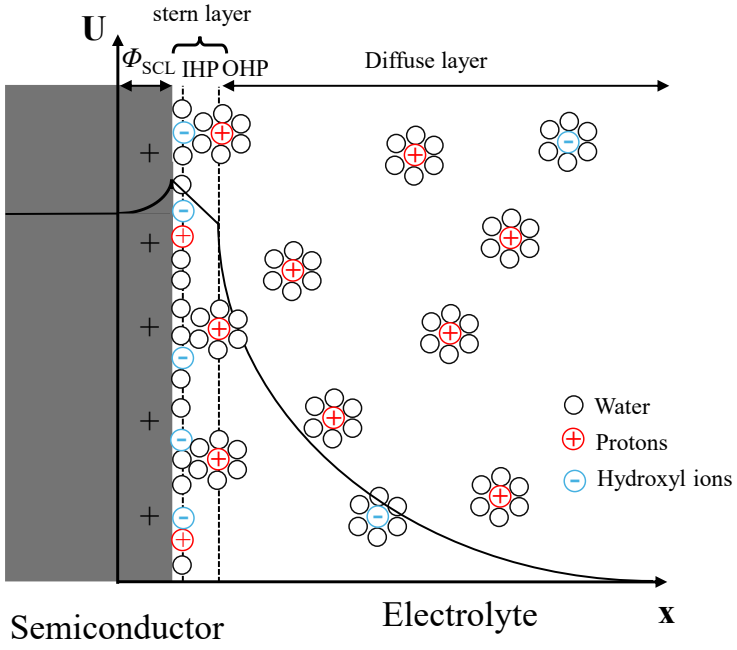

Figure 3.5: Illustration of the potential (black curve) at the semiconductor electrolyte interface in dependency of the distance x. The semiconductor and electrolyte are illustrated in an electrochemical equilibrium. Throughout the stern layer the surface potential decreases linearly. Whereas in the diffuse layer the potential decreases exponentially. Φ_{SCL} is the space charge layer of the semiconductor.

The first and inner layer is called Stern layer, and it consist of the inner HELMHOLTZ plane (IHP) and the outer HELMHOLTZ plane (OHP). To elaborate the IHP is defined as ions which are in direct contact with the surface. Ions that adsorb to the surface at a distance of a few Ångstroms due to their solvation are called OHP. In addition, the second layer is called diffuse layer. Within this layer the remaining surface potential decreases exponentially over distance as it was described by the POISSON-BOLTZMANN model.

Furthermore, the adsorption of protons at the surface leads to a deformation of the crystal lattice. Therefore, surface energy levels form underneath the conduction band minimum. These empty levels can be occupied by free electrons which results in positively charged donors. Due to that the same space charge layer is formed as it was described in the chapter 3.2. Which space charge layer results is again dependent on the FERMI level of the material and the electrolyte.

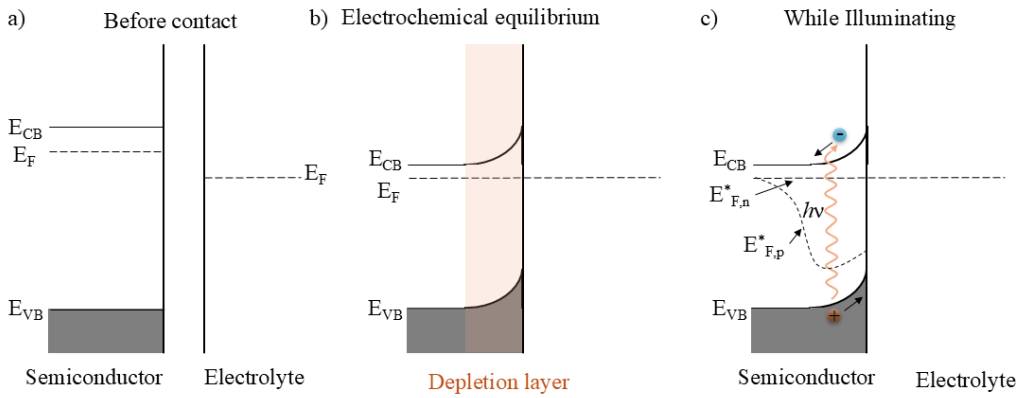

Figure 3.6: Illustration of the formation of a space charge layer. a) Before contact, b) at the electrochemical equilibrium and c) under illumination. The FERMI level is E_F, the quasi-FERMI level of electrons is $E^*_{F,n}$ and the quasi-FERMI level of holes is shown as $E^*_{F,p}$.

It is important to consider that during illumination the FERMI level splits into quasi-FERMI levels. After an absorption of a photon the system is, due to the formation of an electron-hole pair not in an equilibrium anymore. The quasi-FERMI level is therefore a direct indication of the electron and hole concentration in a semiconductor. For instance, in an illuminated n-type semiconductor the change in the electron concentration can be neglected. Therefore, the quasi-FERMI level of electrons ($E^*_{F,n}$) stays constant whereas the increase of the hole concentration results in a decrease in the quasi-FERMI level ($E^*_{F,p}$) of holes (Figure 3.6). The difference between those quasi-Fermi levels is the photovoltage that can be used in redox reactions.

3.4.Semiconductor Heterojunctions

If contacting two semiconductor it is necessary to consider both band positions and FERMI levels to obtain an advantageous heterojunction. There are three possible heterojunctions which are shown in Figure 3.7. A type I heterojunction is formed by one semiconductor having a more positive CB and a more negative VB than the other material simultaneously. This arrangement leads to recombination due to the accumulation on charge carriers at one semiconductor. It is important to notice that a type I heterojunction can still be beneficial. If for example the donor semiconductor suffers from slow surface kinetics, the transfer can increase the charge carrier injection and therefore leads to an overall better performance. In a type II heterojunction, the

VB and CB of one semiconductor are both more negative compared to the other. This leads to an effective charge separation due to the characteristics of electrons and holes moving to lower and higher energy levels, respectively. A type III heterojunction only forms with a large offset in band positions. The VB of one material needs to be more negative than the CB of the other that the complementary charge carriers don't recombine.[37–39]

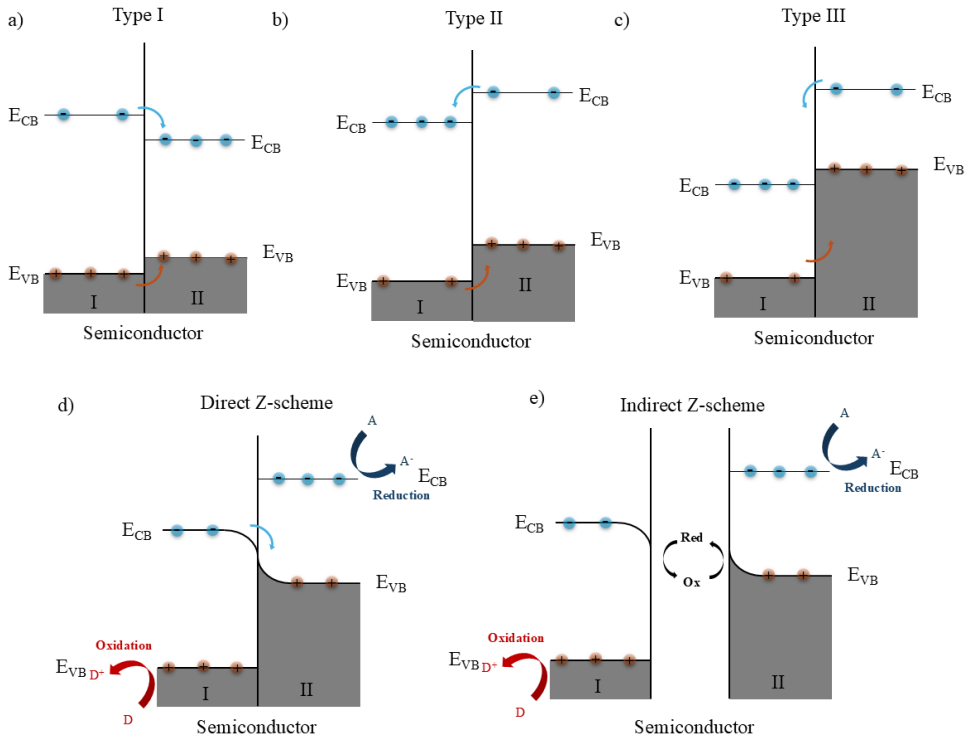

Figure 3.7: Schematic illustration of the charge transfer in different heterojunctions(a-c) and Z-schemes (d,e).

Otherwise, if the recombination of complementary charge carriers is intended it results in different charge carrier mechanism called direct Z-scheme. In that case the oxidation and reduction reaction are spatially separated and occur on different sites of the heterojunction. If the recombination is mediated by a redox agent an indirect Z-scheme is formed. A crucial difference between a type II semiconductor and a Z-scheme is the available redox potential of the semiconductor. Within a type II semiconductor you lose potential because energy difference between the active charge carriers decreases. Whereas in a Z-scheme the potential can be increased due to opposite effect.[40,41]

Additionally, the band bending of the semiconductor is important because it further assists or impedes the charge carrier separation. If the heterojunction forms a SCHOTTKY barrier as it was described in chapter 3.2 the electron flow is hindered which negates the beneficial effect of heterojunction. Therefore, a beneficial band bending combined with a charge separation of a heterojunction is desirable.[42,43]

3.5.Doping

Another common strategy to improve the performance of semiconductors is doping. Herein it is important to distinguish between intrinsic and extrinsic dopant. Intrinsic doping describes native point defects in a crystal lattice. Examples are interstitial defects also called FRENKEL defects, SCHOTTKY defects, vacancies or native substituent (e.g. site exchange of A and B cations in ternary compound AB_xO_y). They are formed by intrinsic defect reaction, exchanging of e.g. oxygen with the gas phase, or nonstoichiometric lattice change. [2]

The Kröger-Vink notation in formula (3.4) and (3.5)describes the possible doping in a binary metal oxide MO.

$$O_O \rightarrow V_O^{\cdot\cdot} + 2\,e' + \frac{1}{2}\,O_2 \tag{3.4}$$

$$\frac{1}{2}\,O_2 \rightarrow V_M'' + 2\,h^{\cdot} + O_O \tag{3.5}$$

Herein the V_x is describing a vacancy in the lattice that leads to accumulation of the respective charge carrier. Prominent examples for intrinsic n-type semiconductor are WO_3[44], $BiVO_4$[45] and $ZnFe_2O_4$[46], whereas CuO[47,48] and $CaFe_2O_4$[49] are belonging to the p-type semiconductor.

Additionally, extrinsic doping introduces elements with a higher or lower valence. In semiconductor metal oxides doping cations with a higher valence (fully occupied *d*-orbitals or empty orbitals) are used to introduce additional donor levels below the CB. Whereas doping the oxygen lattice with less electronegative like nitrogen or phosphor introduces acceptor levels. The difference between these dopant levels and the band position determines the characteristic. If the difference is within ~$2kT$ it can be referred to shallow dopants levels whereas if the difference is larger, it is described as deep dopants levels. An exception are the mid-gap levels which occur if the concentration of dopants is high enough to a form delocalised band inside the band gap (Figure 3.8).[50–52]

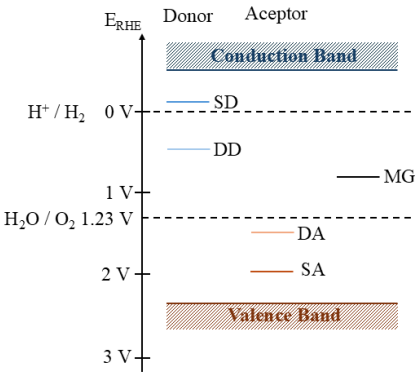

Figure 3.8: a) Schematic illustration of shallow dopant levels (SD, SA), deep dopant levels (DD, DA) and mid-gap levels (MG).

Both intrinsic and extrinsic doping can have an influence on the optical absorption (e.g. reducing the band gap), increasing charge carrier mobility or act as an catalytically active centre.[53–55] It is important to consider that the presence of charged vacancies (e.g. anionic oxygen vacancy) always requires a compensation by a complementary charged iconic vacancy or an excess of the respective charge carrier to retain the charge neutrality.[56]

3.6.Materials

This chapter highlights the materials and heterojunction which are used in this thesis. It elaborates on the physical properties and shows advantages and disadvantages. Furthermore, it summarizes the literature to provide a general understanding of the state-of-the-art. The materials and respective band positions are shown in Figure 3.9.

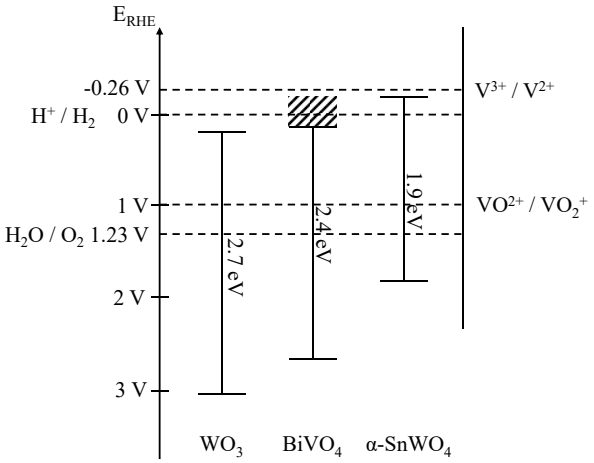

Figure 3.9: The band positions of the used materials in comparison. Distinct lines represent VB and CB positions, whereas dashed rectangles represent a range of possible band positions according to literature.

3.6.1. WO_3

Tungsten trioxide (WO_3) is a metal oxide containing oxygen and tungsten in oxidation state *VI*. It occurs naturally in the form of hydrates. The most common minerals are tungstit, elsomerit and meymacite. At a temperature higher than 588 K the amorphous phase transition irreversible into the crystalline WO_3. The crystalline phase which forms is temperature dependent and can be divided in 5 thermodynamically stable polymorphs. The two low-temperature phases stated monoclinic II (ε-WO_3) between 5-250 K and the triclinic (δ-WO_3) phase between 240-290 K are less common. Instead, the monoclinic I (γ-WO_3) 290-600 K, the orthorhombic (β-WO_3) between 600-1100 K and the tetragonal (α-WO_3) phase from 1010 to 1170 K are often reported and discussed. Beyond 1170 K the "ideal" instable cubic WO_3 can be observed.[57–59] Additionally in presence of cations or water WO_3 can from metastable phases.[60] The hexagonal (h-WO_3) phase can be obtained until 573 K. It converts to γ-WO_3 at higher temperatures.

Furthermore, *h*-WO_3 is known to be less active in photo electrochemistry than γ-WO_3.[61] More importantly, Wang *et al.* could show that the monoclinic II γ-WO_3 can generate high photocurrents of up to 3.7 mA cm^{-2} at 1.23 V vs. reversible hydrogen electrode (RHE) under AM 1.5 G illumination.[62] This corresponded to 93 % of the theoretical photocurrent of WO_3 calculated by integration of the solar radiation spectrum using the bang gap as borders. Therefore γ-WO_3 is further evaluated and described in detail. The γ-WO_3 can be described as a ReO_3 structure which is similar to the perovskite structure AMO_3, without the large A cation at the center. The space group is $P2_1/n$ and the unit cell is shown in Figure 3.10.

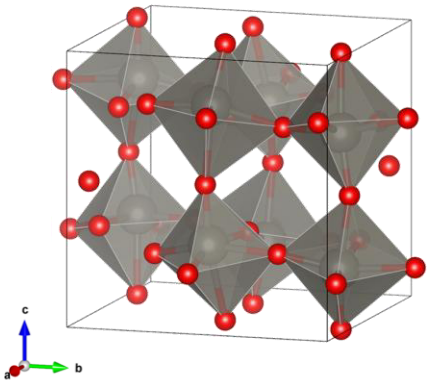

Figure 3.10: The unit cell of γ-WO_3 is indicated as the black line. The gray atoms represent tungsten whereas oxygen is shown as red atoms. The grey area indicates the octahedral coordination.

Tungsten is octahedrally coordinated with 6 oxygen and additionally slightly decentralized. The octahedra are corner-sharing, and tilted due to the decentralization of tungsten. Moreover, the conduction band located at ~0.2 V_{RHE} is formed by the $5d^0$- orbitals of the W^{6+} cations, whereas the oxygen $2p^6$-oribtals contribute to the valence band located at ~2.8 V_{RHE}. This results in a bandgap between 2.6 - 2.7 V.[63,64] The tendency of WO_3 to easily release oxygen out of the anion lattice leads to higher electron density. γ-WO_3 is therefore a naturally intrinsic n-type semiconductor with a FERMI level near to the conduction band.

Due to the n-type character of γ-WO_3 it exhibits outstanding electrical properties. Given its electron conductivity of ~ 12 $cm^{2}V^{1}s^{-1}$ [65], hole diffusion length of ~150 nm [66] and a band gap able to absorb visible light it is a promising material for photoelectrochemical applications. Due to this extensive efforts have been reported to improve properties and efficiencies of WO_3. This includes doping [67], nanostructuring [62,68], co-catalyst decoration [69,70] and loading or building heterojunctions [27,71].

For example, it could be shown that 2D nanoplates of WO_3 grown on a conductive transparent metal oxide exhibit higher photocurrents than 1D nanorods.[72,73] This can be explained by the diffusion pathways for the charge carriers which is described in chapter 0. Furthermore, it was

reported that crystal facet engineering can increase the performance even more.[74] The (002) facet of WO_3 showed the lowest activation energy for oxidizing water. Due to that thin films with enriched (002) exhibit the highest photocurrent reported for WO_3.[62]

Contrary to expectations it could be proven that the electron extraction in WO_3 is still the limiting factor.[29] Therefore it is important to address the interface between WO_3 and the electric back contact, which was not addressed before. Hence this thesis will investigate if optimizing the interface can benefit electron extraction and therefore lead to an increase in performance.

Despites these advantages, it should be noted that WO_3 is not stable in neutral or basic conditions.[75] To operate WO_3 photoanodes it is necessary to maintain a pH value lower than 4. This issue can be resolved by converting WO_3 into other more stable semiconductors like $SnWO_4$.

3.6.2. SnWO4

For tin tungstate there are two polymorphs, the α-$SnWO_4$ and the β-$SnWO_4$ reported. The β-phase exhibits a cubic crystal structure with a larger band gap of 2.68 eV. [76,77] Therefore, it is less interesting for photoelectrochemical applications. Instead, the α-phase with a reported band gap between 1.5-1.9 eV is a promising material due to the ability to absorb a wider range of the solar spectrum. The theoretical maximum photocurrent for the largest reported band gap of 1.9 eV is ~17 mA cm^{-2}.[78–80]

The α-$SnWO_4$ crystal structure can be described as alternating layers of corner linked SnO_4 tetrahedra and WO_6 octahedra in an orthorhombic crystal system (Figure 3.11).

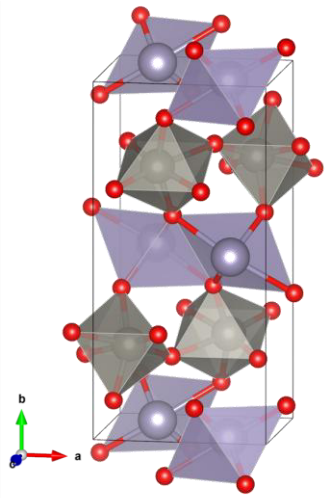

Figure 3.11: The unit cell of α-$SnWO_4$ is indicated as the black line. The gray atoms represent tungsten whereas oxygen is shown as red atoms. The light grey atoms represent Sn. The colored area indicates the polyhedral.

Many studies reported values for the valence and conduction band positions of α-$SnWO_4$. Thin films synthesized via sputtering exhibit flat band potentials between -0.1 to 0.1 V_{RHE} which indicates the conduction band minimum (chapter 0). Whereas the valence band minimum is reported to be 1.5-1.6 V below the fermi level.[79,81,82] This theoretical enables α-$SnWO_4$ to perform both half reactions of water splitting catalysis. Due to stability issues and self-oxidation, α-$SnWO_4$ was mainly tested in photoelectrochemical applications.

Despite the potential photocurrents of α-$SnWO_4$ the reported performances are comparable low.[83] Hence, many efforts were made to convert well performing WO_3 into α-$SnWO_4$ to retain the photocurrent and additionally utilize the smaller band gap. The first conversion of WO_3 was reported in 2015 by Bartlett *et al.* The results showed that with different pH values it is possible to obtain various morphologies. The best performing powder showed a photocurrent of 32 µA cm^{-2} at 1.23 V_{RHE}. [84] Z. Zhu showed further that the phase purity of α-$SnWO_4$ after a conversion is important to address to achieve good performances. The reported hydrothermal conversion of WO_3 exhibit a photocurrent of 0.08 mA cm^{-2} at 1.23 V_{RHE} in presence of a hole scavenger (chapter 3.7.4).[85] More importantly, van de Krol *et al.* could show that it is necessary to avoid the self-oxidation of Sn^{2+} into Sn^{4+}, otherwise α-$SnWO_4$ completely loses the photoelectrochemical activity.[79] Therefore, a few studies have addressed this issue by protecting α-$SnWO_4$ of self-oxidation with a protection layer or sintering in inert atmosphere. The direct conversion of WO_3 film was also reported 2022 by S. Zhu. By using chemical vaper deposition (CVD) of $SnCl_2$ it was possible to convert WO_3 inside a vacuum furnace. The film exhibits a photocurrent of 0.1 mA cm^{-2} at 1.23 V_{RHE}.[82] A different hydrothermal approach of Liu *et al.* was used to successfully grow nail-like α-$SnWO_4$ nanorods on a dense WO_3 film.[86] In addition, there are no examples in the literature present which are reporting a direct hydrothermal conversion of good performing nanostructured WO_3 thin films. Therefore, this thesis is focusing on a hydrothermal conversion of a nanostructured WO_3 thin film.

3.6.3. BiVO4

Bismuth vanadate is a yellow inorganic compound with the formula $BiVO_4$. It naturally occurs in the rare minerals clinobisvanite, pucherite and dreyerite. These minerals also represent the three main crystal phases $BiVO_4$ can exhibit, namely the monoclinic scheelite-type, the tetragonal zircon-type, and the tetragonal scheelite-type.[28,87,88] Within a heat treatment at 670 K - 770 K the tetragonal zircon phase transitions irreversibly into the monoclinic scheelite structure. The transitions between the scheelite polymorphs is reversible and can be induced at a temperature of 528 K.[87] Out of the three crystal phases it could be shown that the monoclinic

$BiVO_4$ (*m*-$BiVO_4$) is photoelectrochemically active whereas the activity of the other is negligible.[89] As a result the *m*-$BiVO_4$ is described in detail and previous work is highlighted.

Given that difference between the *m*-$BiVO_4$ and the tetragonal scheelite $BiVO_4$ (*t*-$BiVO_4$) is only the gamma angle of ~90.3° (*m*-$BiVO_4$) and ~90° (*t*-$BiVO_4$) it is challenging to identify these polymorphs.

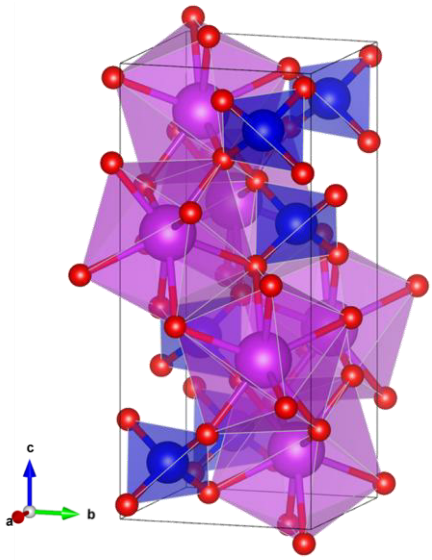

Figure 3.12: The unit cell of *m*-$BiVO_4$ is indicated as the black line. The purple atoms represent bismuth, the blue represents vanadium whereas oxygen is shown as red atoms. The colored area indicates the polyhedral.

As shown in Figure 3.12, bismuth is coordinated with 8 oxygen. Given that 4 oxygen lay in the same plane, 3 oxygen are in the plane below and 1 oxygen is in the plane above this is a distorted non symmetrical surrounding. On the other hand, vanadium is coordinated by 4 oxygen in a tetragonal environment.

More importantly for photo electrochemical application are the physical properties of *m*-$BiVO_4$. The band gap is reported to be 2.4-2.5 eV whereas the band position are under discussion.[89–91] What can be stated is that the valence band is formed by hybridization of Bi *6s* and the O *2p* orbitals. Additionally, the conduction band is formed by V *3d* orbitals. As an n-type semiconductor *m*-$BiVO_4$ exhibit a good hole diffusion length of 70 nm.[92] Additionally, it offers a good stability in neutral aqueous electrolytes without getting self-oxidized.[93,94]

After Kudo discovered the ability of *m*-$BiVO_4$ to photo-oxidize water intensive research was dedicated to optimize and investigate *m*-$BiVO_4$.[95] Many different approaches were reported to synthesis *m*-$BiVO_4$ including precipitation[96–98], hydrothermal synthesis[99–101], sol-gel methods,[28,102,103] and sonochemical methods[104,105].

Notably, to obtain thin films the sol-gel approach with metal organics precursor is the best

method due to possibility to synthesize nanostructured surfaces. Cooper *et al.* were able to show that a nanostructured and polycrystalline film exhibits high efficiencies and doesn't suffer from grain boundaries.[106] Furthermore, van de Krol and Fischer *et al.* showcased that doping of $BiVO_4$ is successful approach to further improve the performance of thin films. In 2013, van de Krol were able to reach 2.3 mA cm^{-2} at 1.23 V_{RHE} with a W-$BiVO_4$ photoanode. By additionally using a cocatalyst the photocurrent increased to 4 mA cm^{-2} at 1.23 V_{RHE}.[107] Following the same approach Fischer were able to reach the highest photocurrent reported of 4.6 mA cm^{-2} at 1.23 V_{RHE} from an unmodified single layer $BiVO_4$ photoanode by using molybdenum as dopant and a CoPi (a cobalt-based water oxidation catalyst developed by Kanan and Nocera[69]) cocatalyst.[28]

Combining the good hole diffusion of $BiVO_4$ and the excellent electron conductivity of WO_3 together with the small band gaps of the materials is promising heterojunction for efficient photoanodes.

3.6.4. WO_3/BiVO4 heterojunctions

To improve efficiency of photoanodes and reduce recombination heterojunctions are a common strategy. A combination of WO_3 and $BiVO_4$ is reported to be type II heterojunction which decreases charge carrier recombination. Additionally, the heterojunction benefits from the extraordinary electron conductivity of WO_3 and the small band gap together with the good hole diffusion length of $BiVO_4$.

The first WO_3/$BiVO_4$ heterojunction was reported from Nosaka *et al.* 2009. Firstly, they showed increased photocatalytic performance due to the heterojunction[108] and continued the investigation with FTO/WO_3/$BiVO_4$ photoanodes in combination with gold nanoparticles for water oxidation.[109] A new solvothermal deposition of a WO_3 nanoroad-array followed by $BiVO_4$ deposition was shown by Grimes *et al*.[110] In particular, the WO_3 photoanodes exhibited a photocurrent of 0.4 mA cm^{-2} and the $BiVO_4$ electrode a photocurrent of 20 µA cm^{-2}. Both single material are known to exhibit higher photocurrents.[28,111] Nonetheless the heterojunctions increased the photocurrent to 0.8 mA cm^{-2} at 1.0 V. This significant enhancement was attributed to the benefits of the type II heterojunctions. Kitamori and Kondo *et al*. where able to boost the WO_3/$BiVO_4$ photocurrent to 6.72 mA cm^{-2}, which is still the highest value reported for a semiconductor photoanode. To achieve this value, a Glancing Angle Deposition of WO_3 was used to fabricate orthogonally-orientated nanorods followed by electrodeposition of $BiVO_4$. The single material WO_3 nanorods exhibited only a ~0.6 mA cm^{-2} whereas a single material photocurrent of $BiVO_4$ is not reported. [27] Since then tremendous efforts were made to investigate the WO_3/$BiVO_4$ heterojunction not only in terms of synthesize and structuring (Table 1**)** but also for the charge carrier dynamics.[112,113]

In table 1 a selection of WO_3/$BiVO_4$ heterojunctions is summarized with the important values for further discussion. Seo *et al.* where the first group that tried to combine good performing WO_3 with good performing $BiVO_4$ by using a combinational hydrothermal and spin coating approach. The resulting photocurrent was enhanced by adding a thin TiO_2 layer to cure deep traps inside the heterojunction.[113] The first only hydrothermal approach was reported by Qurashi 2017 but the photocurrents were comparably low. [114] In 2019 Jang *et al.* used a hydrothermal nanorod and pulsed electrodeposition synthesis to obtain the heterojunction.

Table 1: Literature summary of WO_3/$BiVO_4$ heterojunctions since 2015.

Published	Synthesis	Nano-structure	*j*(WO_3) at 1.23 V_{RHE}	*j*($BiVO_4$) at 1.23 V_{RHE}	WO_3/$BiVO_4$ at 1.23 V_{RHE}	Modification
2017 Yu [115]	Self-assemlby Bi_2WO_6 nanosheets / CVD with $V(acac)_3$	Hierarchical porous film	-	-	~ 1.9 mA cm^{-2} at 1.23 V_{RHE}	FeOOH/NiOOH 5.5 mA cm^{-2} at 1.23 V_{RHE}
2017 Seo[113]	Hydrothermal/ Spin coating	Nanoplates	1.41 mA cm^{-2}	~1.2 mA cm^{-2}	3.17 mA cm^{-2}	Thin TiO_2 layer 3.65 mA cm^{-2}
2017 Qurashi [114]	Hydrothermal	Nanorods	-	-	0.5 mA cm^{-2}	-
2019 Jang [116]	Hydrothermal / pulsed electrodeposition	Nanorods core-shell	1.97 mA cm^{-2}	-	3.23 mA cm^{-2} at 1.23 V_{RHE}	-
2021 Selli [117]	Spin Coating	Thin dense films	-	~0.25 mA cm^{-2}	~1.7 mA cm^{-2}	-
2021 Yu and Wang [118]	Hydrothermal/ Soaking	Nanoflakes	0.60 mA cm^{-2} at 1.6 V_{RHE}	-	1.2 mA cm^{-2} at 1.6 V_{RHE}	Hydrogen treatment + CoPi deposition 2.3 mA cm^{-2} at 1.23 V_{RHE}

~ represent that the value was not stated in the publication but it's an approximate value referred to a graph.

The WO_3 exhibited good performance whereas it was not stated what the single $BiVO_4$ photoanode can achieve. However, the heterojunction boosted the performance to 3.23 mA cm^{-2} at 1.23 V_{RHE}. An interesting layer thickness dependence was reported by Selli *et al.* The results were that a layer thickness of 75 nm of $BiVO_4$ was determined to be the best in a WO_3/$BiVO_4$ heterojunction. It is important to mention that this study was performed with dense films using 200 nm thin WO_3 films.[117] Based on this Selli *et al.* reported additionally an investigation on light absorption of this heterojunction. Herein it was stated that the performance of WO_3/$BiVO_4$ can be enhanced if a majority of light gets absorbed by $BiVO_4$.[119] These results need to be discussed critically due to the thin layers of $BiVO_4$ and WO_3 ranging between 15 – 160 nm and the experimental front side illumination. WO_3 is known to have a low absorption coefficient and therefore needs a sufficient thickness of 4 µm to contribute

notably.[73] Additionally, the front side illumination of the heterojunction raises the question which part of the visible light is getting absorbed by WO_3 due to the smaller band gap of $BiVO_4$. Finally, a hydrothermal synthesis of WO_3 nanoflakes combined with a soaking of 30 min inside an organic metal precursor solution was used by Yu and Wang *et al.*[118] Again the WO_3 single material photoanode exhibited only a 0.6 mA cm^{-2} at 1.6 V_{RHE} whereas no comparison for a single $BiVO_4$ photoanode was reported.

In this thesis $WO_3/BiVO_4$ should be synthesised by a hydrothermal growth of WO_3 followed by a sol-gel dip coating of $BiVO_4$. The focus here is set to use a good performing WO_3 as a base and additionally take advantage of the doping of $BiVO_4$ to obtain a good performing top layer too. The resulting heterojunctions can be further modified with cocatalyst or protective layer. A high performing $WO_3/BiVO_4$ photoanode should then be used as an anode in photo redox flow battery to directly charge the battery by illumination.

3.7.Photoelectrochemistry

The photoelectrochemistry (PEC) utilizes the energy provided by the sun to perform electrochemical reactions. The light harvesting material is therefore the most important component in a photoelectrochemical cell. A semiconducting metal oxide with suitable band gap to absorb light is used as an electrode whereas the counter electrode is usually metal like Pt. A simple illustration of a PEC cell is shown in Figure 3.13a. The addition of a potentiostat enables an electrocatalytic reaction even if the band positions of the semiconductor used would not allow it.

If a photon is absorbed, the electron-hole pair inside the material experiences an external driving force. The electrons diffuse to the back contact and are transported within the outer circuit to the counter electrode. On the other hand, the holes move to the surface due to the band bending at the semiconductor electrolyte interface (Figure 3.13b).

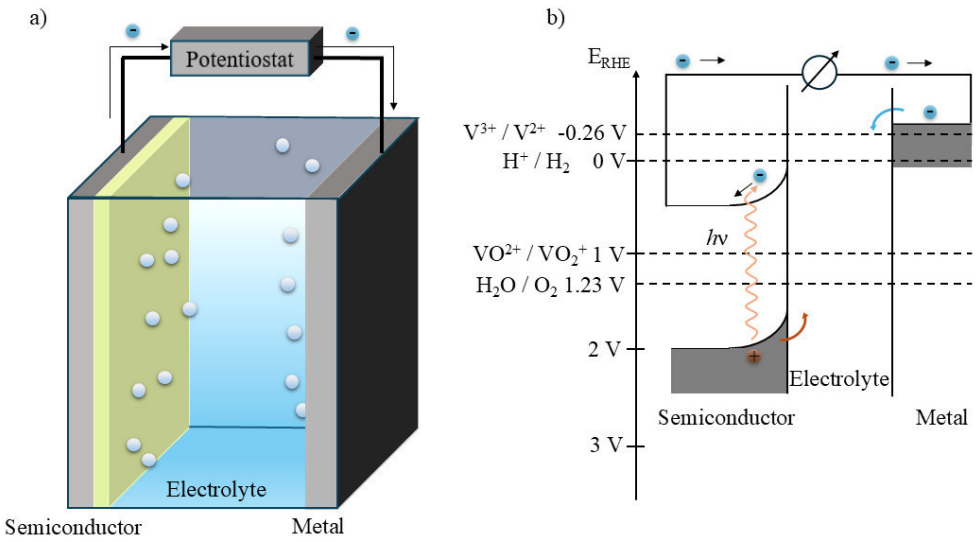

Figure 3.13: Schematic illustration of a a) PEC cell and b) charge transfer inside a semiconductor PEC cell.

The photoelectrochemical water oxidation is one of the most investigated redox reaction due to the possibility to convert regenerative energy into hydrogen as an energy carrier.[120–123] The two half reactions performed in an acidic environment are shown in equation (3.6 and (3.7.

$$4\ H^+ + 4\ e^- \leftrightarrows 2\ H_2 \quad E^0_{red} = 0.00\ \text{V vs. RHE} \tag{3.6}$$

$$2\ H_2O + 4\ h^+ \leftrightarrows 4\ H^+ + O_2 \quad E^0_{ox} = -\ 1.23\ \text{V vs. RHE} \tag{3.7}$$

The anode reaction is considered to be the more challenging and efficiency-limiting reaction due to the necessity of agglomerating four holes at the surface. Therefore, optimizing the photoanode to improve charge carrier transport and suppress recombination is a promising approach. Intensively researched photoanodes are e.g. WO_3, $BiVO_4$ and $ZnFe_2O_4$ due to already discussed advantages in chapter 3.6. [120–123]

It should be noted that the photo electrochemical water oxidation is a thermodynamically uphill reaction. By using the standard reaction conditions (T = 298 K, p = 10^5 Pa, c = 1 mol L^{-1}), the potential difference $\Delta E = -1.23$ V and the equation (3.8 it is possible to calculate the GIBBS free energy of + 237 kJ mol^{-1}.

$$\Delta G = -nF\Delta E. \tag{3.8}$$

This demonstrates the necessity of highly active and efficient photoanodes to facilitate water oxidation. Various approaches can be used to improve the efficiency of photoanodes including nano structuring, using a cocatalyst or hole scavenger. These methods are described in detail below.

3.7.1. Nano structuring and charge carriers

Nano structuring is an established approach to improve the performance of photoanodes due to the shorter diffusion pathways of the charge carriers. Figure 3.14 illustrates the difference between dense and nano structured thin films.

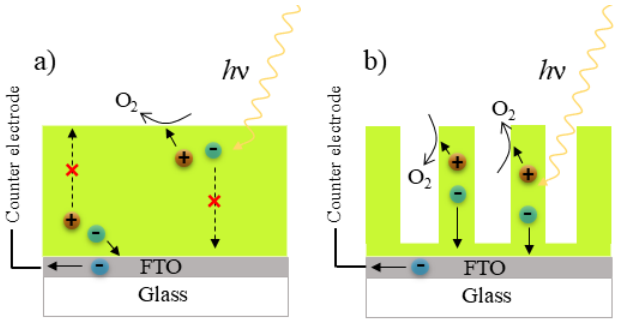

Figure 3.14: A schematic illustration of the diffusion pathways in a) a dense film and b) hierarchical orientated nanorods.

The large aspect ratio of 1D and 2D structured surfaces offer short diffusion pathways while retaining good light absorption.[124–126] Another type of nano structured surfaces can be obtained by porosity. The porous materials also feature short diffusion pathways while providing high surface areas. Porous materials can be divided into three groups. Pore sizes between 0.2–2 nm are defined as microporous, while pores between 2–50 nm and larger than 50 nm are referred to as mesoporous or macroporous respectively. Due to their large pore volumes while offering high surface area mesoporous nano structures have been extensively studied in the last decades.[127,128]

To gain a deeper understanding of charge carrier mobility and its limitations it is important to address each separately. In photoelectrochemistry a simple approach to acquire knowledge about holes and electrons is to change the direction of illumination. By illuminating the electrode from the front (semiconductor-electrolyte interface) or back side (semiconductor-metal interface) it is possible to determine the performance limiting carrier. If the electrode is illuminated from the front side the major charge carriers are generated close to the electrolyte interface. The diffusion path for holes therefore is shorter than for the electrons. If the measured photocurrent is higher than for back side illumination, then the holes are the limiting charge carriers inside the material. For the back side illumination, the conclusion is *vice versa*. In Figure 3.15a a photocurrent measurement from the front and back side illumination is shown.

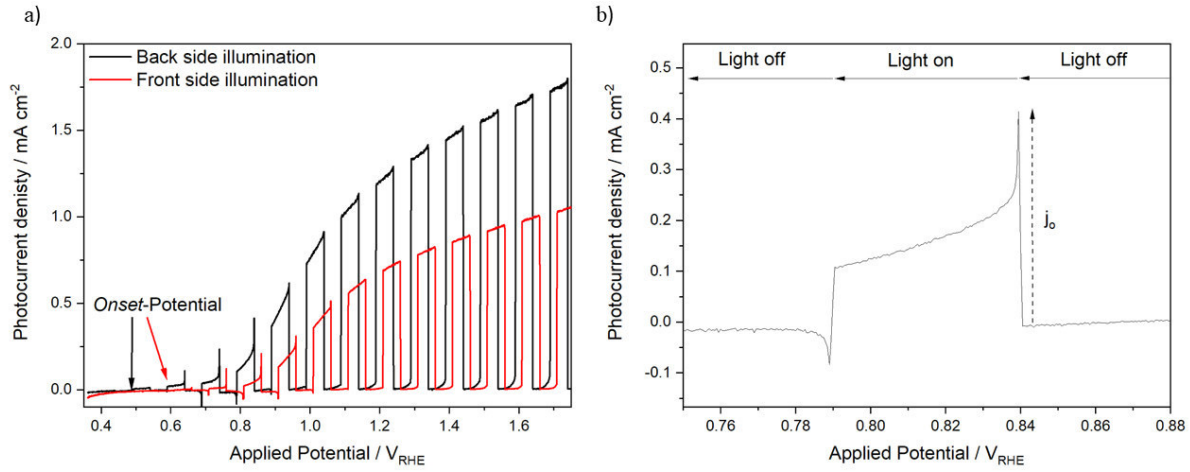

Figure 3.15: a) Linear sweep voltammetry measurement with periodic front (red) und back (black) side illumination of a photoelectrode. b) Magnification between 0.75 – 0.88 V_{RHE}. Straight line indicates light periodicity, dashed line indicates initial photocurrent j_0.

In Figure 3.15b one light period is highlighted to further elaborate the mechanism behind the current measurement. Once the light is switched on, an immediate sharp increase in current is observed, which is referred as the initial photocurrent j_0. Due to recombination within the material, the photocurrent slowly decay until it reaches a steady state when recombination and charge carrier generation have reached an equilibrium j_{SS}. Once the light is switched off, the current drops to a negative value before reaching the origin again. This negative spike is caused by hole agglomeration at the surface and slow kinetics at the surface. Such spikes are called anodic und cathodic transients and provide further insides into the charge carrier dynamics. Anodic transients can be addressed by improving electron extraction (e.g. electron extraction layer), whereas cathodic transients can be reduced by using cocatalysts or hole scavengers.[129,130]

3.7.2. Energy efficiency

Energy efficiency is a key metric for evaluating the performance of a PEC cell and can be determined either directly or indirectly. A direct measurement is desirable as it determines the amount of H_2 produced by the cell and thus allows a clear indication of the energy conversion from solar power to chemical energy. For this reason, the direct measurement is called solar to hydrogen (STH) efficiency and is defined as:

$$\eta_{\mathrm{STH}} = \frac{y_{\mathrm{H_2}} G^0_{\mathrm{f,H_2}}}{P_{\mathrm{Light}}} \tag{3.9}$$

Here y_{H_2} represents the amount of hydrogen per area produced by the cell, G^0_{f,H_2} the GIBBS free energy for the formation of hydrogen and P_{Light} the intensity of the used light source.

The measured photocurrent of the cell is used as indirect determination. Although the efficiency of PEC-cell is indicated, the actual oxidation and reduction products are neglected. This is especially misleading if holes or electron scavengers are present. Assuming that all photogenerated electrons contribute to a water oxidation reaction, the efficiency is defined as follows:

$$\eta_{\mathrm{STH}} = \frac{j_{\mathrm{photo}} \, (V_{\mathrm{redox}} - V_{\mathrm{real}})}{P_{\mathrm{Light}}} \tag{3.10}$$

In equation (3.10 j_{photo} represents the measured photocurrent, V_{redox} the redox potential of the water splitting reaction and V_{real} the applied potential of the PEC cell.[131] It should be noted that V_{real} refers to the actual voltage formed between the working and the counter electrode. An indirect determination with a reference electrode, as used in the 3-electrode setup leads to wrong results.[2]

To ensure comparability, the American Society of Testing and Materials (ASTM) defined a light source with an air mass (AM) intensity of 1.5 G. This standard simulates a spectrum of the sun light on the earth surface.[132] For an industrial application calculations indicated that an STH efficiency of 10 % must be achieved, considering both engineering and economic standpoints.[133] This would be equivalent to a photocurrent of 8 mA cm^{-2} or 420 µmol $s^{-1}m^{-2}$ at an intensity of 1,000 W m^{-2}.

A different approach to evaluate the performance of a PEC cell is by measuring how many photons contribute to the photocurrent measured in the outer circuit. This is defined as an incident photon to current efficiency (IPCE) and is shown in equation (3.11.

$$\mathrm{IPCE}(\lambda) = \frac{hc}{e}\left(\frac{j_{\mathrm{photo}}(\lambda)}{\lambda P(\lambda)}\right) \tag{3.11}$$

An extension of this model is the absorbed photon to current efficiency (APCE), which additionally includes reflection (R) and transmission (T) losses.

$$\mathrm{APCE}(\lambda) = \frac{\mathrm{IPCE}(\lambda)}{A(\lambda)} = \frac{\mathrm{IPCE}(\lambda)}{1 - R - T} \tag{3.12}$$

Due to good charge carrier separation and surface engineering, high IPCE values of 80% have been reported for materials such as WO_3 and TiO_2.[134,135]

3.7.3. Cocatalyst

The main advantages of using a cocatalyst in a PEC cell is the ability to lower the activation energy of the redox reaction and spatially separate the charge carrier. Using the example of the photoanode in a photoelectrochemical water oxidation, the holes formed by the semiconductor

are transferred to the cocatalyst and are subsequently used to oxidize water (Figure 3.16). A noble metal or an oxygen evolving catalyst (OEC) can lower the activation energy due to fast kinetics compared to the semiconductor. The additional charge carrier separation through the additional interface results in an intrinsic electrical field, further improving the efficiency due to suppressed recombination. Additionally, adsorption to the cocatalyst can change the reaction mechanism, which in turn can influence the selectivity.[136–138]

In a photoelectrochemical measurement, this is visible as a shift in the onset potential and an overall higher photocurrent.

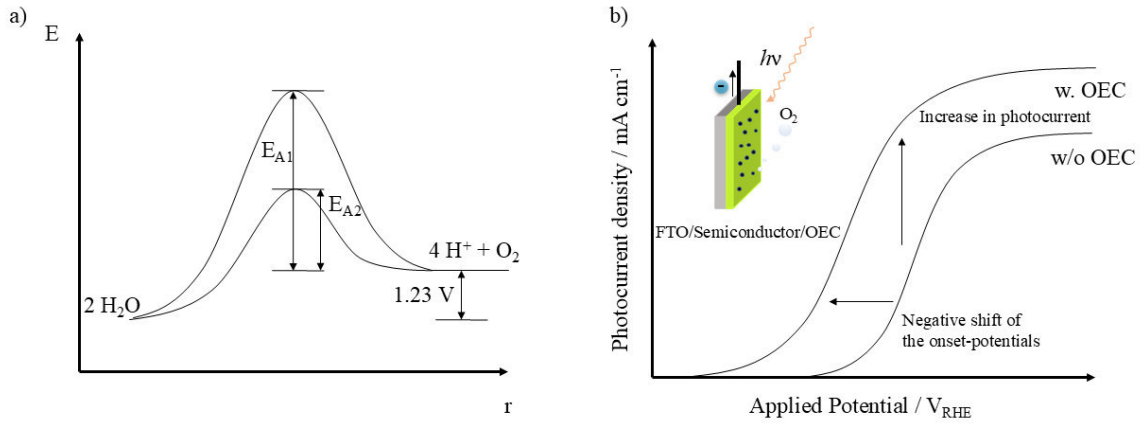

Figure 3.16: Illustration of the cocatalyst effect by a) lowering the activation energy and b) improving the photoelectrochemical performance using the example of water oxidation.

In photoelectrochemical applications, the loading of the cocatalyst is an important factor. High cocatalyst loading can have a negative effect on the efficiency due to shadowing. Cocatalysts not contributing to light absorption cover an area and thereby reduce the amount of photons absorbed. As a result, an optimal cocatalyst loading always needs to be pursued guarantee the best operating conditions.[136–138]

3.7.4. Hole scavengers

A useful tool to study kinetics and evaluate the limiting mechanisms inside a PEC cell are charge carrier scavengers. Charge carrier scavengers can drastically improve either the reduction or oxidation reaction resulting in increased photocurrents. Using the example of water oxidation the measured photocurrent is a product of absorbed photons (J_{abs}), charge carrier separation yield (P_{sep}) and charge carrier injection yield (P_{inj}) to the electrolyte. (3.13)

$$J_{Photocurrent}^{H_2O} = J_{abs} \cdot P_{sep} \cdot P_{inj} \tag{3.13}$$

Hole scavengers (hs) offer a 10 to 100 higher rate constant than water and therefore suppress surface recombination. This is why the charge carrier injection will be 100 % (P_{inj} = 1) and the resulting photocurrent can be described as:

$$J_{Photocurrent}^{hs} = J_{abs} \cdot P_{sep} \tag{3.14}$$

The charge carrier injection yield can be obtained by dividing $J_{Photocurrent}^{H_2O}$ by $J_{Photocurrent}^{hs}$.

It is important to point out that J_{abs} is sensitive to the distribution of the incident light spectrum and can only be compared if the same light source is used. [2,139]

Depending on the hole scavenger used, photocurrent doubling needs to be considered. H_2O_2 for example is known to increase the anodic and cathodic dark current. The reactions are shown in (3.15)(3.15 and (3.16.

$$H_2O_2 + 2\,H^+ + e^- \rightarrow OH^- + OH^{\cdot} + 2H^+ \rightarrow 2\,H_2O + h^+ \tag{3.15}$$

$$H_2O_2 + 2\,h^+ \rightarrow 2H^+ + O_2 \tag{3.16}$$

Whether photocurrent doubling is detected depends also on the semiconductor properties. Whereas this often occurs in III-V semiconductors, [140–142] it had not been detected in hematite electrodes.[2,139,143]

3.7.5. Flat band potential

The flat band potential corresponds to the potential at which the band bending caused by electron transfer between the electrolyte and the semiconductor is compensated (ϕ_{SCL} = 0). This can be achieved by applying a voltage and measuring the capacitance. To better understand the process of flat band potential analysis and the compensation, it is necessary to evaluate the electrical conditions which are present. The nonconductive space charge layer *W* is encapsuled by two conductive plates namely the bulk and the electrolyte and can thus be seen as a capacitor C_W. The same applies for the HELMHOLTZ double layer C_H. Accordingly, the interface can be described as a series connection of capacitors. The total capacitance C_{total} is the reciprocal value of the additive inverse single capacitance shown in equation (3.17.

$$\frac{1}{C_{total}} = \frac{1}{C_W} + \frac{1}{C_H} \tag{3.17}$$

The laws of electricity state that when a voltage is applied to two capacitors in series with unequal capacitance, the capacitor with the lower capacitance will experience a higher voltage. As the capacitance of the space charge layer is generally an order of magnitude lower than the

capacitance of the HELMHOLTZ double layer, the majority of the voltage will drop at the space charge layer and compensate for the band bending.[144]

This electrical fundamentals lead to MOTT-SCHOTTKY equation (3.18 which allows to determine the flat band potential ϕ_{FB}.

$$\frac{1}{C_{total}^2} = \frac{2}{\varepsilon_0 \varepsilon e N_{\mathrm{D}} A^2} \left(\phi - \phi_{\mathrm{FB}} - \frac{k_{\mathrm{B}} T}{e} \right) \tag{3.18}$$

Herein, A represents the electrode surface area, k_{B} the BOLTZMANN constant and T represents the temperature. Understanding that the HELMHOLTZ double layer is pH-dependent and will therefore shift the potential by -59 mV per pH is crucial.[145] To extract the flat band potential, the reciprocal capacitance squared against the applied potential must be plotted and near linear slope extrapolated. The obtained value at the intersection with the x-axis represents the FERMI level or flat band potential of the semiconductor. For an n-type semiconductor, this value is close to the actual conduction band position and is often used for comparison.[2,144]

By determining the donor density N_{D} of the material, it is also possible to calculate the conduction band position. Derived from the MOTT-SCHOTTKY equation the donor density can be defined by using the near linear slope of the MOTT-SCHOTTKY plot (3.19).

$$N_{\mathrm{D}} = \left(\frac{2}{\varepsilon_0 \varepsilon e} \right) \left[\frac{d(1/C_{SCL}^2)}{d\,\phi} \right]^{-1} \tag{3.191}$$

The final calculation of the conduction band position is shown in equation (3.20), and additionally requires the effective electron mass N_{C}. For an n-type semiconductor this value can be approximated to be in the magnitude of $N_{\mathrm{C}} \approx 5 \cdot 10^{19}$ cm^{-3}.[146]

$$E_{\mathrm{LB}} = \phi_{\mathrm{FB}} + \frac{k_{\mathrm{B}} T}{e} \ln \left(\frac{N_{\mathrm{D}}}{N_{\mathrm{C}}} \right) \tag{3.20}$$

Together with the band gap, the position of the valence band can then also be determined (equation (3.21).

$$E_{\mathrm{g}} = E_{\mathrm{CB}} + E_{\mathrm{VB}} \tag{3.21}$$

There are limits to this approach as it relies on assumptions. The electrode surface in equation (3.18 is considered to be perfectly flat and is squared in the denominator. The MOTT-SCHOTTKY plot can therefore lead to wrong results in case of porous or nanostructured surfaces.[147]

3.8.Vanadium Redox-Flow Battery

The storage of renewable energy is one of the emerging technological requirements in our society. Classical batteries such as lead acid batteries and Li-ion batteries can be utilized, but

exhibit significant disadvantages. Lead acid batteries have relatively low energy efficiency and need to handle the toxicity of Pb. On the other hand, Li-ion batteries have poor deep discharge behavior and are dependent on the rare element lithium. A redox flow battery can therefore be a suitable alternative system in which the electrolyte is pumped through an electrochemical cell in a constant flow (Figure 3.17).

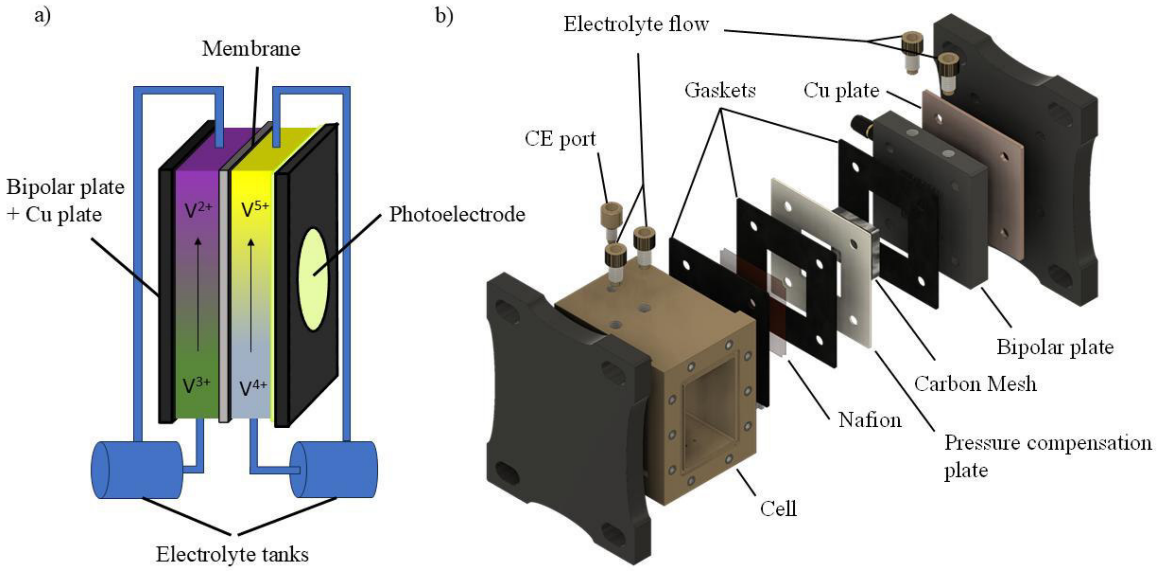

Figure 3.17: a) Schematic illustration of a redox flow battery. b) Exploded-view drawing of the constructed and used RFB in this thesis.

The capacity of a redox flow battery is only limited by the size of the electrolyte tank, while the electrolytes carry a redox active species. In the case of Vanadium redox flow batteries (VRFB) the batterie contains vanadium in four different oxidation states. First reported by M. SKYLLAS-KAZACOS at the University of New South Wales, the system gained the promising properties of an all-vanadium cell. The redox reactions for both half cells are shown in equation (3.22 and (3.23.

$$VO^{2+} + H_2O \leftrightarrows VO_2^+ + 2\,H^+ + e^- \quad E^0 = 1.0\ \text{V vs RHE} \tag{3.22}$$

$$V^{3+} + e^- \leftrightarrows V^{2+} \quad E^0 = -0.26\ \text{V vs RHE} \tag{3.23}$$

The system is characterized by high energy efficiency (up to 80 %), a long lifetime, a flexible design, scalability, and environmentally friendly structures. Furthermore, the electrolyte is a sulfuric acid solution, which is discussed later in chapter 3.8.2. Vanadium exhibits fast kinetics during operation, which enables a rapid change between charging and discharging. Crossover contamination often poisons the redox active species and therefore limits the long-term performance of flow cells or other aqueous based systems. This can be controlled for a VRRFB due to the same redox active element in both half-cell and is described in the following chapter.

These advantages result in an ideal system for the storage of unsteady renewable energy sources like wind or solar power.[148–150]

3.8.1. Crossover

A unique benefit of all vanadium RFB is their resilience to cross-contamination. The diffusion of active redox ions that contaminate the respective half-cell can reduce the capacity of RFBs such as Zn-Br. Those crossover diffusions cannot be avoided in current technology platforms. Therefore, the same species in both half-cells, as present in all vanadium RFBs, can prevent the contamination.

However, vanadium and water crossover indeed affect the capacity of an RFB due to the resulting concentration imbalance. The crossover can be considered as a self-discharging process as the crossed ions can react with the other vanadium ions.[151] The reactions that lead to self-discharging are described in equation (3.24 - (3.29.[152–154]

At the positive electrolyte:

$$V^{2+} + 2VO^{2+} + 2\,H^{+} \rightarrow 3VO^{2+} + H_2O \tag{3.24}$$

$$V^{3+} + VO_2^{+} \rightarrow 2VO^{2+} \tag{3.25}$$

$$V^{2+} + VO_2^{+} + 2\,H^{+} \rightarrow 2V^{3+} + H_2O \tag{3.26}$$

At the negative electrolyte:

$$VO^{2+} + V^{2+} + 2\,H^{+} \rightarrow 2V^{3+} + H_2O \tag{3.27}$$

$$VO_2^{+} + 2V^{2+} + 4\,H^{+} \rightarrow 3V^{3+} + 2H_2O \tag{3.28}$$

$$VO_2^{+} + V^{3+} \rightarrow 2VO^{2+} \tag{3.29}$$

Luo *et al.* demonstrated that the imbalance and crossover during the cycle leads to a decrease in capacity over time.[154] In the cation exchange membrane the vanadium permeability increases in the following order $V^{3+} < VO_2^{+} < VO^{2+} < V^{2+}$.[153] The difference in permeability leads to greater transfer from V^{2+} and V^{3+} to the positive half-cell than from VO^{2+} and VO_2^{+} to the negative half-cell and results in a concentration imbalance.

Furthermore, the water crossover due to the binding water to hydrogen and vanadium ions must also be taken into account. The resulting difference in concentration further promotes osmosis through the membrane. Various studies show that with a cation exchange membrane like

Nafion, the water transfer from the positive to the negative during charge is lower than the water transfer from the negative to positive half-cell during discharge. Since the same amounts of protons are transferred in opposite direction during the cycle, this imbalance can be explained by the water bound to the vanadium ions and the water transfer driven by the osmosis.[155–157] It is therefore crucial to regularly remix and pretreat the electrolyte to ensure optimal conditions in large-scale long term applications.

3.8.2. Vanadium Redox Flow Batterie Mechanism

To reach the highest volumetric and gravimetric energy densities, high vanadium concentrations are necessary. This is limited by the saturation and solubility of vanadium in aqueous electrolytes. A decisive feature of vanadium is the condensation of insoluble vanadium pentoxide at temperatures above 40 °C. V^V dilutes in strongly acidic solutions as yellow VO_2^+ dioxovanadium ions in the hydrated form of $[VO_2^- (H_2O)_4]^+$. The formation of complexes with sulfate and hydrogen sulfate ions in the second coordination sphere induces the deprotonation and decomposition to V_2O_5 at higher vanadium concentrations ($[V^V] > 100$mM). The limited solubility of V_2O_5 (0.25 M) results in precipitation and thereby a loss of energy density (Figure 3.18).[158–160]

Another explanation of the thermal instability of V^V can be the existence of the $[VO_2(H_2O)_3]^+$ complex. This complex is more stable than the $[VO_2^- (H_2O)_4]^+$ complex at low temperature and easily dehydrates to form the neutral $VO(OH)_3$ which finally precipitates as V_2O_5 through deprotonation.[161]

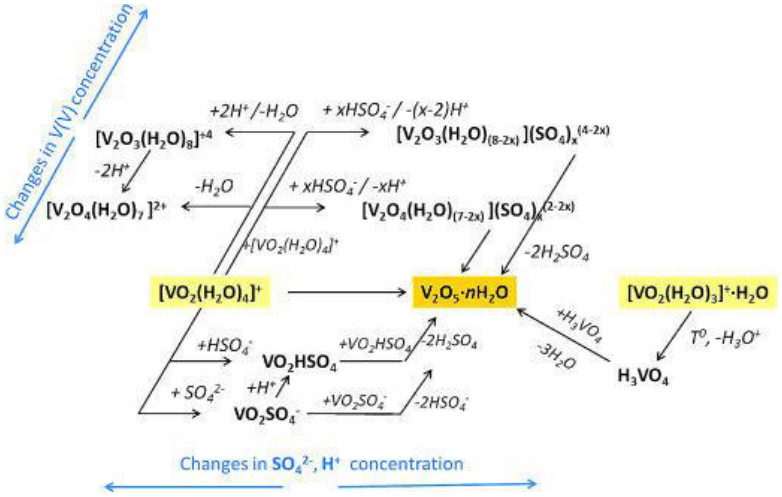

Figure 3.18: Reaction pathways for V^V ions depending on vanadium and sulfuric acid concentrations.[148,162] Reprinted with permission from J. NOACK, N. ROZNYATOVSKAYA and P. FISCHER (Copyright Angewandte Chemie In. Ed. 2015)

Additionally, the V^{IV} species appears as blue-colored octahedral complex $[VO(H_2O)_5]^{2+}$. In presence of high H_2SO_4 concentrations (> 5 M) the complex can undergo ion paring with the sulfate ions.[163,164] In mixed valence (V^{IV}/ V^{V}) electrolytes which correspond to a partially charged battery, additional complexes with a vanadium concentration over 0.8 M and H_2SO_4 concentrations over 3 M can be observed (3.30).[165]

$$VO^{2+} + VO_2^{+} \rightleftharpoons V_2O_3^{3+} \tag{3.30}$$

All these mechanisms influence the stability and the electrochemical behavior of the positive half-cell of an all-vanadium redox flow battery. A few approaches exist to prevent the precipitation of vanadium.

Increasing the acid concentration prevents deprotonation and can stabilize the vanadium complex. However, a high acid concentration can lead to a decrease in solubility of vanadium species in lower oxidation states.[166] The addition of additives like potassium sulfate can increase solubility, but suffers from the disadvantage of being oxidized by V^{V}, leading to a loss of capacity.[167] The final approach to increasing stability is to change the chemical environment. Using chloride containing electrolyte can improve the solubility , but the formation of chlorine gas is a negative side reaction.[168]

To ensure ideal conditions during operation it is therefore important to have a balanced acid concentration and maintain a constant temperature to prevent precipitation. [148,169]

3.9.Photo Redox-Flow Battery

With fossil fuels still accounting for 86%[1] of the global energy mix, the need for new sustainable energy conversion technologies is urgent. Major efforts have been made to research photo responsive batteries that can directly convert solar energy into chemical energy.

A large focus was set on lithium based[170–172] or zinc-based[172–174] light assisted energy storage devices. Only a few examples are known which use dual-liquid active materials as energy carriers, although they exhibit unique advantages such as high flexibility, high reliability, flexible operation and moderate cost in grid-scale energy storage. [175–177]

The first solar redox battery was reported by Hodes *et al.* in 1976. The group used a 3-electrode setup consisting of a S/S^{2-} cathode, an AgS/Ag anode, and polycrystalline CdSe as a photoelectrode. Although the cell showed excellent light responsive properties, the high cost and the toxicity limited the application of this setup.[178] In 2016, McCulloch *et al.* adapted the light responsive battery concept and reported a pH-tunable solar redox flow battery based on a I^{-}/I_3^{-} catholyte and a dye sensitized TiO_2 photoelectrode. As an anolyte the group used anthraquinone-2,7-disulfonic acid (AQDS) to ensure fast electron transfer.[179] Similarly, a

hematite photoelectrode was used together with AQDS/iodide by Khataee *et al*. [180]

The first pure vanadium photo redox flow battery was presented by Wei *et al.* in 2014. The combination of TiO_2 photoanode, a Nafion 117 membrane and a Pt mesh enabled charging during illumination.[181] Following the same approach TiO_2/WO_3[182], TiO_2 nanobelt[183,184], N-doped TiO_2[185], Ti_2O_3[186], TiO_2/Cu_xO[187] and CdS[188] were reported using an pure vanadium electrolyte, too. Importantly, no continuous flow was used in these findings. Instead, they were designed as single cell energy storage systems. The first continuous flow setup was described by Durant *et al.* 2019. In this work, two photoelectrode cells were used, an n-GaP photoanode with a wide band gap and a p-InP photocathode with a narrow band gap.[189]

Additionally, the first heterojunction photoanode was developed 2020 by Sankir *et al.* The photoanode consisted of a thin TiO_2 layer covered by the semiconductor In_2S_3 (Figure 3.19). Sankir reported a photocurrent of 0.72 mA cm^{-2} and a charge separation efficiency of 46 %.[190]

A microfluidic pure vanadium flow cell with a self-doped TiO_2 photoanode was described 2021 by Liao *et al*.[191]

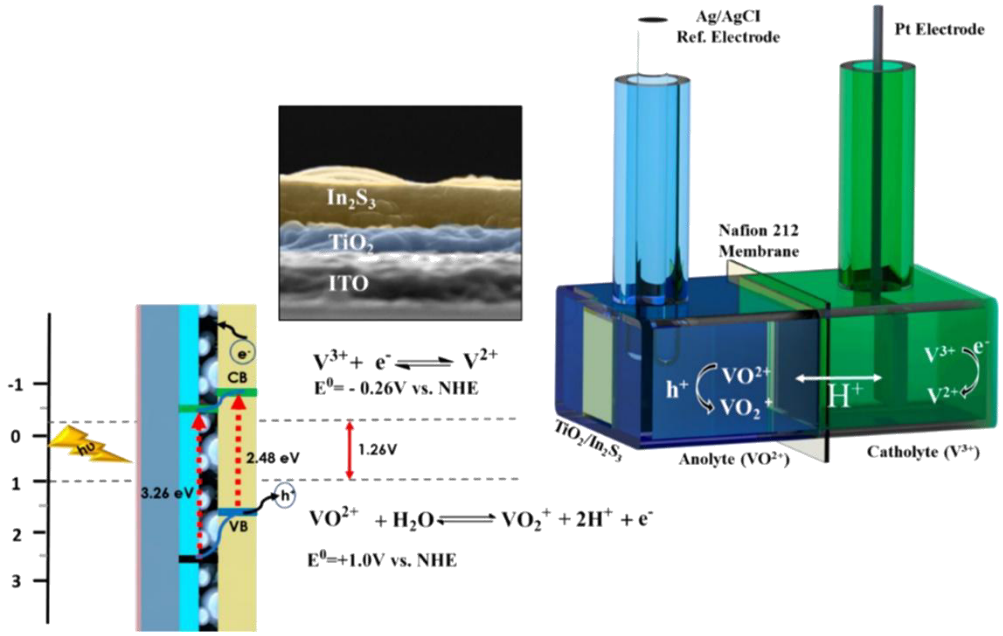

Figure 3.19:Schematic representation of the photoelectrochemical VR-flow cell. Reprinted with permission of Kumtepe & Sankir[190] (Copyright ACS Applied Energy Materials 2020)

Most recently, Tagliabue *et al.* showed that hematite can be used as a high performance photoanode. The solar redox flow setup contained $Na_4Fe(CN)_6$/AQDS electrolytes and a nanostructured α-Fe_2O_3 electrode, which exhibited an unbiased photocurrent of 0.22 mA cm^{-2}.[192]

This summary highlights what has been previously reported in the literature on photo redox flow batteries. This thesis focuses on a continuous photo redox flow battery with a WO_3/Mo:$BiVO_4$ photoanode. This electrode composition was never been used in a flow cell and therefore requires thorough study. The advantageous high photocurrents enable fast and efficient charging of pure vanadium electrolyte.

4. Experimental Part

4.1.Materials

All materials used in this thesis are listed in Table 2 and were used without further purification, with the exception of the FTO glass substrate. The glass was cleaned with ethanol, acetone, and isopropanol in p.a. purity, followed by ultrapure water for 30 min each in an ultrasonic bath.

Table 2: Materials and chemicals used in this thesis/study/work.

Chemical	Spezification	Suppliers
Bis(acetylacetonato) dioxomolybdenum(VI)		Sigma Aldrich
Bismuth(III) 2-ethylhexanoate	~92 %	VWR
Fluorine doped tin (IV) oxide	TEC 8 (8 Ω mm^{-2})	XOP glass
Oxalic acid dihydrate	≥99 %	Sigma Aldrich
Poly vinyl alcohol (PVA)	4-88, M_w ~31.000	Merck
Pluronic P123	Mn ~5,800	Merck
Sodium tungstate hydrate		Merck
Tin (II) chloride	98 %	Merck
Vanadium (V) oxytriethoxide	95 %	Sigma Aldrich
Vanadium(IV) oxide sulfate hydrate	~97 %	Sigma Aldrich

4.2.Synthesis of the WO_3 seed layer

Following the synthesis of WANG *et al.*[62], 1.65 g Na_2WO_4 was dissolved in 25 mL of ultrapure water. Precipitation was induced with 3.5 mL of conc. HCl. The yellow precipitate was then washed with Milli-Q grade water multiple times. After the addition of 10 mL of ultrapure water and 0.5 g PVA, the yellow powder was ultrasonicated until complete dissolution. The solution was then diluted to 30 mL with ultrapure water. 800 µL of the final solution was used for spin coating. The different coating parameters are listed in (Table 4). All coated FTO samples were dried for 8 h at 353 K and subsequently calcinated for 2 h at 773 K on air with a heating rate of 1 K min^{-1}.

4.3.Hydrothermal synthesis of WO_3

The hydrothermal synthesis is a modified one-step growth reaction by WANG *et al.*[62]. 0.165 g Na_2WO_4 was dissolved in 15 mL ultrapure water and subsequently precipitated with 1.5 mL conc. HCl. The yellow precipitant was redissolved by adding 0.9 g oxalic acid. The transparent

solution was diluted to 45 mL and 15 mL of each was used as a precursor solution in the hydrothermal growth reaction. The prepared FTO with seed layer was used inside a 30 mL autoclave. The sample was leaned with an angle of 50° against the wall. The reaction was performed at 453 K for 4 h. After quenching the reaction, the sample was taken out and rinsed (carefully) with ultrapure water. The washed sample was subsequently dried for 8 h at 353 K and additionally annealed for 2 h at 773 K in air with a heating rate of 1 K min^{-1}.

4.4.Synthesis of $BiVO_4$ sol-gel precursor solution

The $BiVO_4$ was adapted from the reported synthesis by FISCHER *et al.*[28] Precursor solution was prepared in an inert atmosphere. 1 wt% of P123 was first dissolved in 6 mL of $CHCl_3$. Next 90.2 mg of $MoO_2(acac)_2$ was added and stirred until complete dissolution. After adding 496 µL of $VO(OEt)_3$ under continuous stirring, the transparent solution turned dark red. The solution is subsequently stirred for 10 min. 1.397 mL of $Bi(OHex)_3$ was added dropwise and the precursor solution was sealed. The final red solution was then stirred for 4 h.

4.5.$BiVO_4$ sol-gel synthesis

The thin film preparation was performed with a dip coating setup using a dip coating container designed for a 6 mL volume. Three FTO substrates were dip coated simultaneously. If nothing else is stated, the dip and withdraw speed was set to 300 mm/min with a dwell and dry time 3 s. After complete evaporation of $CHCl_3$ the samples were heated to 373 K with a heating rate of 1 K min^{-1}. The samples were aged for 12 h and subsequently annealed at 723 K with a heating rate of 0.5 K min^{-1}. After 2 h of calcination the samples were allowed to cool to room temperature.

4.6.SnWO4 synthesis

0.9 g of $SnCl_2$ for a 0.1 M or 4.48 g for a 0.5 M solution was dissolved in 40 mL ultrapure water. If mentioned, the solution was stabilized by adding 2 mL conc. HCl.

4.6.1. Hydrothermal conversion

For each conversion 20 mL of dissolved $SnCl_2$ was used in an autoclave together with hydrothermal grown WO_3 thin film sample. The hydrothermal conversion was conducted for 4 h at 180 h. After quenching the reaction, the sample was annealed for 2 h at 773 K with a heating rate of 10 K min^{-1}. The final sample was additionally cleaned with 1 M HCl to remove SnO_2 residues.

4.6.2. Coating

A WO_3 thin film sample was coated with 800 µL of the prepared $SnCl_2$ solution. The sample was transferred directly into the oven and annealed at 773 K for 2 h with a heating rate of 10 K min^{-1}. The final sample was additionally cleaned with 1 M HCl to remove SnO_2 residues.

4.7. Cocatalyst deposition

The cocatalyst deposition follows the light assisted method reported by KANAN and NOCERA.[69,193,194] The Cobalt oxyhydroxide phosphate (CoPi) OEC was deposited from a 0.1 M phosphate buffer with 0.5 mM $Co(NO_3)_2$ at a pH of 7. A supporting voltage of 0.5 V is applied during the illumination with a white light emitting diode (LED) at 100 W cm^{-2}. The amount of CoPi deposited was controlled by the deposition time and was optimized to 180 s.

4.8. TiO_2 thin film synthesis

1 mL of an organometallic Ti precursor was dissolved in 5 mL of ethanol and stirred for 15 min. As Ti precursor either titanium tetraisopropoxide (TTIP) or Titan(IV)-bis(ammoniumlactato)dihydroxid (TiBALDH) was used. The solution was used in a dip coating setup for small volumes. A substrate was coated with a dip coating speed of 300 mm min^{-1}, 1 s dwell time and a 5 mm min^{-1} withdraw speed. The substrate was dried at 80°C until the entire solvent evaporated. If mentioned, the substrates were calcinated for 1 h at 623 K under atmospheric conditions.

4.9. Atomic layer deposition

The atomic layer deposition (ALD) was performed using an Oxford FlexAL ALD system. The table bench temperature was set to 473 K or 573 K, respectively. Tetrakis(dimethylamino)titan (TDMAT) was used as a Ti precursor with a dose time of 0.5 s and a purge time of 6 s. O_2 plasma at 60 sccm at 300 W ICP power was used as an oxygen precursor with dose time of 4 s and purge time of 10 s. Argon at 200 sccm was used as purge gas.

5. Characterization Methods

5.1.X-ray diffraction

Electromagnetic waves with an energy ranging from 100 eV to 10 MeV are classified as X-rays. If X-rays are focused on a periodically ordered material, different physical phenomena such as absorption, scattering, and diffraction can be observed. Each of these processes provides information for material characterization, but X-ray diffraction (XRD) forms the basis of structural crystallography. The wavelength of a monochromatic X-ray beam (10 – 10^{-3} nm) is of the same order of magnitude as the atomic spacing in a crystal lattice. Therefore, X-rays can be diffracted at the atomic planes of periodically arranged unit cells (Figure 5.1). This interference occurs only at specific angles, which are described by BRAGG's-Law ((5.1)

$$n\,\lambda = 2\,d_{hkl}\,\sin(\theta) \tag{5.1}$$

where n is the order of reflection, λ the X-ray wavelength, θ the angle of incidence, and $d_{(hkl)}$ the distance between lattice planes indexed by the MILLER indicies (hkl).

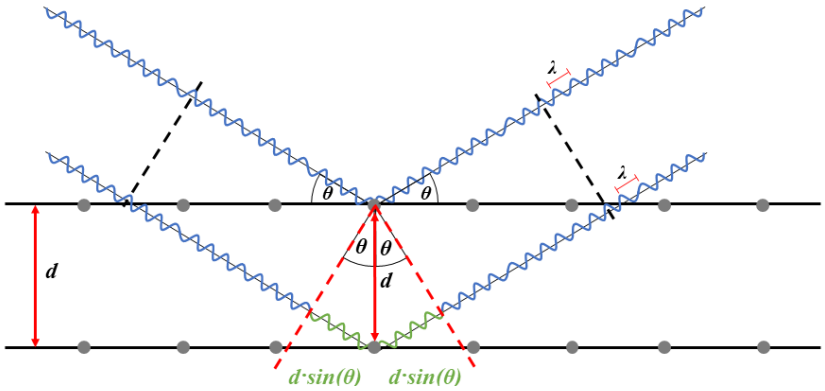

Figure 5.1:Schematic illustration of the BRAGG condition for $n = 2$

These indices define crystallographic planes within a unit cell and are used to describe diffraction geometries. Each plane corresponds to a unique interplanar distance, which determines the angular position of the diffraction signal.

The resulting diffraction pattern consists of a series of sharp reflections, each of which can be assigned to a specific lattice plane, forming a material-specific diffractogram. This diffractogram can be used for phase identification and for analyzing atomic positions, lattice parameters, and electron density distributions within a unit cell.[195]

Different setups were used to analysis the thin film electrodes.

X-ray powder diffraction takes advantage of statistically oriented powder and scans 2θ over θ using a BRAGG-BRENTANO geometry. By using a FTO glass substrate as a support a height deviation is introduced which needs to be corrected by applying equation (5.2.

$$\Delta 2\,\theta \;=\; \frac{2s\,cos\theta}{R} \tag{5.2}$$

Here R is the radius of the BRAGG-BRENTANO geometry and s is the height deviation. It should be noted that a larger sample is defined as a negative deviation. R is set to be 240 mm whereas s is either 0.3 or -1.7 mm depending on the FTO thickness used.[196]

XRD measurements were obtained using a PANalytical Empyrean device equipped with a Cu K_α radiator (λ = 0.15406 nm). Data were recorded in a step scan mode from 10 to 70° with a step size of 0.053°, an acceleration voltage of 400 kV and an emission current of 40 mA. The 1° anti-scatter slit was used, and the divergence silt was set to 0.5°.

Grazing incidence x-ray diffraction (GIXRD) was used to acquire surface sensitive information. The incidence angle ω is fixed while the 2θ is scanned. A low ω value, which is generally close to the critical angle, allows an almost total reflection of the surface by preventing the X-rays penetrating the material. By changing the incidence angle ω the x-ray penetration in the samples can be altered which enables the analysis of layer structures.

The GIXRD was performed with a Rigaku SmartLab multipurpose X-ray diffractometer. The incidence angle ω was set to 0.3° with a 45 kV, 200 mA Cu Kα parallel beam. The measurements were conducted between 10 – 70° with a step width of 0.1° and a scan speed of 4.0 °/min. The incident slit was set to 0.25 mm, while the receiving slit was open.

5.2.X-ray photoelectron spectroscopy

In X-ray photoelectron spectroscopy (XPS) the photoelectric effect is used to determine elements on the surface. An X-ray beam with a particular wavelength and therefore known energy is focused on the material. Electrons at the surface of the sample are excited from molecular orbitals into the continuum. By measuring the kinetic energy (E_{kin}) of the exited electrons the binding energy (E_B) of each emitted electron can be calculated by the following relation:

$$E_B \;= hv - E_{kin} - \Phi \tag{5.3}$$

where hv is the photon energy of the incident X-ray, and Φ is the spectrometer work function. Due to the relatively short penetration depth of 1- 10 nm of the X-rays the analysis is ideally suited to investigate surface composition of a material.

Each element has characteristics binding energies for its core electrons which allows the presence of an element to be confirmed by the appearance of its photoelectron peaks in the spectrum. Furthermore, an XPS study also provides insights into the chemical state of atoms. Oxidation state, local bonding environment, or coordination of the atoms can change the

position and shape of the photoelectron peaks. These so-called chemical shifts can be analyzed by high-resolution scans and provide quantitative insights into surface composition and chemical environment.

By combining sputtering techniques with XPS analysis, depth profiling can be achieved to examine layered, passivated, or surface-treated materials. [197]

XPS measurements were conducted using a Physical Electronics PHO VersaProbe III Scanning XPS Mircoprobe instrument. The X-ray power was 25 W with a beam voltage of 15 kV and a beam diameter of 100 µm. The measurements were done with an energy pass at 224 eV, a step size of 0.4 eV and a holding time of 50 ms per step. Data evaluation was completed using CASA XPS 2.3.25. To analyze the FTO, the samples had to be cut into smaller pieces, which were used for the measurements.

5.3.Diffuse Reflection UV/Vis Spectroscopy

When electromagnetic radiation interacts with matter, a variety of phenomena such as absorption, transmission, and reflection can be observed. Absorption describes the transfer of energy from a photon to an electron, exciting it to a higher state, whereas transmission quantifies the photons that pass through the material without scattering or absorption. Reflection, therefore, accounts for all remaining photons that are scattered at the surface or inside the material.

UV/Vis spectroscopy quantifies these phenomena in the spectral range from the ultraviolet (UV) to the visible (Vis) region, typically between 200–800 nm and beyond. In this thesis, reflection (R) UV/Vis spectrum were recorded and transferred into the pseudo absorption $\mathrm{F}(R)$ of the material with the KUBELKA-MUNK equation (5.4):

$$\mathrm{F}(R) = \frac{(1-R)^2}{2R} \tag{5.4}$$

Additionally, the Tauc plot was used to determine the band gap. In this approach, the transformed absorption data are plotted as $[F(R) \cdot (h\nu)]^{1/n}$ versus photon energy. versus photon energy. The exponent n depends on the type of electronic transition and distinguishes between indirect allowed transitions (n =2) and direct allowed transition (n = ½). Extrapolation of the linear region of the plot to the energy axis allows the band gap energy of the material to be determined.[198,199]

5.4.Raman Spectroscopy

Raman spectroscopy is based on the scattering of monochromatic light to obtain information about atoms, molecules, and their environment. When monochromatic light is focused on a material, the electron cloud around an atom becomes polarized, forming an unstable virtual state with a very short lifetime. The photon emitted from this virtual state exhibits an energy difference compared to the incident beam. This energy difference is detected and depends on the type of scattering that occurs.

A distinction is made between Raman and Rayleigh scattering: Rayleigh scattering is defined as the interaction between an electron and a photon, whereas Raman scattering involves a photon scattered by the atomic nucleus. Due to the large mass of the nucleus, the energy difference in Raman scattering is significantly larger, which is why it is also referred to as inelastic scattering. Rayleigh scattering, also called elastic scattering, remains the dominant phenomenon.

Raman scattering can be further divided into Stokes and Anti-Stokes scattering. In Stokes scattering, an atom or molecule is excited from the ground vibrational state *m* to an excited vibrational state *n* .In Anti-Stokes scattering, the atom or molecule is already in an excited vibrational state due to thermal excitation and relaxes to the ground vibrational state. A schematic illustration of the different scattering phenomena used in Raman analysis is shown in Figure 5.2.

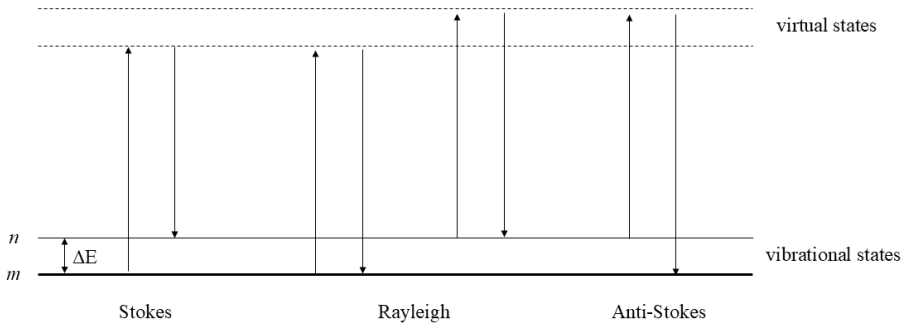

Figure 5.2: Schematic illustration of the rayleigh and raman scattering with the ground vibrational state *m* and the excited vibrational state *n*.a

The energy differences provide information about atoms, bonds and structures which is complementing structure elucidation.[200]

All Raman spectra were measured with the Horiba Jobin Yven Raman spectrometer equipped with a He-Ne laser (λ_{exc} = 633 nm) with a laser power of 20 W and an objective from Olympus (BX41 microscope 100x).

5.5.Scanning Electron Microscopy

To image structures ranging in magnitude from micro- to nanometers scanning electron microscopy (SEM) is applied. The principle of SEM is the interaction of accelerated electrons with high energy and the atoms of the material. The wavelength of the electron beam is inversely proportional to the acceleration voltage of the measurement and can be described by the DE BROGLIE equation (5.5):

$$\lambda = \frac{h}{p} = \frac{h}{\sqrt{2m_e eV}} \tag{5.5}$$

Where λ is the electron wavelength, h the planck constant, p the electron momentun, m_e the electron mass, e the elementary charge and V the accelarting voltage. Higher voltages results in lower wavelengths compared to visible light which allows much higher spatial resolution than optical microscopes.

By using electromagnetic lenses the electron beam is focused onto the sample surface. By scanning the surface of the sample step by step and recording the intensity of the scattered electrons, an image can be generated and evaluated further. Different electrons can be used to obtain sample information. Secondary electrons (SE) which are low energy electrons ejected from the surface layer of the sample contribute to the high resolution imaging. Depending on the ejection point of the electrons they reach the detector at different times which provides the information of contrast for imaging. Backscattered electrons (BSE) however originate from deeper region of the sample and are sensitive to the atomic number providing compositional contrast. Additionally the electron beam can be used to stimulate X-ray emission for elemental information which is described in the next chapter. [201,202]A schematic illustration of the different scattered electrons is shown in Figure 5.3.

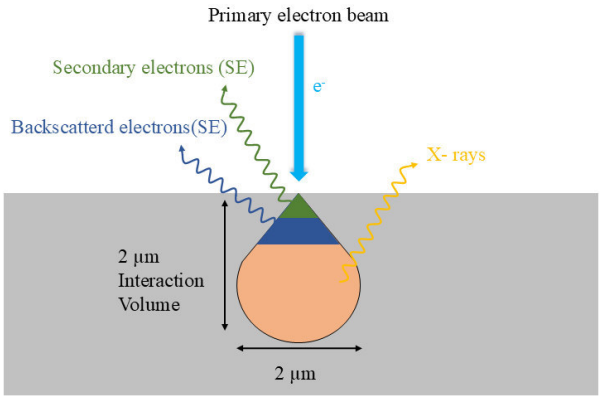

Figure 5.3: Schematic illustraion of the different signal types SE, BSE and X- ray in the scannig electron microscopy.

A ZEISS LEO 1530 and a ZEISS UltraPlus were used for SEM imaging. The acceleration voltage was set to 3 kV with a working distance between 6-8 mm. The experimental setup had a 30 µm aperture and electrons were detected with an InLens and an SE2 Detector. All samples were coated with a 1.5 nm thin Pt layer by a Cressington Sputter Coater 208HR to increase conductivity. For cross-section images the samples were cut before sputtering.

5.6.Energy Dispersive X-Ray Spectroscopy

In energy-dispersive X-ray spectroscopy (EDX), electrons are removed from the inner shells of atoms by an incident electron beam, as described in the previous chapter. Most commonly, these electrons are ejected from the K- or L-shells, leaving a vacancy. This instability is compensated by an electron from a higher energy level falling into the lower energy shell, accompanied by the emission of X-rays. This radiation is element-specific and can therefore be used to determine the elemental composition.

Only certain electronic transitions from higher shells are allowed to fill the vacancy in the inner shell. If the electron originates from the next higher shell, this is called an α transition. For example, when an electron from the L-shell falls into a vacancy in the K-shell, the emitted X-ray is defined as Kα radiation. If the vacancy is filled by an electron from a shell two levels higher, the emitted X-ray is defined as β radiation. A schematic illustration is displayed in Figure 5.4.

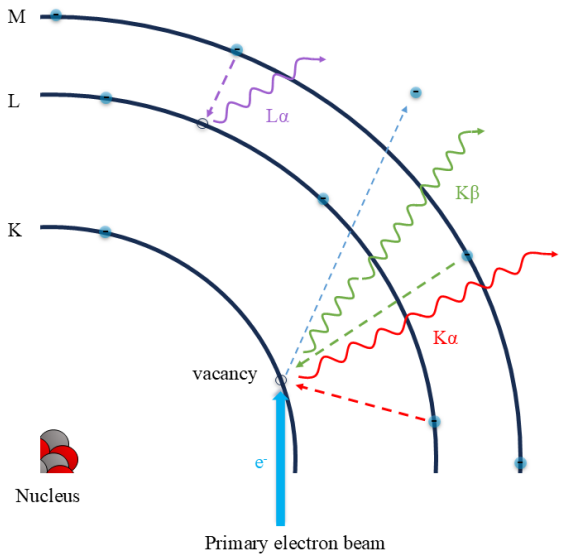

Figure 5.4: Schematic illustration of the allowed electron transition with the resulting X-ray emissions used in the EDX analysis.

A detector is measuring the energy of the X-ray photon and based on the peak appearance and intensity the elemental distribution can be determined.[203]

The EDX measurements were performed on the ZEISS LEO 1530 equipped with a Thermos Fisher scientific NS7 Ultra Dry-EDX detector. The working distance was maintained at 8 mm with an acceleration voltage of 20 kV and an aperture of 60 µm. To increase conductivity, all samples were coated with a 1.5 nm thick Pt layer using a Cressington Sputter Coater 208HR.

5.7.Atomic Force Measurement

Atomic Force Microscopy (AFM) is a technique for scanning surfaces that enables materials to be analyzed on the nanoscale. A sharp tip, only a few nanometers in size, is attached to a flexible cantilever and moves over the surface. The forces between the cantilever and the sample cause the tip to deflect and bend. Typical forces contributing to the bending include van der Waals forces, electrostatic interactions, and mechanical repulsion. The deflection of the cantilever is detected by a laser beam reflected from the back of the cantilever onto a photosensitive detector. This allows a reconstruction of the surface with nanometer precision.

Different operation modes, such as contact, non-contact, and tapping mode, can be used to analyze the surface. In contact mode, the tip of the cantilever remains in continuous contact with the surface, which enables high-resolution imaging but may damage the sample due to scratching. Non-contact mode is the opposite: the tip does not touch the surface but measures only the attractive forces, thereby preserving both the tip and the sample. Finally, in tapping mode, the cantilever oscillates near its resonance frequency, intermittently touching the surface. While contact mode provides high-resolution images, it can damage the sample; non-contact mode is particularly suitable for analyzing forces as a function of distance. Tapping mode is commonly used for topography and adhesion measurements, while also preserving the integrity of both tip and sample.[204]

5.8.Photoelectrochemical Measurements

Photoelectrochemical measurements were conducted with the apparatus shown in Figure 5.5. It consists of a Quantum Design LOT 300 W Xe solar simulator equipped with an AM 1.5 G filter and an electrical shutter. The electrochemical cell is connected to a ZAHNER Zennium CIMPS-PCS system and uses a 3-electrode setup. The counter electrode (CE) is a platinum wire whereas Ag/AgCl (3M NaCl) is used as the reference electrode (RE). The working electrode (WE) is FTO/semiconductor sample linked to a standard copper wire. To connect the sample a 1 cm wide area is cleared from the semiconductor to attach the copper wire directly to the conductive FTO.

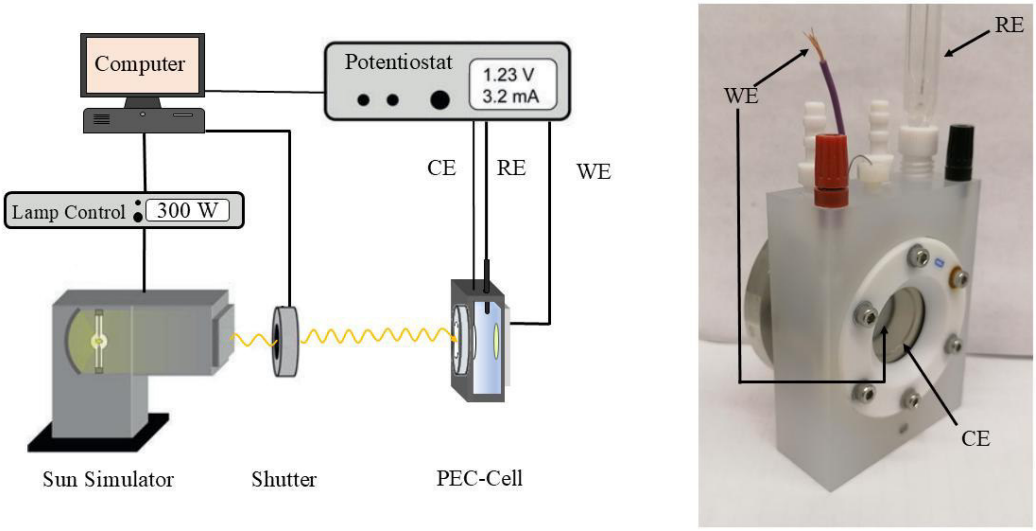

Figure 5.5: Schematic illustration of the PEC used in this thesis. An image of the PEC-cell which shows the 3-electrode setup.

Which electrolyte used depended on the material measured. Either a 0.1 M H_2SO_4 (pH = 0.887), a 0.1 M H_3PO_4/KH_2PO_4 (HP-buffer, pH = 1.92) or a KH_2PO_4/K_2HPO_4 (KP-buffer, pH = 7) buffer was selected. The electrolyte and all parameters involved are specified in the data presented. Thales Z 3.05 software was used to control the potentiostat and to record the measurements.

5.8.1. Chopped Light Voltammetry

In order to determine the performance of the semiconductor anodes, a linear sweep voltammetry was obtained while the sample was periodically illuminated, the so-called chopped light voltammetry (CLV). The measurement allows the estimation of the flat band potential by determining the onset potential and additionally the evaluation of the electrode by comparing the photocurrent at 1.23 V_{RHE}. As the potential was detected by a 3-electode setup, the NERNST-equation (5.6) must be used to convert it to inverse hydrogen potential.

$$E_{\mathrm{RHE}} = E_{\mathrm{Ag/AgCl}} + 0.059\, pH + E^{0}_{\mathrm{Ag/AgCl}} \tag{5.6}$$

$E^{0}_{\mathrm{Ag/AgCl}}$ equals the standard potential 0.209 V of the reference electrode at 298K, while $E_{\mathrm{Ag/AgCl}}$ indicates the measured potential.

The CLVs were recorded between -0.1 $V_{Ag/AgCl}$ and 1.1 $V_{Ag/AgCl}$ with a scan speed of 5 mV s^{-1}, an illumination interval of 10 s and 10 measured points per step. The illumination area was set to 1 cm^2 and the power used to illuminate the surface was 100 W according to company specifications.

5.8.2. Incident Photocurrent Efficiency

In IPCE measurement, several LEDs with distinguished wavelengths and known power are used to calculate the efficiency by equation (3.11). The wavelengths applied to determine the efficiency are listed in Table 3. In addition, a potential in the center middle of the band gap is required to extract the electrons. This is why a potential of 1.23 V_{RHE} was chosen for comparison.

The light source used was a ZAHNER TLS03 with a power of 95 % of the maximum LED power. The IPCE was measured between 300-800 nm with an illumination period of 10 s and a light frequency of 1 Hz. The illuminated area was 10 mm^2.

Table 3: Wavelengths of the LEDs with the maximum power.

Wavelength in [nm]	Power max. in [Wm^{-2}]
308	185
318	183
339	224
368	271
385	484
397	462
408	536
429	1003
455	1018
479	909
523	583
532	507
574	741
593	218
630	563
664	313
709	251
729	191
770	211

To prevent absorption of the FTO at a distance of 1 mm, the IPCE measurement was performed from the front.

5.8.3. Electrochemical Impedance Spectroscopy

Electrochemical impedance spectroscopy (EIS) provides a method for investigating complex inter- and surfaces. By applying a small alternating voltage V_0 over a range of frequencies and measuring the current I_0 response, information can be gained on how the system resists the current flow. The resistance, known as impedance, is described in equation ((5.7). This sheds light on the reaction kinetics, charge transfer processes, diffusion processes and the double-layer capacities.

$$Z = \frac{V_0 \sin(\omega t)}{I_0 \sin(\omega t + \phi)} = Z_0 \frac{\sin(\omega t)}{\sin(\omega t + \phi)} \tag{5.7}$$

$$Z = Z_0 \, (cos\phi + isin\phi) \tag{5.8}$$

EULER'S equation defines the impedance Z as a complex number (5.8). The resulting imaginary part can be used to describe the semiconductor-electrolyte interface. Additionally, the logarithmic plot of the frequency and the imaginary part can be used to determine the frequency at a slope of -1, which is required to perform the MOTT-SCHOTTKY measurements. [205]
The EIS measurements were conducted with the open-circuit potential and an amplitude of 20 mV. The frequency was scanned from 1 Hz to 100 kHz with 10 points per decade.

5.8.4. Mott-Schottky Measurement

A MOTT-SCHOTTKY measurement determines the flat band potential of the semiconductor anode. The capacitance was monitored over a wide potential range. A detailed description can be found in chapter 3.7.5.
The measurements were performed between 1.3 $V_{Ag/AgCl}$ and -0.1 $V_{Ag/AgCl}$. The frequency used was previously determined by an EIS measurement (chapter 5.8.3). The step width was set to 50 mV with an amplitude of 5 mV.

5.8.5. Charigng and Photocharging

A 0.016 M V^{4+} solution was prepared as an electrolyte by dissolving 2.02 g of $VOSO_4$ in 500 mL of 0.04 M H_2SO_4. First, the electrolyte preconditioning was performed with a redox flow cell, graphite electrodes and a Nafion membrane. Both electrolyte tanks were filled with 150 mL of V^{4+} electrolyte. A potential of 1.8 V was applied to the cell and held until the resulting current reached the threshold value of 10 mA cm^{-2}. The oxidized electrolyte was disposed and replaced with a fresh/ V^{4+} electrolyte.

Photocharging was conducted with a dual cell setup using a standard redox flow cell and the designed photo redox flow cell together with the preconditioned electrolyte (Figure 5.6). This allowed simultaneous charging and measurement of the open circuit potential.

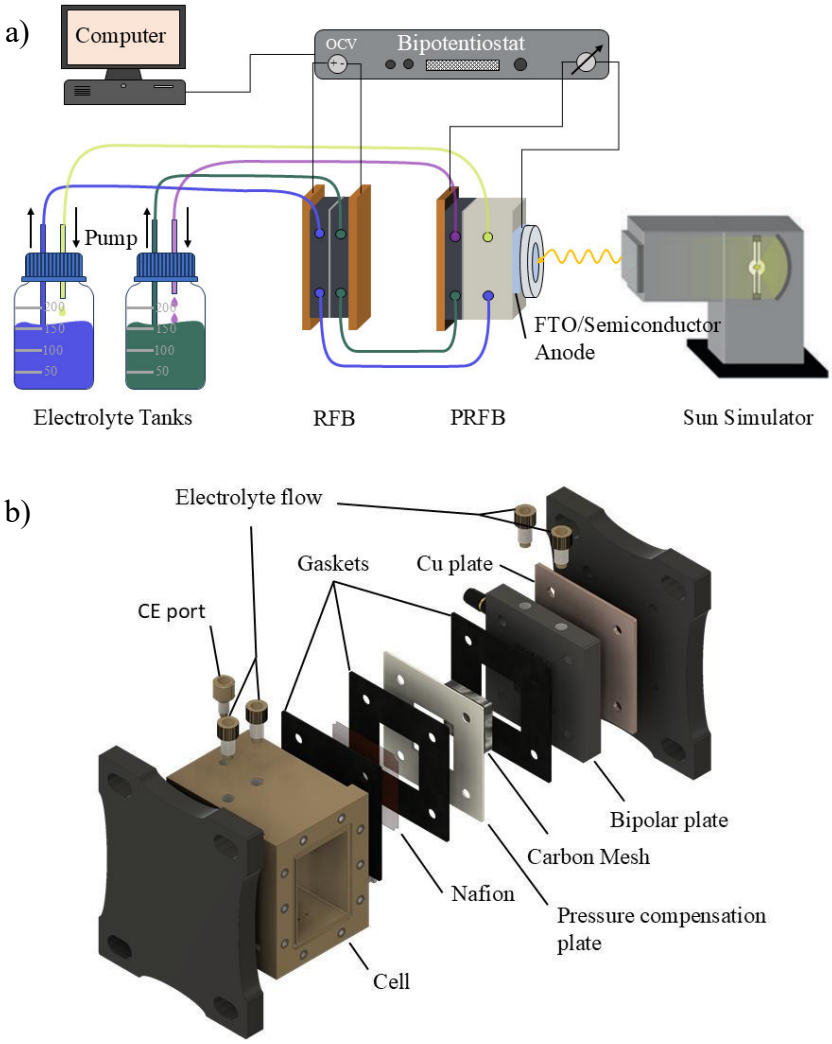

Figure 5.6: a) A schematic illustration of the photocharging configuration during operation. b) An explicit drawing of the designed and used photo redox flow cell.

The entire setup was flushed with nitrogen before and during operation. Photocharging started after a one-hour electrochemical pre-charge with an applied potential of 1.8 V across the redox flow cell. After the pre-charge, the illumination began with a varying support voltage between 0.7 – 1.5 V across the photo redox flow cell. The photocharging was continued until a significant change in the open circuit potential could be detected. The flow rate for preconditioning and pre-charge was set to 100 U/min and was decreased and adjusted for photocharging ranging within 2-10 U/min.

The same lamp as described in chapter 5.8 was used for this setup, a PARSTAT 3000A-DX bipotentiostat was connected together with a REGLO ICC digital dual channel peristaltic pump

to generate the photocharging. A picture of the assembled photo redox flow cell is shown in the appendix (Figure 11.1). The photo redox flow cell was designed and built in collaboration with Dr. Michael Fink.

6. Seed layer formation determines photocurrent response of hydrothermally grown WO_3 photoanodes

6.1. Seed layer and film characterization

To evaluate the role of the seed layer, different seed layers were prepared by adjusting spin speed, spinning duration and using two different spinning techniques. The electrochemical measurements defined the performance of each seed layer. Table 4summarizes the parameters used.

Table 4: Spin coating parameters used for the preparation of the WO_3 seed layers.

Notation	Spinning speed / rpm	Spinning duration / s
A	2000	30
B	2000	10
C	2000	50
D	500	30
E	5000	30
F	8000	30

These parameters were tested with the static and dynamic spin coating approach. The distinction between these methods was defined by the addition of the coating solution. In the static spin coating approach, the surfaces are first covered with the solution and then accelerated gradually to remove the excess.[206] Whereas in the dynamic spin coating approach the samples were first accelerated to the desired spinning speed and the solution was added immediately after reaching the maximum velocity.[207] For clarity the abbreviations "-s" and "-d" referring to static and dynamic are used from now on to highlight the method applied. The notation introduced in Table 4 indicates the spinning speed and duration and correlates with the description of the SEM images. For example the sample A-s stands for the seed layer prepared with static spin coating approach with a maximum spinning speed of 2000 rpm and a duration of 30 s.

The SEM images of the static spin coating approach are shown in Figure 6.1. The comparison of spinning duration (Figure 6.1 A-C) indicates that the duration has little impact on the seed layer formation. For the samples A-s and B-s the seeds are all located in the valleys of the tetragonal FTO structure, and the W/Sn ratio determined by XPS displays only minor differences. The longest spinning duration in sample C-s shows a higher W/Sn ratio with a value of 1.60, indicating a denser seed layer. Comparing different spinning speeds (Figure 6.1 D-F) highlights the influence of the velocity on the seed layer formation. The slowest spinning speed, represented by D-s, results in a completely covered surface. The tetragonal structure of the underlying tin oxide is not visible, which is assumed to be undesirable as the seed layer should initiate crystal growth during the hydrothermal growth reaction to form a dense WO_3

film. Here it was not feasible to determine the density of the seed layer as the penetration depth of the XPS beam was not sufficient to detect Sn.

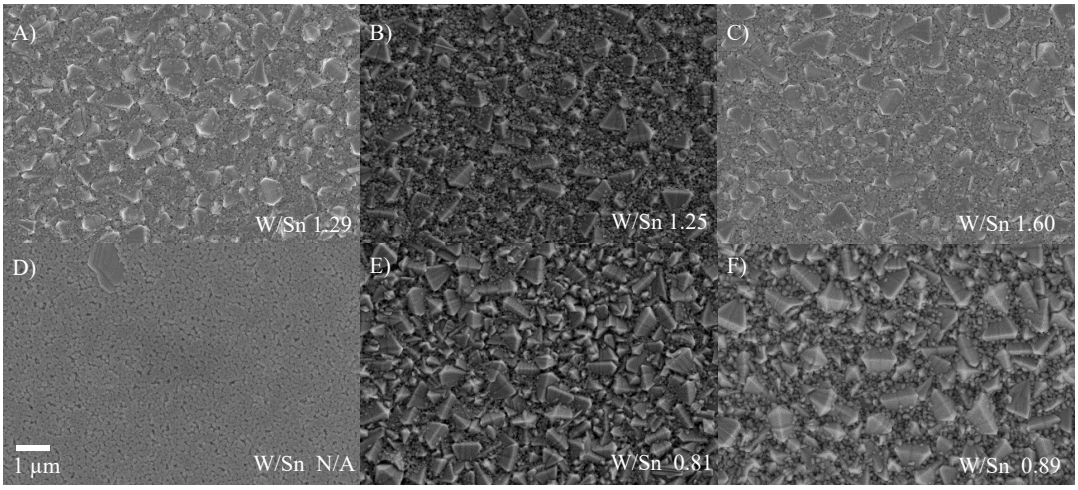

Figure 6.1: SEM images of WO_3 seed layers prepared with different static spin coating parameters. The number shows the W/Sn ratio determined by XPS. The labels were chosen according to the notation in Table 4. (Adapted with permission of the Royal Society of Chemistry 2023).[111]

The higher spinning speeds in Figure 6.1 E and F show clearly that the seed layer density is decreasing significantly. A comparison of Figure 6.1 A with E indicates that there are only a few seeds in the valleys and the layer therefore is less dense. In contrast, the highest spinning speed displayed in Figure 6.1 F has a slightly denser formation compared to E, but still remains less dense than A. This is in good agreement with the XPS results, which provide a W/Sn ratio of 0.81 and 0.89 for the seed layers E-s and F-s, respectively. Additionally, the cross sections of the seed layer are provided in the appendix Figure 11.2, but due to the small size of the seed layer, it is only visible as FTO.

The resulting hydrothermally grown WO_3 films are depicted in Figure 6.2. The films exhibit the typical sheet-like structure of WO_3 thin films reported by WANG *et al.*[62] Moreover, all six WO_3 thin films featured a fully covered surface consisting of thin nanoplates, although the seed layers had different densities. The exception is D-s, which showed an uncontrolled formation of large nanoplates, as confirmed by the cross-sectional SEM images in Figure 11.3 in the appendix and the variation in layer/film thickness seen in Figure 6.4d.

The hydrothermally grown films were then characterized by XRD, Raman and UV-Vis in order to analyze the physical properties of the generated WO_3. These measurements are displayed in Figure 6.4a-c and the film thickness was determined by cross-sectional SEM images (Figure 11.3) and are summarized in Figure 6.4d.

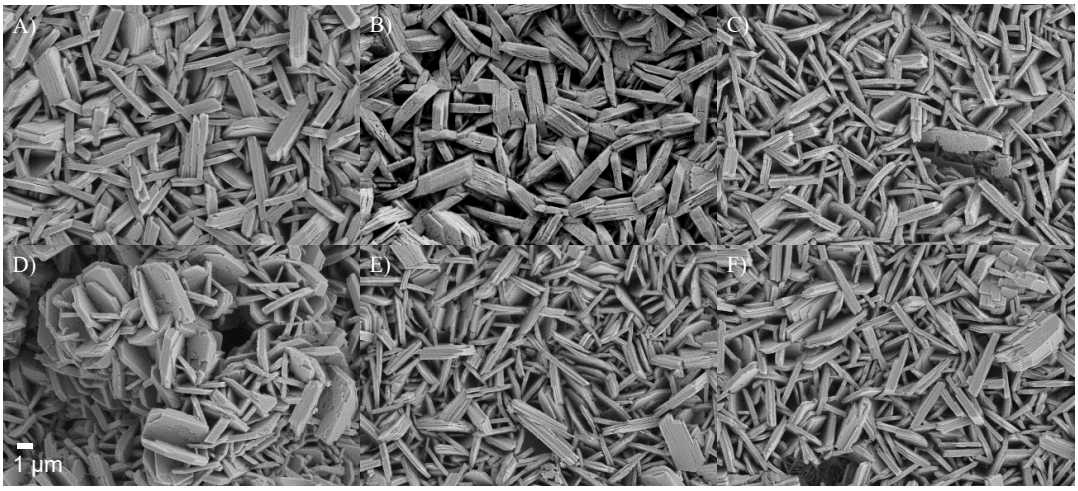

Figure 6.2: SEM images of hydrothermally grown WO_3 films out of static spin coated seed layers. The labels were chosen according to the notation in Table 4. (Adapted with permission of the Royal Society of Chemistry 2023).[111]

The XRD patterns for all six samples show that the *m*-WO_3 phase is dominant. The face enrichment of (002) is clearly seen due to the most intense diffraction at $2\theta = 23.1°$.[62] Sample D-s differs from the other WO_3 films with a clearly visible *h*-phase at $2\theta = 14.0°$ and lower (002) to (200) ratio at $2\theta = 24.4°$. Given the enrichment of the (002) facets, the intensity of the *h*-WO_3 diffraction can easily be overlooked, as the magnification of B-s in Figure 6.3b demonstrates. Therefore, Raman measurements were performed to identify the presence of the *h*-WO_3 phase. Thus, a band at 692 cm^{-1} is found in the measurement in addition to the two most intense bands at 719 cm^{-1} and 807 cm^{-1} which are associated with the stretching vibration of W-O-W[208][209].[68] Accordingly, samples A-s, B-s and D-s show additionally a *h*-WO_3 crystal phase due to the occurrence of the Raman band at 692 cm^{-1}.

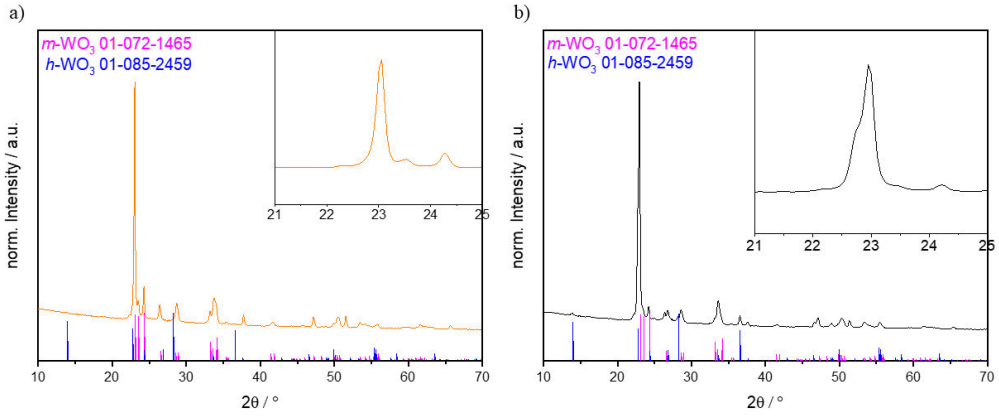

Figure 6.3: Magnification of XRD patterns of a) E-s with no *h*-WO_3 phase and b) A-s with a *h*-WO_3 phase visible. (Adapted with permission of the Royal Society of Chemistry 2023).[111]

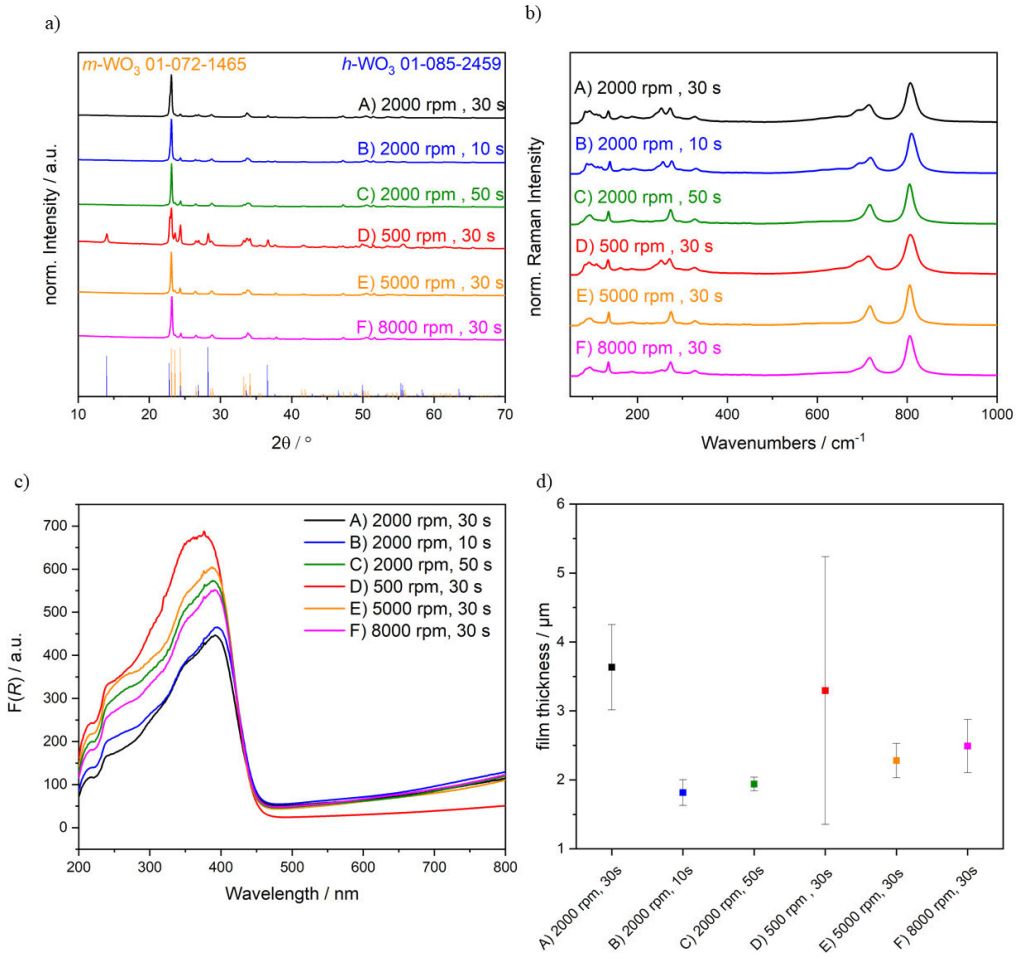

Figure 6.4: Physical characterization of WO_3 films grown from seed layers prepared by static spin coating with different parameters. a) XRD, b) Raman, c) UV-Vis KUBELKA MUNK absorption and d) film thickness determined by cross section SEM analysis. (Adapted with permission of the Royal Society of Chemistry 2023).[111]

To further characterize the WO_3 thin films the absorption together with the film thickness were determined. The film D-s exhibits the highest absorption but also the highest deviation in film thickness as shown in Figure 6.4d and Figure 11.4 in the appendix. This is in good agreement with the SEM images which showed an uncontrolled thicker growth of WO_3. Surprisingly the WO_3 thin film A-s exhibits the lowest absorption, even though it offers the highest film thickness of 3.6 µm in average. Neglecting the 500 rpm WO_3 thin film, the seed layer with high spinning speeds or long duration indicates the highest absorption as it additionally has a comparable film thickness of 2.3 µm (D-s), 1.9 µm (E-s) and 2.4 µm (F-s). All KUBEKA MUNK absorption spectra in Figure 6.4c show an absorption edge at ~450 nm, which corresponds to a band gap of 2.7 eV in the TAUC plot (Figure 6.5). One further significant observation from the absorption spectra is that all thin films, with the exception of B-s, must contain a similar concentration of W^{5+} as the slope matches above 450 nm, which can be attributed to the absorption of W^{5+}.[210,211]

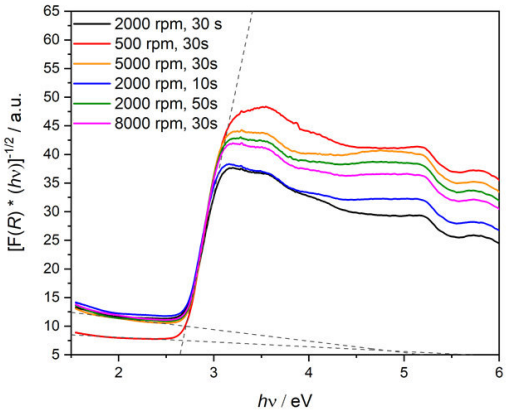

Figure 6.5: Tauc plot of hydrothermally grown WO_3 thin films prepared by static spin coated seed layer synthesis. (Adapted with permission of the Royal Society of Chemistry 2023).[111]

Characterization indicates a trend that high spinning speed or long duration leads to a lower seed layer density. This results in reproducible, phase pure *m*-WO_3 thin films with a film thickness of around 2 µm and high absorption.

The dynamic spin coating seed layers were prepared by following the same parameters listed in Table 4. Comparing Figure 6.1 with Figure 6.6 the influence of the spinning method can be observed. A-d shows a fully covered surface, whereas A-s has a homogeneous distributed seed at the same spinning speed and duration. The W/Sn ratio of 0.76 is lower than expected, as A-s has a higher density of 1.29. The seed layer D-d is comparable to static coated equivalent. It is characterized by a fully covered thick layer, which prevents the XPS analysis from detecting Sn underneath the seed layer. In contrast, the seed layer F-d causes an inhomogeneous covered surface due to high centrifugal force. The XPS analysis results in a W/Sn ratio of 0.75, which is misleading as the surface is merely partially covered and the XPS beam only analyzes a small area. The seed layers B-d and C-d are comparable to B-s and C-s. The seeds are in the valleys of the tetragonal SnO_2 structure with decreasing densities of 1.23 and 0.96 W/Sn due to the increasing spinning duration.

Noteworthy is the seed layer E-d due to the unique seed distribution. The seeds homogenously cover the valleys and are located on top of the tetragonal FTO structure. Moreover, the seeds are smaller compared to B-d or C-d. This results in the lowest W/Sn ratio of all synthesized seed layers with a value of 0.54.

The cross sectional SEM images of the seed layers and the hydrothermally grown films are shown in Figure 11.5 and Figure 11.6 in the appendix, respectively. The grown WO_3 films synthesized with the dynamic coated seed layer are displayed in Figure 6.7, while large areas are presented in Figure 11.7.

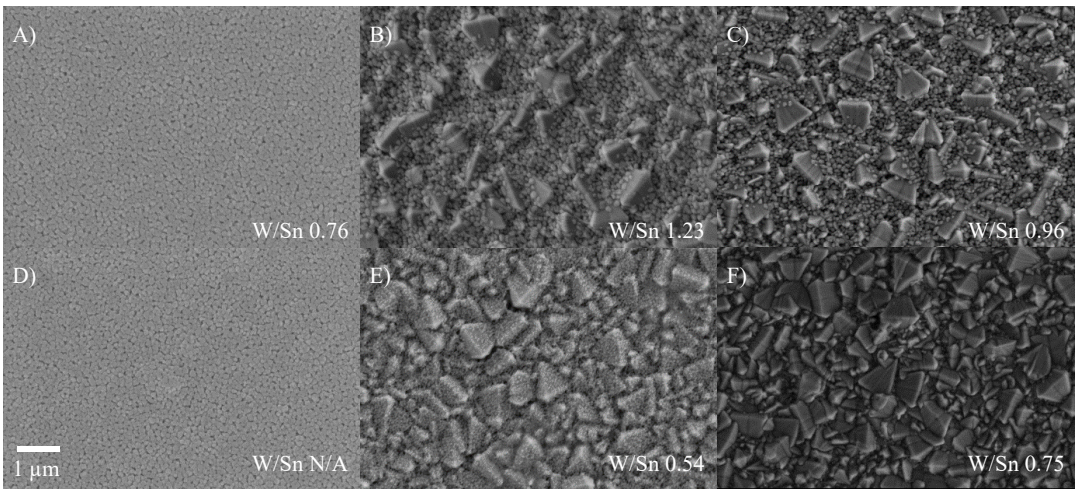

Figure 6.6: SEM images of WO_3 seed layers prepared using different dynamic spin coating parameters. The number shows the W/Sn ratio determined by XPS. The labels were chosen according to the notation in Table 4. (Adapted with permission of the Royal Society of Chemistry 2023).[111]

The comparison between the hydrothermally grown WO_3film from the static and dynamic spin coated seed layer indicates small differences. The nanosheet-like structure is visible, however the nanosheets appear thicker and denser.

To further evaluate the WO_3 thin films XRD, Raman and UV-Vis measurements were performed to identify the physical properties. Furthermore, the film thickness was determined using cross sectional SEM images which are shown in Figure 11.6 and summarized in Figure 6.8d. Accordingly, he spectra and diffractograms are depicted in Figure 6.8a-c.

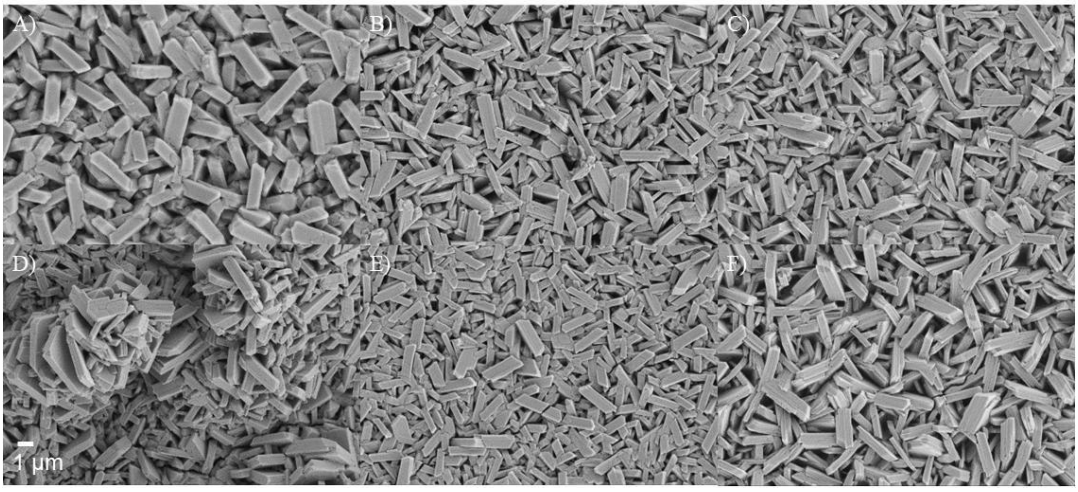

Figure 6.7: SEM images of hydrothermally grown WO_3 films from dynamic spin coated seed layer. The labels were chosen according to the notation in Table 4. (Adapted with permission of the Royal Society of Chemistry 2023).[111]

The XRD pattern is evident again in the facet enrichment of (002) at $2\theta = 23.1°$. As expected, the *m*-WO_3 is the prominent crystal phase observed. Same diffraction at $2\theta = 23.1°$ is asymmetrical in the diffractograms of the samples D-d and E-d, indicating a *h*-WO_3 phase.

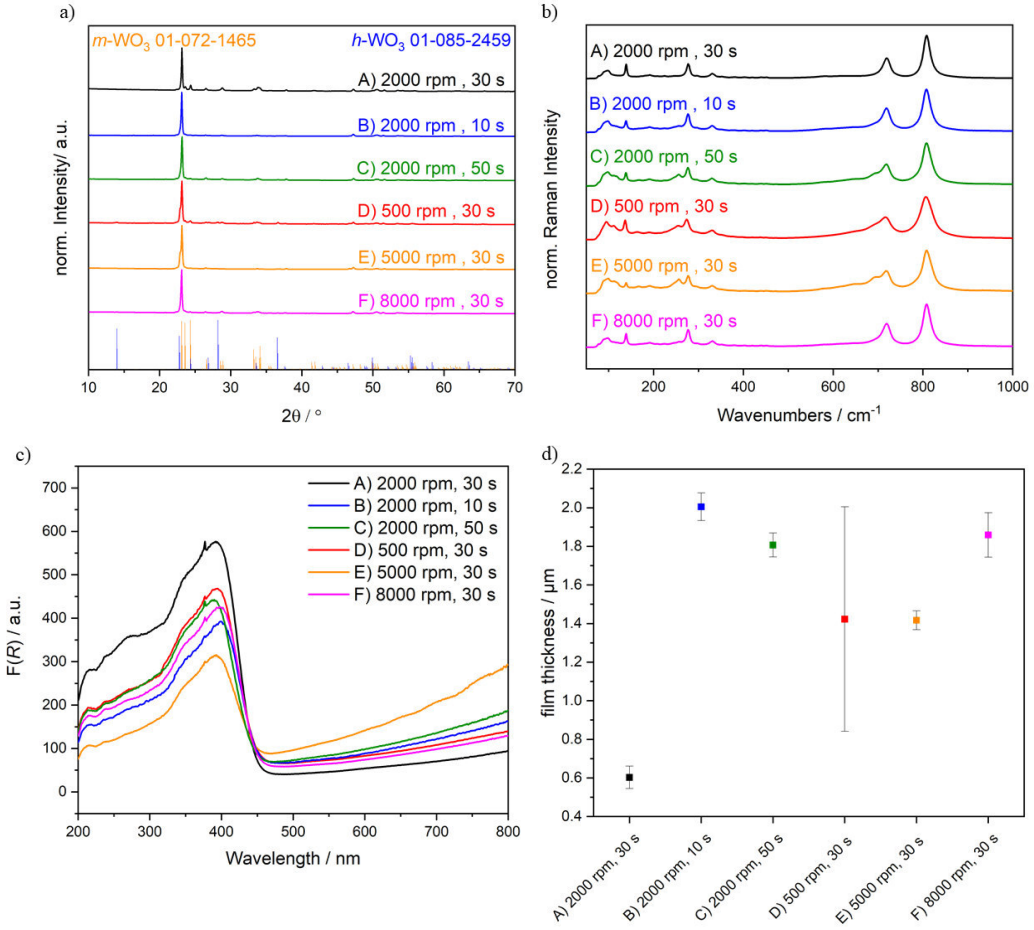

Figure 6.8: Physical characterization of WO_3 films grown from seed layer prepared by dynamic spin coating with different parameters. a) XRD, b) Raman, c) UV-Vis KUBELKA MUNK absorption and d) film thickness determined by cross sectional SEM analysis. (Adapted with permission of the Royal Society of Chemistry 2023).[111]

The Raman spectra confirmed the presence of the *h*-WO_3 phase in the samples C-d, D-d and E-d by the detection of the additional band at 692 cm^{-1}. Hence, phase pure *m*-WO_3 was prepared with the seed layer A-d, B-d and F-d.

The analysis of the absorption spectra in relation to the film thickness indicates that the seed layer A-d exhibits the highest absorption by owning the smallest film thickness with 0.60 µm. The grown film with the seed layer D-d shows the second-highest absorption, albeit with the greatest deviation in film thickness. At a similar film thickness of approximately 1.9 µm, the synthesized WO_3 film with the layer C-d has the highest absorbance, followed by F-d and B-d. The WO_3 film synthesized from the seed layer E-d shows the lowest absorption, on the other

hand presumably the highest concentration of W^{5+} due to the intense/elevated absorption at longer wavelengths.

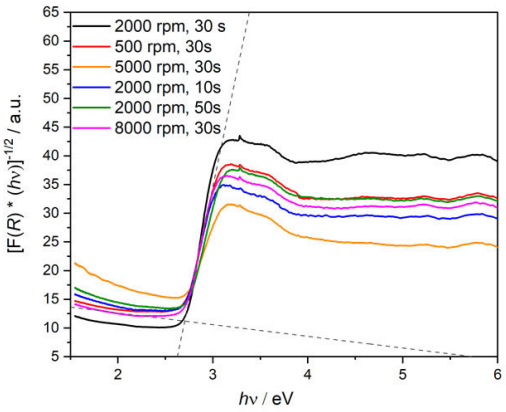

Figure 6.9: Tauc plot of hydrothermally grown WO_3 thin films synthesized by using dynamic spin coated seed layer. (Adapted with permission of the Royal Society of Chemistry 2023).[111]

All samples again exhibit a band gap of 2.7 eV as shown in Figure 6.9, which is in agreement with the values reported in literature.[67,212]

6.2.Photoelectrochemistry

The synthesized WO_3 films were measured with CLV and impedance to determine the photocurrent, the onset potential and using the MOTT-SCHOTTKY approach, additionally the flat band potential and donor density (Table 5). The CLV measurements are shown in Figure 6.10, whereas the MOTT-SCHOTTKY analysis is illustrated in Figure 6.11.

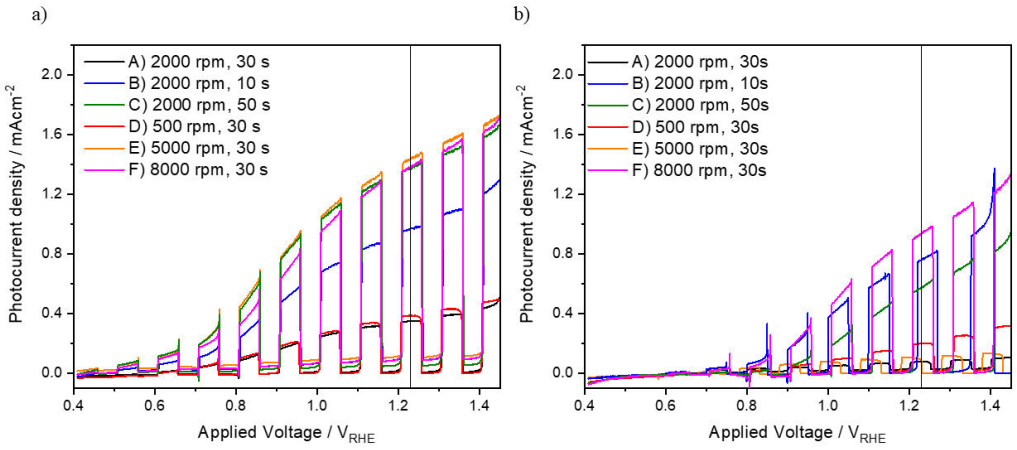

Figure 6.10: Photocurrents of WO_3 photoanodes grown from seed layers prepared by a) static spin coating and b) dynamic spin coating. The resulting photocurrents at 1.23 V_{RHE} are summarized in Table 5. (Adapted with permission of the Royal Society of Chemistry 2023).[111]

The graphs show that the hydrothermally grown WO_3 films synthesized by static spin coating have higher photocurrents than their dynamically coated equivalents. The statically spin coated samples in Figure 6.10a follow a clear trend. The high spinning speeds or the high spinning

durations, which already showed good absorption and phase pure *m*-WO_3, lead to higher photocurrents. Therefore, the highest photocurrents are reached by E-s, C-s and F-s in descending order with 1.51 mA cm^{-2} and 1.38 mA cm^{-2} respectively, indicating that fewer seed layers on the surface lead to better photoelectrochemical performances. The slowest spinning speed of D-s despite the highest absorption together with A-s exhibits the lowest photocurrent of ~0.35 mA cm^{-2}. This is in agreement with the SEM and XRD results. In the SEM images the seed layer D-s shows a fully covered surface and an uncontrolled growth as well as a *h*-WO_3 side phase. The *h*-WO_3 is also present in A-s and is known to have poorer photoelectrochemical performance than the *m*-WO_3 phase.[61] The last statically spin coated sample B-s has a photocurrent of 0.97 mA cm^{-2}, which is expected based on the low seed layer density observed in the SEM analysis. However, the Raman measurements show that *h*-WO_3 phase is present, the resulting in a lower photocurrent than C-s, which has a denser seed layer yet no *h*-WO_3. This highlights the importance of a hydrothermally grown, phase pure *m*-WO_3 film. The thin films synthesized from dynamically spin coated seed layer have not followed a clear trend in terms of performance and spin parameters. In general, all photocurrents are less favorable compared to the equivalents with static spin coating, supporting the argument that static spin coating is the better synthetic method to achieve the highest performance. The seed layer F-d exhibits the highest photocurrent of 0.94 mA cm^{-2} among the dynamically coated WO_3 films.

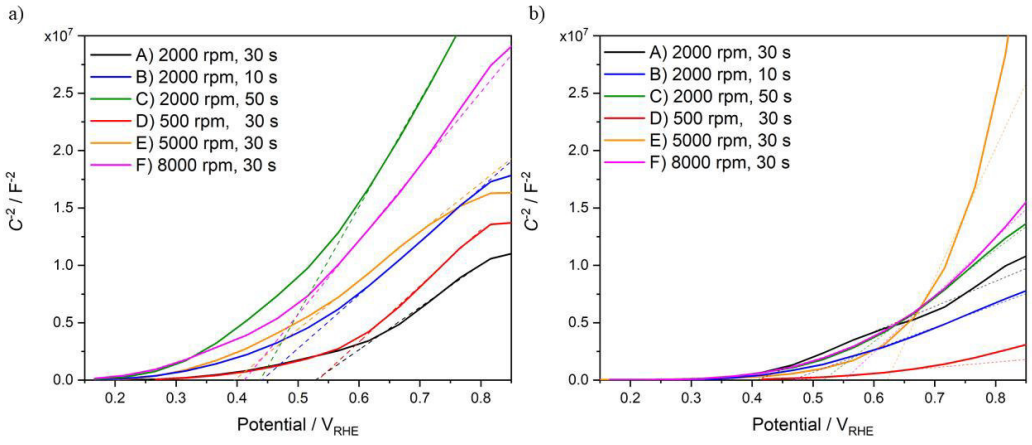

Figure 6.11: Potential-dependent capacitance measurement used for the MOTT-SCHOTTKY analysis of WO_3 photoanodes grown from seed layers prepared by (a) static spin coating and (b) dynamic spin coating. (Adapted with permission of the Royal Society of Chemistry 2023).[111]

The WO_3 film has a decent absorption and a phase pure *m*-WO_3, but an inhomogeneous, partially covered surface. Interestingly, B-d exhibits the second highest photocurrent with a value of 0.76 mA cm^{-2}, which is comparable to the statically coated equivalent, since it has a comparable seed layer density, high absorption and a phase pure *m*-WO_3 crystal structure.

Table 5: Photoelectrochemical findings of hydrothermally grown WO_3 photoanodes.

Sample		Photocurrent density $j_{1.23\ V}$ / mA cm^{-2}	Onset Potential / V_{RHE}	Flat band potential V_{fb} / V_{RHE}	Donor density N_D / m^{-3}
A	s	0.35	0.55	0.53	$1.9 \cdot 10^{21}$
	d	0.08	0.60	0.41	$3.2 \cdot 10^{21}$
B	s	0.97	0.41	0.44	$1.5 \cdot 10^{21}$
	d	0.76	0.59	0.47	$3.6 \cdot 10^{21}$
C	s	1.38	0.40	0.44	$7.5 \cdot 10^{20}$
	d	0.57	0.60	0.52	$1.8 \cdot 10^{21}$
D	s	0.39	0.50	0.53	$1.4 \cdot 10^{21}$
	d	0.20	0.61	0.46	$1.5 \cdot 10^{22}$
E	s	1.51	0.41	0.39	$1.7 \cdot 10^{21}$
	d	0.11	0.60	0.62	$6.2 \cdot 10^{20}$
F	s	1.38	0.40	0.43	$9.8 \cdot 10^{20}$
	d	0.94	0.56	0.55	$1.4 \cdot 10^{21}$

s = static spin coating, d = dynamic spin coating, c = 0.1 M H_2SO_4, P = 100 W cm^{-2}, AM 1.5 G sun simulator

Notably, the WO_3 films with the highest absorption such as A-d and the lowest absorption such as E-d have a comparable photocurrent of ~0.1 mA cm^{-2}. For E-d this can be explained by the presence of the *h*-WO_3 phase impurity. The poor performance of A-d can rather be understood by considering the SEM images, which show a fully covered surface, leading to an uncontrolled growth, observed also for B-d. Finally, the WO_3 film obtained from C-d exhibits a photocurrent of 0.57 mA cm^{-2}, which is in line with the previously proposed analysis of crystal phase purity and performance.

The onset potential of the measured electrodes ranging between 0.4 – 0.6 V_{RHE}. All parameters indicate that the static spin coating has lower onset potential than its dynamically coated equivalent. These results further support the assumption that static spinning coating in general

leads to a better performance. Furthermore, the described trend for photocurrent performance can be extrapolated to the onset potential. High spinning speeds or long spinning durations exhibit an onset potential around ~0.4 V, while slow or short spinning parameters show a higher onset potential.

A more thorough investigation of the onset potential is provided by the MOTT-SCHOTTKY analysis displayed in Table 5. The best performing WO_3 synthesized with the seed layer E-s was found to have the lowest flat band potential of 0.39 V_{RHE}. In comparison to C-s and F-s, which showed the second-best performance, the determined donor density of $1.7 \cdot 10^{21}$ m^{-3} is higher. This may be an indication for better charge carrier separation due to the higher conductivity. The least performing WO_3 prepared from seed layer D-s exhibits a donor density of $1.4 \cdot 10^{21}$ m^{-3} due to the uncontrolled growth leading to defects inside the bulk. The same reasoning can be applied to D-d, which has the greatest measured donor density of $1.5 \cdot 10^{22}$ m^{-3}. The tendency for high donor densities as well as good photoelectrochemical performances and vice versa can be observed for all dynamically spin coated films.

In conclusion, the WO_3 thin film synthesized from the seed layer E-s exhibits the best performance due to the combination of phase purity, strong absorption, low flat band potential and high donor density.

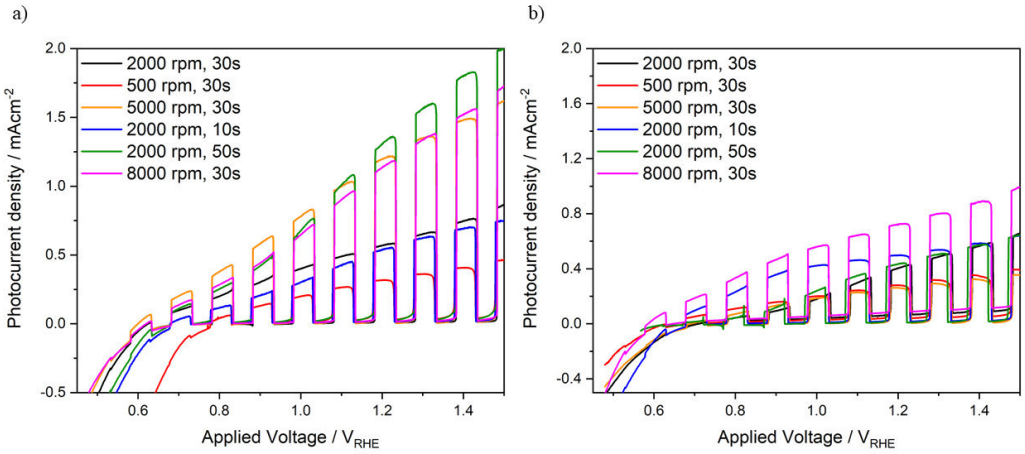

Figure 6.12: CLV in 0.1 M KH_2PO_4 as electrolyte with H_2O_2 as hole scavenger for a) static and b) dynamic spin coating. (Adapted with permission of the Royal Society of Chemistry 2023).[111]

To investigate the charge carrier dynamics in more detail, the charge injection and charge separation efficiencies are calculated according to the method explained in chapter 3.7.4. Therefore, it was necessary to measure CLV of the WO_3 thin films with an additional hole scavenger as shown in Figure 6.12. For this reason, a potassium phosphate buffer was used, which had no effect on the photocurrent displayed in the appendix in Figure 11.8. As expected,

the photocurrents increase with the addition of a hole scavenger, as shown in Figure 6.12. The calculated charge injection efficiencies are presented in Figure 6.13.

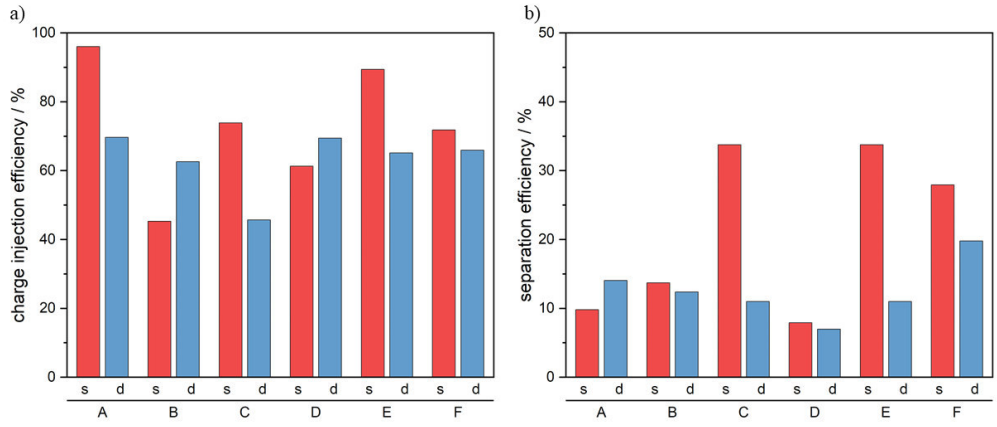

Figure 6.13: a) Charge injection efficiencies and b) charge separation efficiencies at 1.23 V_{RHE} of all samples measured in 0.1 M KH_2PO_4 and 0.1 M H_2O_2. (Adapted with permission of the Royal Society of Chemistry 2023).[111]

Surprisingly, the seed layer A-s has the highest charge carrier efficiency of ~89 %. However, the charge separation with a value of ~9 % is one of the lowest determined. The samples C-s, E-s and F-s show outstanding performances. The charge injection efficiencies belong to the greatest measured ranging around ~80 %, while the charge separation efficiencies are almost twice as high compared to all other WO_3 films. This supports the idea that few seeds improve the performance of hydrothermally grown films due to better electron extraction. The best WO_3 thin film synthesized from E-s exhibits the highest charge carrier separation efficiency of ~34 %. IPCE measurements were preformed on comparable WO_3 films from each seed layer preparation method (E-s and E-d) to further evaluate the photon-current efficiency.

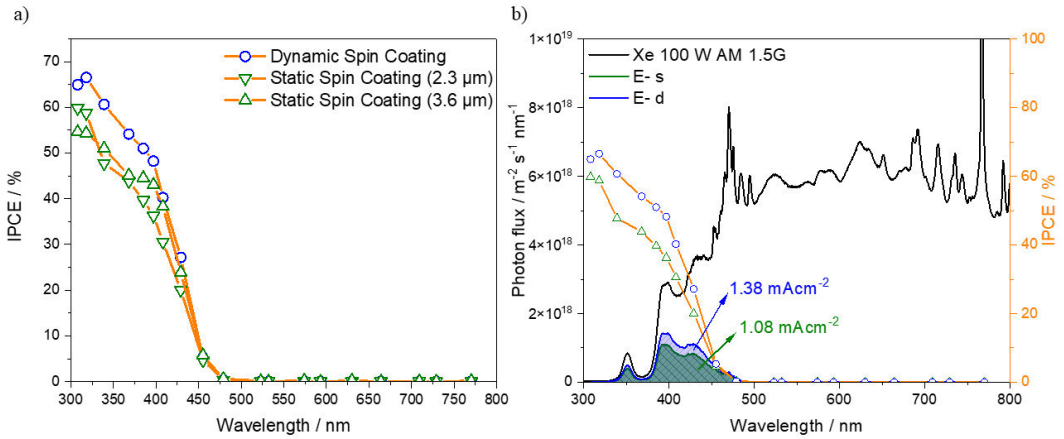

Figure 6.14: IPCE measurements of grown WO3 photoanodes from spin coated seed layers at 5000 rpm per 30 s. (Adapted with permission of the Royal Society of Chemistry 2023).[111]

The IPCE measurements are displayed in Figure 6.14a. The measured WO_3 (E-s) exhibits a maximum efficiency of 60 % at 318 nm. In relation to the film thickness of 2.3 µm, the IPCE of 60 % is a reasonable value. Higher reported values of 80% were measured with thicker films of around 4 µm. [62]

The recorded IPCE measurements can be further used to calculate the theoretically maximal photocurrent according to Patzke *et al.* [213] Here, the solar spectrum is integrated over the measured wavelength using the IPCE trend. This resulted in 1.38 mA cm^{-2} for E-s and 1.08 mA cm^{-2} for E-d. The measured photocurrent of E-s therefore exceeds the theoretical maximum which is impossible. One explanation for this could be that the IPCE was only being measured at certain wavelengths. The interpolation of these data points in conjunction with the measurement errors of the photocurrents leads to an efficiency of 110 %. The value for E-d was determined to be 24 %.

6.3.Conclusion

The seed layer analysis clearly showed that the preparation of the seed layer has a strong influence on the performance. Synthesizing the right seed layer can improve the performance of hydrothermally grown WO_3 without using a cocatalyst. Higher spinning speeds and long spinning durations cause a lower seed layer density. This leads to a more homogeneous, phase pure WO_3 film with strong absorption. Generally, one can say static spin coating leads to better performing photoelectrodes than dynamic spin coating. A reduced seed layer density can drastically promote electron extraction from hydrothermally grown layers, resulting in a maximum photocurrent of 1.51 mA cm^{-2} at a flat band potential of 0.39 V_{RHE}, a donor density of $1.7 \cdot 10^{21}$ m^{-3}, an IPCE of 60%, a charge injection efficiency of 89 % and a charge separation efficiency of 34 %.

7. Optimization of the synthesis of the WO_3/Mo:$BiVO_4$ heterostructure

In order to achieve the highest photocurrents, a heterostructure of WO_3 and Mo:$BiVO_4$ was synthesized to increase the charge carrier separation. Therefore, the optimized WO_3 film synthesized from the seed layer E-s was chosen as the starting material. In the following chapter, the synthetic parameters of the Mo:$BiVO_4$ synthesis are analyzed to obtain a homogeneously covered surface with successful molybdenum doping. The performance of each heterostructure is evaluated by light-induced water splitting. The synthesis described by FISCHER *et al*. was used as starting point as it showed the highest single material photocurrent for $BiVO_4$.[28]

7.1.Solvent Screening

The heterostructure is prepared by dip coating and therefore requires a suitable solvent. The achieve this the solvent must be able to dissolve all organometallic precursors, while at the same time having the necessary polarity to adhere to free hydroxyl groups on the surface of the WO_3 thin film. Five solvents were tested based on their complementary requirements which are listed in Table 6.

Table 6: Solvents tested for the dip coating of the WO_3/Mo:$BiVO_4$ heterostructure.

Solvent	Result
Methanol	-
Ethanol	✓
Diethyl ether	✓
Isopropanol	-
Chloroform	✓

✓ = successful coating

The table above shows that only three solvents namely ethanol, diethyl ether and chloroform lead to a heterostructure. A dark green solid precipitated in methanol after the precursor solution had been stirred for 4 h, indicating that a reaction had taken place. A possible reason could be that a ligand exchange between the vanadium precursor and the solvent which sterically destabilizes the vanadium precursor leading to the formation of V_2O_5. The resulting solid exhibits a low solubility in all solvents except conc. H_2SO_4 and has a dark green color.

The use of isopropanol yielded in a dense solid after 4 h of stirring. This in turn indicates a reaction between the metal precursor and the solvent, presumably polymerization. The remaining three solvents listed in Table 6 were used successfully for coating. Therefore, the

resulted thin films were subsequently characterized by XRD, Raman, UV-Vis and SEM. To analyze the physical properties the dip coating was repeated on a blank FTO sample to prevent overlapping of WO_3 and Mo:$BiVO_4$. The XRD and Raman measurements are displayed in Figure 7.1.

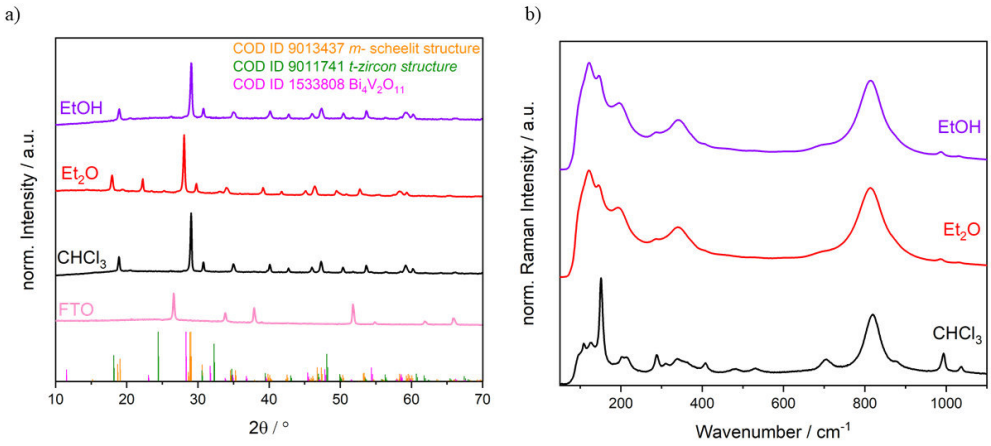

Figure 7.1: a) XRD and b) Raman measurements of Mo:$BiVO_4$ on a blank FTO sample synthesized in different solvents. The FTO diffractogram is used as a negative control to identify unknown reflexes.

The XRD measurements exhibited that the synthesis with chloroform and ethanol yielded in the desired $BiVO_4$ scheelite type structure. In addition, the diffractogram of film synthesized in ethanol displays small reflexes of FTO at ~26 ° 2θ. This indicates that the resulting film is thinner than the film prepared in chloroform, suggesting different adhesion properties. The thin film synthesized in diethyl ether showed a different diffraction pattern than the films prepared in chloroform or ethanol. Some reflexes in agreement with the reported scheelite $BiVO_4$ patterns, but additional reflexes can be attributed to the $Bi_4V_2O_{11}$ polymorph. This material corresponds to the layered Aurivillius-type and is known for the good dielectric, ferroelectric and pyroelectric properties.[214] These results indicate that the synthesis in diethyl ether may generate a scheelite crystal structure due to some well-fitting reflexes, but has other undesirable minor phases. The Raman measurement in Figure 7.1b supports the XRD results. To evaluate if the material is successful doped with Mo Raman spectra were recorded. The thin film prepared in chloroform shows clear distinguishable bands at 710 and 823 cm^{-1} for the V-O stretching vibration. This band is located slightly lower than the 826 cm^{-1} reported for $BiVO_4$ indicating a successful molybdenum doping. The replacement of V^{+5} by Mo^{6+} changes the bond length which results in this band shift.[88,215] The $BiVO_4$ scheelite type is also present in ethanol and surprisingly in diethyl ether. Nevertheless, the Raman bands of the film synthesized in ethanol are broader and less intense, which may be an effect of a thinner film. The Raman spectra of the film generated in diethyl ether are comparable to the resulted film in ethanol,

supporting the assumption that a $BiVO_4$ scheelite type is present. Other additional bands indicating a minor phase were not detected. Further distinction between the *m*-$BiVO_4$ and the *t*-$BiVO_4$ scheelite type structure is important and will be discussed later in this chapter.

To analyze the optical properties UV-Vis spectra were recorded and is shown in Figure 7.2. The KUBELKA MUNK plot illustrates that the thin film synthesized in chloroform exhibits the highest absorption. The films produced in ethanol and diethyl ether have a lower but comparable absorption. This is consistent with the assumption of a thinner $BiVO_4$ film. Applying the KUBELKA MUNK plot to the TAUC plot, it is evident that only the film prepared in chloroform exhibits a band gap of about 2.28 eV, which is in the range of the values reported for the $BiVO_4$ scheelite type. The two films synthesized in diethyl ether and ethanol show a band gap of 1.87 eV and 1.93 eV, respectively.

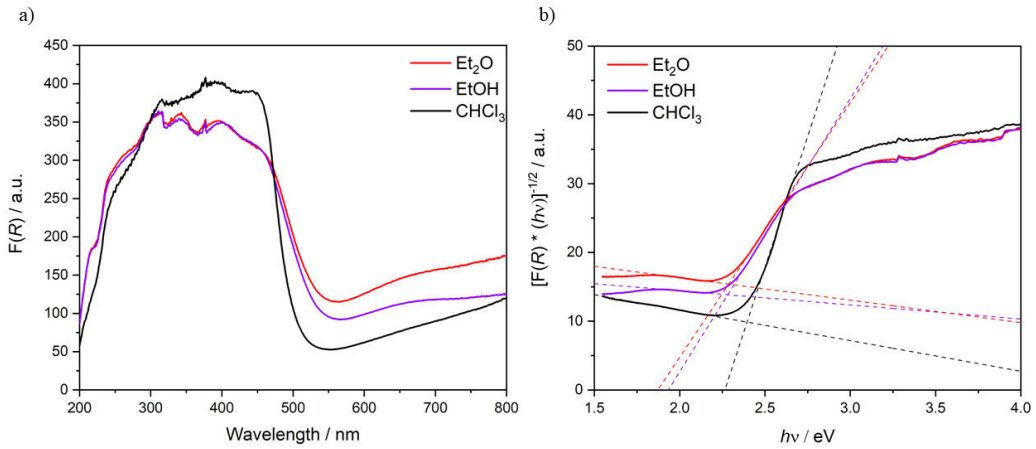

Figure 7.2: a) KUBELKA MUNK and b) TAUC plot of Mo:$BiVO_4$ on bare FTO glass substrate synthesized in different solvents.

The Band gaps for the films prepared in diethyl ether and ethanol are consistent with the reported band gap for $Bi_4V_2O_{11}$.[216] This is in line with the XRD results for the synthesis in diethyl ether. However, the $Bi_4V_2O_{11}$ polymorph was not detected in the synthesis in ethanol. One possible reason would be the introduction of doping impurities and defects, both of which can reduce the band gap,[217] as will be further analyzed later in this chapter with the XPS measurements.

The homogeneous coverage of the surface is equally important as the physical properties of the synthesized film. Therefore, SEM images of the synthesized film were measured and are displayed in Figure 7.3.

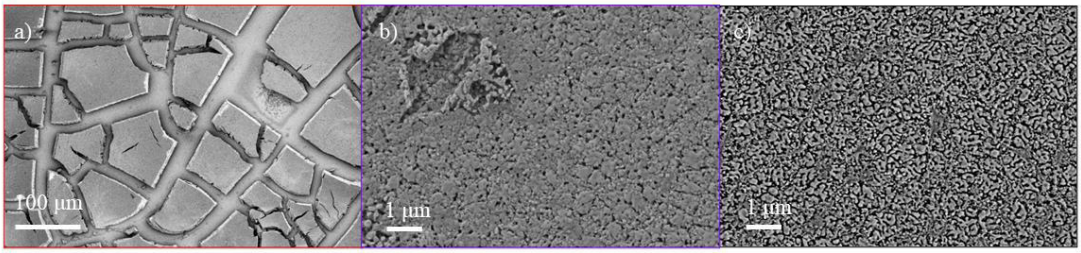

Figure 7.3: SEM images of the Mo:$BiVO_4$ thin film synthesized by dip coating in different solvents. a) Et_2O b) EtOH c) $CHCl_3$.

Figure 7.3 shows that the synthesized film in diethyl ether leads to broken maze-like covered surface which is undesirable for photoelectrochemical applications. In contrast, the films produced in ethanol and chloroform provide a homogenous surface with a sponge-like structure. The comparison between the film made in ethanol and chloroform shows that the sponge-like structure is denser for the film prepared in ethanol than for the film synthesized in chloroform. Fewer and smaller cavities can be observed. The structure visible in Figure 7.2c is in agreement with the reported structure by Fischer *et al.*[28]

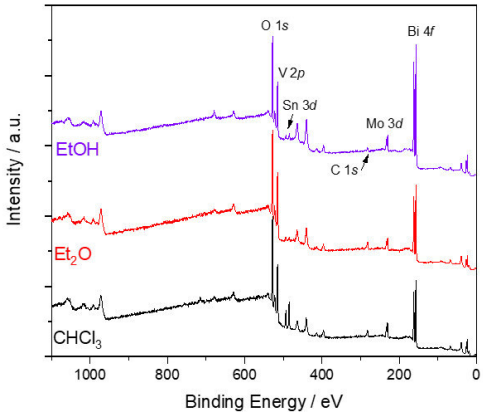

Table 7: XPS results for thin Mo:$BiVO_4$ films synthesized with different solvents. The data was acquired out of measurement displayed in Figure 7.4.

At%	$CHCl_3$	Et_2O	EtOH
Bi	4.8	5.2	8.8
V	18.7	20.5	19.2
O	58.9	56.8	62.7
Mo	3.4	2.5	3.5
Sn	2.6	0.6	0.6
C	11.3	14.1	5.3

Figure 7.4: XPS survey spectra of Mo:$BiVO_4$ thin films synthesized in different solvents. The peaks for the determination of the atom percentage are indicated in the table on the right.

The XPS measurement in Figure 7.4 shows that the doping of Mo was successful, as indicated by the Raman spectrum. The resulting films prepared in Chloroform and ethanol incorporated 3.5 % Mo whereas the film prepared in diethyl ether only incorporated 2.5 %. In all three films it was possible to detect Sn which originates from FTO support. This indicates either a thin film thickness, through which the XPS beam penetrates or an incompletely covered surface. Additionally, the proportions of Bi, V and O differ from the stoichiometry of Mo:$BiVO_4$. One explanation can be that XPS analyzes the surface and therefore measures some coating residues that distort the proportions. The carbon originates from adsorbed CO_2 on the surface which influences the oxygen content accordingly. Doping contamination of ethanol could not be observed in the XPS data.

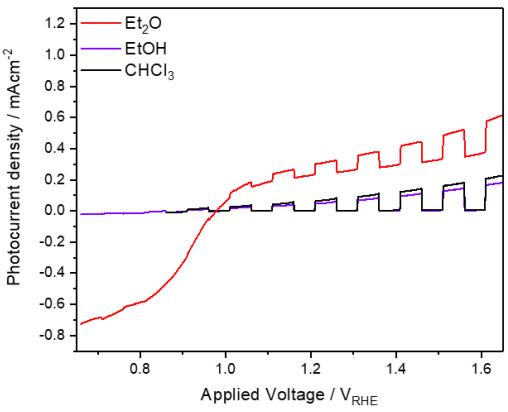

Figure 7.5: CLV measurement of the WO_3/Mo:$BiVO_4$ heterostructure synthesized in different solvents. The electrolyte was 0.1 M KP-buffer.

After the analysis of the single material thin film, a CLV measurement (Figure 7.5) was performed on the WO_3/Mo:$BiVO_4$ heterostructure to evaluate the performance.

Figure 7.5 shows that the performance of the films synthesized in ethanol and chloroform is comparable. Both thin films exhibit an onset potential of 0.8 V_{RHE} while the film prepared in chloroform having slightly higher photocurrent at 1.23 V_{RHE} with 0.07 mA cm^{-2} compared to the film prepared in ethanol with 0.05 mA cm^{-2}. The thin film synthesized in diethyl ether exhibits a different trend with a strongly negative current below 0.95 V_{RHE}. The onset potential is below 0.7 V_{RHE} and the photocurrent shows a steep increase between 0.8 V_{RHE} and 1 V_{RHE}. The measured photocurrent is the highest with 0.31 mA cm^{-2} at 1.23 V_{RHE} but also shows a high dark current of 0.23 mA cm^{-2}. Nevertheless, all photocurrents are much lower than the values reported in the literature, which underlines the importance of optimizing the synthetical parameters.

The solvent screening for the synthesis of WO_3/Mo:$BiVO_4$ in ethanol and chloroform results in a comparable performance with a current of the films with values of 0.05 mA cm^{-2} and 0.07 mA cm^{-2}. Both show a scheelite type $BiVO_4$ structure with a 3.5 % Mo content, a sponge-like surface structure and a homogeneously covered surface. The chloroform thin film exhibits an expected bandgap of 2.28 eV. However, the ethanol thin film exhibited a band gap of 1.93 eV which would indicate a $Bi_4V_2O_{11}$ structure. This structure was present in the film synthesized in diethyl ether which exhibited a band gap of 1.87 eV, a 2.5 % Mo content and a photocurrent of 0.31 mA cm^{-2}. Due to the slightly better performance of the film synthesized in chloroform and uncertainty of the crystal structure in ethanol according to UV-Vis and XRD, chloroform was chosen as the solvent to proceed.

Based on the XPS results, which showed Sn content, SEM images with lower magnification were measured to investigate the origin of Sn. The SEM images are displayed in Figure 7.6.

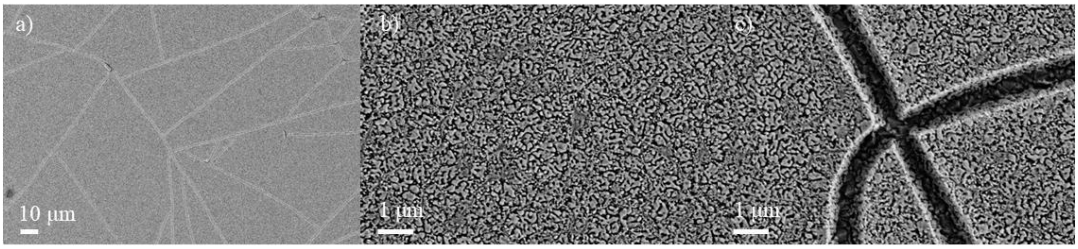

Figure 7.6: SEM images with different magnification of Mo:$BiVO_4$ films synthesized with chloroform.

The low magnification in Figure 7.6a shows that the sponge-like structure is divided in domains, which was also mentioned by FISCHER *et al.* [28] In Figure 7.6c the FTO is visible underneath which explains the XPS results. However, for a heterostructure this is undesirable as it is impossible to distinguish the type of charge carrier separation and transfer.

To finally determine the crystal structure present, a high-resolution powder XRD (HRXRD) was measured to distinguish between the *t*-$BiVO_4$ and the *m*-$BiVO_4$. Therefore, multiple samples were synthesized and scratched off the FTO support to collect a sufficient amount of material to measure a powder XRD with decreased step size and longer sample irradiation. The distinction is feasible with the reflex at ~35° 2θ, which should split in two if the desired*m*-$BiVO_4$ is present.[28] To synthesize enough powder the dip coating was performed with three blank FTOs and then the support was scraped off to obtain the powder. The HRXRD is displayed in Figure 7.7.

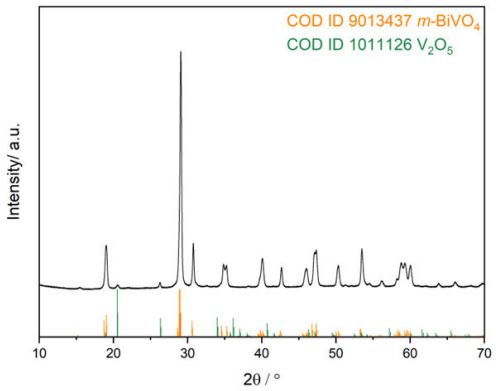

Figure 7.7: HRXRD of $BiVO_4$ powder synthesized in chloroform.

The HRXRD shows that the desired *m*-$BiVO_4$ scheelite type structure is present due to splitting of the reflex at ~35° 2θ. Furthermore, the HRXRD additionally indicates the presence of V_2O_5 which explains the deviating proportions in the XPS measurements. This points out the importance of synthetic accuracy to avoid an excess of the vanadium precursor.

The optimization of the synthetic parameters will therefore be further investigated to achieve the best coverage and performance of a WO_3/Mo:$BiVO_4$ heterostructure.

7.2.Dip Coating parameters

The parameters that affect a dip coating process are immersion time, withdraw speed, number of dip cycles, coating angle, temperature, inertial force, solution viscosity, gravity and surface tension. [218,219] By choosing a solvent to optimize the synthetic parameters the factors can be narrowed down to immersion time, angle, withdraw speed and cycles. The withdraw speed is known to have the strongest influence on the film thickness and film quality.[220] Together with the cycles, which theoretically allow the thickness to be continuously increased by more cycles, these parameters were chosen to investigate in detail. The angle and immersion speed were kept constant at 90° and 3 s, respectively. In this chapter the results of optimization to achieve a homogenous covered surface with only one material exposed to the electrolyte are discussed . The performance is evaluated with CLV measurements in water. Table 8 summarizes the parameters investigated.

Table 8: Synthetic parameters for the optimization of the WO_3/Mo:$BiVO_4$ dip coating process.

Withdraw Speed / mm min^{-1}	Cycles
5	1
5	2
100	1
100	2
100	3
300	1
300	2

Dip coating angle = 90°, Immersion time = 3 s, T = 298 K, Chloroform

The physical properties of the heterostructures were analyzed with GIXRD, Raman and UV-Vis while the film quality was determined by SEM measurements. The GIXRD and Raman measurements are displayed in Figure 7.8.

The GIXRD in Figure 7.8a shows that the crystal phase *m*-$BiVO_4$, the *m*-WO_3 and the *h*-WO_3 are present. In general, it is evident that the single-cycle samples have more distinct WO_3 reflexes than double-coated thin films, which is due to the increase in film thickness. Compared to the single-coated thin films, only the withdrawal speed of 5 mm min^{-1} retains the facet enriched WO_3 phase. The 100 and 300 mm min^{-1} heterostructures exhibit evenly balanced facets between (002), (020) and (200), which are thermodynamically more stable. In addition, the *h*-WO_3 phase becomes more noticeable at faster withdrawal speed. This may also be an

effect of the decreasing facet, which reduces the intensity of the (002) reflex and thus highlights less intensive reflexes.

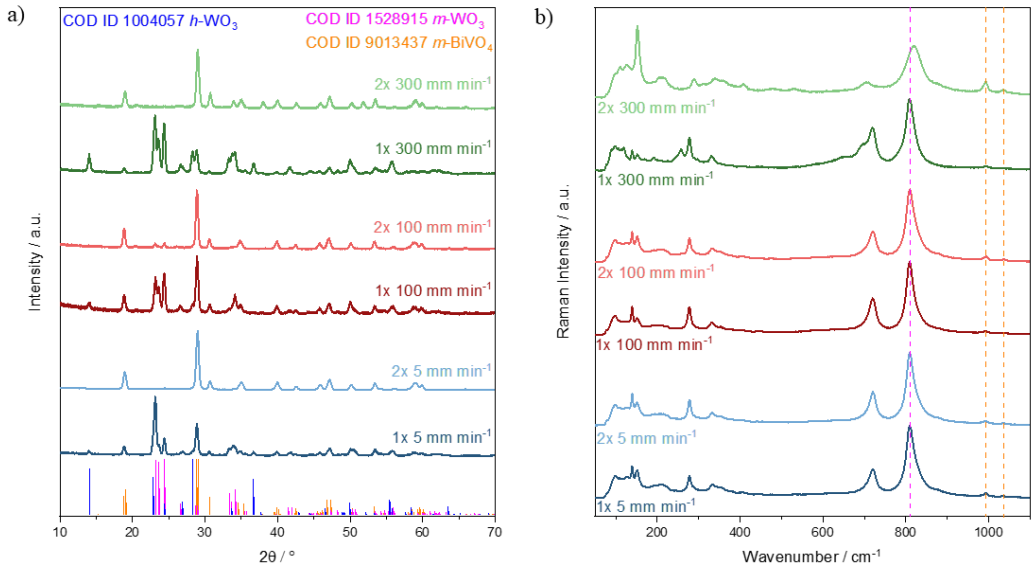

Figure 7.8: GIXRD and Raman measurements of the WO_3/Mo:$BiVO_4$ heterostructure synthesized by different dip coating parameters.

Furthermore, the comparison between the different dip coating parameters reveals that the *m*-$BiVO_4$ phase is most noticeable in the dip coated heterostructure the withdrawal speed of 100 mm min^{-1} due to the most intense reflex at 29 ° 2 theta. This indicates that at a withdrawal speed of 100 mm min^{-1}, the greatest amount of solution adheres to the surface, resulting in a higher $BiVO_4$ content after calcination. This is in contradiction to the expectations which suggest that the fastest withdraw speed results in the thinnest film, and vice versa. A closer look at the Raman spectra also shows that the Raman bands at 990 cm^{-1} and 1035 cm^{-1} are barely visible in the single-cycle coated heterostructures. The most distinctive bands in Raman spectra can all be attributed to the WO_3 vibrations and overlaps with the main band of *m*-$BiVO_4$. Moreover, the heterostructure synthesized with the withdrawal speed of 300 mm min^{-1} additionally exhibits the band at 692 cm^{-1} originating from the *h*-WO_3 phase, which matches the XRD results. For the double-coated heterostructure, each diffractogram shows predominantly the *m*-$BiVO_4$ crystal phase. The resulting diffractogram of the heterostructure synthesized by double dip coating at a speed of 100 mm min^{-1} is the only diffractogram which exhibits the remaining reflexes of the WO_3 film. In contrast, the Raman spectra of the double-coating show only the WO_3 bands, which underlines the importance of the surface sensitive characterization of GIXRD. The exception is the double dip coated heterostructure with a withdrawal speed of 300 mm min^{-1} which only shows the $BiVO_4$ bands at 827 cm^{-1}, 990 cm^{-1} and 1035 cm^{-1} in the Raman spectra.

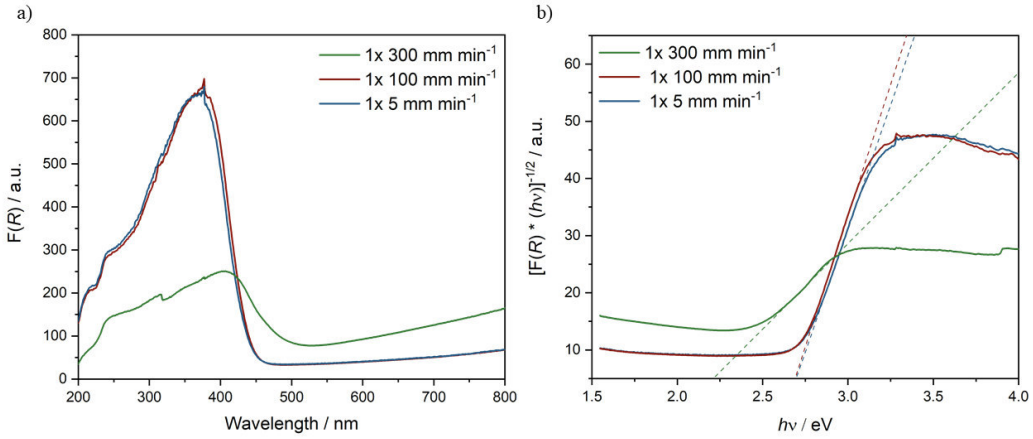

Figure 7.9: KUBELKA MUNK and TAUC plot of the WO_3/Mo:$BiVO_4$ heterostructure synthesized by a single dip coating at different withdraw speeds.

In addition a UV-Vis measurement was performed after the first (Figure 7.9) and the second (Figure 7.10) dip coating. Figure 7.9 shows that only the heterostructure with a withdraw speed of 300 mm min^{-1} exhibits a Mo:$BiVO_4$ absorption edge and the respective band gap of 2.2 eV. The other two withdraw speeds indicate only the WO_3 band edge with a band gap of 2.6 eV. This is contradiction to the XRD results, which showed that the heterostructure with a withdraw speed of 100 mm min^{-1} has the highest Mo:$BiVO_4$ content. Therefore, SEM measurements are needed to determine the coverage and the homogeneity of the heterostructure. In contrast, only the Mo:$BiVO_4$ band edge is observed for all three samples, shown in Figure 7.10 . The double-coated heterostructure with a withdraw speed of 300 mm min^{-1} exhibits the highest absorption followed by the double-coated heterostructure with a withdraw speed of 100 mm min^{-1}, both with a band gap of 2.4 eV. Whereas the double-coated heterostructure with a withdraw speed of 5mm min^{-1} has a band gap of 2.2 eV and the lowest absorption among the double coated samples. This is consistent with the XRD results indicating that Mo:$BiVO_4$ is the major crystal phase detectable on the surface after double dip coating.

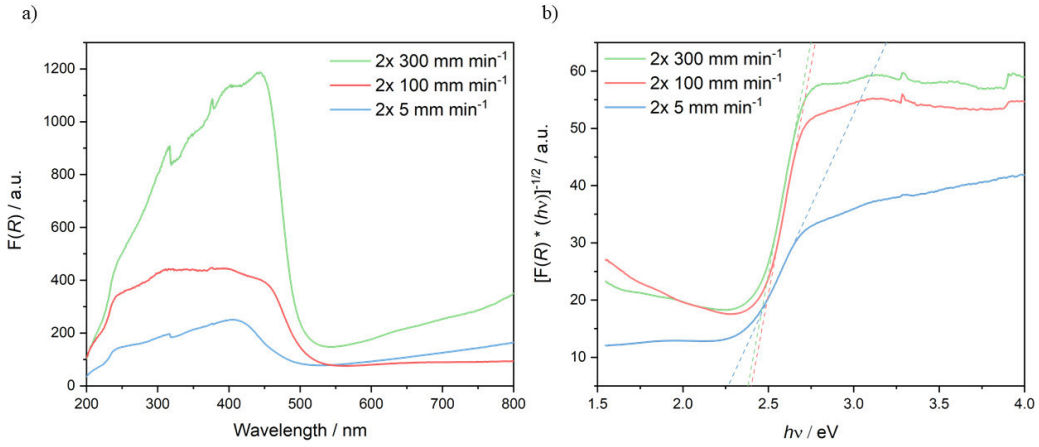

Figure 7.10: KUBELKA MUNK and TAUC plot of the WO_3/Mo:$BiVO_4$ heterostructure synthesized with a two times dip coating at different withdraw speeds.

In order to investigate the surface structure and coverage cross-section, top-view and detailed SEM measurements were performed. The images for the withdraw speed of 5 mm min^{-1} are displayed in Figure 7.11.

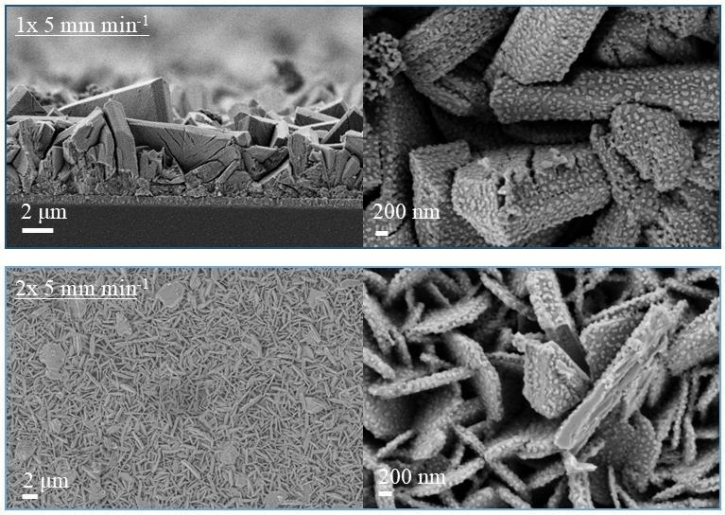

Figure 7.11: SEM images of the WO_3/Mo:$BiVO_4$ heterostructure synthesized by a single and double dip coating at a withdraw speed of 5 mm min^{-1}.

The highly magnified image of the single-coated heterostructure synthesized with the withdraw speed of 5 mm min^{-1} shows an incompletely covered surface. The WO_3 nanoplates are covered with Mo:$BiVO_4$ droplets. As such, the cross-section shows only the FTO and WO_3 layer. The double-coated heterostructure prepared with the withdraw speed of 5 mm min^{-1} displays the same tendency in the SEM images. The Mo:$BiVO_4$ droplets are larger compared to the single-coated heterostructure synthesized with the withdraw speed of 5 mm min^{-1}, however the WO_3 nanoplates are still exposed on the surface, an undesirable effect due to the charge carrier . The low magnification overview image, on the other hand, shows that the entire surface is

homogenously covered with Mo:$BiVO_4$ droplets, confirming the high quality, which can be achieved by the dip coating approach. Figure 7.12 displays the SEM images of the heterostructures, which are synthesized with a 100 mm min^{-1} withdraw speed.

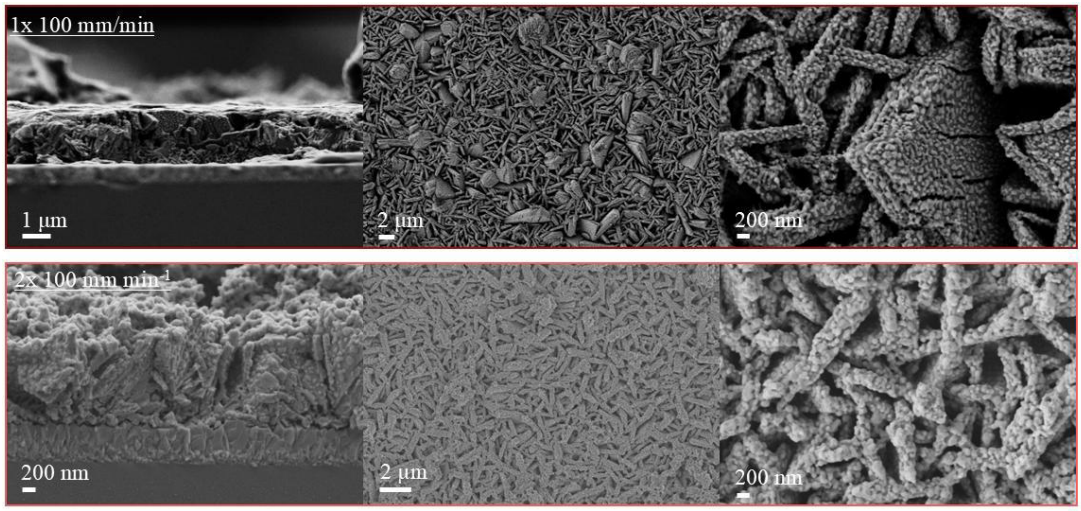

Figure 7.12: SEM images of the WO_3/Mo:$BiVO_4$ heterostructure synthesized by a single and double dip coating at a withdraw speed of 100 mm min^{-1}.

The single-coated heterostructure with a withdraw speed of 100 mm min^{-1} shows a similar trend that has already been previously discussed. The high magnification images reveal a drop-like coverage homogeneously distributed over the entire surface, which is visualized on the low magnification image. The cross-section shows only the WO_3 and FTO layer. However, it can be argued that the droplets are denser compared to the heterostructure which was obtained with the withdraw speed of 5 mm min^{-1}. This can account for the results of the surface sensitive GIXRD measurements. However, the double-coated heterostructure prepared with the withdraw speed of 100 mm min^{-1} exhibits a different surface structure. The high magnification image depicts fully encapsulated WO_3 nanoplates which are comparable to the core shell structures of KITAMORI and KONDO.[27] The cross-section further shows that the Mo:$BiVO_4$ is also present in the valleys and only the direct contact to the FTO is formed by WO_3. This composition should allow a single material electrolyte exposure and therefore the inevitable diffusion of the charge carrier through the material to the surface.

The heterostructure obtained using a withdraw speed of 300 mm min^{-1} is displayed in Figure 7.13 and once again shows a different surface composition. The fastest withdraw speed led to a layered type of heterostructure. The Mo:$BiVO_4$ no longer encapsulates the WO_3 nanoplates as was observed a the withdraw speed of 100 mm min^{-1}. Instead, the structure forms a sponge-like layer on top of the WO_3 nanoplates. The Mo:$BiVO_4$ heterostructure is much more comparable to the already described in chapter 7.1. Additional SEM images in the appendix

(Figure 11.9) also show the domains and broader cross-section. However, the high magnification image illustrates that the layer has some cracks where the underlying nanoplates are observable.

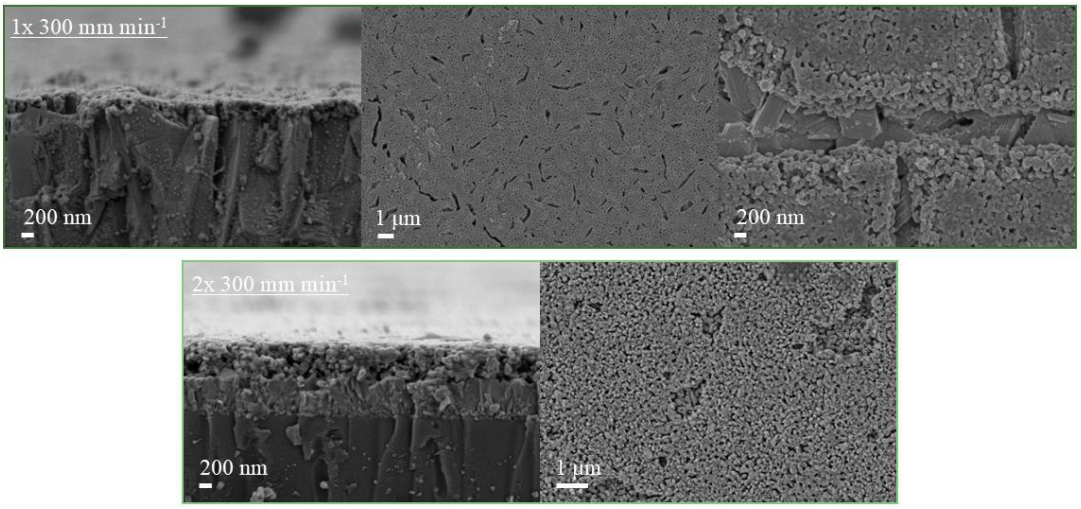

Figure 7.13: SEM images of the WO_3/Mo:$BiVO_4$ heterostructure synthesized by a single and double dip coating at a withdraw speed of 100 mm min^{-1}.The double 300 mm min^{-1} cross section was supplemented from a FTO/$BiVO_4$ sample synthesized with the same parameters to have a comparison and determine the film thickness.

Moreover, the cross-section of the single-coated heterostructure, which was obtained with the withdraw speed of 300 mm min^{-1} reveals a film thickness of ~220 nm, while the film thickness increased to ~530 nm after double dip coating. Additionally, the overview image of the double-coated heterostructure exhibits a fully covered surface. The previous cracks are covered with an additional Mo:$BiVO_4$ layer and no WO_3 is visible underneath. This would enable a comparison between two differently formed heterostructures due to the complete coverage of WO_3. The encapsulated core-shell-like structure that was obtained by the 100 mm min^{-1} withdraw speed and the layered structure which was the result of the faster 300 mm min^{-1} withdraw speed.

These two different types of heterostructures bring into focus whether it is possible to obtain a dense layered structure with the withdraw speed of 100 mm min^{-1} by coating it more often. Therefore, the heterostructure was coated a third time with this withdraw speed to determine the difference. These SEM images are displayed in Figure 7.14.

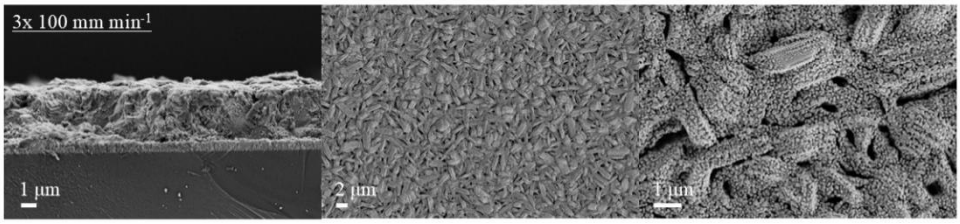

Figure 7.14: SEM images of the WO_3/Mo:$BiVO_4$ heterostructure synthesized by a triple dip coating at a withdraw speed of 100 mm min^{-1}.

The SEM images in Figure 7.14 and the images in Figure 11.10 in the appendix show that the droplets grow on the surface and merge into a denser film. However, some additional riffs appeared, which are comparable to the single coated heterostructure prepared at a withdrawal speed of 300 mm min^{-1}. This leads to the assumption that multiple dip coatings with a withdrawal speed of 100 mm min^{-1} would probably result in a layered structure similar to that already observed at a withdrawal speed of 300 mm min^{-1}.

After the analysis of the physical properties and surface composition of the heterostructure the performance was measured with light assisted water splitting. The CLV measurements of all synthesized heterostructures are shown in Figure 7.15, while the resulting photocurrents at 1.23 V_{RHE} are summarized in Table 9. The CLV measurements were performed on the bare WO_3 thin film for comparison, on the Mo:$BiVO_4$ heterostructure and after deposition of CoPi as a catalyst to enhance the hole diffusion through the Mo:$BiVO_4$ layer.

All photocurrents determined and summarized in Table 9 show that forming of a heterostructure does not enhance the performance of the photoelectrode. In all cases the measured photocurrent after dip coating is lower in order of magnitude compared to the bare WO_3 photoelectrode. This is contrary to the trends reported in literature.

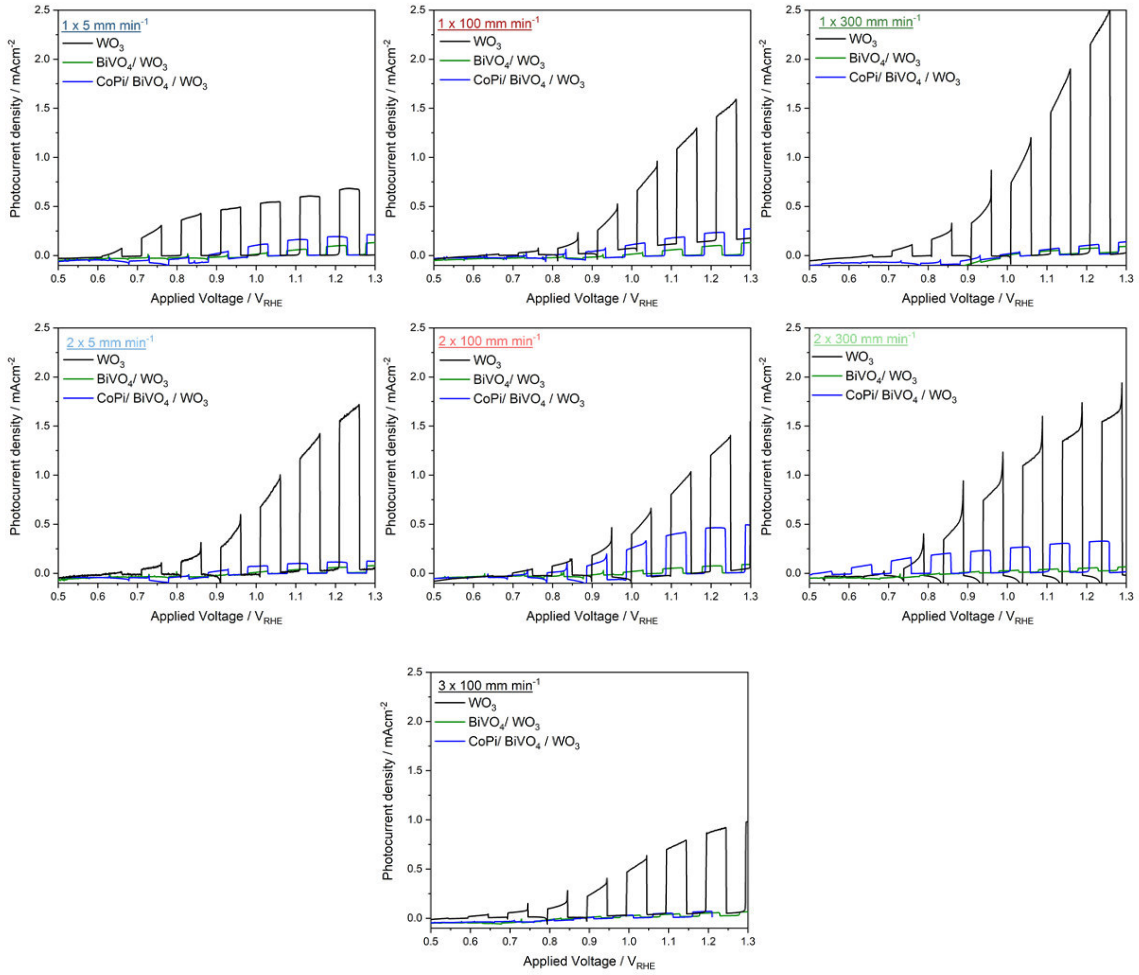

Figure 7.15: CLV measurements of the WO_3/Mo:$BiVO_4$ heterostructures with and without catalyst synthesized with different dip coating parameters. The electrolyte was 0.1 M KP-buffer.

The prepared heterostructures exhibit photocurrents between 0.05 mA cm^{-2} and 0.1 mA cm^{-2} with the heterostructure having the highest photocurrent with a single dip coating with a withdrawal speed of 5 mm min^{-1}. It seems that the surface homogeneity has little effect on the performance, as the photocurrents of the heterostructures synthesized by a single dip coating with a withdrawal speed of 5 mm min^{-1} 300 mm min^{-1}. There is no clear trend between the coating parameters, surface coverage and performance. However, after deposition of the cocatalyst, the photocurrents increase as expected, whilst it is also possible to attribute the performance to the surface coverage and thus to the dip coating parameters. The one cycle heterostructures with cocatalyst doubled the photocurrent on average compared their equivalent without cocatalyst. All samples exhibited an incompletely covered surface supporting the conclusion that the improvement is only attributed to the faster kinetics of the OEC. Despite the comparison the two cycle heterostructure with dip coating, it can be stated that the improvement in performance for heterostructures with a dip coating at a withdrawal speed of

100 and 300 mm min^{-1} from 0.06 mA cm^{-2} and 0.05 mA cm^{-2} to 0.45 mA cm^{-2} and 0.33 mA cm^{-2}, respectively, is additionally due to better charge carrier separation. The completely covered surface is forced to diffuse the charge carriers through the layer. This is further supported by the use of a catalyst due to the increased driving force. This also demonstrates that the formation of the heterostructure can favor charge carrier separation but is overshadowed by other loss-rich effects.

Table 9: Summary of photocurrents determined from the CLV measurements displayed in Figure 7.15.

Dip Coating Speed mm min^{-1}	Cycle	WO_3 $j_{1.23\ V}$ / mA cm^{-2}	Mo:$BiVO_4$/WO_3 $j_{1.23\ V}$ / mA cm^{-2}	With cocatalyst $j_{1.23\ V}$ / mA cm^{-2}
5	1	0.67	0.10	0.18
	2	1.60	0.05	0.11
100	1	1.48	0.09	0.23
	2	1.31	0.06	0.45
	3	0.90	0.06	0.07
300	1	2.05	0.08	0.11
	2	1.53	0.05	0.33

c = 0.1 M KP-buffer, P = 100 W cm^{-2}, AM 1.5 G sun simulator

The comparison between the two different morphologies shows that the core-shell like structure synthesized by a double coating at a withdrawal speed of 100 mm min^{-1} is more favorable than the layer like structure synthesized by a double coating at a withdrawal speed of 300 mm min^{-1} due to the higher photocurrent of 0.45 mA cm^{-2}. To further evaluate the performance, all onset potentials are summarized in Table 10. All onset potentials of heterostructures are ~ 0.52 V_{RHE} with the exception of the heterostructure synthesized by a double coating at a withdrawal speed of 5 mm min^{-1}, which exhibited a higher onset potential of 0.68 V_{RHE}.

Table 10 Summary of onset potentials determined from the CLV measurements displayed in Figure 7.15.

Dip Coating Speed mm min^{-1}	Cycle	WO_3 onset potential / V_{RHE}	Mo:$BiVO_4$/WO_3 onset potential / V_{RHE}	With cocatalyst onset potential / V_{RHE}
5	1	0.61	0.52	0.51
	2	0.61	0.68	0.53
100	1	0.61	0.51	0.51
	2	0.64	0.52	0.54
	3	0.54	0.57	0.65
300	1	0.62	0.53	0.53
	2	0.54	0.57	0.49

c = 0.1 M KP-buffer, P = 100 W cm^{-2}, AM 1.5 G sun simulator

Notably only the heterostructure generated by a double coating at a withdrawal speed of 300 mm min^{-1} show the expected onset potential shift to lower values exhibiting the lowest onset potential of 0.49 V_{RHE}.

The optimization of the dip coating parameters leads to an increase in photocurrents from 0.05 mA cm^{-2} to 0.45 mA cm^{-2} by using two cycle dip coating with a withdrawal speed of 100 mm min^{-1}. Two different morphologies for the heterostructure could be realized, whereby a core-shell like structure proved to be more advantageous. It was also shown that the heterostructure has a beneficial effect on the charge carrier separation. However, the initial photocurrent always drops by an order of magnitude after synthesizing the heterostructure. This indicates that the heterostructure is not yet optimal and that the positive effect of charge carrier separation is overlaid by other effects.

7.3.Absorption inversion

The role of the individual materials forming the heterostructure is important to discuss in order to conduct further investigations. Depending on which material is the main absorber the charge carrier pathways are different and require another optimization. A schematic illustration of the charge carrier pathways is displayed in Figure 7.16. A comparison of the samples between the heterostructures used in this thesis and the samples from the group of SEO *et al*., which investigated the role of the material shows a difference in thickness in addition to a different morphology. The WO_3 base layer in the previous work by Seo *et al*. had a film thickness of ~800 nm covered with 30-100 nm of $BiVO_4$.[113] This ratio of WO_3 to $BiVO_4$ is much lower

than the ratio which is presented in this thesis. The WO_3 exhibits a film thickness of ~2.2 µm, while the thickness of Mo:$BiVO_4$ is ~220 nm. Thus, the question arises, due to the widely varying film thickness, which of the materials should mainly function as an absorber and which material is used to enhance charge carrier separation. This chapter of the thesis is focused on the role of the materials used to determine whether the majority of the photons are absorbed by WO_3 or by $BiVO_4$. This may explain the losses after heterostructure formation and possibly give further insights into the existing carrier dynamics.

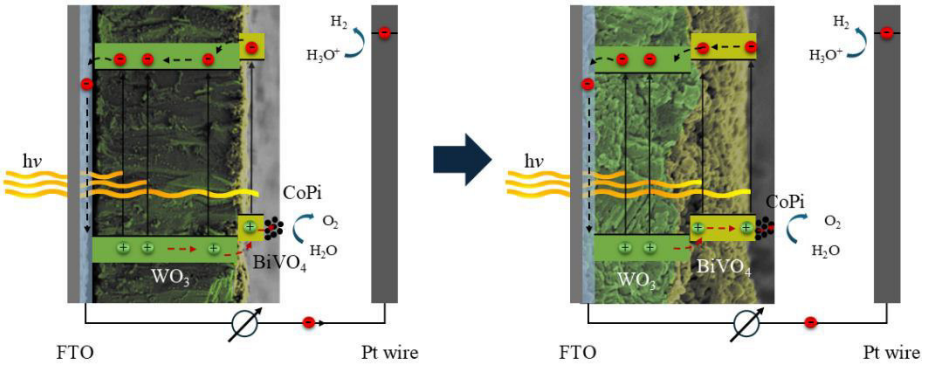

Figure 7.16:Schematic illustration of the charge carrier diffusion of the WO_3/Mo:$BiVO_4$ heterostructures with different film thicknesses.

To achieve an absorption inversion, the thickness of the WO_3 base must be reduced and the thickness of the Mo:$BiVO_4$ top layer increased. As was shown in the previous chapter, the thickness of Mo:$BiVO_4$ can be increased by performing several dip coating cycles. Therefore, two synthetical parameters can be adjusted to decrease the thickness of WO_3. Either reducing the concentration of the hydrothermal precursor solution or shortening the hydrothermal growth reaction. SEM images of the hydrothermal growth reaction at half the concentration are shown in Figure 7.17.

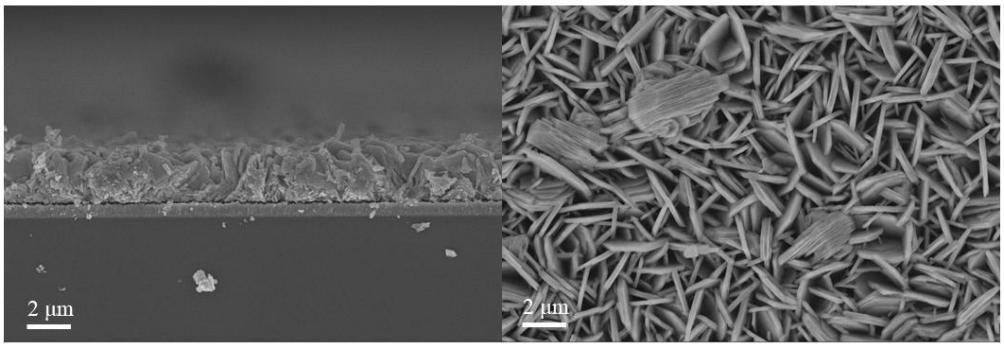

Figure 7.17:SEM images after the hydrothermal growth reaction of WO_3 performed at half the concentration (c= 5mM L^{-1}) described in chapter 4.3.

The cross section of the resulting WO_3 film visible in Figure 7.17 clearly shows that the film thickness is maintained. However, the top view indicates that the thickness of the nanoplates has decreased significantly. This shows that the film thickness is independent of the precursor solution and that the next step to reduce the film thickness is to analyze the growth time. Table 11 lists the variations in growth time and the resulting film thickness determined by SEM cross sectional images displayed in Figure 7.18a.

Table 11: Summary of film thicknesses determined by SEM cross sectional images (Figure 7.18b) of hydrothermaly grown WO_3 films.

Growth time / h	Film thickness / µm
1	-
1.25	0.36 ± 0.45
1.5	1.17 ± 0.07
2	1.73 ± 0.05
3	2.65 ± 0.08
4	2.28 ± 0.25

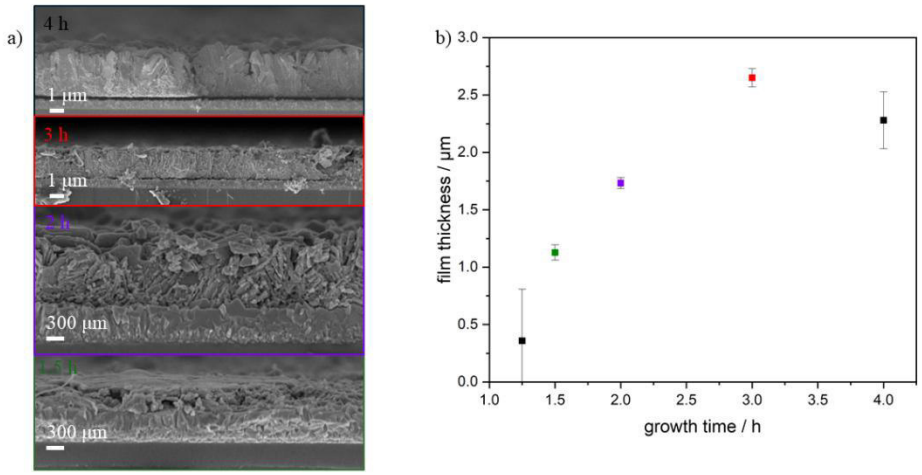

Figure 7.18: a) Cross sectional SEM images of the hydrothermal thickness analysis with b) the total film thickness plotted against the growth time.

Table 11 and Figure 7.18b show that the growth time of 1.25 h leads to a large error which exceeds the determined film thickness. This implies an inhomogeneous coverage of the surface and thus a non-dense WO_3 film. The growth time of 1 h is not sufficient to initiate hydrothermal growth inside the autoclave. Therefore, 1.5 h is the shortest growth time possible with a resulting film thickness of 1.17 ± 0.07 µm. To ensure that the shortening of the growth time has no influence on the physical properties of the grown WO_3 thin film, GIXRD, Raman and UV-

Vis measurements were performed. The results of the GIXRD and Raman analysis are depicted in Figure 7.19 while the UV-Vis measurement is displayed in Figure 7.20.

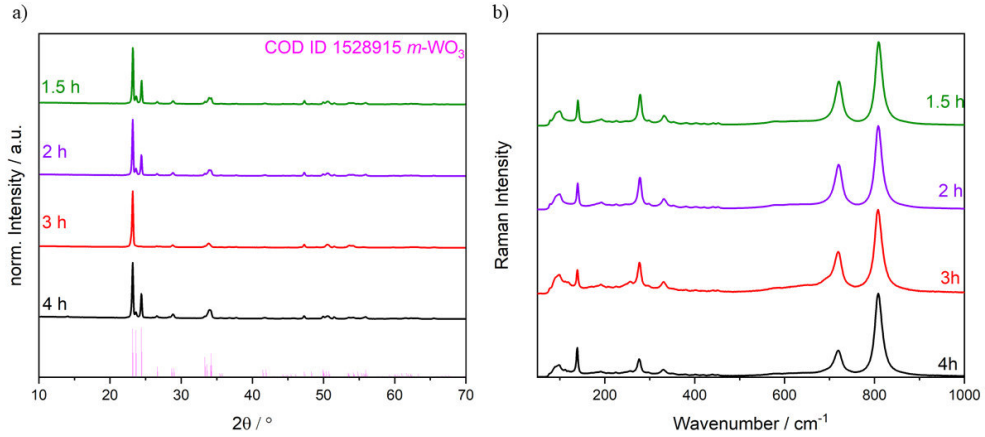

Figure 7.19: a) GIXRD and b) Raman measurements of the growth time analysis of WO_3 thin films.

The GIXRD measurements indicate that the previously discussed facet enrichment is preserved, and no hexagonal phase is observed. This is consistent with the Raman measurements which show a value of 692 cm^{-1} only for the 3 h growth time, indicating a small amount of hexagonal phase in the WO_3 thin film with 3 h growth time. The UV-Vis measurements in Figure 7.20 indicate that the WO_3 thin films with 3 h and 4 h growth time exhibit nearly the same absorption behaviors.

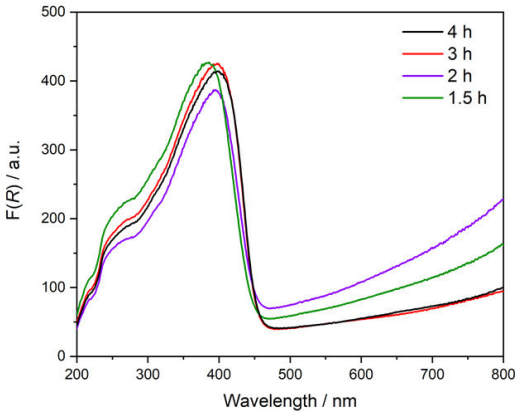

Figure 7.20: UV-Vis measurements of the growth time analysis of WO_3 thin films.

Both thin films exhibit the same amount of W^{5+} as the curves overlap above 500 nm. Interestingly the reduction in absorbance barely affects the absorbance for the WO_3 thin films with a growth time of 2 h and 1.5 h. The WO_3 sample with the 2 h growth time and a corresponding film thickness of 1.73 ± 0.05 µm was found to have the lowest absorbance. This contradicts the expectation that, due to the low absorption coefficient of WO_3, the film with the

minimal film thickness should have the lowest absorption. Additionally, the short growth times of 1.5 h and 2 h exhibit a higher content of W^{5+} due to the steeper curves above 500 nm. This was expected and is in direct correlation with the growth time. Shorter growth time in the hydrothermal growth reaction promotes more defects as the system has insufficient time to harden the defects inside the crystal structure. Subsequent calcination was retained to to maintain the facet enrichment and therefore the shorter growth time exhibit more W^{5+}.

The thin film with a growth time of 1.5 h and a film thickness of 1.17 ± 0.07 µm was selected for dip coating synthesis to form the WO_3/Mo:$BiVO_4$ heterostructure. The optimized dip coating parameters from chapter 7 with a withdrawal time of 100 mm min^{-1} were applied and a maximum of up to three cycles were performed to increase the Mo:$BiVO_4$ film thickness. The resulting heterostructures were analyzed with GIXRD, UV-Vis and SEM imaging, while the performance of the heterostructures were evaluated with CLV and IPCE measurements. The GIXRD and UV-Vis measurements are displayed in Figure 7.21.

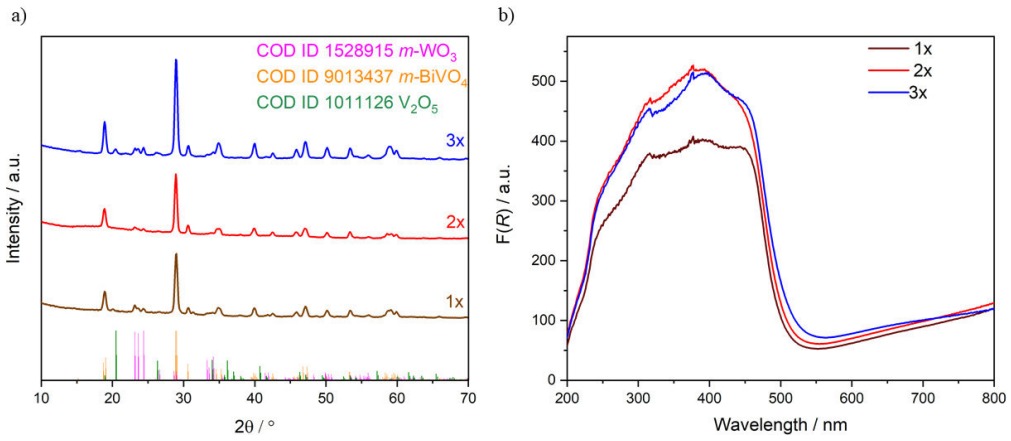

Figure 7.21: a) GIXRD and b) UV-Vis measurements of the WO_3/Mo:$BiVO_4$ heterostructures using the 1.5 h grown WO_3 film as base synthesized with different dip coating cycles.

GIXRD show the same trend as discussed in the previous chapter. The three most intense reflexes of WO_3 between 23.1° and 24.3° 2 theta are still visible in the diffractogram of the heterostructure. In addition, after three cycles of dip coating, the diffractogram shows the most intense reflex of V_2O_5 at 20.4° 2theta. This may indicate that more cycles lead to inhomogeneity, which hinders the sol-gel aging leads to some V_2O_5 residuals. The KUBELKA MUNK plot in Figure 7.21b shows only the Mo:$BiVO_4$ band edge at ~500 nm with a respective band gap of 2.4 eV. The heterostructures synthesized with a single dip coating cycle exhibit the lowest absorption, followed by the triple and double dip coating cycles. The absorption therefore no longer increases after the second dip coating cycle, which confirms the observation

from the GIXRD measurements, that the layer becomes inhomogeneous. The surface morphology can be analyzed with the SEM imaging shown in Figure 7.22.

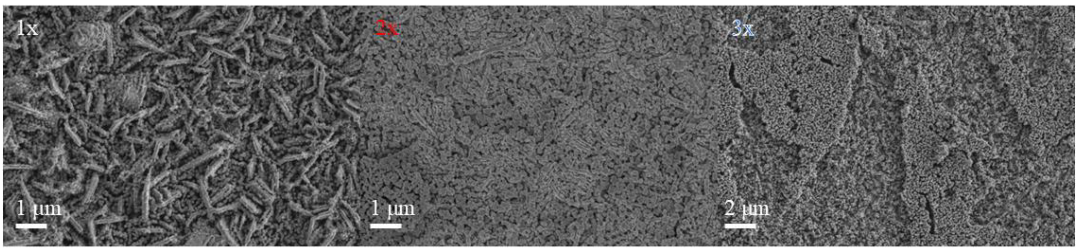

Figure 7.22: Top view SEM images of the WO_3/Mo:$BiVO_4$ heterostructure synthesized with different dip coating cycles.

The first dip coating cycle is comparable to the morphology already described in the previous chapter. As before, it shows the nanoplate-like structure of WO_3 encapsulated by the sponge-like morphology of Mo:$BiVO_4$. The surface is not fully covered and the WO_3 nanoplates are still exposed to the surface. After the second dip coating cycle, the silhouette of the underlying WO_3 nanoplates is observable but the valleys are filled with the sponge-like Mo:$BiVO_4$ structure. The entire surface is covered and only the Mo:$BiVO_4$ is exposed on the surface. The SEM images of the third dip coating cycle confirm the assumption based on the GIXRD and UV-Vis measurements. The top view shows multiple layers covering the surfaces inhomogeneously. The same morphology as observed after two cycles is visible and is partly covered with an additional layer of Mo:$BiVO_4$. In order to determine the film thickness of the Mo:$BiVO_4$, cross sectional SEM images were measured, which are displayed in Figure 7.23.

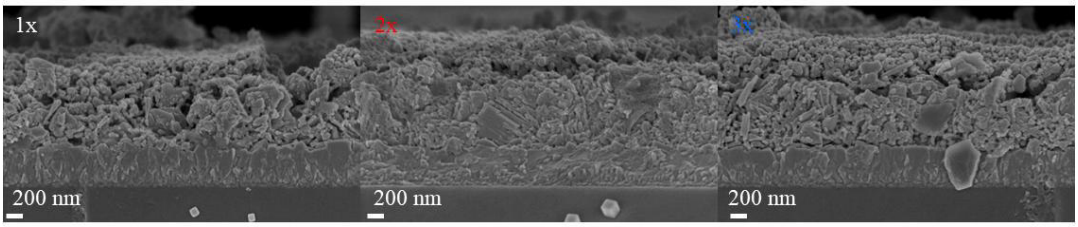

Figure 7.23: Cross sectional SEM images of the WO_3/Mo:$BiVO_4$ heterostructure synthesized with different dip coating cycles.

A single dip coating cycle results in a film thickness of 350 ± 110 nm, which is thicker than the discussed film thickness synthesized with withdrawal speed of 300 mm min^{-1} in the previous chapter. A slower dip coating speed leads to an increased thickness. In addition, the standard deviation is very high, as a result of the nanoplate-like structure. Inside the valley the film thickness is determined to be thicker compared to the encapsulated nanoplates. The second dip coating cycle produced a film thickness of 570 ± 80 nm and the third dip coating cycle ended with thickness of 620 ± 140 nm. It is evident that the third dip coating cycle slightly increases

the film thickness of the Mo:$BiVO_4$ which is in line with the trend described above.

By reducing the WO_3 film thickness to 1.17 ± 0.05 µm and increasing the Mo:$BiVO_4$ thickness to 620 ± 140 nm, the heterostructure ratio could be adjusted to 2:1 and is next evaluated using light-assisted water splitting as shown in Figure 7.24.

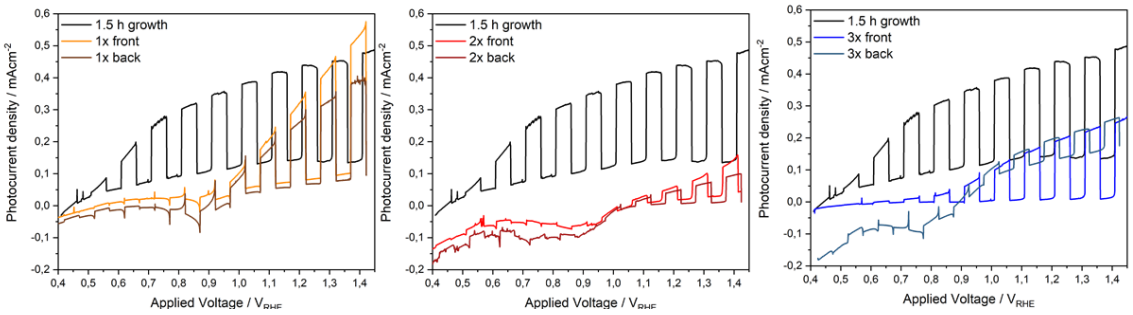

Figure 7.24: CLV measurements of WO_3/Mo:$BiVO_4$ heterostructures synthesized with different dip coating cycles. Shown is a WO_3 measurement and the front and back illuminated CLV for each cycle. *c* = 0.1 M KP-buffer.

Figure 7.24 shows the front and back illumination of the photoelectrode in order to gain a better understanding of the charge carrier diffusion. The theoretical background was described in detail in chapter 3.7.1. The thin film of WO_3 exhibits a photocurrent of 0.44 mA cm^{-2} at 1.23 V_{RHE}. The lower photocurrent can be explained by the thinner film thickness, which reduced the absorption of WO_3 due to the small absorption coefficient. The heterostructure showed a photocurrent of 0.36 mA cm^{-2} and 0.28 mA cm^{-2} at 1.23 V_{RHE} after one dip coating cycle when illuminated from the front and back side, respectively. This indicates that the hole diffusion through the Mo:$BiVO_4$ limits the performance. When illuminated from the front, most of the light is absorbed by Mo:$BiVO_4$ and the electrons are extracted through the WO_3 thin film. The holes generated close to the surface have to diffuse short distances to the surface to react with water. However, the measurement showed that electron extraction is not the limiting factor due to the favorable electronic properties of WO_3. This allows the assumption that to optimize the performance of the heterostructure, Mo:$BiVO_4$ should be the main absorber and WO_3 should serve as an electron extraction support. The heterostructure with two dip coating cycles yielded a photocurrent of 0.06 mA cm^{-2} and 0.05 mA cm^{-2} at 1.23 V_{RHE} when illuminated from the front and back, respectively. The photocurrent is approximately one order of magnitude lower than the heterostructure with one dip coating cycle. This may indicate that the thicker Mo:$BiVO_4$ layer of 570 ± 80 nm is impeding the charge carrier separation. Electrons and holes have to pass longer distances to either be extracted or reach the surface. Nevertheless, hole diffusion is still limiting the performance due to higher photocurrents of the front side illumination. After the third dip coating cycle and with a film thickness of 620 ± 140 nm, the heterostructure exhibited

a photocurrent of 0.19 mA cm^{-2} and 0.20 mA cm^{-2} for the front and back side illumination. Noteworthy is the back side illumination showed a slightly higher photocurrent than the front side illumination. This supports the contention that Mo:$BiVO_4$ with poorer charge carrier diffusion will compromise performance in thicker films. The electrons could no longer be properly extracted before recombining, resulting in the electron extraction leading to the defining factor after three dip coating cycles.

The results of light-assisted water splitting imply that Mo:$BiVO_4$ should act as the main absorber due to the better performance of the front side illumination. Additionally, the film thickness had to be optimized due to the poorer electron and hole diffusion properties of Mo:$BiVO_4$. For further analysis of the heterostructure, IPCE measurements were performed and are displayed in Figure 7.25.

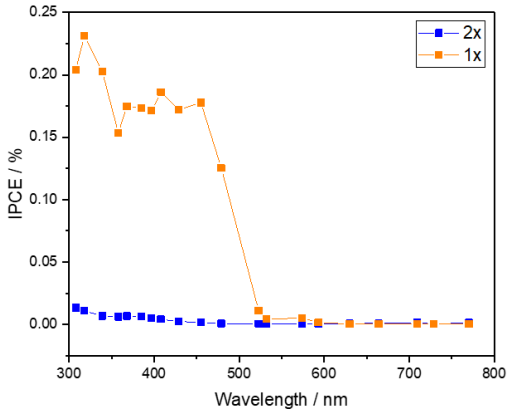

Figure 7.25: IPCE front side measurements of WO_3/Mo:$BiVO_4$ heterostructures synthesized with different dip coating cycles.

Figure 7.25 presents the measurements of the first and second dip coating cycle, while the third dip coating cycle detached during the measurement and for this reason cannot be shown. The IPCE measurement indicates that the heterostructure reaches a a maximum of 23 % at 318 nm after one dip coating cycle, while the efficiency drops to 1 % at 308 nm after the second dip coating cycle. This supports the previously described assumption that the heterostructure will have a low photocurrent after two dip coating cycles. Most of the charge carriers recombine and do not contribute to the current measurement, resulting in an IPCE value of 1 %.

This chapter has shown that Mo:$BiVO_4$ should act as the main absorber of the heterostructure, but the film thickness should be optimized to avoid recombination losses due to the poorer charge carrier diffusion properties. This supports the proposition of SELLI *et al.* made in 2022 that the main absorber should be $BiVO_4$.[119] However, the photocurrents of the heterostructure are still an order of magnitude lower than the values in the literature. Therefore, in the next

chapter, the morphology of the WO_3 surface will be analyzed to gain a better understanding of whether some nanostructures can improve the performance of the heterostructure.

7.4. Morphologies

In this chapter different WO_3 morphologies were investigated and the performance of the resulting heterostructures was tested. For this purpose, different hydrothermal syntheses for nanostructured surfaces, which were used in the literature for the formation of $WO_3/BiVO_4$ heterostructures were collected and reproduced. This included the incorporation of the optimized seed layer for the WO_3 synthesis and the use of the Mo:$BiVO_4$ as a top layer. An exception is the mesoporous WO_3, which was synthesized by a dip coating approach. Additionally, to the nanoplates previously analyzed nanorods, nanoflakes, nanowires, a mesoporous WO_3 and modification of the nanoplates synthesis are presented in this chapter.

7.4.1. Nanorods

The experimental aspects of the hydrothermal synthesis of the nanorods are described in detail by GRIMES *et al.*[110] In particular, the WO_3 base was synthesized using a hydrothermal approach and heterostructure was realized by spin coating the $BiVO_4$ precursor solution. The reported crystal structure and performance are presented in Figure 7.26.

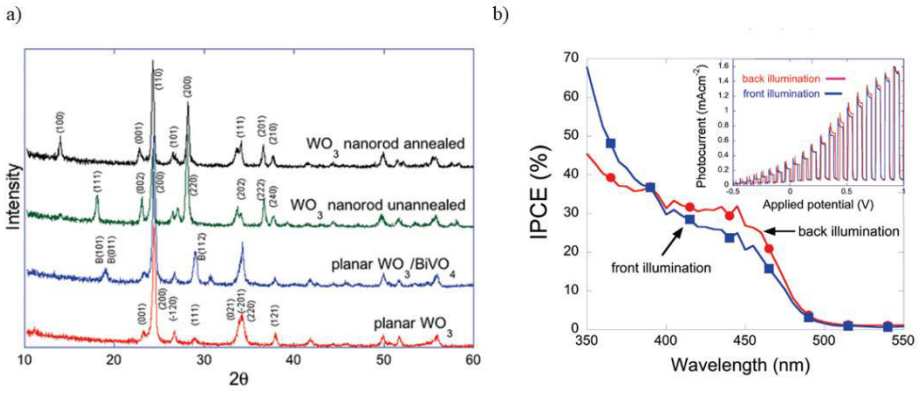

Figure 7.26: a) XRD patterns of annealed (400 °C, 2 h) spin-coated planar WO3 and planar $WO_3/BiVO_4$ heterojunction films and solvothermally deposited WO_3 nanorod films before and after annealing (500 °C, 2 h). b) WO_3 nanorod/$BiVO_4$ heterojunction film. IPCE measurements were conducted in a 0.5 M aqueous Na_2SO_4 solution with a bias of 0.5 V. Insets show current-potential plots measured with chopped AM 1.5 light (100 mW/cm^2) in 0.5 M aqueous Na_2SO_4 electrolyte – reprinted with permission of JINZHAN SU & CRAIG A. GRIMES (Copyright Nano Letters 2011).[110]

The XRD measurements indicate a *m*-WO_3 phase with an enriched (110) facet. In addition, an *h*-WO_3 phase is observed due to reflex at 14° 2 theta. The inset in Figure 7.26b shows the CLV measurement of the WO_3 nanorod/$BiVO_4$ heterostructure, which achieves a photocurrent of 1.6 mA cm^{-2} at 1 V_{NHE}. However, the performance of the blank WO_3 nanorod is not reported, and only the planar WO_3 exhibits a photocurrent of 0.4 mA cm^{-2} at 1 V_{NHE}.

In Figure 7.27, the GIXRD and the UV-Vis of the synthesized nanorods from GRIMES *et al.* using the optimized seed layer is displayed.

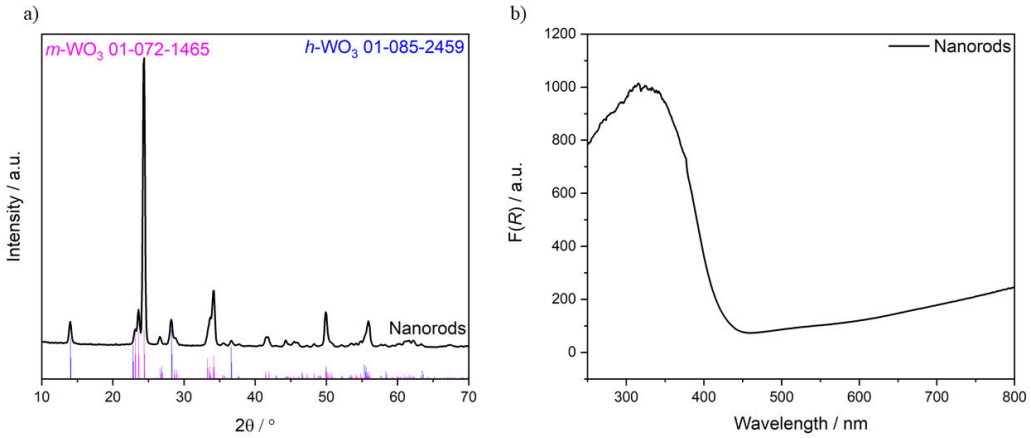

Figure 7.27: a) GIXRD and b) KUBELKA MUNK plot of the WO_3 nanorods synthesis with the optimized seed layer.

The GIXRD measurement shows that the same facet enrichment is present which was reported and that the dominating crystal phase is the *m*-WO_3 phase. Additionally, *h*-WO_3 phase was also detected which is consistent with the result from literature. The KUBELKA MUNK plot displays high absorbance with a low W^{5+} concentration. Further, the CLV measurement of the bare WO_3 nanorods is presented in Figure 7.28.

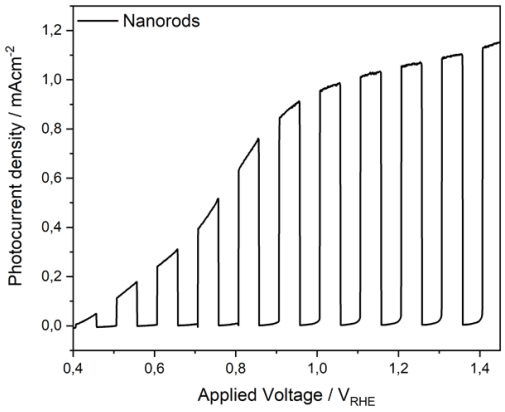

Figure 7.28: CLV measurement of the WO_3 nanorods synthesized with the optimized seed layer.

The CLV measurement reveals a photocurrent of 0.97 mA cm^{-2} at 1 V_{RHE}, which is more than twice the current exhibited by the bare planar WO_3 . Moreover, the current further outperforms the planar $WO_3/BiVO_4$ heterostructure, which is reported to be 0.8 mA cm^{-2} at 1 V_{NHE}. To confirm the morphology of nanorods, SEM imaging was performed and is displayed in Figure 7.29a.

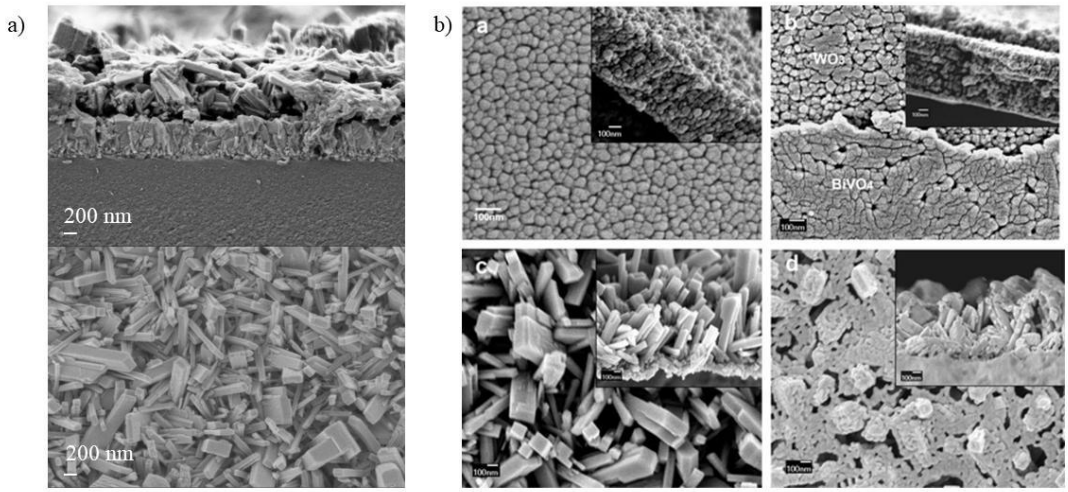

Figure 7.29: a) SEM top and cross-sectional views of the WO_3 nanorod synthesized with the optimized seed layer. b) Top and cross-sectional (inset) views of (a) planar WO_3, (b) planar $WO_3/BiVO_4$ heterojunctions, (c) WO_3 nanorods, and (d) $WO_3/BiVO_4$ nanorod heterojunctions – reprinted with permission of JINZHAN SU & CRAIG A. GRIMES (Copyright Nano Letters 2011).[110]

The cross-sectional and top view images of the nanorod synthesized with the optimized seed layer indicate that a similar morphology is present. Comparing the WO_3 nanorod/ $BiVO_4$ heterostructure (Figure 7.29b bottom right (d)) with the top view image of the WO_3 nanorod/ $Mo:BiVO_4$ displayed in Figure 7.30 reveals a similar structure. The two SEM images are shown at different magnifications, which prevent a detailed comparison, but the sponge-like structure with the holes in the $BiVO_4$ layer is similar.

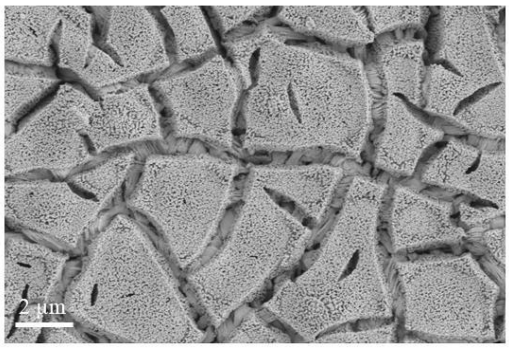

Figure 7.30: SEM image of the WO_3 nanorod/$Mo:BiVO_4$ heterostructure synthesized with the optimized seed layer and dip coating of the $Mo:BiVO_4$ measured from above.

In order to evaluate the WO_3 nanorod/$Mo:BiVO_4$ heterostructure, CLV measurements were performed and are presented later in this chapter for comparison of all morphologies in Figure 7.39.

7.4.2. Nanowires

The synthesis and characterization of nanowires was described by GRIMES *et al.*.[221] The use of the optimized seed layer has not resulted in a higher photocurrent for the WO_3 photoelectrode, for this reason only morphology and photoelectrochemical performance will be highlighted in this chapter. Figure 7.31 shows the CLV measurements and SEM images from the literature to compare the reproduced results.

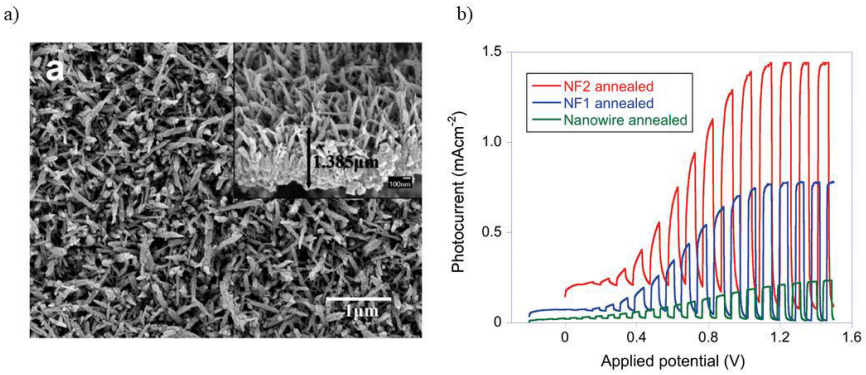

Figure 7.31: a) SEM images of unannealed WO_3 nanowires. The insets show cross section of the film. b) Current-potential plots for annealed nanowires, and two flake samples, under split visible light in an aqueous solution of 0.1 mol/L sodium sulfate (Na_2SO_4) - reprinted with permission of JINZHAN SU & CRAIG A. GRIMES (Copyright Nano Letters 2011).[221]

The photocurrent of the nanowires was not reported in the literature, but can be estimated to be ~ 0.25 mA cm^{-2} at 1.23 V_{RHE} based on from the CLV measurement. The photocurrent of the synthesized nanowires followed the reported results of GRIMES *et al*. and is displayed in Figure 7.32.

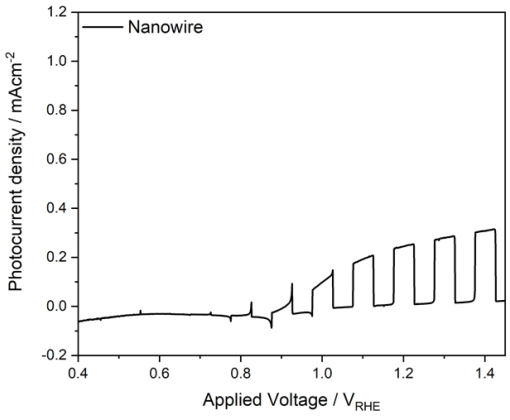

Figure 7.32: CLV measurement of the WO_3 nanowire synthesized with the optimized seed layer.

The measurement exhibits a photocurrent of 0.26 mA cm^{-2} at 1.23 V_{RHE} which is agreement with the results of the literature. The performance of the heterostructure is shown later in Figure 7.39 to compare all morphologies.

7.4.3. Nanoflakes

In addition, to the previously discussed literature by SU *et al.*, which also reported a nanoflakes with a photocurrent of 1.43 mA cm^{-2} [221] an alternative synthesis from ZHENG *et al.* was used for comparison.[222] The use of the optimized seed layer did not result in enhanced performance. Therefore, in this chapter the morphology and the photoelectrochemical performance are highlighted for to compare the reproduced results.

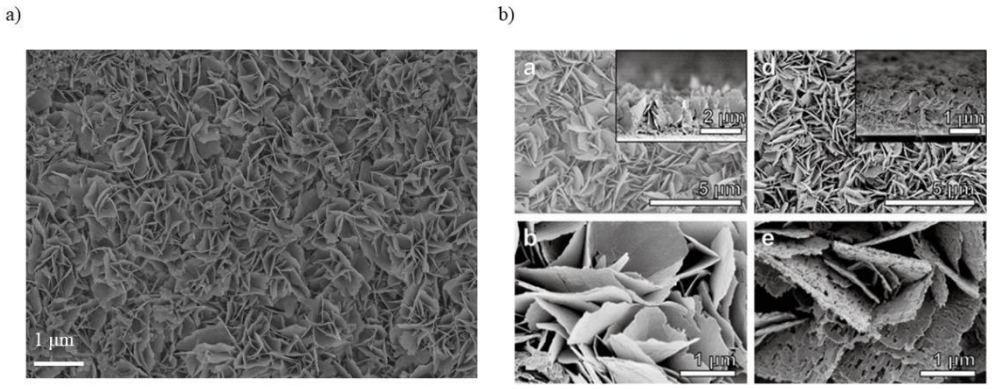

Figure 7.33: a) Top view of measured SEM images of the WO_3 nanorod synthesized with the optimized seed layer. b) (a,b) SEM images of pristine WO3 nanoflakes (d,e) SEM images of the dual etched/ reduced WO3 nanoflakes -) - reprinted with permission of WENJIE LI & GENGFENG ZHENG (Copyright ACS Nano 2014).[222]

Figure 7.39a indicates that the synthesized nanoflakes share the same morphology as the untreated nanoflakes (Figure 7.33b bottom and top left (a,b)) reported by Zheng *et al.* The measured and reported CLV measurements are displayed in Figure 7.34.

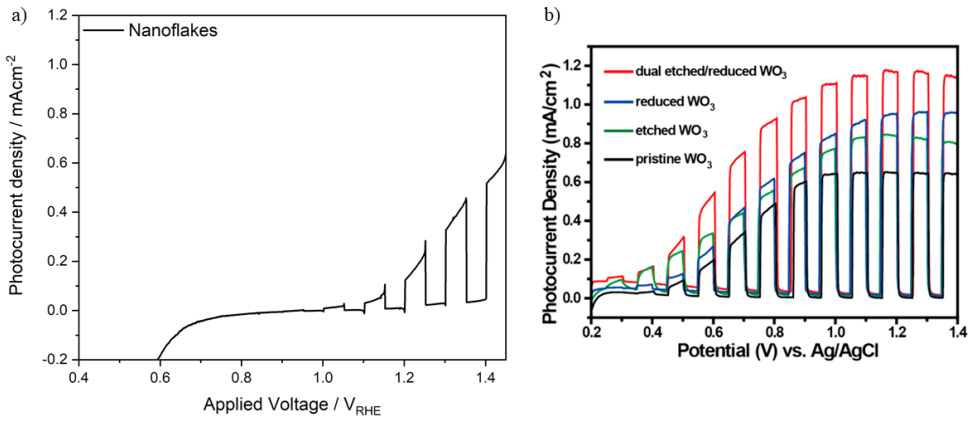

Figure 7.34: a) CLV measurement of the WO_3 nanowires synthesized with the optimized seed layer b) Photocurrent density curves of four types of WO_3 nanoflakes- reprinted with permission of WENJIE LI & GENGFENG ZHENG (Copyright ACS Nano 2014).[222]

The nanoflakes of ZHENG *et al.* exhibit a photocurrent of 0.62 mA cm^{-2} at 1.23 V_{RHE} whereas the synthesized nanoflakes with the optimized seed layer exhibit a photocurrent of 0.21 mA cm^{-2} at 1.23 V_{RHE}. Additionally, the onset potential is shifted to higher values, which

is unusual for WO_3 photoelectrodes.

The heterostructure of the nanoflakes synthesized with the optimized seed layer is shown later in Figure 7.39 to have a comparison between all morphologies.

7.4.4. Mesoporous

The synthesis reported by LABERTY-ROBERT *et al*. was used to obtain a mesoporous WO_3.[223] For comparison the SEM images and CLV measurements are displayed in Figure 7.35.

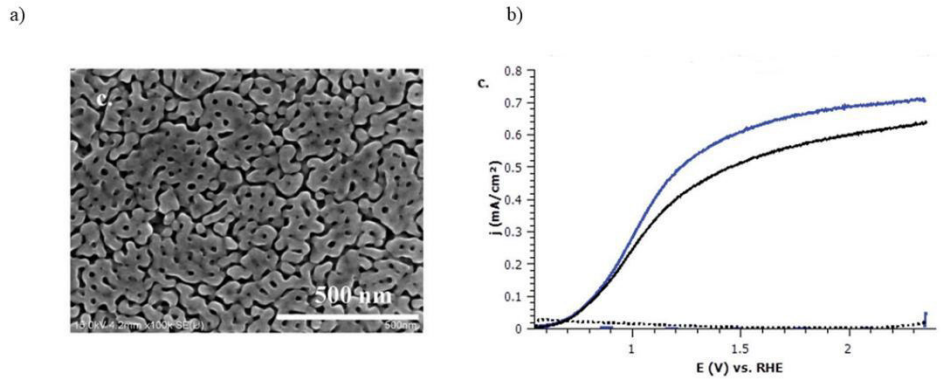

Figure 7.35: a) Top view SEM images and b) linear voltage sweep of the mesoporous (blue) and dense (black) WO_3 photoelectrodes – reprinted with permission from SAMANTHA HILLIARD & CHRISTEL LABERTY-ROBERT (Copyright RSC Sustainable Energy & Fuels 2017).[223]

The mesoporous WO_3 was synthesized by the student Lukas Mayer and all experimental details can be found in his bachelor thesis. Subsequent characterization was performed by me and the GIXRD and SEM images are displayed in Figure 7.36.

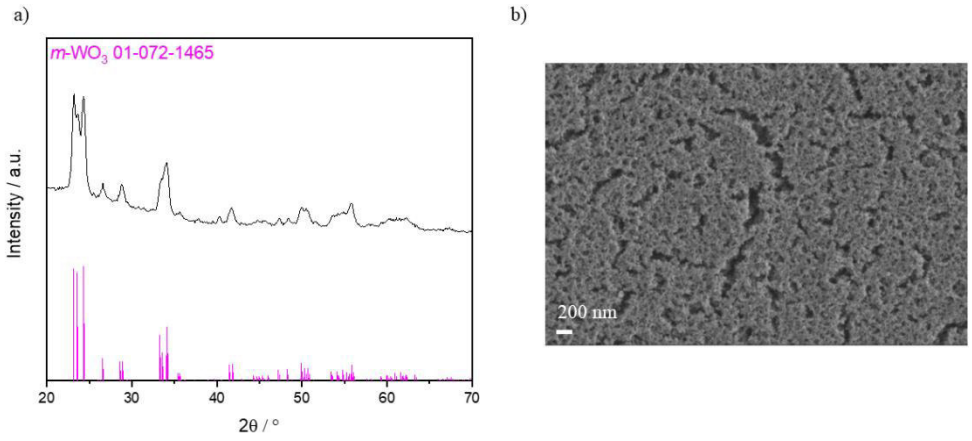

Figure 7.36: a) GIXRD measurement and b) top view SEM image of the mesoporous WO_3.

The GIXRD measurement shows that the *m*-WO_3 crystal phase was synthesized. However, no facet enrichment is present, and the 3 main reflexes are in the thermodynamic equilibrium. Further, the SEM image displays large cavities indicating a mesoporous structure comparable to the SEM image in Figure 7.35a. The CLV measurement is shown in Figure 7.37.

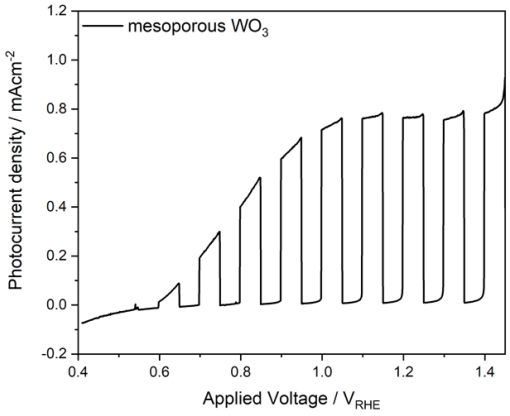

Figure 7.37: CLV measurement of the mesoporous WO_3.

The mesoporous WO_3 exhibits a photocurrent of 0.77 mA cm^{-2} at 1.23 V_{RHE}. According to the literature a photocurrent of 0.7 mA cm^{-2} at 1.5 V_{RHE} is reported, which is lower than the measured WO_3 photoelectrode.[223] This might be due to the different electrolytes used which affect photoelectrochemical measurements. The CLV measurement of the heterostructure is displayed later in this chapter in Figure 7.39.

7.4.5. Adapting the Nanoplates Synthesis

In the previously described synthesis of nanoplates, oxalic acid is used as a structural-directing reagent, which raises the question of which morphology is achieved without oxalic acid. Furthermore, another concern is which morphology results from the hydrothermal synthesis when the addition of concentrated hydrochloric acid, which is used to precipitate H_2WO_4 before redissolution with oxalic acid, is omitted. These two experimental variations were tested to obtain a different morphology, and both resulted in insufficient hydrothermal WO_3 growth as shown in Figure 7.38.

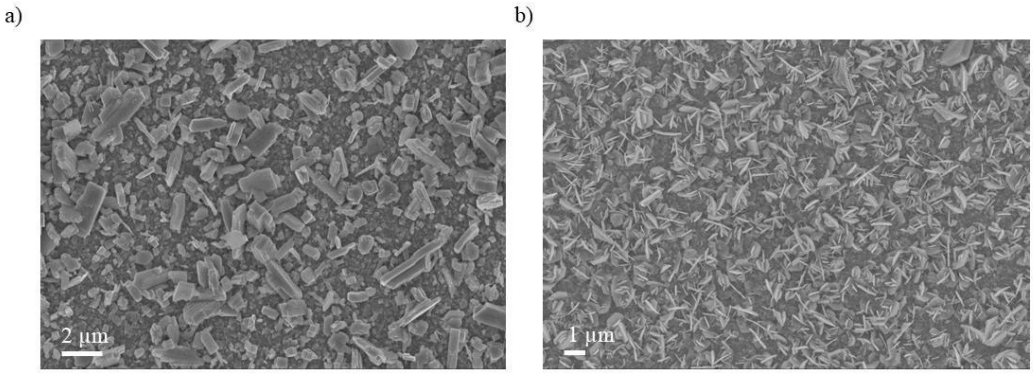

Figure 7.38:Top view SEM images of the synthesized hydrothermal WO_3 nanoplates from above without a) oxalic acid and b) concentrated HCl.

The SEM images illustrate that the synthesis leads to the formation of WO_3 crystals on the surface in both cases. In Figure 7.38b the nanoplate structure is still visible due to the presence of oxalic acid but no thin WO_3 film was formed. For this reason, both electrodes considered further or used to generate a heterostructure.

7.4.6. Photoelectrochemical performance of the heterostructure

Figure 7.39 displays all CLV measurements of the Mo:$BiVO_4$ heterostructure with different WO_3 morphologies.

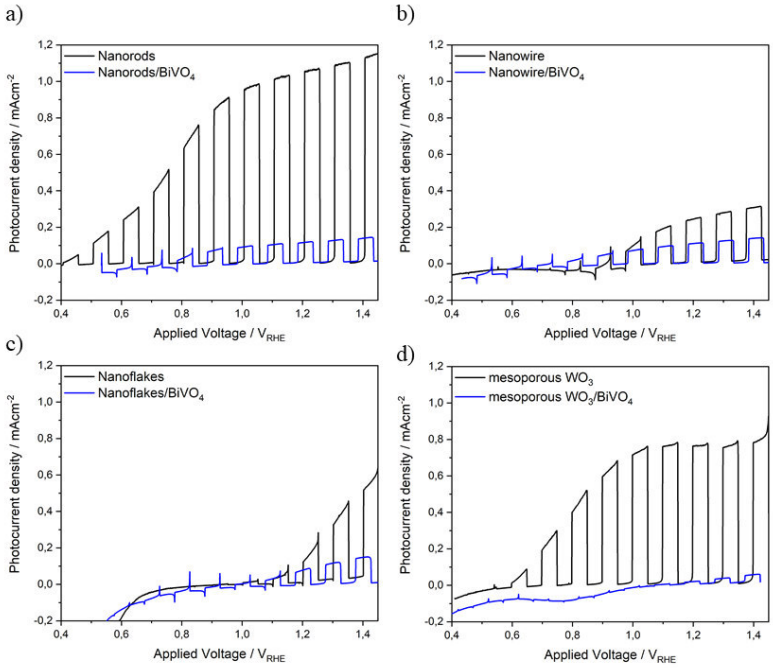

Figure 7.39: CLV measurements of WO_3/Mo:$BiVO_4$ heterostructures synthesized with different WO_3 morphologies. For comparison, the corresponding CLV measurements for bare WO_3 are plotted.

The CLV measurements show that all heterostructures are inferior to their respective WO_3 photoelectrode. The mesoporous WO_3 exhibited the greatest losses with a value of 0.02 mA cm^{-2} at 1.23 V_{RHE}, after 0.77 mA cm^{-2} was achieved with the bare WO_3. This is followed by the nanorods, which decrease from 0.97 mA cm^{-2} to 0.11 mA cm^{-2} at 1.23 V_{RHE}. The nanowires have comparatively low losses, dropping from 0.26 mA cm^{-2} to 0.10 mA cm^{-2} at 1.23 V_{RHE}. Notably, the nanowires exhibit the second lowest WO_3 photocurrent among the different morphologies. In the case of the nanoflakes heterostructure, the photocurrent falls from 0.21 mA cm^{-2} to 0.09 mA cm^{-2} at 1.23 V_{RHE}. All morphologies perform poorer than the nanoplates with the optimized parameters for the dip coating reaching 0.45 mA cm^{-2}. However, it was shown that other morphologies can perform equally as well as the optimized nanoplates but further testing on the formation of heterostructures is required. This can be considered in

future studies as optimization of heterostructure formation for mesoporous and nanorod WO_3 can lead to better performance.

7.5.Conclusion

In this chapter various synthetic parameters were tested to optimize the WO_3/Mo:$BiVO_4$ heterostructure formation. As a solvent $CHCl_3$ proved to be the most suitable as all precursors can be dissolved, it provides good adhesion properties and achieves the highest photocurrent after dip coating a photoelectrode. Further, the dip coating parameters for the WO_3 nanoplate morphology were optimized with the (002) facet enrichment. It was shown that two different heterostructure morphologies can be achieved by adjusting the dip coating parameters. One of them is the core-shell-like structure in which the Mo:$BiVO_4$ encapsulates the WO_3 nanoplates and another morphology is the layer-like structure in which the Mo:$BiVO_4$ covers the WO_3 surface. The core-shell-like structure achieves the highest photocurrent of 0.45 mA cm^{-2} at 1.23 V. However, the layer-like structure should not be neglected as it exhibits a photocurrent of 0.33 mA cm^{-2} at 1.23 V_{RHE} which may be beneficial depending on the application and WO_3 morphology. Due to the lack of improvement, an absorption analysis was performed to gain insights into the charge carrier diffusion pathways and to determine the role of the materials within the heterostructure. It was shown that the main absorber in the heterostructure should be Mo:$BiVO_4$ while WO_3 should act as an electron extraction layer. Therefore, an optimal film thickness of Mo:$BiVO_4$ is sought to avoid recombination due to the poorer charge carrier diffusion properties. Lastly, various WO_3 morphologies were analyzed for the generation of heterostructures. Results showed that without optimizing the dip coating parameters for each morphology, the photocurrents are generally lower than with the optimized synthesis. The nanorods and mesoporous WO_3 exhibited promising photocurrents but loose photocurrent after the heterostructure formation resulting in 0.11 mA cm^{-2} and 0.02 mA cm^{-2} at 1.23 V_{RHE}. Optimization of the WO_3/Mo:$BiVO_4$ resulted in insufficient performances, in contrast to the values described in the literature. While comparing the results to the reported values, it should always be considered which photocurrent achieved by the bare WO_3, which morphology is present and which material is the actual absorber. Furthermore, as noted above, future studies may consider the optimization of the heterostructure formation with different WO_3 morphologies in terms of the resulting type of heterostructure and Mo:$BiVO_4$ thickness.

8. Hydrothermal conversion of WO_3 to $SnWO_4$

The beginning of this study was conducted in collaboration with Prof. LIANZHOU WANG from The University of Queensland. Therefore, some experimental details in this chapter differ from the parameters listed in chapter 4. All changes are mentioned in the respective measurements.

The first step of the study was the synthesis of the optimized WO_3 thin film with the parameters previously explained. Initially, the focus for the conversion was centered on the hydrothermal approach with a 0.1 M $SnCl_2$ solution. The resulting films were calcined at different heating rates to obtain the $SnWO_4$ crystal phase. All final samples were measured with a different setup and are shown in Figure 8.1.

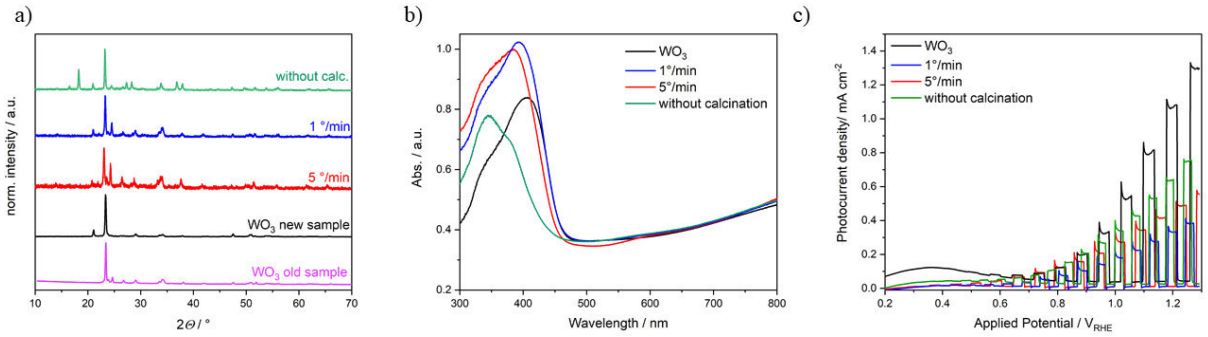

Figure 8.1: a) XRD patterns of hydrothermally grown WO_3 thin films measured with Rigaku MiniFlex. b) UV-Vis absorption acquired with an integrated sphere enabling transmission and reflection measurments. c) CLV data obtained with a self-constructed PEC cell with epoxy tape exposes only 0.26 cm^2 of the film to the electrolyte. The photocurrents were calculated in each case.

The XRD measurements show that the WO_3 thin film recorded with the new setup (Figure 8.1c black) lacks the three reflexes of WO_3 due to the high intensity of the (002) reflex and the less sensitive detector of the Rigaku MiniFlex. After conversion and the subsequent calcination, the three reflexes were observed due to the reduced intensity of the (002) reflex. Additionally, one reflex at 21° 2 theta was not assignable to a WO_3 crystal phase but is unaffected by the heat treatment. The XRD further shows that $SnWO_4$ could be detected after neither hydrothermal conversion nor calcination. This is consistent with the absorption spectra shown in Figure 8.1b, in which only the WO_3 band edge can be observed. However, the crystal phase changes after the hydrothermal conversion. The diffractogram exhibits *h*-WO_3 reflexes, which disappear after calcination. Furthermore, CLV measurements show that among the samples the converted film performs poorer than the WO_3 thin film. Here, the WO_3 achieves a photocurrent of 1.26 mA cm^{-2} at 1.23 V_{RHE} whereas the sample without calcination reaches 0.75 mA cm^{-2} at 1.23 V_{RHE} and the best performing sample after conversion yields 0.49 mA cm^{-2} at 1.23 V_{RHE}.

As the calcination heating ramp caused no effect on the WO_3 crystal phases the concentration of $SnCl_2$ was raised to 0.5 M. The result of the conversion with the higher concentration was a delamination of the thin WO_3 which is why no characterization could be performed. Therefore, the following experiments were conducted with a $SnCl_2$ concentration of 0.1 M. In order to obtain a $SnWO_4$ crystal phase the hydrothermal growth time was increased to 24 h with the aim of testing whether the conversion time affects the conversion. The samples hydrothermally converted for 24 h are shown in Figure 8.2.

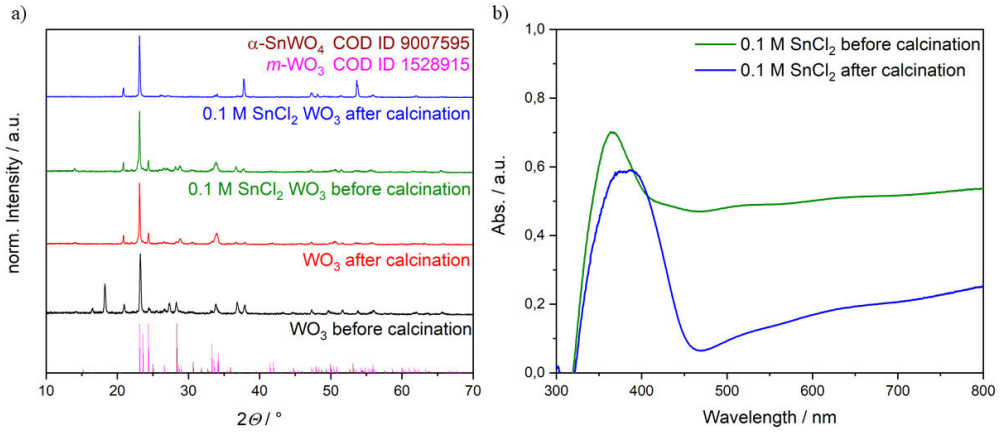

Figure 8.2: a) XRD measured with Rigaku MiniFlex and b) UV-Vis absorption spectra measured with an integrated sphere of the 24 h hydrothermal conversion with a 0.1 M $SnCl_2$ solution.

Figure 8.2a shows that the conversion time exerted no effect on the WO_3 crystal structure. The XRD measurements indicate no $SnWO_4$ crystal phase, neither after hydrothermal conversion nor calcination. This is also reflected in the UV-Vis absorption spectra with only the WO_3 band edge showing. The UV-Vis absorption spectra measured directly after the conversion showed a higher absorption above 400 nm. This could indicate a high W^{5+} concentration after the hydrothermal conversion. A possible reason could be that the Sn^{2+} is oxidized to the thermodynamically more stable Sn^{4+} while tungsten is reduced to W^{5+}. After calcination under atmospheric conditions, the tungsten gets oxidized, which is why the absorption decreases above 400 nm resulting in a single-phase *m*-WO_3 thin film. As a consequence, the hydrothermal conversion could lead to a reduction reaction instead of a conversion. It is important to note that the increase in absorption of the hydrothermally converted WO_3 is not stable and returns to the previous state over time when exposed to oxygen.

Another approach to convert WO_3 is the coating method with a subsequent calcination. Therefore, the calcined WO_3 thin films were coated with the prepared $SnCl_2$ solution. The results are displayed in Figure 8.3.

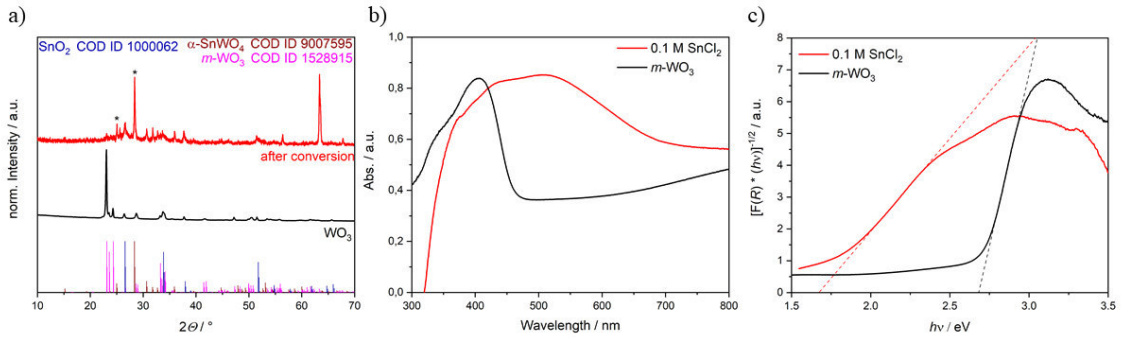

Figure 8.3: a) XRD measured with the Rigaku MiniFlex, b) UV-Vis absorption spectra measured with an integrated sphere and c) the TAUC plot of the coated and calcinated conversion with a 0.1 M $SnCl_2$ solution. The highlighted reflexes can be directly attributed to the α-$SnWO_4$ crystal phase.

After coating and calcination, XRD measurements reveal an intense reflex of the α-$SnWO_4$ crystal structure. This is in agreement with the UV-Vis absorption spectra which depict a shifted absorption band edge leading to band gap of 1.7 eV for the converted sample. This band gap is consistent with the value reported in literature. However, the XRD showed additional reflexes of WO_3 and SnO_2 indicating that the conversion was incomplete and SnO_2 forms on the surface of the film due to excess of $SnCl_2$ solution.

To avoid the formation of SnO_2 various approaches can be tested. The addition of hydrochloric acid can stabilize the $SnCl_2$ in solution. Another approach is the subsequent treatment with concentrated HCl due to the ability of SnO_2 to dissolve in strong acids. Therefore, the next step in this study was the conversion with added HCl, $SnCl_2$ dissolved in concentrated acid and a subsequent treatment with HCl after the conversion. The results of these experiments are displayed in Figure 8.4.

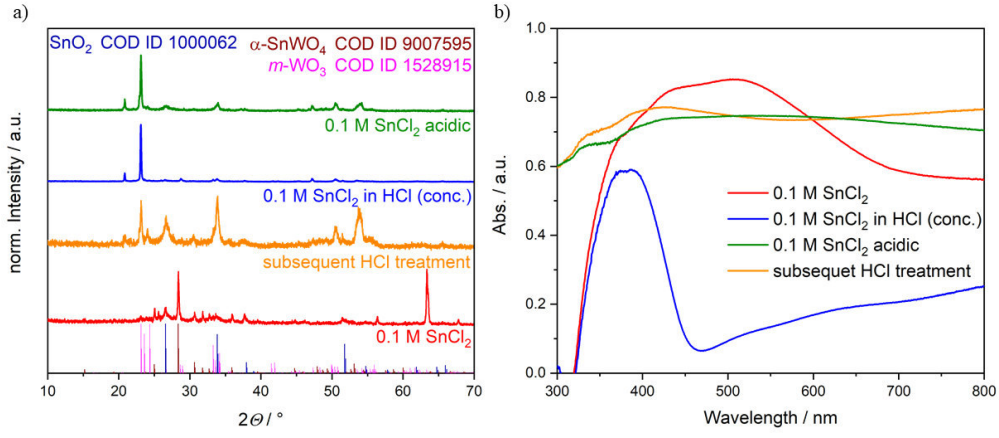

Figure 8.4: a) XRD measured with the Rigaku MiniFlex and b) UV-Vis absorption spectra measured with an integrated sphere of the coated and calcinated conversion with a 0.1 M $SnCl_2$ solution and different HCl treatments. 0.1 M $SnCl_2$is displayed for comparison.

It can be observed from the XRD measurements that the addition of HCl to the solution prevents the conversion. Subsequent HCl purification, on the other hand leads to a completely different diffractogram lacking the α-$SnWO_4$ crystal phase. The SnO_2 is still clearly present and could not be removed entirely. The WO_3 reflexes are distinguishable which permits the conclusion that the conversion never took place and only SnO_2 was formed on top of the WO_3 thin film.

This work was continued by the student Sofie Knies at the University of Bayreuth. A summary of the experiments conducted and results is provided here. The initial aim was to reproduce the results of the study done at The University of Queensland and initiate a more detailed hydrothermal conversion analysis. The XRD and UV-Vis data is supplemented by SEM and GIXRD measurements.

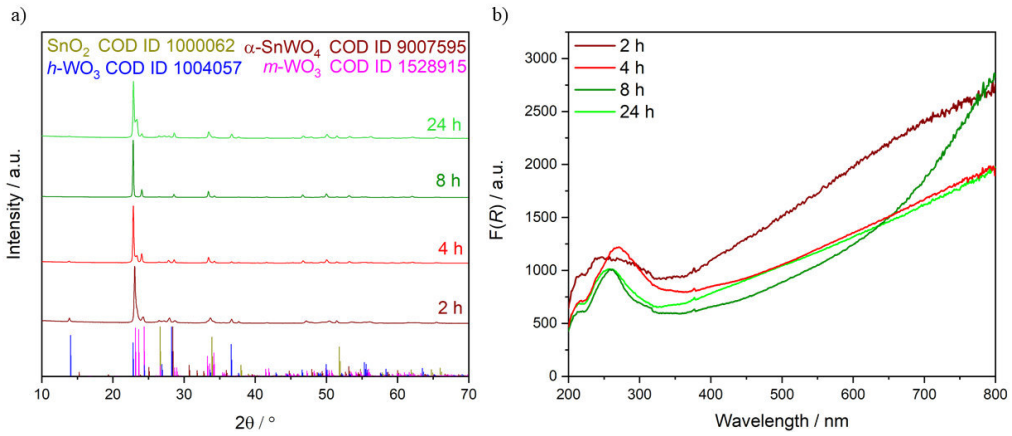

Figure 8.5: a) GIXRD and b) KUBELKA MUNK plot from the hydrothermal conversion of WO_3 thin films with a 0.1 M $SnCl_2$ solution at different conversion times.

GIXRD measurements in Figure 8.5 show that the hydrothermal conversion caused no conversion to the desired α-$SnWO_4$ crystal structure. The conversion time had no influence on the results. After 24 hours of conversion the XRD measurement indicates no significant difference to the WO_3 thin film either prior to conversion or to the 2 h converted thin film. The UV-Vis measurements exhibit the previously described trend with a strong increase in the absorption, resulting in the dark blue color. To further evaluate the thin films, SEM and EDX measurements were performed to gain insight into the surface structure and composition. The results are displayed in Figure 8.6.

The SEM images in Figure 8.6 a show that the nanostructured surface of the WO_3 remains intact. However, small crystals can be observed on the nanoplates, which are distributed homogeneously over the entire surface. These can be residuals of SnO_2 or $SnCl_2$ that remained from the hydrothermal conversion reaction. Therefore, HCl purification of the converted thin films was performed. The purified thin film is displayed in Figure 8.6b. This study from Sofie

Knies was then expanded with EDX and XPS measurements on both samples to distinguish between SnO_2 and $SnCl_2$. The EDX results are summarized in Table 12.

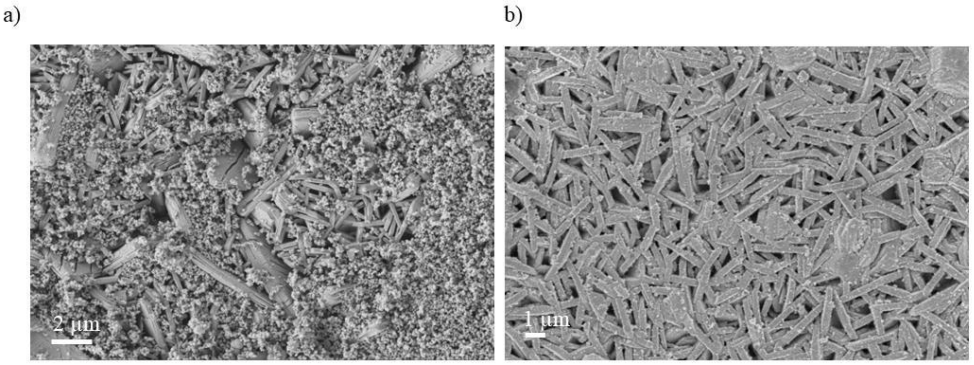

Figure 8.6: SEM measurements of hydrothermally converted WO_3 thin films for 24 h a) prior and b) after HCl purification.

Purification with HCl led to significantly fewer crystals on the surface which allows the assumption that these are SnO_2 crystals as SnO_2 is soluble in strong acids.

Table 12: EDX results for thin WO_3 films converted with $SnCl_2$ by coating and subsequent calcination.

Atom %	W	Sn	O	C	Cl	Pt
Before cleaning	16.4	9.7	65.9	7.7	<0.1	<0.1
After cleaning	18.8	3.9	68.3	9,0	<0.1	<0.1

From the EDX results, hardly any Cl can be detected on the surface of the converted film. This indicates that the crystals on the surface are SnO_2 residuals. In addition, some Pt was detected which originates from the sample preparation. Furthermore, the Sn content decreases after the HCl purification which is consistent with the SEM images showing fewer crystals on the surface. To determine the oxidation state of the WO_3 after the conversion an XPS measurement was conducted. The high resolution XPS (HR-XPS) of the W 4f and Sn 3d region are displayed in Figure 8.7.

The HR-XPS of tungsten in Figure 8.7 contains no W^{5+} related peaks. The peaks at 35.8 eV and 38.0 eV belong to the W^{6+} oxidation state. Additionally, the Sn-XPS only exhibits Sn^{4+} peaks at 487.1 eV and 495.5 eV. The absence of peaks at 493.58 eV and 485.02 eV confirmed that the all of the Sn was thermodynamically oxidized to Sn^{4+}.[224] However this contradicts the assumption made by the XRD and UV-Vis analysis which implied a reduction of W^{6+} to W^{5+}

due to the strong increase in absorption after the hydrothermal treatment. The XPS measurements indicate the absence of surface reduction, suggesting that the observed absorption shift originated from other factors.

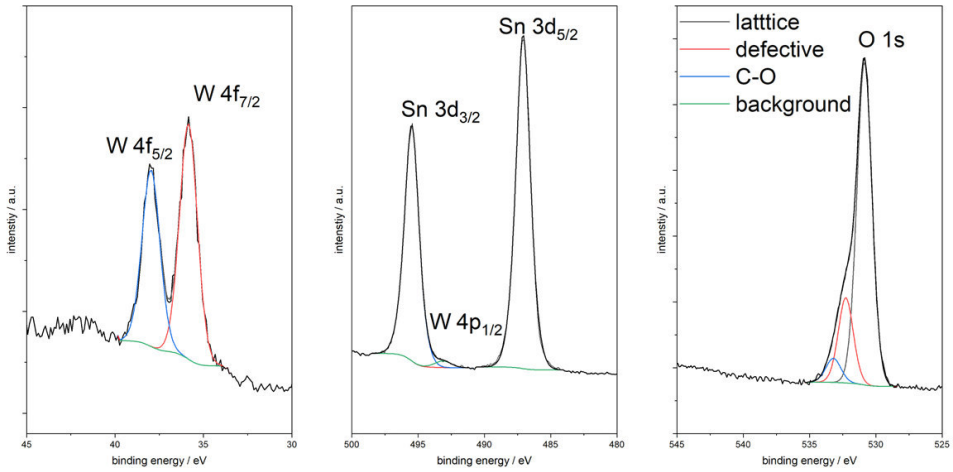

Figure 8.7: HR-XPS of W 4f, Sn 3d and O 1s of the hydrothermally converted WO_3 thin film after HCl purification.

A further possible interpretation for the strong increase in absorption in the UV-Vis analysis may be the formation of WCl_6 which has a dark violet color. This reasoning can be supported by the higher Cl content of 3.3 At% determined by XPS. However, it is not distinguishable whether this Cl content originates from the HCl or a WCl_6 phase. If some WCl_6 crystal phase is present, the surface-sensitive GIXRD shown in Figure 8.5 should exhibit some additional reflexes which are not observed. Therefore, it is not feasible to provide sufficient explanation for the absorption shift of the UV-Vis analysis with the present data and further research is required.

To continue the investigation of the $SnWO_4$ conversion, a calcination study was conducted to identify the critical parameters for conversion using the coating and calcination approach. The parameters tested are summarized in Table 13. To minimize the SnO_2 residuals on the surface, the coating volume was adjusted first. The results show that 0.25 mL is not sufficient to cover the entire surface and leads to a partially treated surface. Therefore, 0.5 mL was set as the minimum volume for conversion. Additionally, the heating rate and HCl concentration were varied and evaluated. The XRD and UV-Vis spectra for all synthetic variations are shown in Figure 8.8 and Figure 8.10 accordingly.

Table 13: Synthetic parameters for the coating and calcination study to convert WO_3 to $SnWO_4$.

HCl	V / mL	c / M	$\frac{T}{t}$ / K min^{-1}	T / K
1 M	DC	0.1	10	773
1 M	1	0.1	10	773
1 M	0.5	0.1	10	773
1 M	0.25	0.1	10	773
1 M	0.5	0.1	5	773
1 M	0.5	0.1	1	773
conc.	0.5	0.1	10	773

DC = dip coating

From the UV-Vis measurements of the coating and calcination study, displayed in Figure 8.8, it is evident that α-$SnWO_4$ is no longer detectable after calcination. This is in agreement with the XRD data displayed in Figure 8.10. Additionally, for large volumes such as 1 or 0.5 mL the same trend was observed as for the hydrothermal conversion. The WO_3 band edge is not visible and a strong increase in absorption was detected above 450 nm. The dip coated sample is an exception. The lower volume led to an increase above 450 nm but the band edge of the WO_3 is still distinguishable. The thin film coated with a 1 mL $SnCl_2$ solution exhibits a strong absorption edge at 350 nm. The TAUC plot in Figure 8.9 indicates a band gap energy of 3.6 eV which is too high for WO_3 or α-$SnWO_4$. This band gap energy can be attributed to SnO_2 which was reported to have higher band gap energy between 3.4 - 3.6 eV. The same band gap is also present in the heating time variations shown in Figure 8.8b and Figure 8.9b. As a result, the WO_3 band edge remains visible after the calcination and the TAUC plot leads to a band gap of 2.5 and 3.4 eV, respectively.

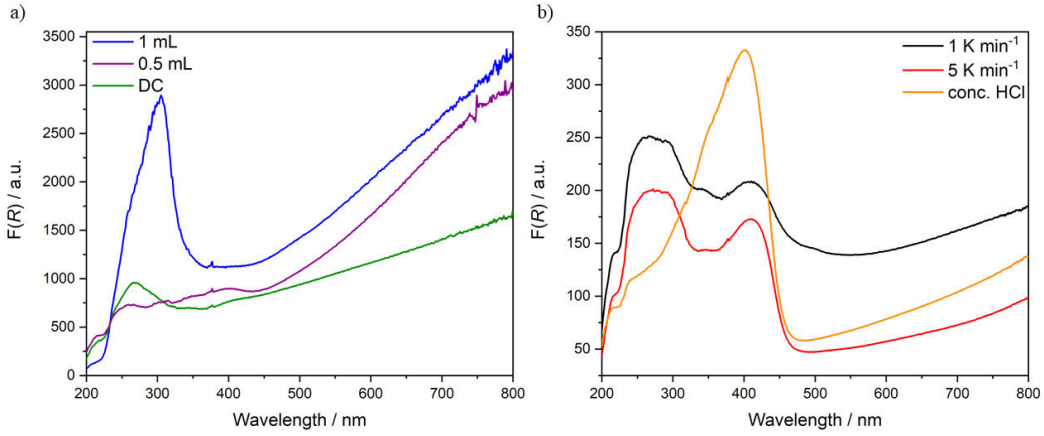

Figure 8.8: KUBELKA MUNK plots from the coating and calcination study on the conversion of WO_3 to $SnWO_4$. Names refer to the notation in Table 13.

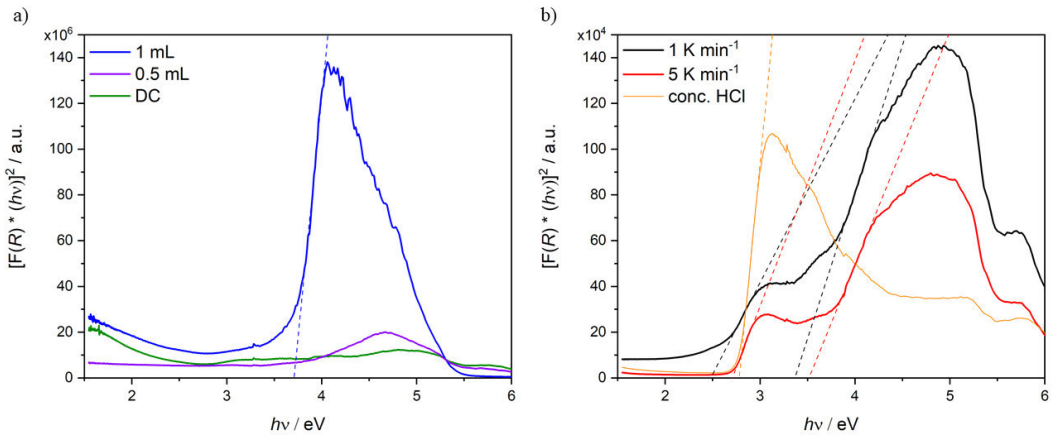

Figure 8.9: TAUC plots from the coating and calcination study on the conversion of WO_3 to $SnWO_4$. Names refer to the notation in Table 13.

The thin film coated with the precursor solution mixed with conc. HCl showed the same result as described above. The high acidic concentration prevents any kind of SnO_2 formation and therefore only the WO_3 absorption is visible.

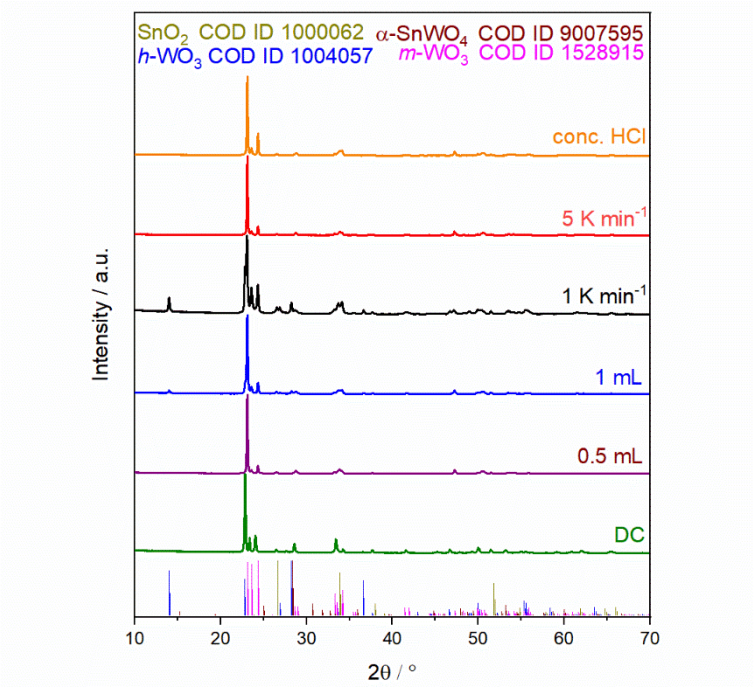

Figure 8.10: XRD measurements from the coating and calcination study of the WO_3 to $SnWO_4$ Conversion. Names refer to the notation in Table 13.

The XRD measurements confirm the previously described findings that neither the coating nor the calcination led to the conversion of WO_3 to $SnWO_4$ in any experiment. Reproducing the results of this study at The University of Queensland remained a challenge. This may be explained by the fact that the experimental conditions at the facilities in Brisbane were never

fully reproducible, due to the shared equipment used for all types of reactions, including gas flow reduction reactions.

8.1.Conclusion

The conversion study to synthesize α-$SnWO_4$ from WO_3 thin films yielded a partially converted thin film after a coating and calcination approach. All other attempts to reproduce this output were unsuccessful in converting WO_3 to $SnWO_4$. The hydrothermal conversion approach led to an absorption increase above 450 nm which was assumed to be the reduction of W^{6+} to W^{5+}. The XPS analysis revealed that W^{5+} was not detected on the surface suggesting the rise in absorption must be due to other contributions. However, identification of the major contribution remained elusive and further research is required to determine the reason for the absorption increase.

Due to the time constraints and the findings shown this study remains incomplete. Further tests/work are (is (if you chose work)) necessary to determine the crucial parameters for the conversion of WO_3 to $SnWO_4$. Potential approaches may include the calcination in inert atmosphere to prevent oxidation to SnO_2. Gas phase conversion may be promising, as demonstrated by KUANG *et al.* with a CVD approach using $SnCl_2$ and WO_3 electrodes. [82] Further optimization may involve alternative Sn sources to prevent chloride poisoning of the surface and the formation of heterostructures by converting the surface of a WO_3 thin film, which benefit from the excellent electron transport properties of WO_3 and the narrower band gap and band positions of α-$SnWO_4$.

9. Photo Redox Flow Battery

To evaluate the performance of the synthesized thin film electrodes, measurement of the state of charge (SOC) are essential. In a photo redox flow battery setup, as described in chapter 5.8, two different approaches such as the open circuit potential (OCP) measurement and the absorption change determined by UV-Vis can be used to accomplish this. With the different colors of the electrolyte the SOC can be determined applying the LAMBERT law, by measuring the transmission of the electrolyte. An experiment to obtain the SOC by UV-Vis spectroscopy is displayed in Figure 9.1.

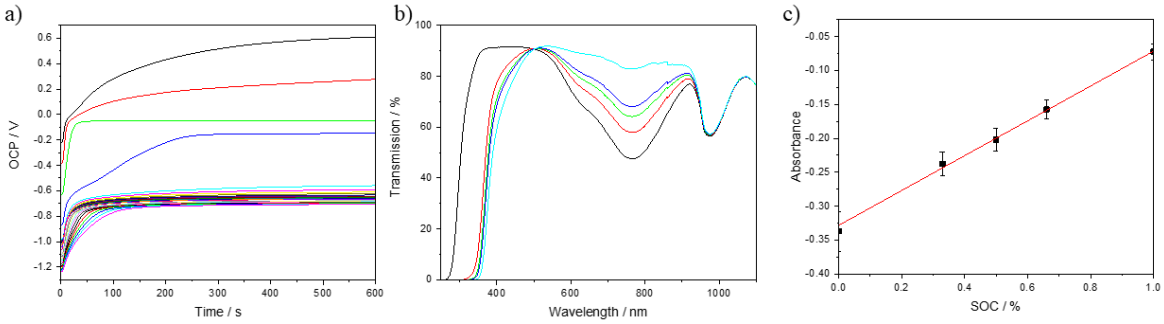

Figure 9.1: a) Open circuit potential measurements after different time spans. b) Transmission spectra after different time spans corresponding to the OCP measurement. c) SOC determination using LAMBERTS law and the transmission determined in b).

Figure 9.1a depicts the OCP measurements over different timespans. The OCP and the transmission each exhibit a logarithmic decrease as described in the LAMBERT law. A linear fit was performed by using the uncharged and fully charged electrolyte and mixing these two in known ratio to obtain different SOCs.

This approach involves several disadvantages. Firstly, the concentration of the electrolyte used is too high. LAMBERT law is only applicable for low concentrations. Therefore, the electrolyte must be diluted prior to measuring the transmission. Besides, the electrolyte equilibrium between the two half cells becomes progressively less accurate over time as samples are taken for transmission measurements. Furthermore, the catholyte is air sensitive and discharges quickly in contact with air which further complicates accurate SOC determination with UV-Vis. All of these drawbacks can lead to large systematic errors causing the determination of small changes of a photo charged photo redox flow battery to be unreliable. Therefore, the *in operando* OCP measurement is used in this work to determine the SOC. As shown in Figure 5.6, the setup uses two electrochemical cells to measure OCP and perform assisted charging simultaneously. This enables a more precise determination of the SOC by capturing the small changes of photo charge using the NERNST-equation.

Before the start of the photocharging under a continuous flow, several experiments are necessary to obtain optimal working conditions and to ensure the designed cell works as expected. Two experiments to evaluate the PRFB are shown in Figure 9.2.

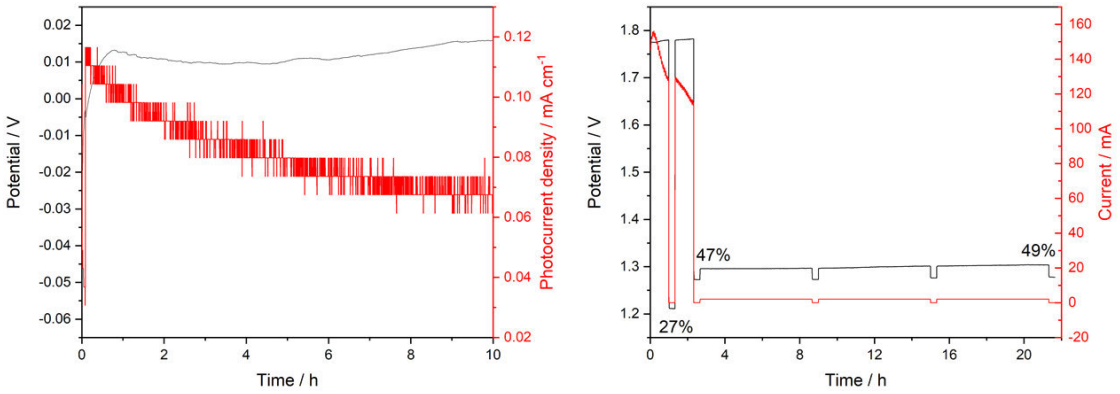

Figure 9.2: a) TiO_2 spray coated electrode with assisted charging at 1.2 V support potential. b) 2 mA simulation after precharging the electrolyte for 2 h.

The chronoamperometric measurements in Figure 9.2 prove that the PRFB setup works as intended. Figure 9.2a depicts a chronoamperometry performed with a spray-coated TiO_2 (P25) electrode. TiO_2 is known to charge the electrolyte during illumination.[187,191] The open circuit potential increases over time which is an indication of charging. The photocurrent declines over time which can be attributed to the electrode slowly detaching under a continuous flow. This experiment also demonstrates clearly why precharging is crucial for precise SOC measurements. The OCP for full vanadium redox flow battery according to the NERNST equation is supposed to be between 0.9 and 1.5 V. In extreme cases, such as a completely uncharged battery, the system will behave differently, and the NERNST equation will be invalid. Therefore, precharging is essential to obtain precise SOC values. This is demonstrated in Figure 9.2b by precharging the electrolyte twice for one hour with an applied potential of 1.8 V. After one hour of charging the SOC reaches 27 % whereas another hour charging leads to an SOC of 47 %. The measurement was continued, but after two hours of precharging a current of 2 mA was applied to determine the time required to detect difference in SOC. 2 mA was chosen based on the fact that this value is representative of the actual power of a semiconductor electrode. Chronopotentiometry was conducted in intervals of 18 h to determine the SOC between charges. After 18 h in which 2 mA was applied, the SOC increased from 47 to 49 %. This illustrates that a measurement period of at least 18 h is required for a recognizable SOC change during photo charging, especially if even lower photocurrents are considered.

Considering the materials used in the PRFB, an auxiliary voltage is unavoidable. As described in chapter 3, the band positions of WO_3 are not capable to reduce V^{3+} to the desired V^{2+} without applied voltage. For this reason, the optimal voltage for efficient charging must be determined. Equation (9.1) can be used to calculate this, where j_{Photo} represents the measured photocurrent, V_{bias} is the applied potential, V_{redox} the required redox potential and P_{light} the power of the light source.

$$\eta = \frac{j_{Photo}\,(V_{redox} - V_{bias})}{P_{light}} \tag{9.1}$$

An important point to note about the measurement is that it must be performed in a two-electrode setup. Efficiency in relation to the applied voltage for WO_3 and $BiVO_4$ is shown in Figure 9.3.

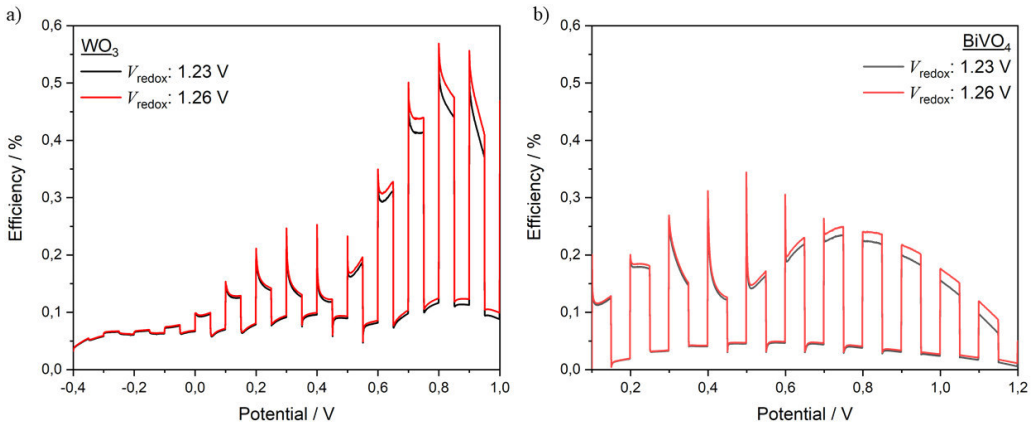

Figure 9.3: Efficiency in relation to the applied voltage for the vanadium redox cell with 1.26 V and the water splitting reaction with 1.23 V, as determined by equation (9.1) for a) WO_3 and b) $BiVO_4$. The corresponding CLV measurements was conducted in a 0.16 M $VOSO_4$ solution.

In Figure 9.3, the efficiency for water splitting and the vanadium redox reaction is displayed, as the redox reaction for charging the battery is always in competition with the water splitting reaction when a potential is applied. However, the one-electron reduction and oxidation reaction of the battery should be kinetically faster than the four-electron oxidation of water. Therefore, a high concentration of vanadium species should facilitate the redox reaction. The efficiency optimization for WO_3 indicates that 0.8 V yields the highest efficiency of 51 %, whereas $BiVO_4$ reaches its optimum at 0.7 V with 27 %. At these voltages, not only the efficiency is highest, but also the difference in efficiency between the water splitting reaction and all vanadium redox reactions which can additionally benefit the charging. These voltages will be used as starting conditions for the light assisted charging of the PRFB.

9.1.WO_3

Different setups were tested at the beginning of the study of light assisted charging in order to evaluate the stability of the electrode and the influence of the electrolyte flow. A range of electrochemical setups were used and chronoamperometric measurements were performed, which are shown in Figure 9.4.

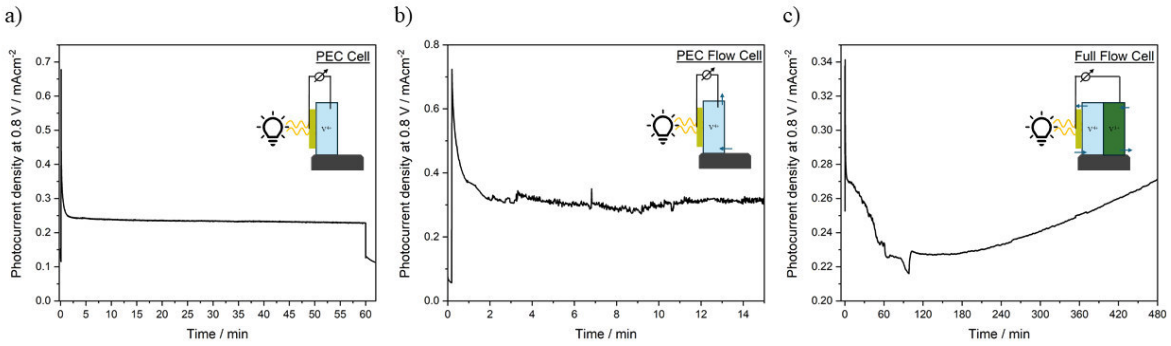

Figure 9.4: WO_3 chronoamperometry measurements at 0.8 V with different electrochemical setups illustrated in the graph. The arrows represent the flow direction. The measurement was performed at a vanadium concentration of 0.16 M and a flow rate of 5 mL/min.

All chronoamperometric measurements indicate a spike in the photocurrent after the light is switched on, followed by a drop to a lower steady state. The chronoamperometry in Figure 9.4a proves that the WO_3 electrode is stable in the electrolyte used and maintains a stable photocurrent of 0.23 mA cm^{-2} for 60 min. This is in line with the expectations due to the known high stability of WO_3 under acidic conditions. After adding a continuous flow to the PEC cell, the photocurrent decreased and showed an unstable photocurrent after 4 min. In both setups the reduction product is hydrogen due to the lack of a reduction half-cell. In a closed setup as used in Figure 9.4b, an unstable photocurrent can result due to bubble formation. In addition, these highly reductive conditions can promote degradation of the WO_3 electrode. Lastly, the full setup exhibits a different photocurrent trend. The photocurrent spikes and then decreases over time until 100 min of illumination is reached, then begins to steadily increase for 370 min. This is contrary to expectations, as the photocurrent should slowly decrease with ongoing charging due to the lower concentration of redox-active species. Consequently, no charging was achieved with these experimental setups. To verify whether this was the case, UV-Vis measurements were performed after 480 min of charging. The spectra are displayed in Figure 9.5.

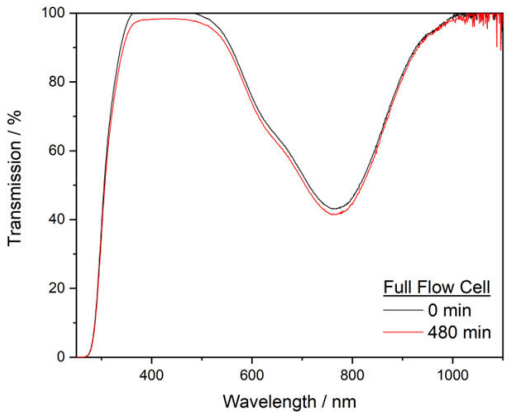

Figure 9.5: UV-Vis transmission spectra of the vanadium catholyte charged with 0.8 V in a full flow cell at different times.

The UV-Vis spectra indicate that after 480 min of light assisted charging the catholyte exhibits no change in transmission. In order to detect a decrease of V^{4+}, the transmission after 480 min has to decrease. Moreover, the absorption edge must shift to higher wavelength in order to prove the presence of V^{5+}. In Figure 9.5, the transmission rises after 480 min. This may be an effect of the measuring method and is not necessarily an increase in V^{5+} concentration. However, it demonstrates that these experimental parameters caused no change in the SOC. This may be explained by voltage applied being too low to reduce V^{3+} to V^{2+} and therefore the electrochemical potential not being sufficient to facilitate charging. The current detected in Figure 9.3 does not distinguish between oxidizing V^{4+} and oxidizing O^{2-} which can lead to a misinterpretation of the parameters used. Therefore, a CLV measurement was performed on the complete cell to evaluate the voltage required to charge the electrolyte. The CLV measurement is shown in Figure 9.6a.

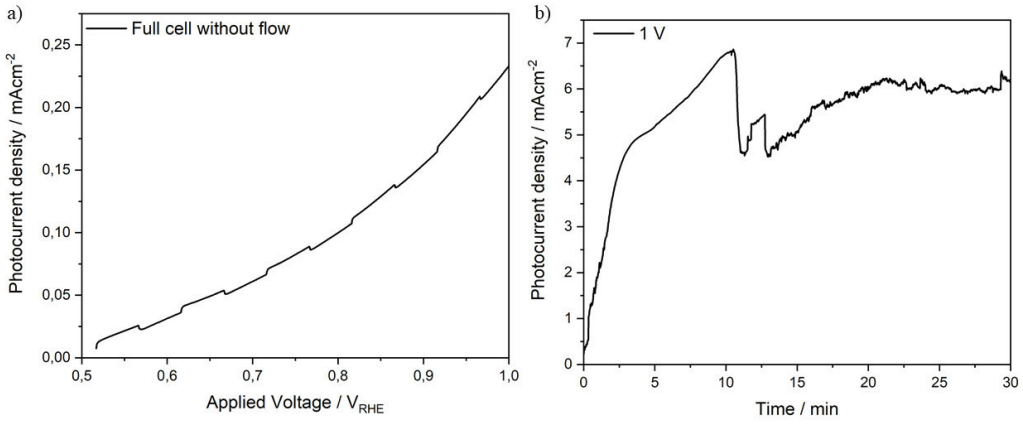

Figure 9.6: a) CLV measurement in a full cell without flow and WO_3 electrode. b) Chronoamperometry measurement at 1 V with a WO_3 electrode. The measurement was performed at a vanadium concentration of0.16 M and a flow rate of 5 mL/min.

The CLV measurement shows hardly any response to the light when the cells are full. However, a periodic increase in the photocurrent was observed at low voltages. This indicates that the photoresponse originates from the competing water oxidation. As a result, the redox reactions should be conducted at higher voltages, as the electrochemical potential of V^{3+} is with -0.26 V higher than the reduction potential of hydrogen. Therefore, higher voltages of 1 V and 1.2 V will be tested. The chronoamperometry of the light assisted charging process at an applied voltage of 1 V is displayed in Figure 9.6b.

The chronoamperometry indicates a steep rise in photocurrent during the first 12 min which is an order magnitude higher than the previously measured photocurrents. This may be an indication of charging due to the high abundance of active redox species. After 12 min the photocurrent declined and stabilized at 6 mA cm^{-2}. However, the photocurrent is unstable and has a highly fluctuating character which in turn can be attributed to the effects described above. To determine a charge, UV-Vis measurements were performed which are shown in Figure 9.7.

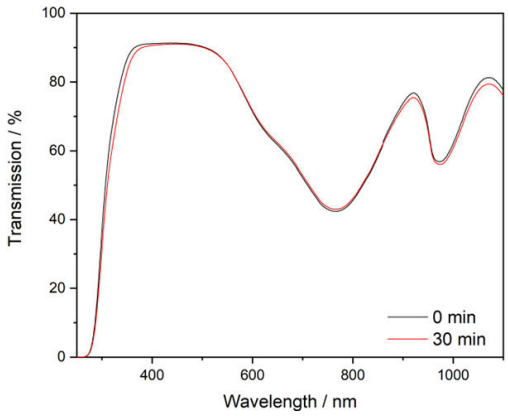

Figure 9.7: UV-Vis transmission spectra of the vanadium catholyte charged with 1 V in a full flow cell at different times.

The transmission spectra in Figure 9.7 reveal the similar trend as described for the charge of 0.8 V. No change in transmission was observed which refutes the assumption made after the chronoamperometry. In order to gain an additional conformation of the SOC, the chronoamperometry measurement was repeated at a charge of 1 V after precharging the electrolyte. This enabled simultaneous determination using OCP and UV-Vis. The chronoamperometry sequence and chronopotentiometry are displayed in Figure 9.8.

The precharging of the electrolyte is shown in Figure 9.8a which exhibits an SOC increase of 34 % after 1 h of charging. The SOC falls by 1 % after 3 h which indicates a slow self-discharge without applying a potential. This is known for vanadium RFBs due to the electrolyte crossover. The 48 h light assisted charging with 1 V is performed after the precharging and is displayed in

Figure 9.8b. Chronopotentiometry analysis revealed a steady reduction from 33 % to 27 % after 48 h which confirmed the results of the UV-Vis transmission spectra.

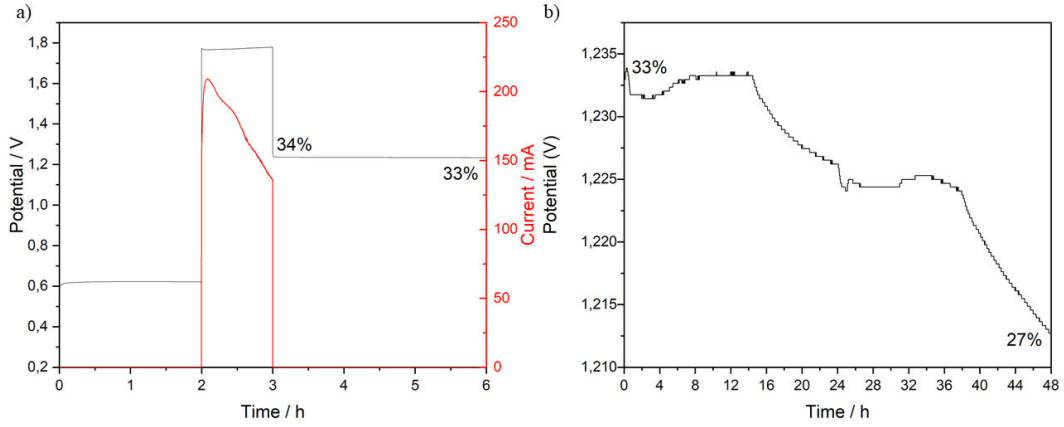

Figure 9.8: a) Precharging sequence of the VRFB for 6 h with the resulting current (red) and potential (black). b) Chronopotentiometry measured from light assisted charging at 1 V for 48 h. The measurements were performed with a vanadium concentration of 0.16 M and a flow rate of 5 mL/min.

The analysis demonstrated that applying a charge of 1 V at the WO_3 electrode is insufficient to charge the battery. Furthermore, the performance of the photoelectrode is unable to sustain the SOC leading to a decline of the SOC over time. Due to the poor information obtained by the UV-Vis measurements, OCP determination will be used primarily to track the charging process.

In order to further increase the electrochemical potential, another experiment was conducted with a potential of 1.2 V. The chronoamperometry sequence and chronopotentiometry measurements are shown in Figure 9.9.

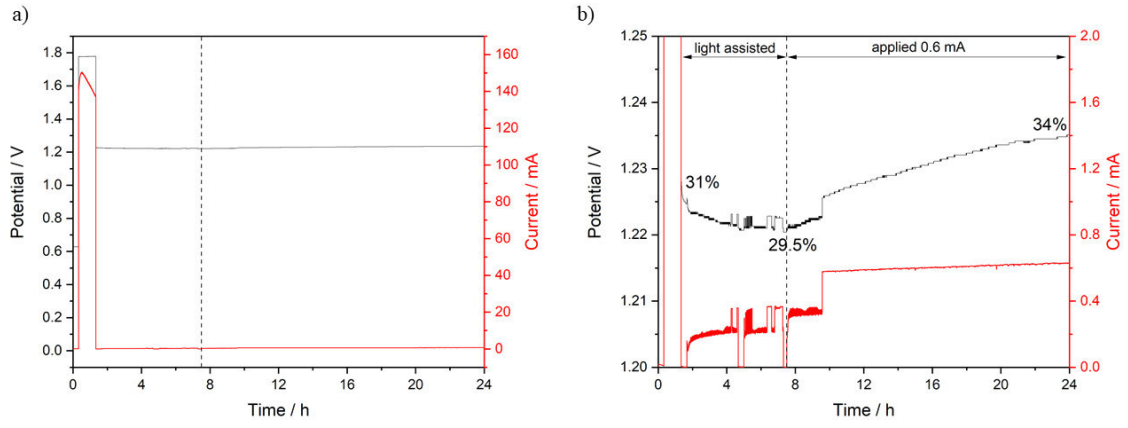

Figure 9.9: a) Precharging sequence of the VRFB for 1 h with the resulting current (red) and potential (black). b) Chronopotentiometry measured from the light assisted charging at 1.2 V for 7.5 h. The dashed line represents the light turn-off. The measurements were performed with a vanadium concentration 0.16 M and a flow rate of 5 mL/min.

Precharging for 1 h resulted in an SOC of 31 %, as can be seen in Figure 9.9b. Light assisted charging for 7.5 h with an applied potential of 1.2 V led to a decrease in the SOC. The charging experiment was therefore aborted and a current of 0.6 mA was subsequently applied to the WO_3 electrode. The aim was to investigate whether the WO_3 electrode can facilitate vanadium oxidation at the surface. The applied current was maintained for 16.5 h and Figure 9.9b shows that a small current of 0.6 mA can recharge the battery and increase the SOC by 4 %. This experiment also demonstrated that the WO_3 surface can facilitate the oxidation reaction at the surface. Therefore, the potential was elevated to 1.5 V since the WO_3 is able to oxidize V^{4+}, yet the light assisted charging still results in a SOC decrease. Chronoamperometry was performed in a single RFB setup to eliminate measurement errors of the setup with two RFB cells.

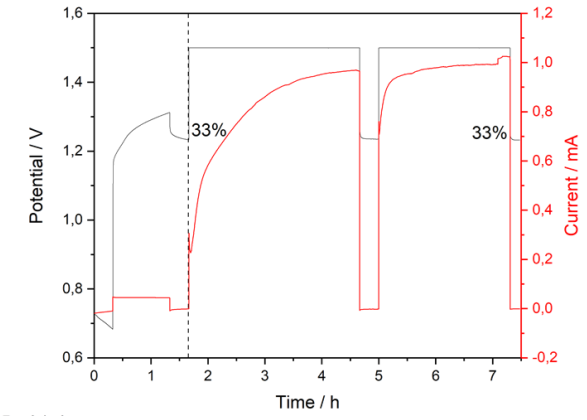

Figure 9.10: Precharging sequence of the VRFB for 1 h. The dashed line represents the beginning of light assisted charging. Chronopotentiometry measured in intervals of light assisted charging at 1.5 V for 6 h with the resulting current (red) and the potential (grey). The measurement was performed with a vanadium concentration of 0.16 M and a flow rate of 5 mL/min.

Figure 9.10 shows the periodic light assisted charging with an applied voltage of 1.5 V to determine the SOC in between. The chronoamperometry exhibits a different trend compared to the previous measurements. The current displays a flat rise in current over time. This may be an indication of charging or, given the high potential applied, an indication of water electrolysis. The OCP determination after 6 h showed that the SOC was maintained. However, gas formation could be observed inside the tubes during the charging process which supports the assumption of water electrolysis. Hence, the maintenance of the SOC is difficult to attribute to a successful light assisted charging due to a change in the concentration of the electrolyte. This experiment demonstrates that a further increase in potential may not be feasible due to gas formation and possible damage to the cell.

Another approach may be the use of differently synthesized WO_3 with a modified morphology. Lukas Mayer therefore synthesized a mesoporous WO_3 thin film which was then used in the

PRFB setup to evaluate the influence of surface structure on charging. Important to note is that the measurement displayed in Figure 9.11 was conducted at a higher flow rate and at 1.2 V to prevent gas formation.

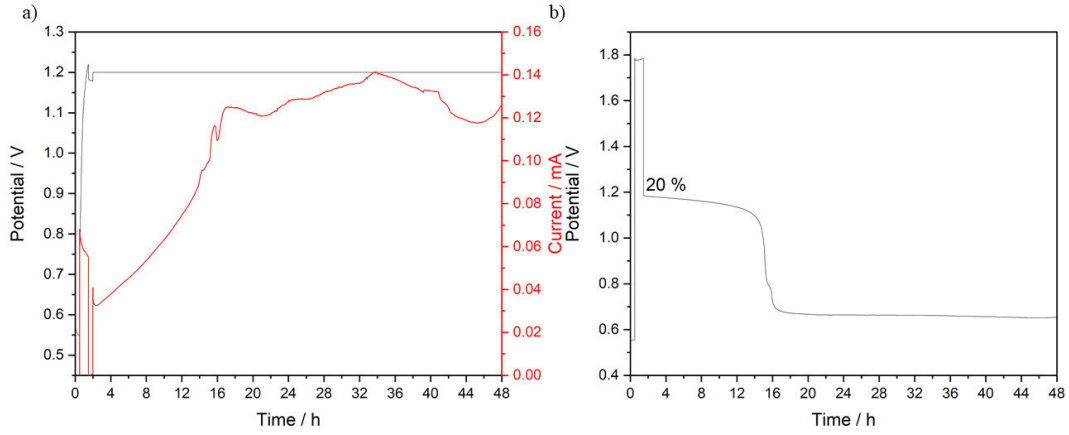

Figure 9.11: a) Precharging sequence of the VRFB for 1 h with the resulting current (red) and the potential (grey). b) Chronopotentiometry measured from light assisted charging at 1.2 V for 48 h. The measurements were performed with a vanadium concentration of 0.16 M and a flow rate of 10 mL/min.

The chronoamperometry displayed in Figure 9.11a indicates that the photocurrent of 0.02-0.12 mA cm^{-2} is significantly lower compared to the nanostructured WO_3 electrodes. However, the current rose during the charging process and stabilized at ~0.12 mA cm^{-2} after 16 h. The chronopotentiometry shown in Figure 9.11b demonstrates that the PRFB reached an SOC of 20 % after 1 h of precharging. This can be attributed to the higher flow rate limiting the charging process. Furthermore, the higher flow rate also led to a faster discharge. After 16 h, the entire SOC was lost and the PRFB remained unchanged for the rest of the time. This corresponds to the current trend, which in turn underlines that the current originates from the water splitting and not from the charge reaction.

The ineffective charging with a WO_3 electrode may be explained by several theoretical approaches. The first theory is based on the FERMI-level splitting described in detail in chapter 3.3. This splitting actually leads to a lower electrochemical potential than what would be expected from the band positions. This would result in an insufficient electrochemical potential to facilitate the redox reaction due to the higher potential of the reduction of V^{3+} to V^{2+}. Therefore, the applied potential is required to be higher than 1.5 V to enable the redox reaction which is limited by the water electrolysis. An alternative explanation could be that the WO_3 electrode is optimized for the water oxidation reaction. As noted above the (002) facet is the energetically favored crystal facet for the oxidation of water. Therefore, the PRFB charging is always in competition with the water oxidation reaction which should be kinetically slower, yet

is enhanced by the nanostructured WO_3 electrode.

Due to insufficient charging of the PRFB with a WO_3 electrode, the following material $BiVO_4$ will be investigated in greater detail. The conduction band of $BiVO_4$ is higher than the band of WO_3 and should therefore allow charging at lower applied potentials compared to WO_3.

9.2.BiVO4

The first characteristic to consider when working with $BiVO_4$ under non-neutral conditions is stability. It has been repeatedly shown that $BiVO_4$ is unstable in acidic or basic solutions.[225,226] Therefore, a concentration screening was performed to evaluate the stability of $BiVO_4$ in the VRFB electrolyte. The commercial electrolyte was found to have a concentration of a 4 M H_2SO_4 and 1.6 M $V^{3.5+}$ (1:1 V^{3+} and V^{4+}) which is the highest concentration tested in the screening. Then, the solution is diluted to 2 M, 1 M, 0.4 M and 0.04 M H_2SO_4. The vanadium concentration changes respectively to ensure there is no segregation of the vanadium species as discussed in chapter 3.8.1. The thin films were immersed in the respective concentrations and the results are displayed in Figure 9.12.

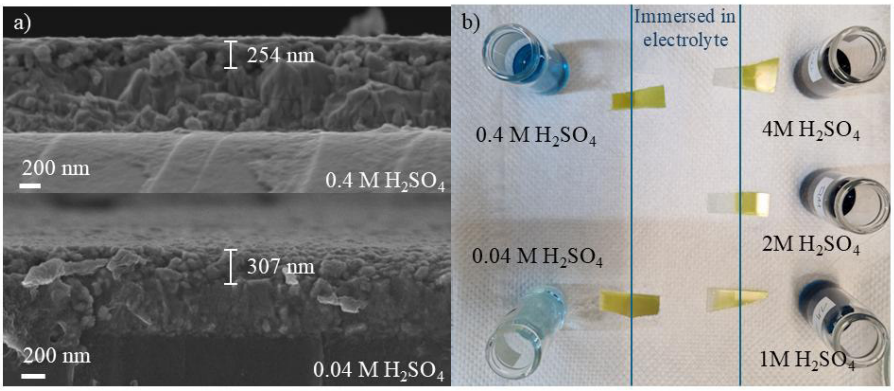

Figure 9.12: a) $BiVO_4$ thin films immersed in the respective concentrations for 30 min with slow stirring to simulate flow. Between the blue lines is the area that was exposed to the electrolyte, while outside the lines the thin film is shown as it was prepared. b) The cross-sectional SEM image was measured from samples with a thin film still visible.

Figure 9.12 clearly demonstrates that after 30 min in 4 M, 2 M and 1 M H_2SO_4 no $BiVO_4$ is left on the surface, only the glass slide. The sample immersed in 1 M H_2SO_4 showed a slight yellow coloration which indicates that some $BiVO_4$ phase is still present after 30 min. Lower concentrations of 0.4 M and 0.04 M exhibit a visible $BiVO_4$ phase on the surface. Therefore, cross-sectional SEM images were performed to evaluate the film thickness after immersion. The $BiVO_4$ thin films were synthesized with a double coating and the withdrawal speed of 300 mm min^{-1} as described in chapter 7 with a film thickness ranging from 450-500 nm. The cross-sectional SEM images showed a film thickness of 254 nm and 307 nm for a 0.4 M and

0.04 M H_2SO_4 concentration, respectively. This indicates that the sample immersed in the lowest concentration of 0.04 M H_2SO_4 loses ~100 nm of material within 30 min. This highlights the importance of improving the stability of a $BiVO_4$ electrode used in a VRFB. To confirm the stability issues, a chronoamperometry measurement was performed in addition to the CLV which should verify the possible performance of the $BiVO_4$ electrode. The two measurements are displayed in Figure 9.13. Considering the results of the WO_3 study, the applied potential was set to 1 V.

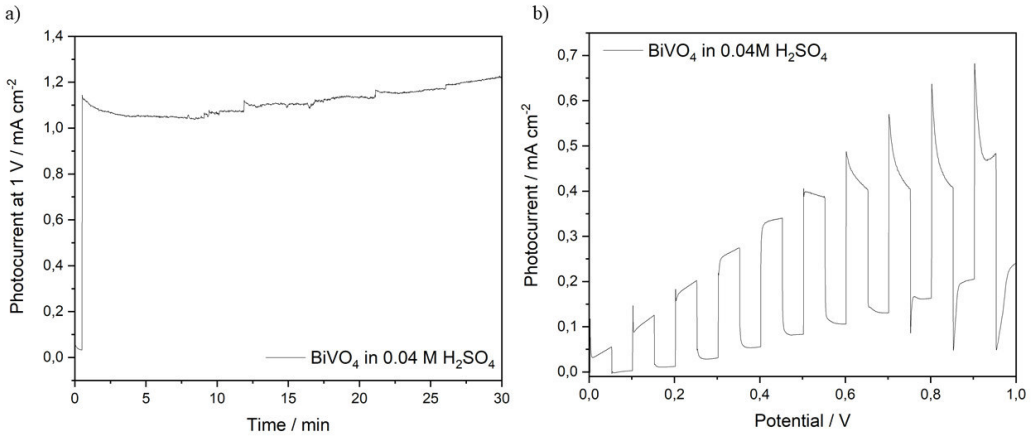

Figure 9.13: a) Chronoamperometry measured from the light assisted charging at 1 V for 30 min. The measurement was performed with a vanadium concentration of 0.016 M. b) CLV measurement of a thin $BiVO_4$ film in a PEC cell.

The chronoamperometry in Figure 9.13a shows that the $BiVO_4$ can reach a current of 1.1 mA cm^{-2} during light assisted charging at 1 V. However, the CLV in Figure 9.13b demonstrates that a lower current can be detected even at lower potentials which in turn is an indication of the water splitting reaction. Therefore, after solving the stability issue the same study previously shown for WO_3 should be performed to distinguish between light assisted charging and water splitting. Nevertheless, the chronoamperometry again shows stability problems after 8 min of light assisted charging.

One potential method of improving the stability of $BiVO_4$ electrodes is the protection with an acid-stable semiconductor. The fact that a protective layer can improve the stability of $BiVO_4$ photoanodes was reported for basic media by CHOI *et al.* in 2018.[226] For acidic media, the choice of semiconductor materials that withstand strong acids such as H_2SO_4 effectively shrinks to WO_3 and TiO_2. TiO_2 offers a wide range of synthetic routes to produce thin films and is a well-studied material. Therefore, the investigations started with a TiO_2 protection layer by coating and ALD.

9.3.BiVO4/TiO2

The requirements for a protective layer for the photocatalytic setup are high. Firstly, entire surface must be perfectly covered in order to effectively protect the semiconductor material. Furthermore, it is crucial that the protective layer is not too thick due to poor diffusion properties of TiO_2 for hole transfer. Therefore, a thin and homogenous TiO_2 is required to protect and enable diffusion of charge carriers. For this reason, ALD has emerged as one of the best methods to prepare high quality TiO_2 protective layers.[227–229] However, ALD has some drawbacks like the high cost of the method and the ability to cover only the exposed surface which causes issues for porous and highly nanostructured surfaces. An alternative low-cost synthesis is the coating approach with sol-gel hydrolysis of an organic Ti precursor. The sol-gel approach to synthesize TiO_2 thin films is a well-studied method and can lead to homogenous coating. [230–232] However, it is crucial that the thickness of such coated thin films is as low as possible to allow the diffusion of the charge carriers. Both approaches described were tested in this chapter and evaluated based on the aforementioned criteria of homogeneity and thickness. The ALD synthesis was performed in collaboration with Prof. Martin Eickhoff from the University of Bremen.

9.3.1. Coating of TiO_2

For the coating, TTIP was tested with and without calcination and TiBALDH was used as an alternative Ti precursor. To evaluate presence of TiO_2 bare FTO samples were coated simultaneously to characterize the thin film without $BiVO_4$. The results of the three substrates are shown in Figure 9.14.

The bare FTO reference exhibits anatase reflexes for both TTIP substrates. The most intense anatase reflex at 25.2° 2θ is clearly evident after calcination and can also be observed without calcination. The diffractogram of the substrate coated with TiBALDH shows no anatase reflexes. However, it exhibits an amorphous phase due to the uneven background. The same background elevation can be found in the TTIP-coated and calcined sample. This contradicts the exception as the TiO_2 should be more crystalline than amorphous after calcination. Furthermore, the substrate coated with TTIP and without calcination, which should therefore be more amorphous than crystalline, exhibited no strong increase in background. The GIXRD measurements of the $BiVO_4/TiO_2$ substrates showed small reflexes of V_2O_5 and *t*-zircon in addition to the desired *m*-scheelit type structure, indicating that the aging process of the precursor solution was not completed in this batch. However, as these samples are tested for stability and not performance this can be neglected.

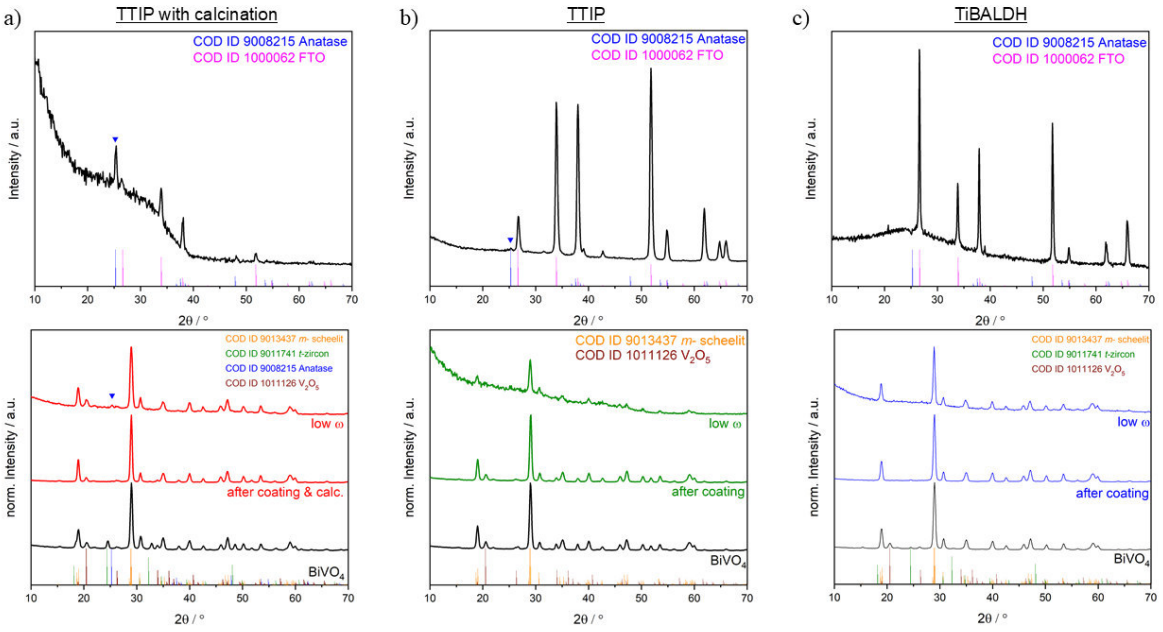

Figure 9.14: GIXRD measurements of FTO coated with TiO_2 (top three) and $BiVO_4$ coated with TiO_2 respectively (bottom three) of a) TTIP with subsequent calcination b) TTIP without calcination and c) TiBALDH without calcination. The blue triangle indicates the reflex attributed to the anatase crystal phase.

The GIXRD measurement was performed a second time with a low ω angle to potentially reveal anatase reflexes on the surface. The sample coated with TTIP and subsequently calcinated showed an anatase reflex at 25.2° 2θ. However, the other two samples were free of anatase reflexes. In summary, the substrate coated with TTIP and subsequently calcinated exhibited anatase reflexes indicating TiO_2 coverage of the surface. The TTIP sample without calcination showed only a small reflex on the FTO control sample. This would suggest that a reflex is also present on the surface of the $BiVO_4$ but is undetectable due to the low intensities. Lastly, the TiBALDH showed no anatase reflexes in either the control or the $BiVO_4$ sample. However, an amorphous phase was detectable indicating that the surface is covered with an additional material.

To gain more information about the surface composition of the $BiVO_4$ sample SEM images were measured. For comparison, a bare $BiVO_4$ and FTO coated with TTIP and subsequently calcinated is measured before and displayed in Figure 9.15. The detection of the TiO_2 layer was impossible in the FTO/TiO_2 control sample. The cross-sectional and top view images only show the tetragonal tin oxide structure. This alone indicates that the coating has not resulted in a homogenous covered surface. The $BiVO_4$ control sample, on the other hand, exhibits the surface structure previously described and expected.

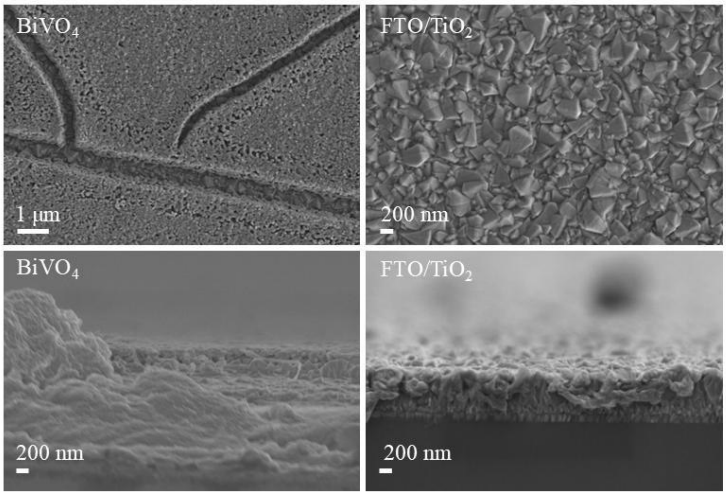

Figure 9.15: Top view SEM images of $BiVO_4$ and FTO/TiO_2 (top) and cross sectional SEM images (bottom) to assess the film thickness.

The top view and cross-sectional SEM images of the $BiVO_4/TiO_2$ samples are shown in Figure 9.16. As a note, no cross-sectional images were obtained of the sample coated with TTIP and calcination due to the uneven fracture edge.

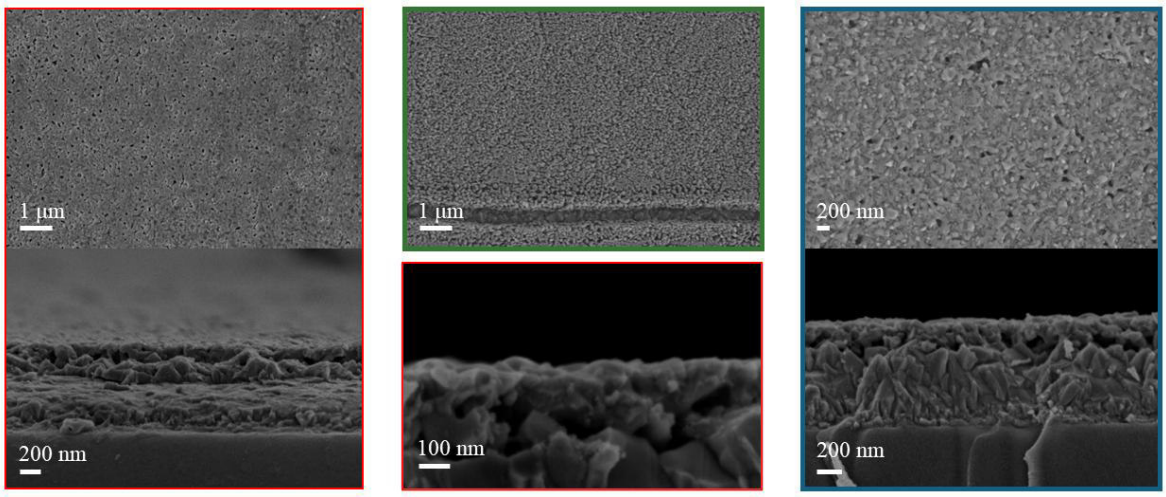

Figure 9.16: Top view SEM images of $BiVO_4/TiO_2$ samples (top) and cross sectional SEM images (bottom). The colored frame corresponds to the colors in the GIXRD and represents red TTIP with calcination, green TTIP without calcination and blue TiBALDH.

In Figure 9.16 the SEM images of the different samples, synthesized with varying Ti precursors or varying synthetical parameters indicate no detectable TiO_2 protective layer. The highly magnified cross-sectional image of the TTIP sample with subsequent calcination shows only the FTO and $BiVO_4$ layer. Overall, results confirm those previously obtained for the FTO/TiO_2 control sample and indicate that further analysis is required to evaluate the presence of TiO_2. Therefore, an EDX measurement of the TTIP sample with subsequent calcination was performed. The analytical findings are summarized in Table 14.

Table 14: EDX result of the $BiVO_4/TiO_2$ sample coated with TTIP and subsequently calcinated.

Atom %	Sn	O	V	Bi	Ti
TTIP with calc.	20.8	70.0	4.3	2.2	-

The EDX result is consistent with the SEM results as no Ti is detectable. Therefore, the GIXRD measurement is the only method which confirms the presence of TiO_2. Nevertheless, the protective layer is not present, so the synthetic parameters have to be adjusted. The chronoamperometry measurements are expected to be comparable to the previous measurements due to absence of a homogenous TiO_2 protective layer. The chronoamperometry measurements are displayed in Figure 9.17.

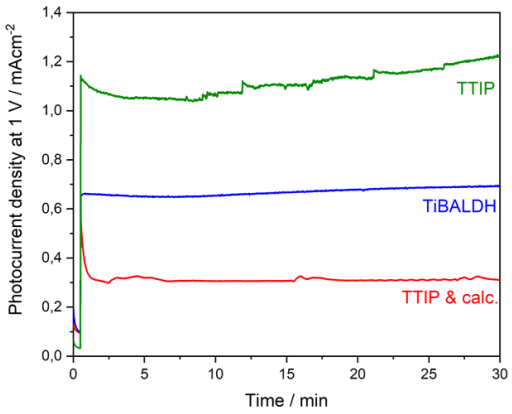

Figure 9.17: Chronoamperometric measurements in the PEC cell of the $BiVO_4/TiO_2$ samples synthesized by coating and calcination. The color code is equal to the SEM and GIXRD measurements.

The chronoamperometry exhibits the expected trend. All samples show a tendency to dissolve after 10 min due to the unstable photocurrent. Although all samples were synthesized in the same batch, all three exhibit different photocurrents. The calcinated TTIP sample has the lowest current of 0.3 mA cm^{-2}. The TiBALDH sample reaches a current of 0.65 mA cm^{-2} and the TTIP sample without calcination achieves the highest current with 1.1 mA cm^{-2}. The lowest current may be due to calcination which may affect the $BiVO_4$ or the insignificant amounts of TiO_2 on the surface. The TTIP without calcination likely delaminates quickly into the solution leaving only $BiVO_4$. Lastly, the lower TiBALDH photocurrent might also be due to organic or Ti residuals on the surface, yet to be further analyzed.

At the end of the first experiments, evidence was found that the parameters used did not lead to a sufficient TiO_2 protective layer. The synthetic parameters will have to be changed to increase the TiO_2 content on the surface. This could involve adjusting the Ti precursor concentration in

the dip coating solution and the dip coating parameters adding more cycles or reducing the withdrawal speed.

9.3.2. ALD

The ALD was performed by Dr. Alonso Orts and the XPS analysis as well as the AFM were conducted by Dr. Alexander Karg in collaboration with Prof. Dr. Martin Eickhoff at the University of Bremen.

The bare Mo:$BiVO_4$ were analyzed by AFM to evaluate the surface composition and later compare with the TiO_2 deposited samples. The AFM images are shown in Figure 9.18.

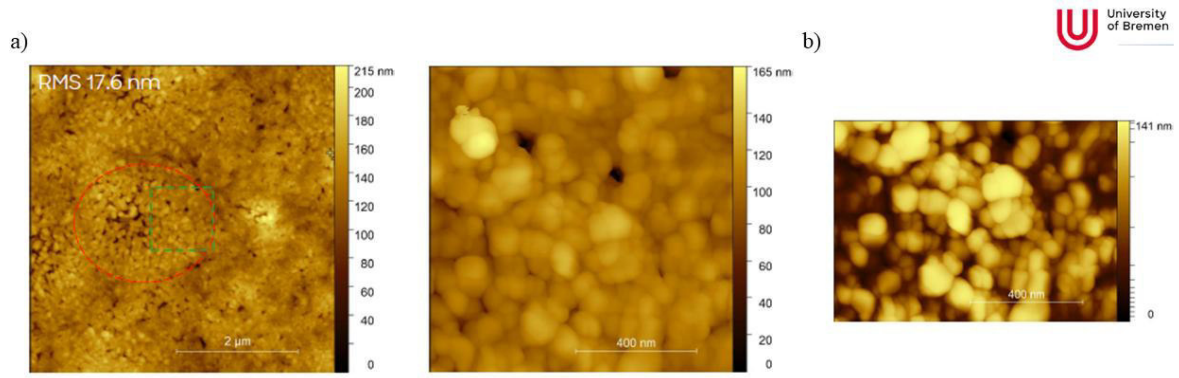

Figure 9.18: a) AFM images of the bare Mo:$BiVO_4$ bare surface and b) false color image to highlight the distinguishable crystallites. Performed by Dr. Alexander Karg at the University of Bremen.

AFM indicates that surface structure is composed of small crystallites that form a sponge-like structure as described earlier in this thesis. To achieve varying film thicknesses with the ALD a number of different cycles were performed. The targeted film thickness was 3, 5, 7 and 10 nm was achieved with 40, 67, 93 and 133 cycles, respectively. Figure 9.19 shows AFM images after ALD coating with different numbers of cycles.

The images reveal the same morphology as the bare $BiVO_4$, confirming that no apparent changes occur due to the TiO_2 deposition. In addition, the holes of the sponge-like structure remain, which may be an issue for the stability of the electrode due to the lack of coating inside the structure. The root mean square (RMS) represents the roughness of the surface and has no clear trend. Therefore, it is most likely an effect of a random scattering or tip uptake. In addition to AFM, XPS measurements were performed to analyze the surface composition and thickness of the deposited electrodes. The XPS study is displayed in Figure 9.20.

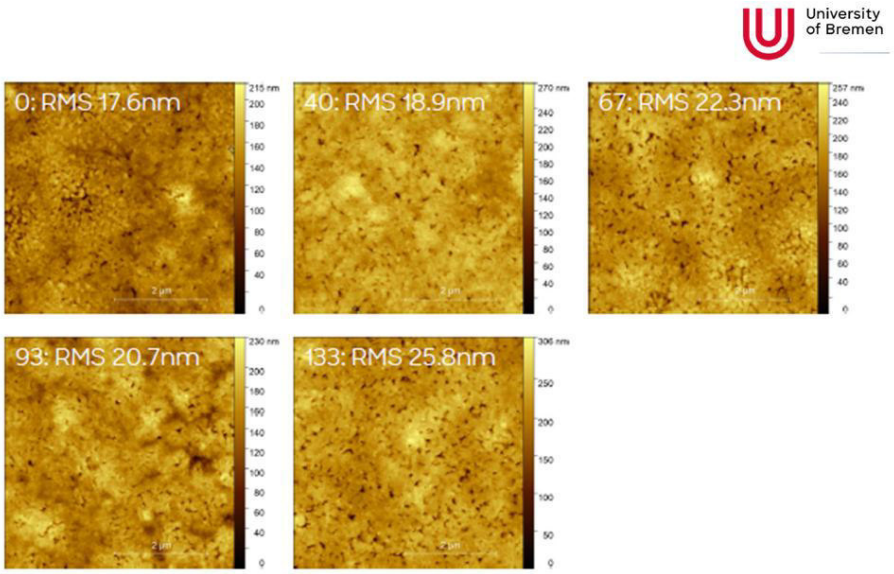

Figure 9.19: AFM images of the atomic layer deposited Mo:$BiVO_4$/TiO_2 electrode surfaces with different numbers of cycles. Performed by Dr. Alexander Karg at the University of Bremen.

The XPS analysis shows the predicted trend for TiO_2 deposition, observed in the overview spectra and in the magnified peaks for Bi and Ti. Figure 9.20b shows that the intensity of the Bi peaks decreases, while the Ti peaks emerge with the increasing number of cycles. In addition to the element distribution, the film thickness has also been determined and summarized in Table 15.

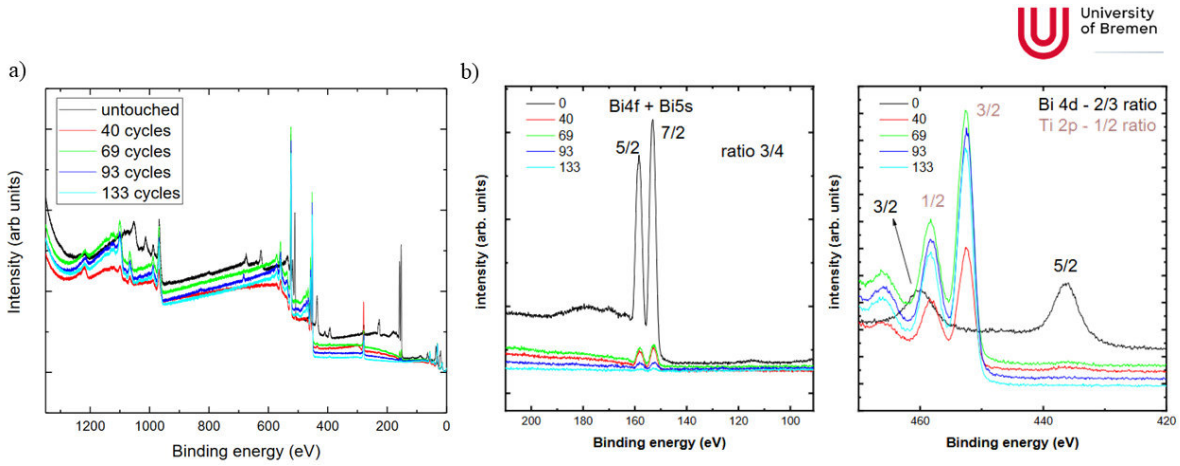

Figure 9.20: XPS analysis of Mo:$BiVO_4$/TiO_2 electrodes synthesized by ALD with a different number of cycles at 573 K. Performed by Dr. Alexander Karg at the University of Bremen. a) Overview spectra and b) Magnification of Ti 2p and Bi 4f peaks.

The findings demonstrate that the targeted film thickness is achieved in all cases. At higher numbers of cycles, the estimated film thickness exceeds the target film thickness yet still corresponds to the trend and can therefore be used for chronoamperometric stability measurements.

Table 15: Film thickness of the ALD-deposited TiO_2 protective layer on $BiVO_4$ at 573 K, determined by XPS analysis. Performed by Dr. Alexander Karg at the University of Bremen.

Number of cycles	Targeted TiO_2 thickness / nm	Estimated thickness from XPS analysis / nm
133	10	12.0 – 13.7
93	7	8.4 – 9.6
67	5	6.0 – 6.9
40	3	3.6 - 4.1
0	0	0

The chronoamperometry measurements were performed in the PEC and PRFB setups with the $BiVO_4/TiO_2$ electrodes synthesized by ALD. The results are displayed in Figure 9.21.

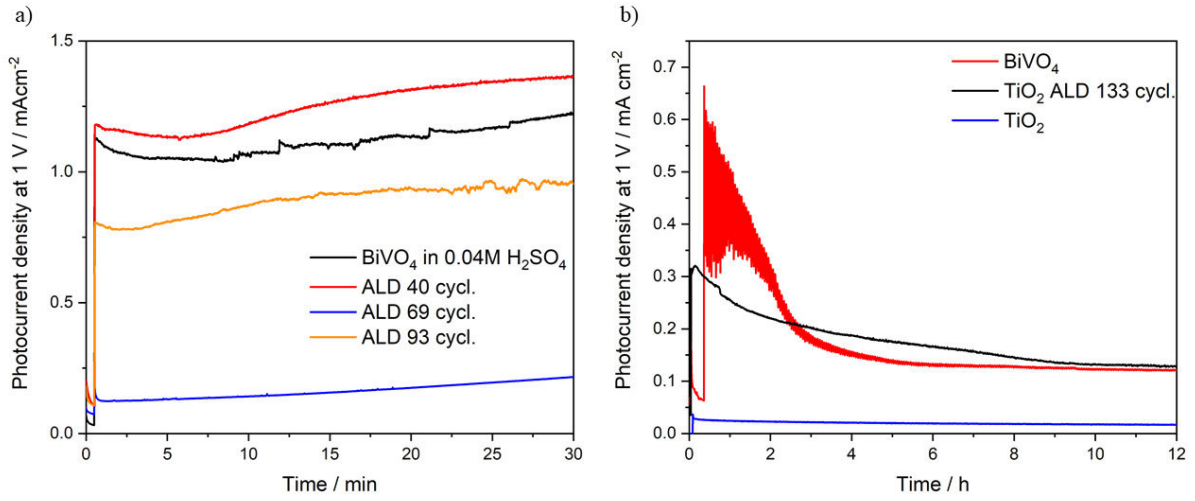

Figure 9.21: a) Chronoamperometry measurements in the PEC cell of the $BiVO_4/TiO_2$ electrodes with different film thickness synthesized by ALD. b) Long term stability chronoamperometry performed in the PRFB setup.

Chronoamperometry exhibits the same trend as discussed above for the coated samples. The current can be maintained for about 10 min until it starts to fluctuate. This indicates the dissolution of the $BiVO_4$ in the electrolyte. Interestingly, the performance of the electrode corelates not with film thickness of the protective layer. This is demonstrated by the electrode with 69 cycles achieving the lowest photocurrent with 0.13 mA cm^{-2}, whereas the 93 cycles exhibit a photocurrent of 0.80 mA cm^{-2} at 1 V. The thickest protective layer with an estimated film thickness of 12.0 - 3.7 was used for long term measurements shown in Figure 9.21b. It indicates that the stability of the electrode could be increased. The bare $BiVO_4$ loses the entire photocurrent after ~4 h, while the $BiVO_4/TiO_2$ can maintain its performance for about 9 h. Therefore, the decrease in the current has slowed down. However, to use the electrode in a light

assisted charging cycle, stability must be enhanced. Thus, the ALD table temperature was lowered to 473 K and the TDMAT precursor rinse time was doubled to achieve a more effective coverage of the sponge-like morphology. The number of cycles was adjusted to the previous findings to obtain the targeted film thickness as summarized in Table 16.

Table 16: Film thickness of the ALD deposited TiO_2 protective layer on $BiVO_4$ at 473 K, determined by XPS analysis. Performed by Dr. Alexander Karg at the University of Bremen.

Number of cycles	Targeted TiO_2 thickness / nm
242	12.85
170	9
122	6.45
73	3.85
0	0

The corresponding XP spectra are displayed in Figure 9.22.

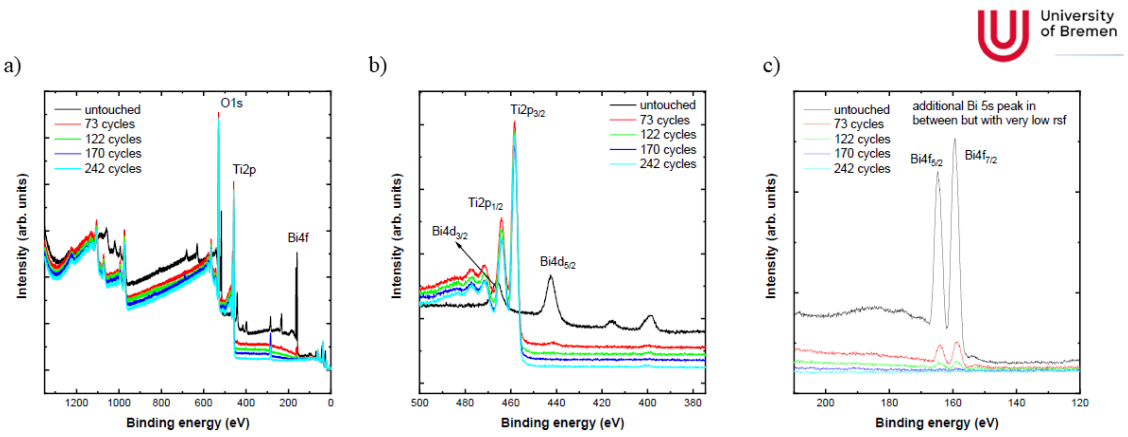

Figure 9.22: XPS analysis of Mo:$BiVO_4$/TiO_2 electrodes synthesized by ALD with different number of cycles at 473 K. Performed by Dr. Alexander Karg at the University of Bremen. a) Overview spectra and magnification of b) Ti 2p and c) Bi 4f peaks.

The XPS analysis reveals the same tendency as described for the previous samples. By increasing the number of cycles, the intensity of Bi signals decreases. At the same time, the intensity of Ti signals increases. This shows a successful TiO_2 deposition on the surface with increasing thickness due to a higher number of cycles.

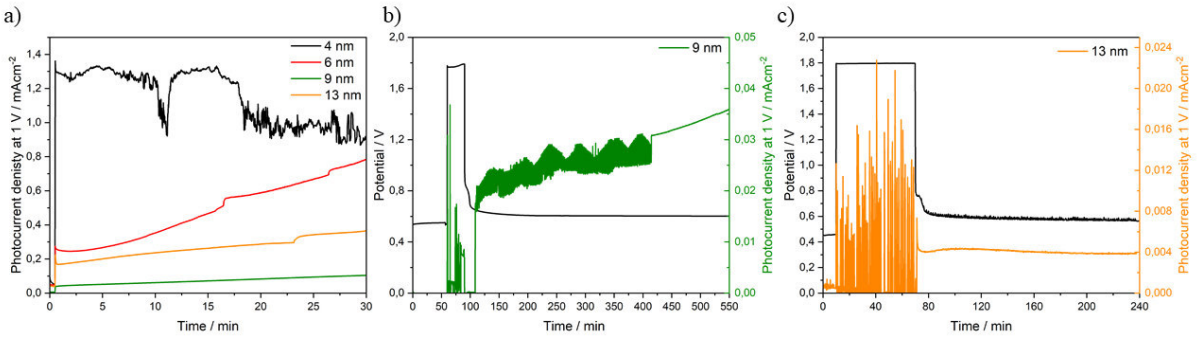

Figure 9.23: a) Chronoamperometry measured during the light assisted charging at 1 V for 30 min in the PEC cell. b) for 550 min and c) for 240 min in the PRFB cell. The measurements were performed with a vanadium concentration of 0.016 M and a flow rate of 5 mL/min.

The chronoamperometry in Figure 9.23a shows that the thin film thicknesses of 4 and 6 nm exhibit the same instability as previously observed and discussed. However, the film thicknesses of 9 and 13 nm show a lower photocurrent but most likely a better stability. Therefore, long term measurements were performed with the PRFB setup. Note, that in Figure 9.23b the first 100 min and in Figure 9.23c the first 70 min correspond to the precharging step and therefore not represent the performance of the electrode. However, after the precharging step the photocurrent of both electrodes exhibits an unstable current during the long-term charging, which in turn indicates the dissolution of the $BiVO_4$.

9.4.Conclusion

The transfer of the electrodes into the PRFB to perform light assisted charging caused stability issues with the $BiVO_4$ electrode and no charging with the WO_3 electrode. Although the WO_3 electrode showed good stability under acidic condition of the all-vanadium PRFB, the applied potential was not sufficient to accomplish light assisted charging. Potentials ranging between 0.7 - 1.5 V were tested whereby bubble formation could be observed at 1.5 V, indicating water electrolysis. This leads to the assumption that WO_3 would require a higher potential to shift the conduction band to a suitable level to facilitate the redox reaction but is limited by the water electrolysis.

$BiVO_4$ could provide a higher conduction band position but suffers from the highly acidic conditions of the electrolyte. A TiO_2 protective layer was tested by coating and ALD. The coating approach resulted in TiO_2 residuals on the surface which could be detected by GIXRD, however, the dip coating failed to cover the entire surface with an effective TiO_2 layer. Therefore, this approach will require further research regarding the synthetical parameters in order to coat the surface with a thin TiO_2 protective layer. As an alternative, the ALD method led to a TiO_2 protective layer with a variable film thickness between 3 and 14 nm. Nevertheless, this approach was insufficient to cover the sponge-like structure exposing $BiVO_4$ underneath. This could be detected in chronoamperometry measurements which showed increased stability for the thick protective layer, yet still affected by dissolution of $BiVO_4$ in the electrolytes.

In order to effectively protect the $BiVO_4$ from exposure to electrolytes further experiments are necessary. As previously described, the synthetic parameters for the dip coating could be adjusted. Another potential approach to protect the $BiVO_4$ is to spin coat a dense WO_3 seed layer as described in chapter 6. Given the good stability of WO_3 in acidic media this may enhance stability but may also lead to the same challenge of insufficient applied potential to facilitate the redox reaction.

10.Summary and Outlook

The aim of this thesis was to optimize a semiconductor electrode for the application of light assisted charging of an all-vanadium redox flow battery. Therefore, the goal was to synthesize a WO_3/Mo: $BiVO_4$ heterojunction to benefit from the good electric properties of WO_3, the more suitable band positions of $BiVO_4$ and the improved charge carrier separation of a heterojunction.

The WO_3 electrode was optimized by investigating the interface between WO_3 and FTO. Thus, a seed layer was used in a hydrothermal growth reaction to synthesize a highly crystalline WO_3. A spin coating study led to an optimal seed layer formation to promote the electron extraction of hydrothermal grown WO_3 electrode, which is yet the limiting performance factor. By spin coating the seed layer at 5000 rpm for 30 s, a seed layer density of W/Sn 0.81 was achieved yielding a photocurrent of 1.51 mA cm^{-2} at 1.23 V_{RHE} with a flat band potential of 0.39 V_{RHE} and a donor density N_D of $1.7 \cdot 10^{21}$ m^{-3}. The analysis also demonstrated that an insufficiently synthesized seed layer leads to poorer performance compared to WO_3 electrode grown without a seed layer. Furthermore, the thin film exhibited a thickness of 1.9 µm, an IPCE of 60% and a charge injection efficiency of 89 %.

The next step was the WO_3/Mo:$BiVO_4$ heterojunction formation by optimizing the solvent and the dip coating parameters. Two different morphologies could be achieved by adjusting the dip coating parameters alone. A slower dip coating withdrawal speed of 100 mm min^{-2} resulted in core-shell-like morphology while a faster dip coating withdrawal speed led to a layer-like structure. However, the expected improvement in performance was not observed. All heterojunctions performed worse than the bare WO_3 or Mo:$BiVO_4$ electrodes. For this reason, an absorption inversion study was conducted to determine the different roles of each material within the heterojunction. It was shown that Mo:$BiVO_4$ should act as the main absorber while WO_3 should promote the charge carrier separation due to its excellent electron extraction properties. Therefore, an optimal film thickness ratio between WO_3 and Mo:$BiVO_4$ is required to achieve higher photocurrents. Lastly, different nanostructured surfaces of the WO_3 electron extraction layer were synthesized to obtain an optimal ratio of WO_3 to Mo:$BiVO_4$. The nanostructure consisted of nanorods, nanowires, nanoflakes and a mesoporous WO_3 electrode. However, all heterojunctions performed worse than the single material electrodes. The generation of heterojunction therefore led to no increase in performance and needs further investigation. A detailed transmission and absorption study in combination with the charge carrier kinetics acquired with IMVS can provide additional information.

The hydrothermal conversion of a WO_3 electrode to α-$SnWO_4$ was the goal of a collaboration with The University of Queensland. Finding a reproducible synthetic route for the effective conversion of WO_3 to α-$SnWO_4$ was not feasible. A coating and calcination approach showed a $SnWO_4$ crystal phase, however, could not be optimized to reliably convert the electrode. Further research indicated that W^{6+} is reduced to W^{5+} during hydrothermal conversion which was refuted by XPS analysis. Therefore, this study remains incomplete and requires further experiments to provide an explanation for the resulting absorption shift after conversion. Moreover, it may help to identify crucial synthetic parameters to facilitate the conversion in the future.

In this work, a PRFB battery for light assisted charging with constant flow was successfully developed. Due to the poorer performance of the WO_3/Mo:$BiVO_4$ heterojunction, only the single material electrodes were tested in charging experiments. The WO_3 electrode was found to withstand the acidic conditions of the all-vanadium electrolyte but was unable to sustain the redox reaction to charge the battery. The applied potential must be higher to shift the position of the conduction band to a suitable level, but is limited by the water electrolysis.
In contrast, a $BiVO_4$ electrode would provide more suitable band positions yet suffers from dissolution due to acidic conditions. Therefore, a TiO_2 protective layer was synthesized by dip coating and ALD. The obtained TiO_2 layer failed to cover the entire surface of $BiVO_4$ and to protect the material from electrolyte exposure. Nevertheless, the ALD TiO_2 layers were able to increase stability so that the dissolution of $BiVO_4$ was reduced but not entirely prevented. Additional experiments to adjust the dip coating parameters should be performed in the future to achieve a homogenous TiO_2 layer.

Although no light assisted charging of a PRFB with a semiconductor material was achieved, the knowledge gained in this thesis will contribute to the optimization and development of new materials for this application.

11.Appendix

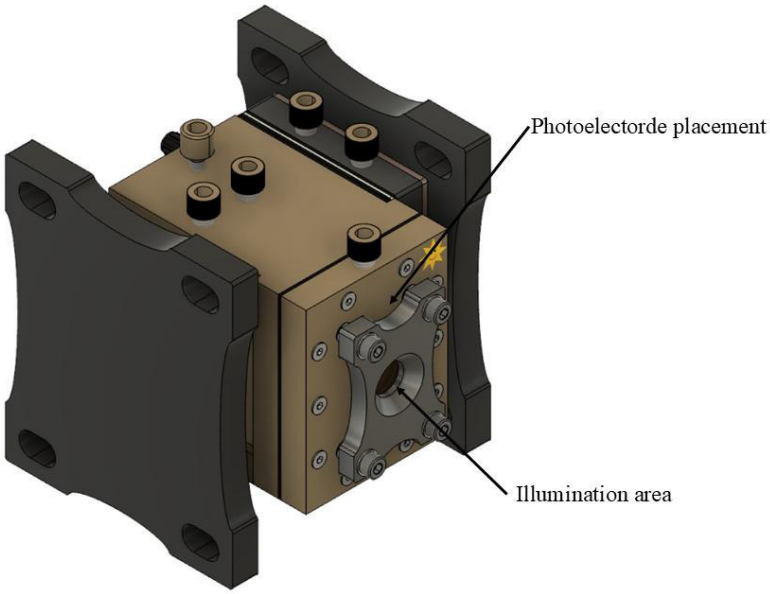

Figure 11.1: Assembled photo redox flow cell which highlights the electrode placement and the illumination area.

11.1. Additional Figures for chapter 6

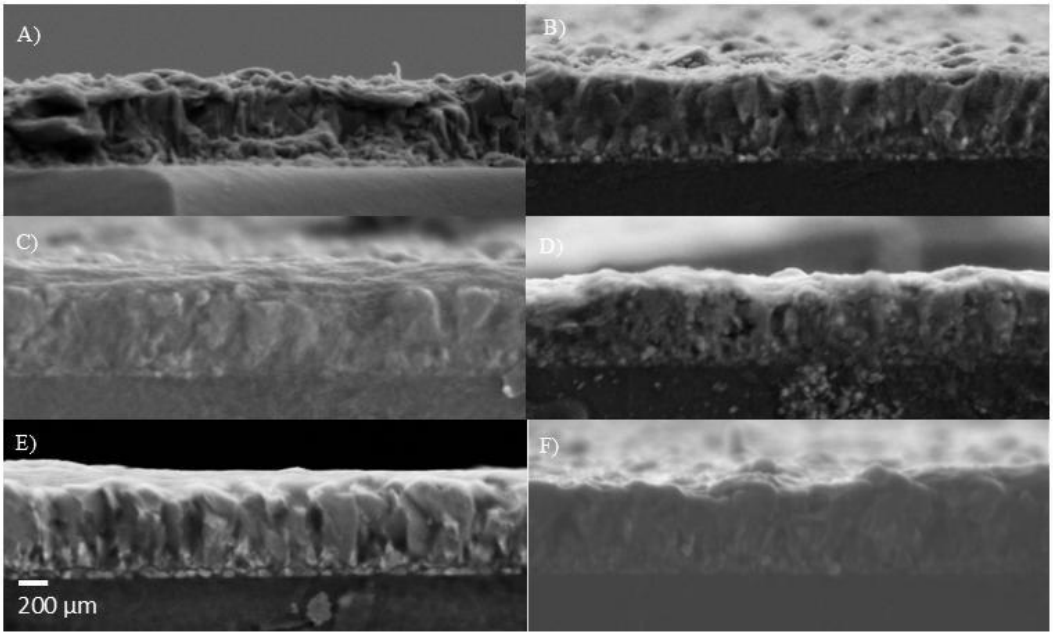

Figure 11.2: SEM images cross section of the statically coated seed layer. The labels are chosen according to the notation in Table 4. (Reprinted with permission of the Royal Society of Chemistry 2023).[111]

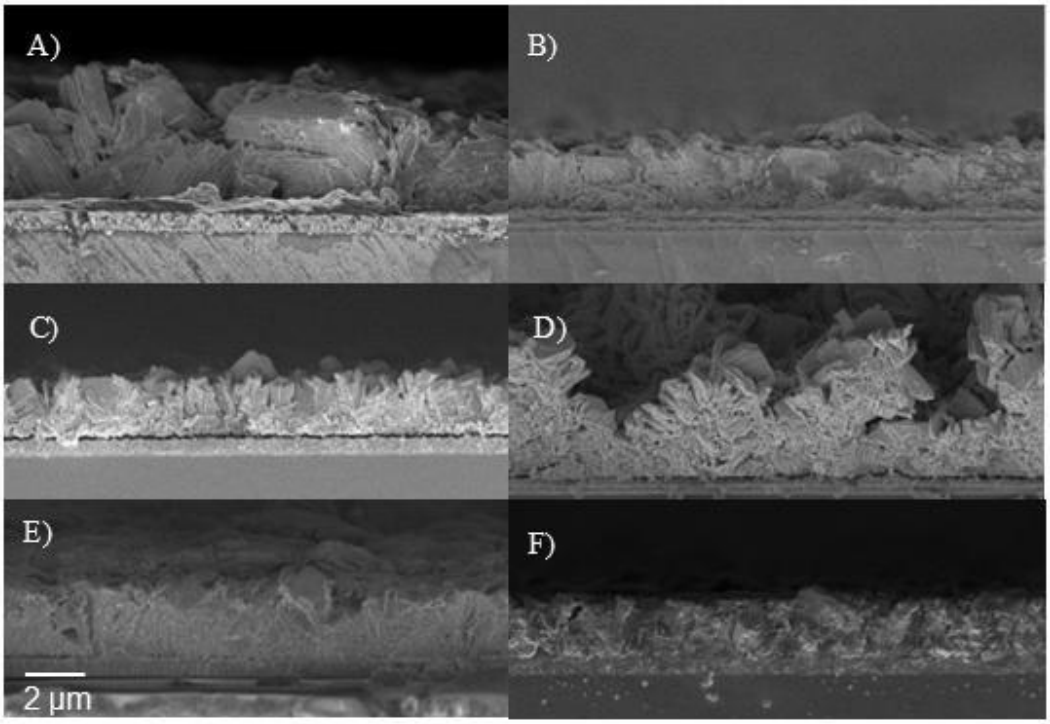

Figure 11.3: SEM images cross section of the hydrothermally grown WO_3 thin films synthesized from the static spin coated seed layer. The labels are chosen according to the notation in Table 4. (Reprinted with permission of the Royal Society of Chemistry 2023).[111]

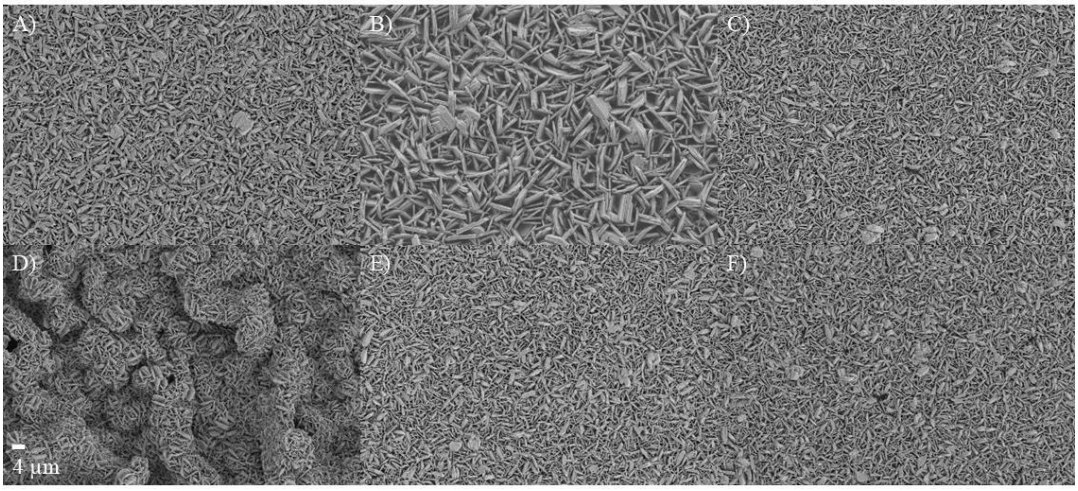

Figure 11.4: Overview SEM images of hydrothermally grown WO_3 films from the seed layer using static spin coating. Same scale for all measurements. (Reprinted with permission of the Royal Society of Chemistry 2023).[111]

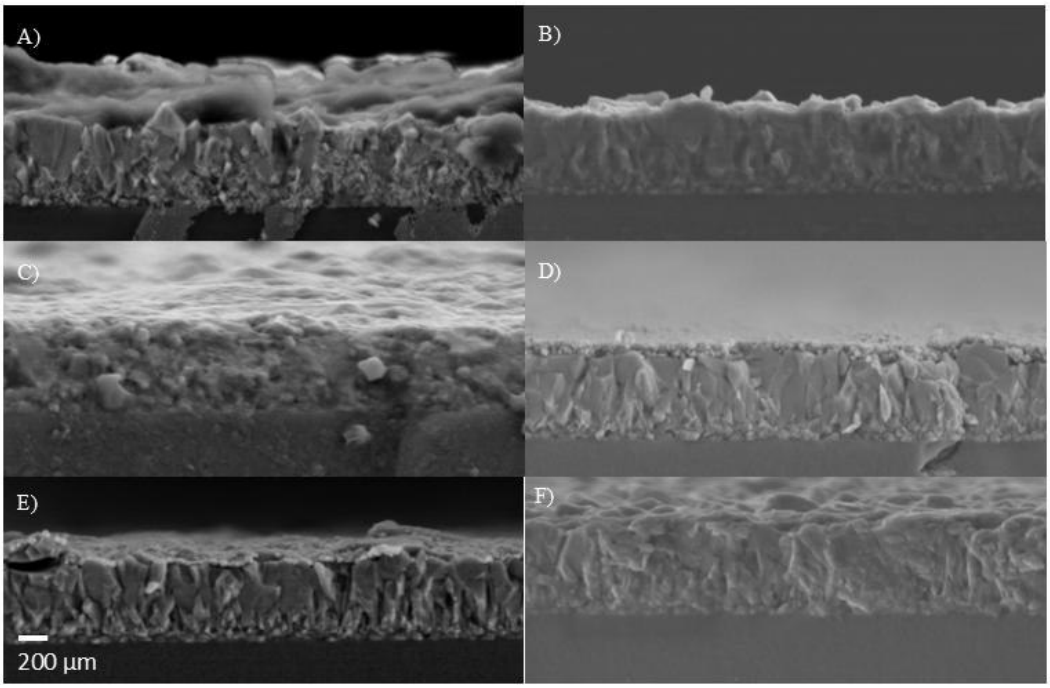

Figure 11.5: SEM images cross section of the dynamically coated seed layer. The labels are chosen according to the notation in Table 4. (Reprinted with permission of the Royal Society of Chemistry 2023).[111]

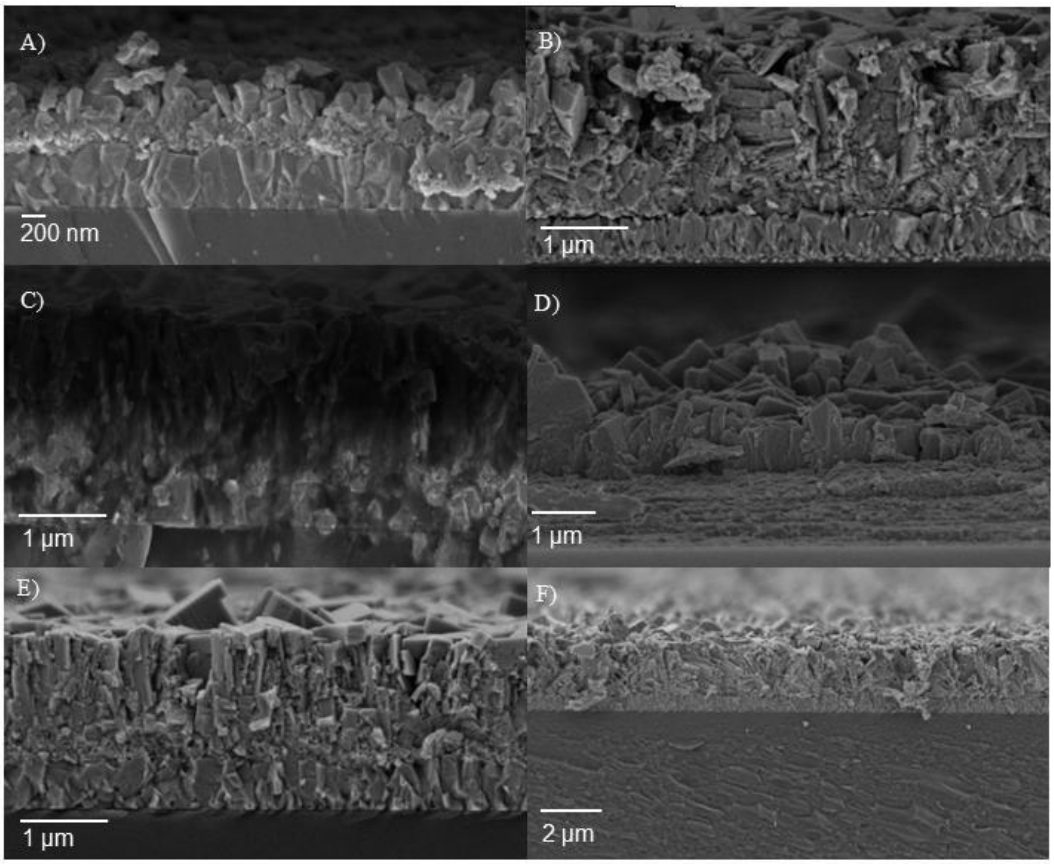

Figure 11.6: SEM images cross section of the hydrothermally grown WO_3 thin films synthesized from the dynamic spin coated seed layer. The labels are chosen according to the notation in Table 4. (Reprinted with permission of the Royal Society of Chemistry 2023).[111]

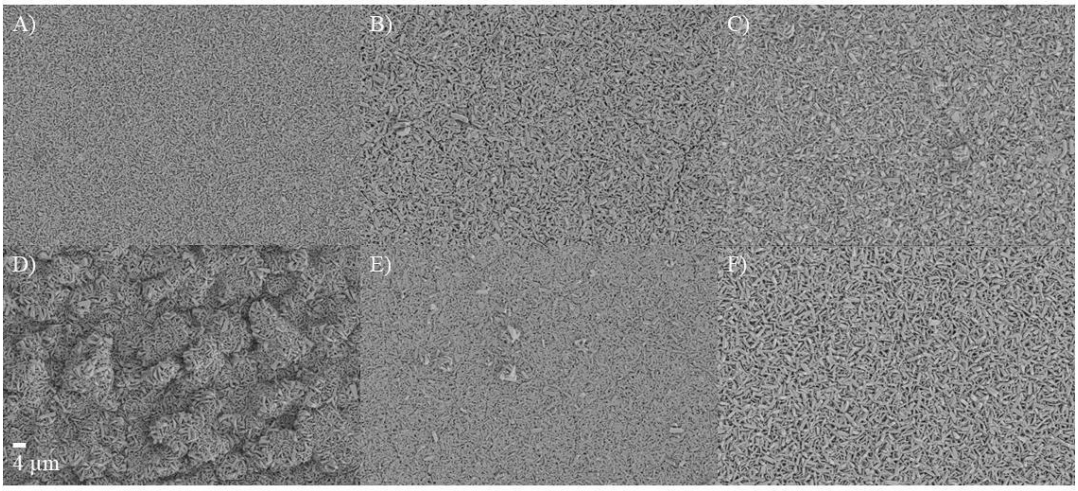

Figure 11.7: Overview SEM images of hydrothermally grown WO_3 films from the seed layer using dynamic spin coating. Same scale for all measurements. (Reprinted with permission of the Royal Society of Chemistry 2023).[111]

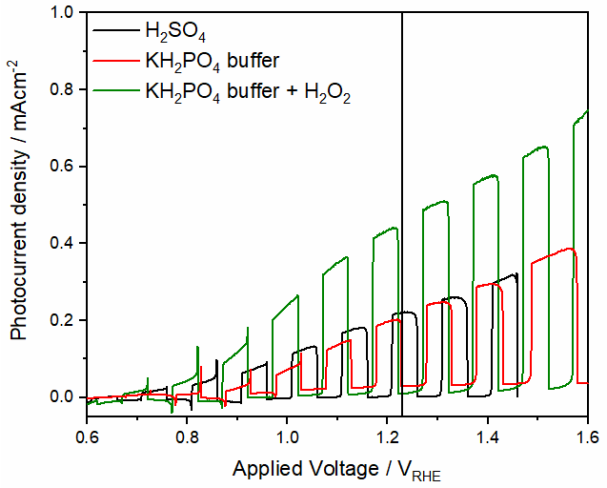

Figure 11.8: CLV measurements in KH_2PO_4 as electrolyte with and without H_2O_2 as a hole scavenger. The black line represents the water splitting potential 1.23 V_{RHE} (Reprinted with permission of the Royal Society of Chemistry 2023).[111]

11.2. Additional figures for chapter 7

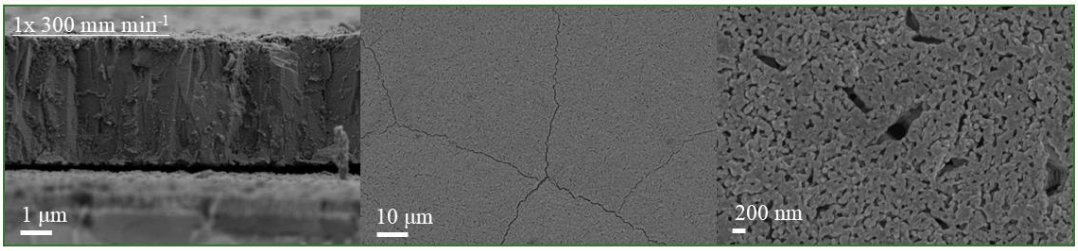

Figure 11.9: Additional SEM images of the WO_3/Mo:$BiVO_4$ heterostructure synthesized by single dip coating with a withdrawal speed of 300 mm min^{-1}.

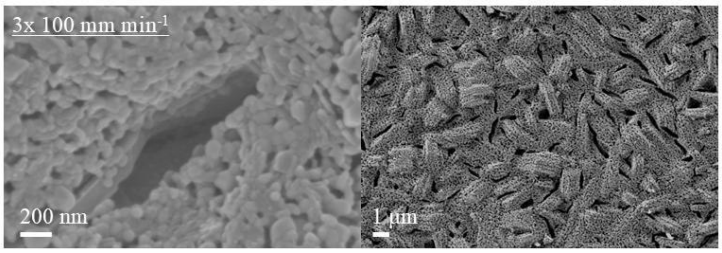

Figure 11.10: SEM images of the WO_3/Mo:$BiVO_4$ heterostructure synthesized by triple dip coating using a withdrawal speed of 100 mm min^{-1}.

12.References

[1] IEA, *World Energy Balance*, Paris, **2024**.

[2] R. van de Krol, M. Grätzel, *Photoelectrochemical Hydrogen Production*, Springer Science And Business Media LLC, New York, **2012**.

[3] K. Calvin, D. Dasgupta, G. Krinner, et al., *IPCC, 2023: Climate Change 2023: Synthesis Report. Contribution of Working Groups I, II and III to the Sixth Assessment Report of the Intergovernmental Panel on Climate Change [Core Writing Team, H. Lee and J. Romero (Eds.)]. IPCC, Geneva, Switzerland.*, **2023**.

[4] IPCC, *Global Warming of 1.5°C. An IPCC Special Report on the Impacts of Global Warming of 1.5°C above Pre-Industrial Levels and Related Global Greenhouse Gas Emission Pathways, in the Context of Strengthening the Global Response to the Threat of Climate Change, IPCC, Geneva, Switzerland.* **2018**.

[5] W. J. Ripple, C. Wolf, T. M. Newsome, P. Barnard, W. R. Moomaw, *Bioscience* **2020**, *70*, 8–12.

[6] J. Oppenheim, E. D. Beinhocker, *Climate change and the economy - Myths versus Realities*, *Davos, Switzerland. McKinsey Company, Inc.* **2009**.

[7] G. Krinner, M. Shongwe, J. Arblaster, J.-L. Dufresne, T. Fichefte, P. Friedlingstein, X. Gao, W. Gutowski Jr., T. Johns, C. Tebaldi, A. J. Weaver, M. Wehner, *Long-Term Climate Change: Projections, Commitments and Irreversibility*, **2013**.

[8] H. Ritchie, M. Roser, *Fossil Fuels*, **2020**.

[9] F. Kourougianni, A. Arsalis, A. V. Olympios, G. Yiasoumas, C. Konstantinou, P. Papanastasiou, G. E. Georghiou, *Renew. Energy* **2024**, 120911.

[10] United Nations Framework Convention on Climate Change, Paris, **2015**.

[11] A. M. Waple, J. H. Lawrimore, *Bull. Am. Meteorol. Soc.* **2019**, *100*.

[12] bp, *BP Statistical Review of World Energy*, London, **2022**.

[13] E. Kabir, P. Kumar, S. Kumar, A. A. Adelodun, K. H. Kim, *Renew. Sustain. Energy Rev.* **2018**, *82*, 894–900.

[14] M. Perez, R. Perez, *Sol. Energy Adv.* **2022**, *2*, 100014.

[15] D. Larcher, J.-M. Tarascon, *Nat. Chem.* **2015**, *7*, 19–29.

[16] J.-M. Tarascon, M. Armand, *Nature* **2001**, *414*, 359–367.

[17] K. Mazloomi, C. Gomes, *Renew. Sustain. Energy Rev.* **2012**, *16*, 3024–3033.

[18] B. A. Pinaud, J. D. Benck, L. C. Seitz, A. J. Forman, Z. Chen, T. G. Deutsch, B. D. James, K. N. Baum, G. N. Baum, S. Ardo, H. Wang, E. Miller, T. F. Jaramillo, *Energy Environ. Sci.* **2013**, *6*, 1983–2002.

[19] C. Sorrell, *Int. J. Hydrogen Energy* **2010**, *27*, 991–1022.

[20] G. Collodi, F. Wheeler, *Chem. Eng. Trans.* **2010**, *19*, 37–42.

[21] M. Katebah, M. Al-Rawashdeh, P. Linke, *Clean. Eng. Technol.* **2022**, *10*, 100552.

[22] M. Kayfeci, A. Kecebas, M. Bayat, *Solar Hydrogen Production*, Elsevier, **2019**.

[23] B. D. Alexander, P. J. Kulesza, I. Rutkowska, R. Solarska, J. Augustynski, *J. Mater. Chem.* **2008**, *18*, 2298–2303.

[24] J. Cheng, T. J. Deming, *Pept. Mater.* **2011**, *310*, 1–26.

[25] Z. F. Huang, L. Pan, J. J. Zou, X. Zhang, L. Wang, *Nanoscale* **2014**, *6*, 14044–14063.

[26] Z. F. Huang, J. Song, L. Pan, X. Zhang, L. Wang, J. J. Zou, *Adv. Mater.* **2015**, *27*, 5309–5327.

[27] Y. Pihosh, I. Turkevych, K. Mawatari, J. Uemura, Y. Kazoe, S. Kosar, K. Makita, T. Sugaya, T. Matsui, D. Fujita, M. Tosa, M. Kondo, T. Kitamori, *Sci. Rep.* **2015**, *5*, 11141.

[28] M. Rohloff, B. Anke, S. Zhang, U. Gernert, C. Scheu, M. Lerch, A. Fischer, *Sustain. Energy Fuels* **2017**, *1*, 1830–1846.

[29] S. Corby, L. Francàs, S. Selim, M. Sachs, C. Blackman, A. Kafizas, J. R. Durrant, *J. Am. Chem. Soc.* **2018**, *140*, 16168–16177.

[30] R. Gross, A. Marx, *Festkörperphysik*, De Gruyter, Leipzig, **2014**.

[31] R. S. Muller, T. I. Kamins, *Device Electronics for Integrated Circuits*, **2002**.

[32] M. G. Helander, M. T. Greiner, Z. B. Wang, W. M. Tang, Z. H. Lu, *J. Vac. Sci. Technol. A Vacuum, Surfaces, Film.* **2011**, *29*, 011019.

[33] A. I. Martínez, L. Huerta, J. M. O-Rueda De León, D. Acosta, O. Malik, M. Aguilar, *J.*

Phys. D. Appl. Phys. **2006**, *39*, 5091–5096.

[34] R. F. Pierret, *Semiconductor Device Fundamentals*, Addison-Wesley, Reading, Massachusetts, **1996**.

[35] M. A. Butler, *J. Electrochem. Soc.* **1978**, *125*, 228.

[36] H. Butt, K. Graf, M. Kappl, *Physics and Chemistry of Interfaces*, **2003**.

[37] R. Marschall, *Adv. Funct. Mater.* **2014**, *24*, 2421–2440.

[38] J. Low, J. Yu, M. Jaroniec, S. Wageh, A. A. Al-Ghamdi, *Adv. Mater.* **2017**, *29*, DOI 10.1002/adma.201601694.

[39] S. J. A. Moniz, S. A. Shevlin, D. J. Martin, Z.-X. Guo, J. Tang, *Energy Environ. Sci.* **2015**, *8*, 731–759.

[40] L. Schumacher, R. Marschall, *Top. Curr. Chem.* **2022**, *380*, 53.

[41] B. Ng, L. K. Putri, X. Y. Kong, Y. W. Teh, P. Pasbakhsh, S. Chai, *Adv. Sci.* **2020**, *7*, DOI 10.1002/advs.201903171.

[42] S. Bai, J. Jiang, Q. Zhang, Y. Xiong, *Chem. Soc. Rev.* **2015**, *44*, 2893–2939.

[43] J. S. Jang, H. G. Kim, J. S. Lee, *Catal. Today* **2012**, *185*, 270–277.

[44] P. A. Shinde, S. C. Jun, *ChemSusChem* **2020**, *13*, 11–38.

[45] Y. Park, K. J. Mc Donald, K. S. Choi, *Chem. Soc. Rev.* **2013**, *42*, 2321–2337.

[46] J. H. Kim, Y. J. Jang, J. H. Kim, J. W. Jang, S. H. Choi, J. S. Lee, *Nanoscale* **2015**, *7*, 19144–19151.

[47] Z. Zhang, P. Wang, *J. Mater. Chem.* **2012**, *22*, 2456–2464.

[48] D. Barreca, P. Fornasiero, A. Gasparotto, V. Gombac, C. Maccato, T. Montini, E. Tondello, *ChemSusChem* **2009**, *2*, 230–233.

[49] A. Bloesser, J. Timm, H. Kurz, W. Milius, S. Hayama, J. Breu, B. Weber, R. Marschall, *Sol. RRL* **2020**, *4*, DOI 10.1002/solr.201900570.

[50] P. S. Basavarajappa, S. B. Patil, N. Ganganagappa, K. R. Reddy, A. V. Raghu, C. V. Reddy, *Int. J. Hydrogen Energy* **2020**, *45*, 7764–7778.

[51] R. Shwetharani, M. Sakar, C. A. N. Fernando, V. Binas, R. G. Balakrishna, *Catal. Sci.*

Technol. **2019**, *9*, 12–46.

[52] M. Ksibi, S. Rossignol, J.-M. Tatibouët, C. Trapalis, *Mater. Lett.* **2008**, *62*, 4204–4206.

[53] S. Sato, *Science (80-.).* **2002**, *295*, 626–627.

[54] W. Shao, H. Wang, X. Zhang, *Dalt. Trans.* **2018**, *47*, 12642–12646.

[55] A. Kudo, H. Kato, I. Tsuji, *Chem. Lett.* **2004**, *33*, 1534–1539.

[56] Y. Feng, J. Wu, Q. Chi, W. Li, Y. Yu, W. Fei, *Chem. Rev.* **2020**, *120*, 1710–1787.

[57] E. Lassner, W.-D. Schubert, in *Tungsten*, Springer US, Boston, MA, **1999**, pp. 1–59.

[58] P. Roussel, P. Labbe, D. Groult, *Acta Crystallogr. Sect. B* **2000**, *B56*, 377–391.

[59] B. Rodríguez, J. Dolado, J. López-Sánchez, P. Hidalgo, B. Méndez, *Nanomaterials* **2023**, *13*, 884.

[60] S. Balaji, Y. Djaoued, A.-S. Albert, R. Z. Ferguson, R. Brüning, *Chem. Mater.* **2009**, *21*, 1381–1389.

[61] J. Y. Zheng, Z. Haider, T. K. Van, A. U. Pawar, M. J. Kang, C. W. Kim, Y. S. Kang, *CrystEngComm* **2015**, *17*, 6070–6093.

[62] S. Wang, H. Chen, G. Gao, T. Butburee, M. Lyu, S. Thaweesak, J. H. Yun, A. Du, G. Liu, L. Wang, *Nano Energy* **2016**, *24*, 94–102.

[63] M. Ling, C. S. Blackman, R. G. Palgrave, C. Sotelo-Vazquez, A. Kafizas, I. P. Parkin, *Adv. Mater. Interfaces* **2017**, *4*, DOI 10.1002/admi.201700064.

[64] J. E. Yourey, K. J. Pyper, J. B. Kurtz, B. M. Bartlett, *J. Phys. Chem. C* **2013**, *117*, 8708–8718.

[65] K. Mahmood, B. S. Swain, A. R. Kirmani, A. Amassian, *J. Mater. Chem. A* **2015**, *3*, 9051–9057.

[66] M. A. Butler, *J. Appl. Phys.* **1977**, *48*, 1914–1920.

[67] B. Cole, B. Marsen, E. Miller, Y. Yan, B. To, K. Jones, M. Al-Jassim, *J. Phys. Chem. C* **2008**, *112*, 5213–5220.

[68] Y. Djaoued, S. Balaji, R. Brüning, *J. Nanomater.* **2012**, *2012*, 1–9.

[69] M. W. Kanan, D. G. Nocera, *Science (80-.).* **2008**, *321*, 1072–1075.

[70] J. A. Seabold, K. S. Choi, *Chem. Mater.* **2011**, *23*, 1105–1112.

[71] G. Wang, Y. Ling, D. A. Wheeler, K. E. N. George, K. Horsley, C. Heske, J. Z. Zhang, Y. Li, *Nano Lett.* **2011**, *11*, 3503–3509.

[72] J. Zhang, P. Zhang, T. Wang, J. Gong, *Nano Energy* **2015**, *11*, 189–195.

[73] G. Wang, Y. Ling, Y. Li, *Nanoscale* **2012**, *4*, 6682.

[74] Y. P. Xie, G. Liu, L. Yin, H. M. Cheng, *J. Mater. Chem.* **2012**, *22*, 6746–6751.

[75] M. Pourbaix, *Mater. Sci. Forum* **1974**, 43–54.

[76] A. Kuzmin, A. Anspoks, A. Kalinko, J. Timoshenko, R. Kalendarev, *Sol. Energy Mater. Sol. Cells* **2015**, *143*, 627–634.

[77] I. S. Cho, C. H. Kwak, D. W. Kim, S. Lee, K. S. Hong, *J. Phys. Chem. C* **2009**, *113*, 10647–10653.

[78] M. Harb, A. Ziani, K. Takanabe, *Phys. status solidi* **2016**, *253*, 1115–1119.

[79] M. Kölbach, I. J. Pereira, K. Harbauer, P. Plate, K. Höflich, S. P. Berglund, D. Friedrich, R. Van De Krol, F. F. Abdi, *Chem. Mater.* **2018**, *30*, 8322–8331.

[80] F. Bozheyev, E. M. Akinoglu, L. Wu, H. Lu, R. Nemkayeva, Y. Xue, M. Jin, M. Giersig, *Int. J. Hydrogen Energy* **2020**, *45*, 8676–8685.

[81] I.-S. Cho, C. H. Kwak, D. W. Kim, S. Lee, K. S. Hong, *J. Phys. Chem. C* **2009**, *113*, 10647–10653.

[82] S. Zhu, D. Liu, J. Li, Y. Kuang, *ACS Appl. Energy Mater.* **2022**, *5*, 14372–14380.

[83] H. Kong, F. F. Abdi, *Inorg. Chem. Front.* **2023**, *10*, 7109–7125.

[84] K. J. Pyper, T. C. Evans, B. M. Bartlett, *Chinese Chem. Lett.* **2015**, *26*, 474–478.

[85] Z. Zhu, P. Sarker, C. Zhao, L. Zhou, R. L. Grimm, M. N. Huda, P. M. Rao, *ACS Appl. Mater. Interfaces* **2017**, *9*, 1459–1470.

[86] Y. Liu, W. Qiu, G. He, K. Wang, Y. Wang, L. Chen, Q. Wu, W. Li, J. Li, *J. Phys. Chem. C* **2022**, *126*, 15596–15605.

[87] S. Tokunaga, H. Kato, A. Kudo, *Chem. Mater.* **2001**, *13*, 4624–4628.

[88] J. Yu, A. Kudo, *Adv. Funct. Mater.* **2006**, *16*, 2163–2169.

[89] A. Kudo, Y. Miseki, *Chem. Soc. Rev.* **2009**, *38*, 253–278.

[90] J. K. Cooper, S. Gul, F. M. Toma, L. Chen, P.-A. Glans, J. Guo, J. W. Ager, J. Yano, I. D. Sharp, *Chem. Mater.* **2014**, *26*, 5365–5373.

[91] Y. Hermans, A. Klein, K. Ellmer, R. van de Krol, T. Toupance, W. Jaegermann, *J. Phys. Chem. C* **2018**, *122*, 20861–20870.

[92] F. F. Abdi, T. J. Savenije, M. M. May, B. Dam, R. van de Krol, *J. Phys. Chem. Lett.* **2013**, *4*, 2752–2757.

[93] T. Yao, X. An, H. Han, J. Q. Chen, C. Li, *Adv. Energy Mater.* **2018**, *8*, DOI 10.1002/aenm.201800210.

[94] J. H. Kim, J. S. Lee, *Adv. Mater.* **2019**, *31*, DOI 10.1002/adma.201806938.

[95] A. Kudo, K. Ueda, H. Kato, I. Mikami, *Catal. Letters* **1998**, *53*, 229–230.

[96] M. Gotić, S. Musić, M. Ivanda, M. Šoufek, S. Popović, *J. Mol. Struct.* **2005**, *744–747*, 535–540.

[97] W. Yin, W. Wang, L. Zhou, S. Sun, L. Zhang, *J. Hazard. Mater.* **2010**, *173*, 194–199.

[98] B. Anke, M. Rohloff, M. G. Willinger, W. Hetaba, A. Fischer, M. Lerch, *Solid State Sci.* **2017**, *63*, 1–8.

[99] J. Yu, A. Kudo, *Adv. Funct. Mater.* **2006**, *16*, 2163–2169.

[100] D. Ke, T. Peng, L. Ma, P. Cai, K. Dai, *Inorg. Chem.* **2009**, *48*, 4685–4691.

[101] J. Liu, H. Wang, S. Wang, H. Yan, *Mater. Sci. Eng. B* **2003**, *104*, 36–39.

[102] G. Liu, S. Liu, Q. Lu, H. Sun, F. Xu, G. Zhao, *J. Sol-Gel Sci. Technol.* **2014**, *70*, 24–32.

[103] H. Liu, R. Nakamura, Y. Nakato, *J. Electrochem. Soc.* **2005**, *152*, G856.

[104] W. Liu, L. Cao, G. Su, H. Liu, X. Wang, L. Zhang, *Ultrason. Sonochem.* **2010**, *17*, 669–674.

[105] L. Zhou, W. Wang, S. Liu, L. Zhang, H. Xu, W. Zhu, *J. Mol. Catal. A Chem.* **2006**, *252*, 120–124.

[106] J. Eichhorn, C. Kastl, J. K. Cooper, D. Ziegler, A. M. Schwartzberg, I. D. Sharp, F. M. Toma, *Nat. Commun.* **2018**, *9*, 2597.

[107] F. F. Abdi, N. Firet, R. van de Krol, *ChemCatChem* **2013**, *5*, 490–496.

[108] P. Chatchai, Y. Murakami, S. Kishioka, A. Y. Nosaka, Y. Nosaka, *Electrochim. Acta* **2009**, *54*, 1147–1152.

[109] P. Chatchai, S. Kishioka, Y. Murakami, A. Y. Nosaka, Y. Nosaka, *Electrochim. Acta* **2010**, *55*, 592–596.

[110] J. Su, L. Guo, N. Bao, C. A. Grimes, *Nano Lett.* **2011**, *11*, 1928–1933.

[111] M. Ade, L. Schumacher, R. Marschall, *Sustain. Energy Fuels* **2023**, *7*, 4332–4340.

[112] S. Y. Chae, C. S. Lee, H. Jung, O.-S. Joo, B. K. Min, J. H. Kim, Y. J. Hwang, *ACS Appl. Mater. Interfaces* **2017**, *9*, 19780–19790.

[113] S. S. Kalanur, I.-H. Yoo, J. Park, H. Seo, *J. Mater. Chem. A* **2017**, *5*, 1455–1461.

[114] N. Iqbal, I. Khan, Z. H. A. Yamani, A. Qurashi, *Sol. Energy* **2017**, *144*, 604–611.

[115] Y. Zhou, L. Zhang, L. Lin, B. R. Wygant, Y. Liu, Y. Zhu, Y. Zheng, C. B. Mullins, Y. Zhao, X. Zhang, G. Yu, *Nano Lett.* **2017**, *17*, 8012–8017.

[116] B. R. Lee, M. G. Lee, H. Park, T. H. Lee, S. A. Lee, S. S. M. Bhat, C. Kim, S. Lee, H. W. Jang, *ACS Appl. Mater. Interfaces* **2019**, *11*, 20004–20012.

[117] I. Grigioni, G. Di Liberto, M. V. Dozzi, S. Tosoni, G. Pacchioni, E. Selli, *ACS Appl. Energy Mater.* **2021**, *4*, 8421–8431.

[118] J. Liu, W. Chen, Q. Sun, Y. Zhang, X. Li, J. Wang, C. Wang, Y. Yu, L. Wang, X. Yu, *ACS Appl. Energy Mater.* **2021**, *4*, 2864–2872.

[119] I. Grigioni, A. Polo, M. V. Dozzi, K. G. Stamplecoskie, D. H. Jara, P. V. Kamat, E. Selli, *ACS Appl. Energy Mater.* **2022**, *5*, 13142–13148.

[120] T. Hisatomi, J. Kubota, K. Domen, *Chem. Soc. Rev.* **2014**, *43*, 7520–7535.

[121] I. Roger, M. A. Shipman, M. D. Symes, *Nat. Rev. Chem.* **2017**, *1*, 0003.

[122] J. Yang, D. Wang, H. Han, C. Li, *Acc. Chem. Res.* **2013**, *46*, 1900–1909.

[123] W. Wang, M. Xu, X. Xu, W. Zhou, Z. Shao, *Angew. Chemie Int. Ed.* **2020**, *59*, 136–152.

[124] A. Enesca, A. Duta, J. Schoonman, *Thin Solid Films* **2007**, *515*, 6371–6374.

[125] X. Liu, F. Wang, Q. Wang, *Phys. Chem. Chem. Phys.* **2012**, *14*, 7894–7911.

[126] D. A. Wheeler, G. Wang, Y. Ling, Y. Li, J. Z. Zhang, *Energy Environ. Sci.* **2012**, *5*, 6682–6702.

[127] W. Li, J. Liu, D. Zhao, *Nat. Rev. Mater.* **2016**, *1*, 16023.

[128] N. Linares, A. M. Silvestre-Albero, E. Serrano, J. Silvestre-Albero, J. García-Martínez, *Chem. Soc. Rev.* **2014**, *43*, 7681–7717.

[129] L. M. Peter, J. Li, R. Peat, *J. Electroanal. Chem.* **1984**, *165*, 29–40.

[130] P. Salvador, C. Gutiérrez, *J. Electroanal. Chem.* **1984**, *160*, 117–130.

[131] Z. Chen, H. N. Dinh, E. Miller, *Photoelectrochemical Water Splitting*, **2013**.

[132] 2003e1 ASTM Standard G173, **2003**, DOI 10.1520/G0173-03E01.

[133] D. Gunawan, J. Zhang, Q. Li, C. Y. Toe, J. Scott, M. Antonietti, J. Guo, R. Amal, *Adv. Mater.* **2024**, DOI 10.1002/adma.202404618.

[134] C. Santato, M. Ulmann, J. Augustynski, *Adv. Mater.* **2001**, *13*, 511–514.

[135] L. Kavan, M. Grätzel, *Electrochim. Acta* **1995**, *40*, 643–652.

[136] S. Chen, T. Takata, K. Domen, *Nat. Rev. Mater.* **2017**, *2*, 17050.

[137] X. Zou, Y. Zhang, *Chem. Soc. Rev.* **2015**, *44*, 5148–5180.

[138] J. Ran, J. Zhang, J. Yu, M. Jaroniec, S. Z. Qiao, *Chem. Soc. Rev.* **2014**, *43*, 7787–7812.

[139] H. Dotan, K. Sivula, M. Grätzel, A. Rothschild, S. C. Warren, *Energy Environ. Sci.* **2011**, *4*, 958–964.

[140] H. Gerischer, N. Müller, O. Haas, *J. Electroanal. Chem. Interfacial Electrochem.* **1981**, *119*, 41–48.

[141] B. P. Minks, D. Vanmaekelbergh, J. J. Kelly, *J. Electroanal. Chem. Interfacial Electrochem.* **1989**, *273*, 133–145.

[142] A. Theuwis, I. E. Vermeir, W. P. Gomes, *J. Electroanal. Chem.* **1996**, *410*, 31–42.

[143] A. Duret, M. Grätzel, *J. Phys. Chem. B* **2005**, *109*, 17184–17191.

[144] J. Wu, *Chem. Rev.* **2022**, *122*, 10821–10859.

[145] M. Radecka, P. Sobas, M. Wierzbicka, M. Rekas, *Phys. B Condens. Matter* **2005**, *364*, 85–92.

[146] R. Memming, *Semiconductor Electrochemistry*, Wiley-VCH, Weinheim, **2001**.

[147] K. Sivula, *ACS Energy Lett.* **2021**, *6*, 2549–2551.

[148] J. Noack, N. Roznyatovskaya, T. Herr, P. Fischer, *Angew. Chemie - Int. Ed.* **2015**, *54*, 9776–9809.

[149] M. Guarnieri, P. Mattavelli, G. Petrone, G. Spagnuolo, *IEEE Ind. Electron. Mag.* **2016**, *10*, 20–31.

[150] M. Gencten, Y. Sahin, *Int. J. Energy Res.* **2020**, *44*, 7903–7923.

[151] E. Agar, K. W. Knehr, D. Chen, M. A. Hickner, E. C. Kumbur, *Electrochim. Acta* **2013**, *98*, 66–74.

[152] A. Tang, J. Bao, M. Skyllas-Kazacos, *J. Power Sources* **2011**, *196*, 10737–10747.

[153] C. Sun, J. Chen, H. Zhang, X. Han, Q. Luo, *J. Power Sources* **2010**, *195*, 890–897.

[154] Q. Luo, L. Li, W. Wang, Z. Nie, X. Wei, B. Li, B. Chen, Z. Yang, V. Sprenkle, *ChemSusChem* **2013**, *6*, 268–274.

[155] T. Mohammadi, S. C. Chieng, M. Skyllas Kazacos, *J. Memb. Sci.* **1997**, *133*, 151–159.

[156] T. MOHAMMADI, M. S. KAZACOS, *J. Appl. Electrochem.* **1997**, *27*, 153–160.

[157] C. Choi, S. Kim, R. Kim, Y. Choi, S. Kim, H. young Jung, J. H. Yang, H. T. Kim, *Renew. Sustain. Energy Rev.* **2017**, *69*, 263–274.

[158] C. Madic, G. M. Begun, R. L. Hahn, J. P. Launay, W. E. Thiessen, *Inorg. Chem.* **1984**, *23*, 469–476.

[159] N. Kausar, R. Howe, M. Skyllas-Kazacos, *J. Appl. Electrochem.* **2001**, *31*, 1327–1332.

[160] X. Lu, *Electrochim. Acta* **2001**, *46*, 4281–4287.

[161] M. Vijayakumar, L. Li, G. Graff, J. Liu, H. Zhang, Z. Yang, J. Z. Hu, *J. Power Sources* **2011**, *196*, 3669–3672.

[162] M. Gattrell, J. Park, B. MacDougall, J. Apte, S. McCarthy, C. W. Wu, *J. Electrochem. Soc.* **2004**, *151*, A123.

[163] M. Vijayakumar, S. D. Burton, C. Huang, L. Li, Z. Yang, G. L. Graff, J. Liu, J. Hu, S. K. Maria, *J. Power Sources* **2010**, *195*, 7709–7717.

[164] X. Wu, J. Wang, S. Liu, X. Wu, S. Li, *Electrochim. Acta* **2011**, *56*, 10197–10203.

[165] D. N. Buckley, X. Gao, R. P. Lynch, N. Quill, M. J. Leahy, *J. Electrochem. Soc.* **2014**, *161*, A524–A534.

[166] C. Ding, H. Zhang, X. Li, T. Liu, F. Xing, *J. Phys. Chem. Lett.* **2013**, *4*, 1281–1294.

[167] M. Skyllas-Kazacos, *Electrochem. Solid-State Lett.* **1999**, *2*, 121.

[168] L. Li, S. Kim, W. Wang, M. Vijayakumar, Z. Nie, B. Chen, J. Zhang, G. Xia, J. Hu, G. Graff, J. Liu, Z. Yang, *Adv. Energy Mater.* **2011**, *1*, 394–400.

[169] D. C. Crans, A. S. Tracey, *ACS Symp. Ser.* **1998**, *711*, 2–29.

[170] X. Yu, G. Liu, T. Wang, H. Gong, H. Qu, X. Meng, J. He, J. Ye, *Chem. – A Eur. J.* **2022**, *28*, DOI 10.1002/chem.202202104.

[171] X. Dong, X. Chen, X. Jiang, N. Yang, *Adv. Energy Mater.* **2023**, *13*, DOI 10.1002/aenm.202301143.

[172] Y.-X. Tan, X. Zhang, J. Lin, Y. Wang, *Energy Environ. Sci.* **2023**, *16*, 2432–2447.

[173] X. Lin, Z. Liu, X. Wang, P. Li, D. Yu, *Small Sci.* **2023**, *3*, DOI 10.1002/smsc.202300034.

[174] H. Feng, D. Liu, Y. Zhang, X. Shi, O. C. Esan, Q. Li, R. Chen, L. An, *Adv. Energy Mater.* **2022**, *12*, 1–28.

[175] X. Ke, J. M. Prahl, J. I. D. Alexander, J. S. Wainright, T. A. Zawodzinski, R. F. Savinell, *Chem. Soc. Rev.* **2018**, *47*, 8721–8743.

[176] Y. Ding, C. Zhang, L. Zhang, Y. Zhou, G. Yu, *Chem. Soc. Rev.* **2018**, *47*, 69–103.

[177] Z. Fang, X. Hu, D. Yu, *Chempluschem* **2020**, *85*, 600–612.

[178] G. HODES, J. MANASSEN, D. CAHEN, *Nature* **1976**, *261*, 403–404.

[179] W. D. McCulloch, M. Yu, Y. Wu, *ACS Energy Lett.* **2016**, *1*, 578–582.

[180] A. Khataee, J. Azevedo, P. Dias, D. Ivanou, E. Dražević, A. Bentien, A. Mendes, *Nano Energy* **2019**, *62*, 832–843.

[181] Z. Wei, D. Liu, C. Hsu, F. Liu, *Electrochem. commun.* **2014**, *45*, 79–82.

[182] D. Liu, W. Zi, S. D. Sajjad, C. Hsu, Y. Shen, M. Wei, F. Liu, *ACS Catal.* **2015**, *5*, 2632–2639.

[183] H. Feng, X. Jiao, R. Chen, X. Zhu, Q. Liao, D. Ye, B. Zhang, *J. Power Sources* **2018**, *404*, 1–6.

[184] Z. Wei, Y. Shen, D. Liu, C. Hsu, S. D. Sajjad, K. Rajeshwar, F. Liu, *Nano Energy* **2016**, *26*, 200–207.

[185] H. Feng, X. Jiao, R. Chen, X. Zhu, Q. Liao, D. Ye, B. Zhang, W. Zhang, *J. Power Sources* **2019**, *419*, 162–170.

[186] Y. Y. Lin, H. Feng, R. Chen, D. D. Ye, B. Zhang, Y. X. Yu, J. W. Li, *Sci. China Technol. Sci.* **2019**, *62*, 1628–1635.

[187] H. Yoo, D. Lee, J. H. Kim, *Green Energy Environ.* **2022**, *7*, 704–711.

[188] Z. Peimanifard, S. Rashid-Nadimi, *J. Power Sources* **2015**, *300*, 395–401.

[189] B. K. Durant, Y. She, P. Wang, T. Kraus, B. A. Parkinson, *J. Electrochem. Soc.* **2019**, *166*, H3001–H3008.

[190] A. Kumtepe, C. T. Altaf, N. S. Sahsuvar, N. Abdullayeva, E. Koseoglu, M. Sankir, N. D. Sankir, *ACS Appl. Energy Mater.* **2020**, *3*, 3127–3133.

[191] J. Li, Y. Lin, R. Chen, X. Zhu, D. Ye, Y. Yang, Y. Yu, D. Wang, Q. Liao, *J. Energy Storage* **2021**, *43*, 103228.

[192] J. Ma, Z. Pan, G. Tagliabue, *Sol. RRL* **2024**, *8*, DOI 10.1002/solr.202400477.

[193] D. K. Zhong, M. Cornuz, K. Sivula, M. Grätzel, D. R. Gamelin, *Energy Environ. Sci.* **2011**, *4*, 1759–1764.

[194] M. R. Nellist, F. A. L. Laskowski, J. Qiu, H. Hajibabaei, K. Sivula, T. W. Hamann, S. W. Boettcher, *Nat. Energy* **2017**, *3*, 46–52.

[195] Y. Waseda, E. Matsubara, K. Shinoda, *X-Ray Diffraction Crystallography*, Springer Berlin Heidelberg, Berlin, Heidelberg, **2011**.

[196] L. Spieß, G. Teichert, R. Schwarzer, H. Behnken, C. Genzel, *Moderne Röntgenbeugung*, **2019**.

[197] J. F. Watts, J. Wolstenholme, *An Introduction to Surface Analysis by XPS and AES*, J. Wiley, Chichester, UK, **2003**.

[198] T. Owen, *Fundamentals of Modern UV-Visible Spectroscopy*, Agilent Technologies,

Santa Clara, **1996**.

[199] P. Makuła, M. Pacia, W. Macyk, *J. Phys. Chem. Lett.* **2018**, *9*, 6814–6817.

[200] E. Smith, G. Dent, *Modern Raman Spectroscopy - A Practical Approach*, John Wiley & Sons, Ltd, Chichester, **2005**.

[201] J. I. Goldstein, D. E. Newbury, J. R. Michael, N. W. M. Ritchie, J. H. J. Scott, D. C. Joy, *Scanning Electron Microscopy and X-Ray Microanalysis*, Springer Science And Business Media LLC, New York, **2017**.

[202] A. Ul-Hamid, *A Beginners' Guide to Scanning Electron Microscopy*, Springer Nature Switzerland AG, Cham, **2018**.

[203] J. I. Goldstein, D. E. Newbury, P. Echlin, D. C. Joy, C. E. Lyman, E. Lifshin, L. Sawyer, J. R. Michael, *Scanning Electron Microscopy and X-Ray Microanalysis*, Springer US, Boston, MA, **2003**.

[204] P. Eaton, in *Kirk-Othmer Encycl. Chem. Technol.*, Wiley, **2011**, pp. 1–19.

[205] M. E. Orazem, B. Tribollet, *Electrochemical Impedance Spectroscopy*, John Wiley & Sons, Ltd, Hoboken, New Jersey, **2017**.

[206] F. C. Krebs, *Sol. Energy Mater. Sol. Cells* **2009**, *93*, 394–412.

[207] F. Yang, D. W. Kang, Y. S. Kim, *RSC Adv.* **2017**, *7*, 19030–19038.

[208] E. I. Ross-Medgaarden, I. E. Wachs, *J. Phys. Chem. C* **2007**, *111*, 15089–15099.

[209] F. S. Manciu, J. L. Enriquez, W. G. Durrer, Y. Yun, C. V. Ramana, S. K. Gullapalli, *J. Mater. Res.* **2010**, *25*, 2401–2406.

[210] Y. H. Li, P. F. Liu, L. F. Pan, H. F. Wang, Z. Z. Yang, L. R. Zheng, P. Hu, H. J. Zhao, L. Gu, H. G. Yang, *Nat. Commun.* **2015**, *6*, 8064.

[211] V. Chakrapani, M. Brier, A. Puntambekar, T. DiGiovanni, *J. Mater. Res.* **2016**, *31*, 17–27.

[212] R. Liu, Y. Lin, L.-Y. Chou, S. W. Sheehan, W. He, F. Zhang, H. J. M. Hou, D. Wang, *Angew. Chemie* **2011**, *123*, 519–522.

[213] H. Chen, J. Li, W. Yang, S. E. Balaghi, C. A. Triana, C. K. Mavrokefalos, G. R. Patzke, *ACS Catal.* **2021**, *11*, 7637–7646.

[214] X. Chen, J. Liu, H. Wang, Y. Ding, Y. Sun, H. Yan, *J. Mater. Chem. A* **2013**, *1*, 877–883.

[215] M. Tayebi, B. K. Lee, *Catal. Today* **2021**, *361*, 183–190.

[216] X. Zhao, N. Zhang, Y. Yu, T. Fang, J. Hu, J. Feng, Z. Chen, *Photocatal. Res. Potential* **2023**, *1*, 10002–10002.

[217] B. S. Kalanoor, H. Seo, S. S. Kalanur, *Mater. Sci. Energy Technol.* **2021**, *4*, 317–328.

[218] D. Lončarević, Ž. Čupić, in *Ind. Appl. Nanomater.*, Elsevier, **2019**, pp. 91–122.

[219] S. K. Sahoo, B. Manoharan, N. Sivakumar, in *Perovskite Photovoltaics*, Elsevier, **2018**, pp. 1–24.

[220] T. Schneller, R. Waser, M. Kosec, D. Payne, Eds. , *Chemical Solution Deposition of Functional Oxide Thin Films*, Springer Vienna, Vienna, **2013**.

[221] J. Su, X. Feng, J. D. Sloppy, L. Guo, C. A. Grimes, *Nano Lett.* **2011**, *11*, 203–208.

[222] W. Li, P. Da, Y. Zhang, Y. Wang, X. Lin, X. Gong, G. Zheng, *ACS Nano* **2014**, *8*, 11770–11777.

[223] S. Hilliard, G. Baldinozzi, D. Friedrich, S. Kressman, H. Strub, V. Artero, C. Laberty-Robert, *Sustain. Energy Fuels* **2017**, *1*, 145–153.

[224] A. de O. Jorgetto, M. V. Boldrin Zanoni, M. O. Orlandi, *Sci. Rep.* **2023**, *13*, 14774.

[225] S. Zhang, I. Ahmet, S. H. Kim, O. Kasian, A. M. Mingers, P. Schnell, M. Kölbach, J. Lim, A. Fischer, K. J. J. Mayrhofer, S. Cherevko, B. Gault, R. Van De Krol, C. Scheu, *ACS Appl. Energy Mater.* **2020**, *3*, 9523–9527.

[226] T. W. Kim, K. S. Choi, *J. Phys. Chem. Lett.* **2016**, *7*, 447–451.

[227] X. Li, H. Zhao, J. Huang, Y. Li, H. Miao, G. Shi, P. K. Wong, *J. Mater. Chem. A* **2024**, *12*, 16605–16616.

[228] T. Moehl, J. Suh, L. Sévery, R. Wick-Joliat, S. D. Tilley, *ACS Appl. Mater. Interfaces* **2017**, *9*, 43614–43622.

[229] J. Choi, J. T. Song, H. S. Jang, M.-J. Choi, D. M. Sim, S. Yim, H. Lim, Y. S. Jung, J. Oh, *Electron. Mater. Lett.* **2017**, *13*, 57–65.

[230] P. Yang, D. Zhao, D. I. Margolese, B. F. Chmelka, G. D. Stucky, *Nature* **1998**, *396*, 152–

155.

[231] B. Pant, M. Park, S. J. Park, *Coatings* **2019**, *9*, DOI 10.3390/coatings9100613.

[232] S. Obregón, V. Rodríguez-González, *J. Sol-Gel Sci. Technol.* **2022**, *102*, 125–141.

13. List of Scientific Contributions, Tables, Figures, Abbreviations and Symbols

13.1. Scientific Contributions

13.2. Peer-Reviewed Journals

M. Ade, L. Schumacher, R. Marschall

”Seed layer formation determines photocurrent response of hydrothermally-grown WO_3 photoanodes“, *Sustain. Energy Fuels* 2023, *7*, 4332 - 4340

13.3. Conference Contribution

Poster contribution to the 23rd International Conference on Photochemical Conversion and Storage of Solar Energy (IPS) 2022 in Lausanne, Switzerland, 02.08.2022 - 05.08.2022: M. Ade, L. Schumacher, R. Marschall, ”Seed layer formation determines photocurrent response of hydrothermally-grown WO_3 photoanodes“

Poster contribution to the 8^{th} International Conference on Semiconductor Photochemistry 2023 in Strasbourg, France, 11.09.2023 - 15.09.2023: M. Ade, L. Schumacher, R. Marschall, ”Seed layer formation determines photocurrent response of hydrothermally-grown WO_3 photoanodes“

13.4. List of Tables

13.5. List of figures

13.6. List of Abbreviation

Abbreavtion	Meaning
AFM	Atomic force measurement
ALD	Atomic layer deposition
APCE	Applied bias photon to current effieciency
AQDS	Anthraquinone-2,7-disulfonic acid
CLV	Chopped light voltammetry
CVD	Chemical vapor deposition
EDX	Energy dispersive X-ray spectroscopy
EIS	Electrochemical impedance spectroscopy
FTO	Fluorine doped tin oxide
GHG	Greenhouse gas
GIXRD	Gracing incidence X-ray diffraction
ICP	Inductively coupled plasma
IHP	Inner HELMHOLTZ plane
IMVS	Intensity modulated photovoltage spectroscopy
IPCC	International panel of climate change
IPCE	Incident photo to current efficiency
LCA	Life cycle assessment
OCP	Open circuit potential
OEC	Oxygen evolving catalyst
OHP	Outer HELMHOLTZ plane
PEC	Photo electrochemistry
PRFB	Photo Redox Flow Battery
PVA	Polyvinyl alcohol
RFB	Redox flow battery
RHE	Reversible hydrogen electrode
RMS	Root mean square
SCL	Space charge layer
SEM	Scanning electron microscopy
SOC	State of charge
STH	Solar to hydrogen efficiency

TDMAT	Tetrakis(dimethylamino)titan
TTIP	Titanium isopropoxide
VRFB	All vanadium redox flow battery
XPS	X-ray photoelectron spectroscopy
XRD	X-ray diffraction

13.7. List of Symbols

Symbol	Unit	Description
E^0_{red}	V	Reduction potential
E^0_{ox}	V	Oxidation potential
N_D	m^{-3}	Donor density
P_{light}	W	Light Power
j_{photo}	A	Current
k_B	$J\ K^{-1}$	BOLTZMANN constant
y_{H_2}		The amount of hydrogen produced per area
ε_0	$F\ m^{-1}$	Vacuum permittivity
η_{STH}		Efficiency
ΔE	V	Normal potential difference
ΔG	$kJ\ mol^{-1}$	Gibbs free energy
A	m^2	Area
c	$m\ s^{-1}$	Light speed
C	F	Capacity
e	C	Elemental charge
e^-		Electron
EA_{HL}	eV	Electron affinity
E_F	eV	FERMI Level
E_{CB}	eV	Conduction band energy level
E_{VB}	eV	Valance band energy level
F	$C\ mol^{-1}$	FARADY constant
F(R)	a.u.	KUBELKA-MUNK function
h	$J\ s^{-1}$	PLANK constant
h^+		holes
n		Number of electrons
R		Reflection
V	V	Voltage
ν	Hz	Frequency
Φ_M	eV	Work function
Φ_{SCL}	V	Space charge layer potential
ε	$F\ m^{-1}$	Vacuum permittivity

λ	nm	Wavelength
θ	°	Diffraction angle

14. Eidesstattliche Versicherungen und Erklärungen

(§ 9 Satz 2 Nr. 3 PromO BayNAT)

Hiermit versichere ich eidesstattlich, dass ich die Arbeit selbstständig verfasst und keine anderen als die von mir angegebenen Quellen und Hilfsmittel benutzt habe (vgl. Art. 97 Abs. 1 Satz 8 BayHIG).

(§ 9 Satz 2 Nr. 3 PromO BayNAT)

Hiermit erkläre ich, dass ich die Dissertation nicht bereits zur Erlangung eines akademischen Grades eingereicht habe und dass ich nicht bereits diese oder eine gleichartige Doktorprüfung endgültig nicht bestanden habe.

(§ 9 Satz 2 Nr. 4 PromO BayNAT)

Hiermit erkläre ich, dass ich Hilfe von gewerblichen Promotionsberatern bzw. -vermittlern oder ähnlichen Dienstleistern weder bisher in Anspruch genommen habe noch künftig in Anspruch nehmen werde.

(§ 9 Satz 2 Nr. 7 PromO BayNAT)

Hiermit erkläre ich mein Einverständnis, dass die elektronische Fassung der Dissertation unter Wahrung meiner Urheberrechte und des Datenschutzes einer gesonderten Überprüfung unterzogen werden kann.

(§ 9 Satz 2 Nr. 8 PromO BayNAT)

Hiermit erkläre ich mein Einverständnis, dass bei Verdacht wissenschaftlichen Fehlverhaltens Ermittlungen durch universitätsinterne Organe der wissenschaftlichen Selbstkontrolle stattfinden können.

Bayreuth den _____

_____

Mirco Ade